

# **Nanoparticles and nanocomposites for display applications**

Submitted by James Parsons

to the University of Exeter  
as a thesis for the degree of

Doctor of Philosophy in Physics

August 2009

**This thesis is available for Library use on the understanding that it is copyrighted material and no quotation from the thesis may be published without proper acknowledgement.**

**I certify that all material in this thesis which is not my own work has been identified and that no material has previously been submitted and approved for the award of a degree by this or any other University.**

**Signature:**.....

**Date:**.....

## Abstract

---

The optical response of metallic structures has attracted significant interest for various applications in recent years. Of particular relevance to display applications is the ability to optimize the intensity and wavelength of the radiation which is scattered by the structure. In this thesis, original studies are presented across three main sections which investigate the optical response of a variety of composite structures formed from metal and dielectric elements.

In the first section, the optical response of planar structures comprised of continuous metal and dielectric layers is discussed. An extensive study is conducted into the transmission pass-band characteristics exhibited by these structures, in particular the dependence on parameters such as metal layer thickness, layer spacing and the number of periods.

The second and third sections include examples of structures in which the metallic elements are non-continuous. The simulations required here are considerably more involved, and so an introduction is given to the computational techniques used in subsequent chapters, accompanied with results for a test structure. The structures in the second section include single metallic nanoparticles and particle pairs which exhibit localised surface plasmon resonances (LSPRs). It is also shown that when particles are arranged into periodic arrays, the properties of the LSPR may be significantly modified by long-range and short-range interactions. This has implications both in terms of the line shape of the optical response, and the sensitivity of the optical response to changes in the surrounding refractive index.

The third section includes an investigation into metallic layers which have been perforated with periodic arrangements of holes. These structures have attracted considerable attention in recent years due to the enhanced transmission which is observed when the periodicity of the hole array facilitates grating coupling to surface plasmon-polariton (SPP) modes associated with the metal film. It is shown that these structures also support localised resonances similar to those of metallic nanoparticles. A comparison is made between the LSPRs observed in metallic nanoparticle and nanohole arrays for which the periodicity is non-diffracting for frequencies in the vicinity of LSPRs. In the final part of the thesis the role of LSPRs in facilitating a negative index of refraction in electromagnetic metamaterials having a fishnet-type structure is investigated.

## Acknowledgements

---

I would like to take this opportunity to thank everybody who has contributed (both directly and indirectly) towards this project. It was towards the end of my undergraduate degree, when I first expressed an interest in possible PhD projects that I arranged an informal meeting with Roy. Somewhat fearful of the unknown, I was soon to be amazed by his enthusiasm for Science and a willingness to engage in discussion as if time stood still. This was incredibly reassuring to me, and I can honestly say that feeling of openness has never changed throughout this project. On my first meeting with Bill I found he too was bursting with ideas, offering plenty of useful advice and suggestions for the project which lay ahead of us. I have always found him to be extremely approachable and he has always made a considerable effort to pass by the office and ask how things were going. Without the supervision and guidance from Roy and Bill, I would not be in a position to write these acknowledgements at all.

Thanks to Hewlett Packard, firstly for their funding of this PhD, but also for the immense help from their staff based at the Bristol and Palo Alto research labs. Particular thanks to Adrian, Steve, Chris, Suzanne, Steph and Tim for all the useful advice and for their input to discussions at regular review meetings.

I must also express my thanks to the other members of the electromagnetic materials group with whom I have worked during the past three years. To Euan and Ian for the numerous discussions which have helped to clarify my understanding of so many aspects of plasmonics, and for their assistance with my publications. Thanks to Andy and Chris B for your help and expertise as regards all things SEM/FIB and microscope related. Also to Sharon who has had to put up with me in her office, frequently talking to myself or cursing at the computer screen. Two former partners in crime with whom I regularly enjoyed a few practical jokes are Baptisite and Martyn (“wrong-un”) Gadsdon, most of which are too inappropriate to be written here. In the final months of this project their presence has been greatly missed. To the members of the basement: Edmund, Chris H and Caroline, whose simultaneous arrival lead to a decrease in my productivity levels by at least a factor of 3. To the microwave crew – thanks to everyone, particularly Alastair, Matt and Celia with whom I have collaborated on some of the research into multilayer structures. Alastair and Roy have established a world leading microwave research facility and things look very promising indeed for this group. Matt and Ian too have produced some excellent

publications in recent years and I wish them both well for the future. Then there are the members of the technical workshop, particularly Pete Cann, Dave Jarvis and Matt Wears who have had the pleasure (if it can be called that) of providing me with the invaluable advice and numerous pieces of equipment for the evaporation system. To David Colridge, for allowing me to raid your laboratory for various bits and bobs, and for advice in recent months.

Finally, there have been many evenings of late when I have returned home with Physics on the brain, wanting to get my laptop out and finish various elements of my thesis, or check the results of calculations. I would like to thank my fantastic wife for her love and support throughout my PhD, and for putting up with me for many years. Without her none of this would have been possible.

## Table of contents

---

<b>Abstract</b>	<b>1</b>
<b>Acknowledgements</b>	<b>2-3</b>
<b>Table of Contents</b>	<b>4-6</b>
<b>List of Tables and Figures</b>	<b>7-18</b>
<b>Chapter 1 – Introduction</b>	<b>19-23</b>
1.1 Aim of Research	19
1.2 Outline of Thesis	21
<b>Chapter 2 – The optical response of continuous metal-dielectric multilayer structures exhibiting Fabry-Perot transmission resonances</b>	<b>24-53</b>
2.1 Introduction	24
2.2 Simulating the optical response of metal-dielectric multilayer structures	25
2.3 A review of previous studies involving multilayer structures	26
2.4 Experimental studies of single cavity structures (Ag-MgF <sub>2</sub> -Ag)	30
2.5 Multiple cavity structures (Ag-MgF <sub>2</sub> -Ag-MgF <sub>2</sub> .....)	34
2.6 Analogy with the classical example of masses coupled by springs	41
2.7 Transmittance enhancement through multiple cavity structures	42
2.8 Studies of Fabry-Perot transmission resonances at microwave frequencies	47
2.9 Concluding remarks	52
<b>Chapter 3 – Techniques used to simulate the scattering of electromagnetic radiation from metallic nanoparticle and nanohole structures</b>	<b>54-81</b>
3.1 Introduction	54
3.2 Mie Theory	54
3.3 The ‘T Matrix’ method	63
3.4 The Discrete Dipole Approximation (DDA)	64
3.5 The Finite Element method	65
3.6 The Finite Difference Time Domain method	69
3.7 Example scattering calculations for an 80 nm diameter Au sphere	70
3.8 Summary of results and concluding remarks	79
<b>Chapter 4 – The scattering of electromagnetic radiation from metallic nanoparticles</b>	<b>82-122</b>
4.1 Introduction	82
4.2 Fabrication using EBL and FIB techniques	83
4.3 The electromagnetic response of small metallic particles	86
4.4 Optical characterisation using dark-field spectroscopy	95
4.5 Excitation of higher-order LSPR modes	100
4.6 Arrangements of nanorods	110
4.7 Concluding remarks and summary of results	120

<b>Chapter 5 – The optical response of metallic nanoparticles arranged in periodic arrays</b>	<b>123-150</b>
5.1 Introduction	123
5.2 Modification of the single particle response in regular arrays	124
5.3 The effects of particle size variation	133
5.4 Refractive index sensitivity of nanoparticle arrays	136
5.5 Interparticle coupling and variations in the array period	142
5.6 Concluding remarks	149
<b>Chapter 6 – The optical response of nanometric films perforated with subwavelength holes</b>	<b>151-170</b>
6.1 Introduction	151
6.2 Enhanced transmission through optically thick perforated metal films	152
6.3 Localised resonances of holes in optically thin metal films	157
6.4 Studies of complementary metallic nanoparticle and nanohole arrays	159
6.5 Interhole coupling and variations in the array period	161
6.6 Effects of hole size and geometrical variations	165
6.7 Possible applications	168
6.8 Concluding remarks	169
<b>Chapter 7 – Interactions between Fabry-Perot and nanohole resonances</b>	<b>171-188</b>
7.1 Introduction	171
7.2 Optical response of a perforated metallic layer	172
7.3 Fabry-Perot resonances in metal-dielectric multilayer structures	173
7.4 Interactions between LSPRs and FP modes in perforated structures	175
7.5 Effects of hole diameter variation	179
7.6 Effects of metallic dispersion	181
7.7 Increasing the number of periods within the multilayer structure	184
7.8 Tunability of the interaction between LSPR/FP modes	186
7.9 Summary of results and concluding remarks	188
<b>Chapter 8 – The role of localised resonances in negative index metamaterials</b>	<b>189-213</b>
8.1 Introduction	189
8.2 The concept of a perfect lens, and negative refraction in perfect lensing applications	190
8.3 The response of a composite structure formed from metallic wires and split rings	192
8.4 Negative index response of fishnet-type metamaterial structures	197
8.5 Extraction of effective parameters	200
8.6 Localised resonances in fishnet-type metamaterials	205
8.7 Coupled LSPRs in stacked metallic nanohole and nanoparticle structures	207
8.8 Concluding remarks	213

<b>Chapter 9 – Conclusions and future work</b>	<b>214-220</b>
9.1 Summary	214
9.2 Possible applications	216
9.3 Future work	218
9.4 Publications	219
9.5 Disclosure	219
9.6 Conference presentations	219
<b>APPENDIX A – Multilayer optics</b>	<b>221-226</b>
A.1 Transmission and reflection at a single interface	221
A.2 The recursive Fresnel method	225
<b>APPENDIX B- Legendre polynomials and the solution of 2<sup>nd</sup> order ODE's</b>	<b>227-229</b>
<b>APPENDIX C - The generation of solutions to Bessel's equation</b>	<b>230-234</b>
<b>APPENDIX D - Fabrication of samples using a thermal evaporation technique</b>	<b>235-241</b>
D.1 Introduction	235
D.2 Experimental apparatus	235
D.3 Overview of operation	240
<b>List of References</b>	<b>242-249</b>

## List of Figures and Tables

---

**Figure 2.1:** The transmission and reflection of light in an arrangement formed from  $N$  isotropic layers.

**Figure 2.2:** The simulated transmittance spectrum<sup>10</sup> is shown for a multilayer structure comprised of 2.5 periods of 38 nm Ag and 233 nm MgF<sub>2</sub>. The structure is illuminated at normal incidence in air.

**Figure 2.3** *reproduced from reference 13:* A Gaussian wave packet (TM polarisation) with carrier wavelength 400 nm is incident at 45 degrees on an Ag-MgF<sub>2</sub> stack. The figure shows several snapshots of magnetic field intensity. The centre of the output pulse is shifted upwards by approximately 266 nm.

**Figure 2.4** *reproduced from reference 13:* A TM-polarized beam or pulse is incident from vacuum onto a metal layer at frequencies below the plasma frequency where the real part of the dielectric constant is negative. The preservation of the continuity of the normal component of the electric displacement vector (**D**) leads to a sign change in the  $E_z$  field component when the dielectric constants have opposite signs.

**Figure 2.5:** Experimental and simulated transmittance spectra for a structure consisting of 1.5 periods of 20 nm Ag / 140 nm MgF<sub>2</sub> on a silica slide ( $n_r = 1.46$ ,  $n_i = 0.00$ ), illuminated at normal incidence in air. The dashed line shows the simulated transmittance of a single 40 nm Ag film. Inset (a) shows a colour photograph of the structure viewed in transmission when illuminated with a diffuse white light source (the image has been normalised to the lamp spectrum), and inset (b) shows a schematic of the layering arrangement.

**Figure 2.6:** The time-averaged electric field intensity is shown for a cross section taken perpendicular to the 20 nm Ag / 140 nm MgF<sub>2</sub> / 20 nm Ag stack at an incident wavelength of 560 nm.

**Figure 2.7:** Simulated and experimental transmittance spectra are shown for two 20 nm Ag layers separated by 140, 180 and 200 nm of MgF<sub>2</sub>. The structure is on a silica slide ( $n_r = 1.46$ ,  $n_i = 0.00$ ) and is illuminated at normal incidence in air. The inset shows colour photographs of the structures viewed in transmission when illuminated with a diffuse white light source (normalised for the lamp spectrum).

**Figure 2.8:** Simulated transmittance and absorbance spectra for a structure consisting of 4.5 periods of 20 nm Ag / 110 nm MgF<sub>2</sub>. The structure is illuminated at normal incidence and is surrounded by glass ( $n_r = 1.52$ ,  $n_i = 0.00$ ).

**Figure 2.9:** The time-averaged electric field magnitude is plotted for a cross section taken perpendicular to the multilayer stack at the resonant wavelengths marked A-D in Figure 2.8.

**Figure 2.10:** Simulated transmission and absorbance spectrum of a structure consisting of 10.5 periods of 20 nm Ag / 110 nm MgF<sub>2</sub>. The structure is illuminated at normal incidence and is surrounded by glass  $n_r = 1.52$ ,  $n_i = 0.00$ .

**Figure 2.11:** The high frequency band edge of a multilayer structure formed from a periodic arrangement of Ag and MgF<sub>2</sub> is solved numerically in terms of  $k_0$ .

**Figure 2.12:** The low frequency band edge of a multilayer structure formed from a periodic arrangement of Ag and MgF<sub>2</sub> is solved numerically in terms of  $k_0$ .

**Figure 2.13:** A one-dimensional classical analogy of two weakly coupled oscillators.

**Figure 2.14:** Simulated transmittance (i), absorbance (ii) and reflectance (iii) spectra for 50 layers of Ag with thickness 5 nm (A), 25 layers of Ag with thickness 10 nm (B), 10 layers of Ag with thickness 25 nm (C) and 5 layers of Ag with thickness 50 nm (D), each separated by 110 nm of MgF<sub>2</sub>. The dashed line is the response of a single layer of 250 nm Ag. The structure is illuminated at normal incidence and is surrounded by glass ( $n_r = 1.52$ ,  $n_i = 0.00$ ).

**Figure 2.15:** A diagram showing the electric field distribution for a section (metal-air-metal) of a multilayer structure at the low frequency band edge, where the metal layers have thickness (a) 20 nm and (b) 10 nm.

**Figure 2.16:** Time-averaged electric field profiles at the high frequency band edge for the multilayer structures in Figure 2.14 consisting of 5 nm (A), 10 nm (B), 25 nm (C) and 50 nm (D) thick Ag layers separated by 110 nm of MgF<sub>2</sub>. The structure is illuminated at normal incidence and is surrounded by glass ( $n_r = 1.52$ ,  $n_i = 0.00$ ).

**Figure 2.17:** The simulated transmittance and reflectance spectra are shown for two layers of 20 nm thick Ag ( $\epsilon = -10^4 + 10^7 i$ ) separated by 10 nm of vacuum. The sample is illuminated at normal incidence with frequencies ranging from 30 – 60 GHz ( $3.0 - 6.0 \times 10^{10}$  Hz).

**Figure 2.18** reproduced from reference 29 (Butler et al.) : Experimental transmission spectrum of a metamaterial comprising a stack of metallic grid and dielectric layers at microwave frequencies with dielectric cavity thickness ( $t_d$ ) 6.35 mm and metal layer thickness ( $t_m$ ) 18  $\mu$ m. The inset shows the schematic of the structure and a plan view of the hole geometry, with parameters  $\lambda_g = 5$  mm,  $w_m = 0.15$  mm,  $w_n = 4.85$  mm.

**Figure 2.19** reproduced from reference 29 (Butler et al.): Instantaneous electric-field amplitude distributions as a function of distance perpendicular to the metallic grid-dielectric stack at each of the resonant frequencies marked A-D in Figure 2.18. The vertical dashed lines indicate the positions of the metallic grid layers.

**Figure 3.1:** The unit vectors of the spherical polar coordinate system are represented on Cartesian axes.

**Figure 3.2:** The scalar spherical harmonics are shown for  $l = 1$  to 5 and  $m = 1$  to  $l$  where  $\theta$  is varied from 0 to 90° and  $\phi$  is varied from 0 to 360°. The colour scale represents the magnitude of the product of the azimuthal and polar solutions to Equation 3.12, which have been normalised to the same scale (-1 to +1).

**Figure 3.3:** Electric field patterns (viewed in cross section) showing the normal modes of a sphere as proposed by Mie in 1908<sup>1</sup>.

**Figure 3.4:** The Whitney tetrahedron – an example of a vector finite element.

**Figure 3.5:** The Cartesian grid configuration proposed by Yee in 1966.

**Figure 3.6:** The real and imaginary components of the permittivity are shown for Au for wavelengths in the range 400 – 750 nm. Permittivity values were obtained from reference data, published by Johnson & Christy<sup>32</sup>.

**Figure 3.7:**  $Q_{sca}$  plotted as a function of frequency for an 80 nm diameter Au sphere in vacuum, based upon simulated data obtained using Mie Theory (black), FDTD with an element length of 3.00 nm (red), T-Matrix (green), FEM with an element length of 3.11 nm (blue) and DDA with an interdipole spacing of 3.00 nm (cyan) methods. For the Mie Theory, T-Matrix, DDA and FEM simulation techniques the Au permittivity values were obtained from Johnson & Christy<sup>32</sup>. For the FDTD method a Drude model was used to calculate permittivity values ( $\omega_p = 1.3 \times 10^{16} \text{ s}^{-1}$  and  $\gamma = 5.0 \times 10^{13} \text{ s}^{-1}$ ).

**Figure 3.8:** Mie vs DDA:  $Q_{sca}$  simulated using Mie Theory for a 80 nm Au sphere in vacuum is directly compared with that obtained using the DDA method. The coloured data points show the effect of varying the inter-dipole spacing across a 2 nm to 5 nm range. *Inset* – relative error is plotted as a function of wavelength for different mesh sizes.

**Figure 3.9:** Mie vs FEM:  $Q_{sca}$  simulated using Mie Theory for a 80 nm Au sphere in vacuum is directly compared with that obtained using a FEM approach. The coloured data points show the effect of varying the mesh element length. *Inset* – relative error is plotted as a function of wavelength for different mesh sizes.

**Figure 3.10:**  $Q_{sca}$  simulated using Mie Theory for a 80 nm diameter Au sphere in vacuum is directly compared with that obtained using the FDTD method. A Drude model ( $\omega_p = 1.3 \times 10^{16} \text{ s}^{-1}$  and  $\gamma = 5.0 \times 10^{13} \text{ s}^{-1}$ ) is used to calculate Au permittivity values for both models. The coloured data points show the effect of varying mesh element length. *Inset* – relative error is plotted as a function of wavelength for different mesh sizes.

**Table 3.1:** Comparison of computation time, advantages and disadvantages of five commonly used computational techniques used to simulate light scattering from metallic nanoparticle and nanohole structures. Computations were performed on a Dell Vostro 200 personal computer, having a dual-core processor (each with a clock speed of 2.19 GHz), 2 Gb of RAM and 250 Gb of available hard drive space).

**Figure 4.1:** The main stages of an electron beam lithography process used to fabricate Au nanoparticles. The SEM image shows a single Au nanoparticle with diameter 90 nm and height 20 nm.

**Figure 4.2:** Spin speed curves for A2 (2%), A4 (4%) and A7 (7%) concentrations of PMMA dissolved in anisole.

**Figure 4.3:** Schematic representation of the material removal process. The inset shows SEM images of a cylindrical hole with 90 nm diameter and 20 nm depth and a square particle with 90 nm side length and 20 nm depth fabricated using FIB milling.

**Figure 4.4:** The real and imaginary components of the polarisability are plotted for a 60 nm diameter Ag sphere (left) in vacuum. This is compared against the scattering efficiency ( $Q_{sca}$ ) which has been simulated using Mie Theory (right).

**Figure 4.5:** Schematic of an ellipsoidal particle, showing the axes of symmetry and the semi axis lengths  $a$ ,  $b$  and  $c$ .

**Figure 4.6:** Using Equation 4.31, the shape factor  $L_a$  is plotted against the ratio of  $a : (b,c)$  for an ellipsoid in which length  $a$  is fixed and lengths  $b,c$  are increased such that  $b = c$ .

**Figure 4.7:** The real and imaginary components of the polarisability are plotted as a function of wavelength for the incident electric field polarised parallel to the long and short axes of an Ag rod with dimensions  $30 \text{ nm} \times 80 \text{ nm} \times 80 \text{ nm}$  (left). A T-Matrix method has been used to simulate the scattering efficiency of the rod illuminated with light polarised along the long and short axes (right).

**Figure 4.8:** An SEM image showing an example of cylindrical Au nanoparticles fabricated by EBL. These particles have height 35 nm and diameters ranging from 45 nm to 160 nm. *Note:* On the sample the particles are separated by  $2 \mu\text{m}$  but the images have been merged for visualisation.

**Figure 4.9:** Schematic illustrating the experimental configuration for dark-field spectroscopy.

**Figure 4.10:** CCD image obtained from a dark field microscope used to observe scattering from Au discs with height 35 nm and diameters ranging from 45 nm to 160 nm. The image has been normalised to the lamp spectrum.

**Figure 4.11:** Dark field scattering spectra (a) of Au discs with height 35 nm and diameters ranging from 45 to 160 nm are compared with simulated spectra (b) obtained using a T-Matrix method. In (c) the resonant wavelengths and widths (d) from the experimental and simulated scattering spectra are compared.

**Figure 4.12:** Desired scattering response of a nanoparticle which could be hosted within a liquid crystal cell. In the diagram,  $\theta$  represents the illumination angle of the incident beam which is polarized either parallel ( $E_{zy}$ ) or perpendicular ( $E_x$ ) to the plane of angular variation and  $\phi$  represents the scattering angle of the radiated field.

**Figure 4.13:** The scattering efficiency of an Ag disc with height 25 nm and diameter 80 nm has been simulated using a T-Matrix method for light incident at various illumination angles  $\theta$  ranging from 0 to 80 degrees. The incident beam is polarised parallel (a) and perpendicular (b) to the plane of angular variation. In the lower graph (c) the magnitude of the maxima from the scattering efficiency curves in (c) have been normalised to 1, and are plotted against a  $\cos^2\theta$  function.

**Figure 4.14:** The scattered electric field distribution from the Ag disc has been simulated using a FEM technique and has been projected onto a spherical surface in the far field. A polar plot of the radiated field in the upper half space is shown for a cross section through the YZ plane. The electric field intensity has been plotted as a function of the scattering angle  $\phi$ .

**Figure 4.15:** The instantaneous charge and field distributions are illustrated for two metallic nanoparticles which interact through the overlap of their resonant electromagnetic fields. Plasmon hybridisation can occur in particles separated by distances which are a few 10s of nm in vacuum, resulting in two coupled LSPRs associated with the anti-symmetric (a) and symmetric (b) distribution of charge across the structure.

**Figure 4.16:** The scattering efficiency of a 200 nm diameter Ag sphere in vacuum has been simulated using Mie Theory, with light incident at 45 degrees. A FEM technique has been

used to simulate the time-averaged electric field distributions for a cross section taken through the centre of the sphere at the resonant frequencies labelled A, B and C (intensity scales are arbitrary). The incident electric field is polarised along the direction shown by the arrow above the figures.

**Figure 4.17:** The scattered electric field distribution from a 200 nm diameter Ag sphere has been simulated using a FEM technique at the resonant frequency corresponding to the quadrupolar LSPR, and has been projected onto a spherical surface in the far field. A polar plot of the radiated field is shown on a polar plot as a function of the scattering angle  $\phi$  for a cross section through the YZ plane.

**Figure 4.18:** The instantaneous field distribution is shown for a point dipole emitting a spherical wave (a), two point dipoles separated by  $\lambda/2$  (along the y direction) emitting spherical waves which are out of phase by  $\pi$  radians (b), and (c) the sum of (a) and (b).

**Figure 4.19:** A FEM technique is used to simulate the optical response of an Ag nanorod in vacuum having dimensions length 80 nm, width 30 nm and height 25 nm respectively. The rod is illuminated in the configuration shown in (a). The angle of incidence  $\theta$  is varied from 0 to 90 degrees in 15 degree increments, and the scattering efficiency is plotted as a function of wavelength in (b). In (c) the magnitude of the  $Q_{sca}$  maxima at 575 nm are plotted as a function of incident angle  $\theta$  and are shown against a normalised  $\cos^2\theta$  function.

**Figure 4.20:** Diagram showing three identical metallic rods separated by 20 nm in a linear chain, the resonant frequencies are shown below each rod. In the left of the figure, the direction of the incident wave vector and the polarisation of the incident electric field are shown.

**Figure 4.21:** Diagram showing three metallic rods separated by 20 nm in a linear arrangement, the resonant frequencies are shown below each rod. The outer rods have length  $L_1$  and the centre rod has length  $L_2$ . In the left of the figure, the direction of the incident wave vector and the polarisation direction of the incident electric field are shown.

**Figure 4.22:** A FEM technique is used to simulate the optical response of three Ag nanorods in vacuum. The central rod has length 60 nm, width 30 nm and height 25 nm. The upper and lower rods have length 80 nm, width 30 nm and height 25 nm. The rods are separated by 20 nm and are illuminated in the configuration shown in (a). The angle of incidence  $\theta$  is varied from 0 to 90 degrees, and the scattering efficiency is plotted as a function of wavelength in (b). In (c) the magnitude of the  $Q_{sca}$  maxima at 615 nm are plotted as a function of incident angle and are shown against a normalised  $\cos^2\theta$  function.

**Figure 4.23:** The time-averaged electric field distribution is shown for a cross section through the centre of the rods, which is shown for a plane lying perpendicular to the incident wave vector.

**Figure 4.24:** Several  $\cos^n\theta$  functions are plotted as a function of  $\theta$ , where n is varied from 2.0 to 6.0 and  $\theta$  is varied from  $0^\circ$  to  $90^\circ$ .

**Figure 4.25:** The values of  $\theta$  at  $f(\theta) = 0.5$  (a) and the gradient of  $f(\theta)$  at  $f(\theta) = 0.5$  (b) are plotted as function of n.

**Figure 4.26:** In (a), the scattering efficiency of a single Ag rod (80 nm length, 30 nm width, 25 nm height) is plotted as a function of incident angle  $\theta$  and wavelength. At each wavelength, the angular response is fitted to a  $\cos^n\theta$  function, and in (b) the fitted value of  $n$  is plotted as a function of incident wavelength.

**Figure 4.27:** In (a), the scattering efficiency of an arrangement of three Ag rods (from Figure 4.22) is plotted as a function of incident angle  $\theta$  and wavelength. At each wavelength, the angular response is fitted to a  $\cos^n\theta$  function, and in (b) the fitted value of  $n$  is plotted as a function of incident wavelength. The dashed line represents the spectral position of the single scattering efficiency maximum which is observed at normal incidence.

**Figure 4.28:** The scattered electric field distribution for the arrangement of three Ag rods in Figure 4.22 has been simulated using a FEM technique and has been projected onto a spherical surface in the far field. A polar plot of the radiated field in the upper half space is shown for a cross section through the YZ plane. The electric field intensity has been plotted as a function the scattering angle  $\phi$ .

**Table 4.1:** A summary of the angular response characteristics evaluating the behaviour of the scattering intensity as a function of the incident ( $\theta$ ) and scattering angle ( $\phi$ ).

**Figure 5.1:** An individual dipole  $i$  is positioned within an infinite square array of identical dipoles  $j$ . The local electric field at the origin is a sum of the incident electric field plus the retarded fields from all other dipoles.

**Figure 5.2:** When using an FEM approach to simulate infinite arrays of particles, periodic boundary conditions are imposed along  $x$  (i) and  $y$  (ii) directions.

**Figure 5.3:** The scattering of an incident plane wave by a small metallic nanoparticle.

**Figure 5.4:** The electric field distributions at the upper and lower boundaries of the unit cell are used to determine the transmission and reflection coefficients of the structure.

**Figure 5.5:** A diagram of the experimental apparatus for characterising the optical response of particle arrays using bright-field spectroscopy.

**Figure 5.6:** SEM images of sections of gold nanoparticle arrays with height 35 nm, periodicity 300 nm and mean diameters ranging from 72 nm to 130 nm.

**Figure 5.7:** The experimental (i) and simulated (ii) extinction spectra are compared for regular arrays of nanoparticles with 300 nm periodicity and particle diameters ranging from 72 nm to 130 nm. The simulated and experimental resonant wavelengths (iii) and widths (iv) are also compared. The discs are illuminated at normal incidence, and are surrounded by a medium with refractive index  $n_r = 1.52$ ,  $n_i = 0.00$ .

**Figure 5.8:** The simulated extinction cross section  $C_{ext}$  is shown in (a) for individual discs having height 35 nm and diameters ranging from 72 to 130 nm. In (b), the resonant wavelengths from the single particle simulations are plotted against those determined from the experimental extinction spectra of the arrays. The discs are illuminated at normal incidence, and the surrounding medium has refractive index  $n_r = 1.52$ ,  $n_i = 0.00$ .

**Figure 5.9:** In (a) the calculated values of  $d\lambda/dn$  from Equation 5.31 are shown for incident wavelengths across the range 300 – 1000 nm, and  $n_{lreal}$  varying between 1.5 and 4.5. The dashed arrows represent the wavelengths at which the resonant condition in Equation 5.28 is satisfied. In (b) and (c) the values of  $\varepsilon_{metal}$  at the resonant condition and the LSPR wavelength are plotted as a function of  $n_{lreal}$ . The scattering particle is an Au sphere with dimensions  $\ll \lambda$ , the permittivity values have been obtained using a lossless Drude model ( $\omega_p = 1.3 \times 10^{16} \text{ s}^{-1}$ ).

**Figure 5.10:** Simulated extinction spectra are shown for arrays of cylindrical Au nanoparticles with height 35 nm, diameter 90 nm and periodicity 300 nm. The refractive index of the glass ( $n_r = 1.52$ ,  $n_i = 0.00$ ) substrate is fixed whilst the refractive index of the superstrate is varied from  $n_r = 1.0$  to 2.0.

**Figure 5.11:** The time-averaged electric field distribution is shown at the resonant frequency for a cross section through the particle, taken perpendicular to the substrate. The arrow above the field profile represents the direction of the incident electric field. The arrow above the field profile represents the polarisation direction of the incident electric field.

**Figure 5.12:** The simulated extinction spectra are shown for an array of Au cylinders with 35 nm height, 90 nm diameter and 300 nm periodicity embedded in a glass ( $n_r = 1.52$ ,  $n_i = 0.00$ ) substrate, with the superstrate refractive index being varied across the range  $n_r = 1.0$  to 2.0.

**Figure 5.13:** The simulated extinction spectra are shown for an array of Au cylinders with 35 nm height, 90 nm diameter and 300 nm periodicity raised on a glass ( $n_r = 1.52$ ,  $n_i = 0.00$ ) ‘plinth’ of thickness 20 nm, with the superstrate refractive index being varied across the range  $n_r = 1.0$  to 2.0.

**Figure 5.14:** The simulated extinction spectra are shown for arrays of Au cylinders (90 nm diameter, 35 nm height) in which the periodicity of the arrays has been varied from 100 nm to 175 nm in increments of 25 nm. The arrays are illuminated at normal incidence in air on a glass ( $n_r = 1.52$ ,  $n_i = 0.00$ ) substrate.

**Figure 5.15:** The time-averaged electric field distribution is shown for a cross section taken parallel to the substrate at the resonant frequency for a periodicity of 100 nm. The arrow above the field profile represents the polarisation of the incident electric field along the line of the unit vector  $\hat{x}$ .

**Figure 5.16:** Plan view of a  $3 \times 3$  array of nanoparticles with radius  $r$  and periodicity  $d$ . The red arrows represent the direction of the induced dipole moment across the particles, whilst the blue arrows represent the direction of the induced dipole moment between particles. In the left of the figure, the direction of the incident wave vector and the polarisation of the incident electric field are shown.

**Figure 5.17:** The simulated extinction spectra are shown for arrays of Au cylinders (90 nm diameter, 35 nm height) in which the periodicity of the arrays has been varied from 200 nm to 400 nm in increments of 25 nm. The arrays are illuminated at normal incidence in air on a glass ( $n_r = 1.52$ ,  $n_i = 0.00$ ) substrate.

**Figure 5.18:** Plan view of a  $3 \times 3$  array of nanoparticles with radius  $r$  and periodicity  $d$ . The red arrows represent the direction of the induced dipole moment across the particles,

whilst the blue arrows represent the direction of the radiated electric field. In the left of the figure, the direction of the incident wave vector and the polarisation of the incident electric field are shown.

**Figure 5.19:** Experimental extinction spectra published by Auguie et al.<sup>16</sup> are shown for square arrays of rectangular Au nanoparticles (35 nm height, 85 nm width, 123 nm length), with periodicities ranging from 480 to 560 nm. The surrounding medium has refractive index  $n_r = 1.52$ ,  $n_i = 0.00$ . The incident electric field is polarised along the long axis of the particles.

**Figure 6.1:** A metal film with thickness  $t$  is perforated with a square array of cylindrical holes having diameter  $a$  and square periodicity  $d$ . The diagrams show the structure as viewed from above (left) and in cross section (right).

**Figure 6.2:** Schematic representations of the dispersion relations are shown for (a) an air - Ag planar interface and (b) an air-Ag shallow monograting. The red lines represent the SPP dispersion curves, and dashed black lines are the diffracted and non-diffracted light lines. It is assumed that the dielectric function of the Ag may be described using a Drude model.

**Figure 6.3:** The simulated zeroth-order transmittance spectrum is shown for a 200 nm thick Ag film perforated with an array of cylindrical holes with diameter 150 nm and periodicity 600 nm. The sample is illuminated at normal incidence in air, and is situated on a glass ( $n_r = 1.52$ ,  $n_i = 0.00$ ) substrate.

**Figure 6.4:** The time-averaged electric field distribution is shown for the structure in Figure 6.3. A cross section is taken parallel to the upper metal surface (a) and through the centre of the structure (b). The sample is illuminated at normal incidence with an incident wavelength of 700 nm.

**Figure 6.5:** The simulated zeroth-order transmittance spectrum is shown for a 200 nm thick Ag film perforated with an array of cylindrical holes with diameter 150 nm and periodicity 900 nm. The sample is illuminated at normal incidence in air, and is situated on a glass ( $n_r = 1.52$ ,  $n_i = 0.00$ ) substrate.

**Figure 6.6 reproduced from reference 11:** The dark field scattering intensity is shown for nanoholes with diameters ranging from 60 nm to 500 nm, fabricated from a 20 nm thick Au film. The samples are fabricated on a glass ( $n_r = 1.52$ ,  $n_i = 0.00$ ) substrate and are illuminated at normal incidence in air.

**Figure 6.7:** Experimental transmittance spectra are compared against simulated transmittance and absorbance spectra obtained for 8  $\mu\text{m}$  square arrays of 90 nm diameter holes in a (a) 20 nm thick Au film and (b) 90 nm diameter, 20 nm height cylindrical Au particles with periodicity 200 nm, illuminated at normal incidence in air. The dashed gray curve in both (a) and (b) shows the experimental transmittance spectrum obtained from a 20 nm Au film illuminated at normal incidence in air.

**Figure 6.8:** Field profiles are shown at the absorbance maximum of the hole and particle array structures. The upper profiles show the instantaneous scattered electric field vector for (a) the hole and (b) the particle arrays, taken at the same instant in phase for each structure. The arrows above (a) and (b) indicate the vector of the incident electric field. The centre plots show the time-averaged scattered electric field profiles for (c) the hole and (d) the particle. In (e) and (f), a line plot has been taken through the centre of the

structures along the dashed line shown in (c) and (d), and the time-averaged electric field magnitude is shown as a function of position across the unit cell.

**Figure 6.9:** Comparison between experimental and simulated transmission spectra for 90 nm diameter hole ((a) and (c)) and particle ((b) and (d)) arrays with periodicity 200, 225 and 250 nm.

**Figure 6.10:** The experimental (left) and simulated (right) transmittance spectra are shown for hole arrays with periodicity 250 nm and hole diameters ranging from 70 nm to 100 nm. The arrays are on a glass ( $n_r = 1.52$ ,  $n_i = 0.00$ ) substrate, and are illuminated at normal incidence in air. The dashed gray curves show the experimental and simulated data for a planar Au film with thickness 20 nm.

**Figure 6.11:** The simulated transmittance spectra are shown for hole arrays with periodicity 200 nm. The solid black line represents the simulated transmittance for arrays of 70 nm diameter cylindrical holes. The dashed and dash-dot lines represent the simulated transmittance of rectangular holes with dimensions 45 nm  $\times$  90 nm illuminated with light having the electric field polarised along the long (dashed) and short (dash-dot) axes. The arrays are on a glass substrate ( $n_r = 1.52$ ,  $n_i = 0.00$ ), and are illuminated at normal incidence in air.

**Figure 7.1:** Simulated transmittance (T) and absorbance (A) spectra at normal incidence for a planar Ag layer (20 nm thickness) perforated with an infinite square array of 60 nm diameter cylindrical holes with periodicity 150 nm (shown in the inset). The surrounding medium has refractive index ( $n_r = 1.52$ ,  $n_i = 0.00$ ).

**Figure 7.2:** Simulated transmittance (T) and absorbance (A) spectrum at normal incidence for a single Ag layer (20 nm thickness) and a multi-layer structure consisting of 5 layers of 20 nm Ag separated by 110 nm (A). The surrounding medium has refractive index  $n_r = 1.52$ ,  $n_i = 0.00$ . The grey line illustrates the resonant frequency for a single layer of 20 nm Ag perforated with holes having diameter 60 nm and periodicity 150 nm. The inset figures (B-E) show the time-averaged electric field magnitude at the resonant frequencies of the FP modes for a cross section taken perpendicular to the stack.

**Figure 7.3:** Simulated transmittance (T) and absorbance (A) spectra for a planar structure consisting of 5 layers of Ag with thickness 20 nm separated by 110 nm, perforated with an infinite square array of cylindrical holes with 60 nm diameter and 150 nm periodicity. The surrounding medium has refractive index  $n_r = 1.52$ ,  $n_i = 0.00$ . The solid line corresponds to illumination at normal incidence, the dashed and dotted lines correspond to illumination with TE polarized light at angles 23.5° ( $\sin \theta = 0.4$ ) and 36.9° ( $\sin \theta = 0.6$ ) respectively. The grey line at 545 THz represents the resonant frequency for a single layer of Ag perforated with an identical array of holes (Figure 7.1).

**Figure 7.4:** Contour plot showing the magnitude of the simulated absorbance as a function of frequency and  $\sin \theta$  (where  $\theta$  is the incident angle) for TE polarized light illuminating the structure in Figure 7.3.

**Figure 7.5:** The magnitude of the simulated absorbance is plotted as a function of frequency and spacing between two non-perforated (top) and perforated (bottom) Ag layers with thickness 20 nm. The perforated structure consists of an infinite square array of cylindrical holes with diameter 60 nm and periodicity 150 nm. The results are for normal incidence, with surrounding medium  $n_r = 1.52$ ,  $n_i = 0.00$ . The dashed line

represents the separation of the metal layers in the structures described in Figures 7.2 and 7.3.

**Figure 7.6:** The simulated transmittance is shown for a structure comprised of 6.5 periods of 20 nm Ag / 120 nm glass ( $n_r = 1.52$ ,  $n_i = 0.00$ ), perforated with an infinite square array of cylindrical holes having periodicity 300 nm and diameters ranging from (a) 20 nm to 100 nm and (b) 20 nm to 45 nm. The structure is illuminated at normal incidence in a glass surrounding medium.

**Figure 7.7:** (a) The simulated transmittance is shown for a structure comprised of 6.5 periods of 20 nm Ag / 120 nm glass, perforated with an array of cylindrical holes having periodicity 200 nm and diameters ranging from 60 nm to 100 nm. The permittivity of the metal is assumed to be  $\epsilon = -32 + 1.8i$  across all wavelengths. (b) The simulated transmittance (T) and absorbance (A) is shown for 60 nm diameter holes. The structures are illuminated at normal incidence in a glass surrounding medium.

**Figure 7.8:** The simulated transmittance is shown for a 12.5 period structure of 20 nm Ag / 120 nm glass, perforated with an array of square cylindrical holes having periodicity 300 nm and diameters ranging from 40 nm to 100 nm. The structure is illuminated at normal incidence in a glass surrounding medium ( $n_r = 1.52$ ,  $n_i = 0.00$ ).

**Figure 7.9:** The simulated transmittance (T) and absorbance (A) spectra are shown for (a) a single layer of Ag with thickness 20 nm, perforated with an infinite square array of cylindrical holes with periodicity 225 nm and diameter 90 nm, (b) a multilayer structure comprised of 4.5 periods of planar 20 nm Ag / 140 nm glass layers. The structures are illuminated at normal incidence in a glass surrounding medium.

**Figure 7.10:** Simulated transmittance (T) and absorbance (A) spectrum at normal incidence for a planar structure consisting of 5 layers of Ag with thickness 20 nm separated by 140 nm, perforated with an infinite square array of cylindrical holes with 90 nm diameter and 225 nm periodicity. The structure is illuminated at normal incidence in a glass surrounding medium.

**Figure 8.1:** A conventional lens having a positive index of refraction ( $n_1$ ) is used to form an image of a point source. The arrows represent ‘ray’ directions.

**Figure 8.2:** The use of a planar isotropic slab having  $n_l = -1 + 0i$  and thickness  $d$  for the imaging of a point source. The arrows represent ‘ray’ directions.

**Figure 8.3 reproduced from 9:** The experimental sample used by Shelby et al. consisted of copper split ring resonators and copper wire strips on circuit board material. The rings and wires are positioned on opposite sides of the board.

**Figure 8.4:** The magnetic response of a continuous metallic ring (CMR).

**Figure 8.5:** Split ring resonators exhibit an LC resonance which is associated with the effective capacitance of the dielectric gap and the effective inductance of the loop which defines the ring.

**Figure 8.6:** An example of a circular pair of split ring resonators (SRRs), with illustrated dimensions corresponding to those in Equation 8.11.

**Figure 8.7** reproduced from reference 4: Diagram of a 21 layer fishnet structure formed from layers of Ag with thickness 30 nm and MgF<sub>2</sub> with thickness 50 nm. The structure has been milled to produce a square array of rectangular holes with dimensions 565 nm × 265 nm, and periodicity 860 nm (a). Simulated and experimental index of refraction data obtained for the ‘fishnet’ structure shown in (b).

**Figure 8.8:** The structural dimensions of a single layer of the fishnet structure which was analysed by Soukoulis et al.<sup>15</sup> is shown (a), this layer stacked to form periodic structure where the layers are separated by  $t$  (b). Assuming the incident electric field is polarized in the direction shown, the equivalent electrical circuit model for this arrangement may be simplified to that shown in (c).

**Figure 8.9:** An illustration of the surface currents which are formed in the slab and neck regions of the fishnet structure in the uppermost layer of the fishnet structure at the frequency of the magnetic resonance  $\omega_m$ . In a metamaterial, the directions of the surface currents in adjacent layers are aligned anti-parallel.

**Figure 8.10:** The real (hollow circles) and imaginary (solid circles) components of the effective refractive index obtained using Equation 8.19 are shown for three homogeneous layers with parameters (a)  $\epsilon = 3, \mu = 2$  (b)  $\epsilon = -3, \mu = 2$  and (c)  $\epsilon = -3, \mu = -2$ .

**Figure 8.11:** The real (hollow circles) and imaginary (solid circles) components of the effective refractive index obtained using Equation 8.20 are shown for three homogeneous layers with parameters (a)  $\epsilon = 3, \mu = 2$  (b)  $\epsilon = -3, \mu = 2$  and (c)  $\epsilon = -3, \mu = -2$ .

**Figure 8.12:** The extraction procedure described in section 8.2 was used to determine the effective refractive index from the simulated transmission and reflection coefficients obtained from finite element simulations (a). This is compared with the published data of Zhang et al.<sup>4</sup> (b).

**Figure 8.13:** The time-averaged electric field distribution is shown at the resonant frequency for a single metallic layer of the fishnet structure in Figure 8.7. The arrows above and alongside the field distributions indicate the polarisation direction of the incident electric field.

**Figure 8.14:** Simulated transmittance (i) and absorbance (ii) spectra are shown for an infinite array of 90 nm diameter holes in a 20 nm thick Ag film with periodicity 225 nm (A), an infinite array of 90 nm diameter, 20 nm height cylindrical Ag particles with periodicity 225 nm (B) and a 20 nm thick continuous Ag film (C). In all simulations the structures were illuminated at normal incidence in vacuum. The inset of (ii) shows the instantaneous scattered electric field vector across the unit cell of the hole and particle array structures. Both profiles are shown at the same instant in phase for radiation incident with frequency  $6.25 \times 10^{14}$  Hz ( $\lambda_{\text{vac}} = 480$  nm). The arrows above the field distributions indicate the direction of the incident field vector.

**Figure 8.15:** The simulated absorbance is plotted as a function of frequency and spacing between two layers of hole (i) and particle (ii) arrays. In both structures the Ag layer thickness is 20 nm, and the cylindrical holes/particles with diameter 90 nm are arranged into regular square arrays with periodicity 225 nm. For 20 nm layer spacing (shown by the dashed line) the absorbance of each arrangement is plotted as a function of frequency as an inset figure. In (a-d), the instantaneous scattered electric field vector has been plotted for a cross section perpendicular to the stack at the resonant frequencies labelled A-D in the

greyscales (i) and (ii). The arrows above the field profiles indicate the direction of the incident electric field vector.

**Figure 8.16:** The instantaneous charge and field distributions are illustrated for two metallic nanoparticles which interact through the overlap of their resonant electromagnetic fields. Plasmon hybridisation can occur in particles separated by distances which are a few 10s of nm in vacuum, resulting in two coupled LSPRs associated with the anti-symmetric (a) and symmetric (b) distribution of charge across the structure.

**Figure 8.17:** The effective refractive indices are shown as a function of frequency for the five layer stacked hole array (i) and particle array (ii) structures. In the inset, the real and imaginary parts of the effective permittivity  $\epsilon$  and permeability  $\mu$  are shown for the stacked hole array (a,b) and particle array (c,d) structures. The dashed vertical lines in plots (i) and (ii) represent the resonant frequencies of the symmetric (dashed vertical black line) and anti-symmetric (dashed vertical gray line) coupled LSPRs for the equivalent two layer structure studied in Figure 8.15.

**Figure A.1:** An incident wave  $\mathbf{k}_i$  strikes a planar interface between two media with different dielectric properties, giving rise to a reflected wave  $\mathbf{k}_r$ , and a refracted wave  $\mathbf{k}_t$ .

**Figure A.2:** Reflection and refraction of an incident plane wave which is polarised perpendicular to the plane of incidence.

**Figure A.3:** Reflection and refraction of an incident plane wave which is polarised parallel to the plane of incidence.

**Figure A.4:** The transmission and reflection of light in an arrangement formed from  $N$  isotropic layers.

**Figure D.1:** Labelled photographs of the external connections of the thermal evaporation system are shown (a) and (b). Other types of evaporation chambers may be formed using glass bell-jars (c).

**Figure D.2:** Labelled photographs of the internal connections of the thermal evaporation system.

**Figure D.3:** Photographs of two samples (20 nm Ag – 120 nm SiO<sub>x</sub> – 20 nm Ag) viewed in reflection at normal incidence are shown. In (a) the vector from the source to the substrate is parallel to the surface normal of the substrate. In (b), the sample has been aligned at an angle of 60° and is rotated at 120 revolutions per minute.

# Chapter 1

---

## Introduction

### 1.1 Aim of research

The primary aim of the work in this thesis is to investigate the optical response of arrangements of metallic nanoparticles, with a view to controlling the intensity, wavelength and angular dependence of the scattered radiation. The knowledge which is gained from these studies has particular relevance in the development of future electronic displays, such as those which are manufactured by Hewlett Packard corporation. Liquid crystal based devices are often the preferred choice for display applications as opposed to other types of displays such as Plasma Display Panel (PDP) or Organic Light Emitting Diode (OLED) technology. A particular disadvantage with PDPs is that they are significantly heavier than other display types due to the rigid glass panels which enclose the noble gas mixtures. Similarly, the lifetime of the organic materials within OLED devices may be quite short, and the intensity of the emitted radiation decreases significantly as a function of operation time.

It is well known that the optical response of liquid crystal display (LCD) devices can be readily switched using an applied electric field. The majority of devices, however, operate by modulating the transmitted light from an illumination source located behind the cell. This can make viewing difficult when the device is illuminated from the front by strong ambient light, such as in bright sunlight. One possible solution is to consider hosting metallic nanoparticles within a liquid crystal cell, such that the device operates solely by scattering ambient light. For such a solution to be feasible, the nanoparticles must exhibit two contrasting regimes of strong and weak scattering, which are dependent on the illumination angle of the incident radiation. It is known that the scattering and absorption response of small metal nanoparticles (for example rods with dimensions  $\ll \lambda$ ) follow a  $\cos^2\theta$  dependence with respect to the incident angle,  $\theta$ , of the illuminating radiation. The initial stages of this project were concerned with investigating a variety of particle configurations which may offer an improved angular response in comparison to that of small metallic nanorods. Previous work by Grigorenko<sup>1</sup> suggested that one possible route was to use pairs of metallic nanorods separated by a few tens of nm. At a similar time,

Giessen <sup>2</sup> had also made similar observations to those of Grigorenko <sup>1</sup> using stacked arrangements of small metallic discs.

Whilst we used numerical simulations to investigate optimising the optical response of particle structures which satisfied the relevant criteria, experimental work assessed possible routes towards fabricating these structures. One such route is to use Electron Beam Lithography (EBL) to selectively induce chemical changes in a layer of resist, which can subsequently be used as a template for the deposition of metal/dielectric layers by thermal evaporation. Following a lift-off procedure the remaining structure should consist of stacked layers within the exposed regions. An alternative route is to first deposit the metal/dielectric layers and then use Focused Ion Beam (FIB) milling to produce the stacked particles. The deposition of planar multilayer structures was achieved with considerable success, and Chapter 2 contains several examples of experimental structures which have been characterised. However it became evident that FIB milling was not appropriate for producing the particles, since the high degree of surface roughness associated with the multilayer structures led to strong scattering of the ion beam and non-uniform milling across the surface. At this point it could be concluded that EBL was more appropriate for this purpose, and examples of work using this technique are shown in Chapters 4 and 5.

Although FIB milling was deemed inappropriate for the fabrication of nanoparticle structures, the results obtained from milling of individual metallic layers were found to be of significant interest. In samples of optically thin metal films which were perforated with periodic arrays of subwavelength holes, we observed resonant features which had not been identified elsewhere. It is this topic to which the remainder of the thesis is dedicated. These resonant features are shown to exhibit a high degree of spectral tunability as a function of hole size and array geometry, something which was very relevant to the original optical criteria. From further numerical simulations and experimental studies it was established that the resonant modes were localised surface plasmon resonances (LSPRs) induced in the vicinity of the nanometric holes. Furthermore, it was also shown that these modes were strongly coupled through interactions with the surface plasmon-polariton (SPP) modes associated with the metal film. Although a hole array was not the structure perhaps first envisaged at the outset for meeting the desired optical criteria, it was nevertheless important to understand the observed results whilst continuing to pursue other candidate structures.

## 1.2 Outline of Thesis

The structure of the thesis can be divided into three main sections. The first section (Chapter 2) contains an investigation into the optical response of planar multilayer structures comprised of continuous metal and dielectric layers. The second (Chapters 3-5) and third (Chapters 6-8) include a discussion of structures in which the metallic elements are non-continuous. The optical response of metallic nanoparticle structures has been investigated, in addition to considering the modification of the single particle LSPR when particles are arranged into periodic arrays. The third section includes a discussion of the optical characteristics of metallic layers have been perforated with holes, and the interactions which may arise when two or more hole- and particle-array layers are stacked to form a metamaterial. A brief outline of the contents of each chapter is now given.

In Chapter 2 the optical response of multilayer structures comprised of planar metal and dielectric layers is considered. An investigation is conducted into the dependence of the spectral position and width of the transmission pass band on parameters such as metal/dielectric layer thickness and the number of periods. Some of the applications which have utilized multilayer structures, both at visible and non-visible frequencies are discussed.

In Chapter 3 there is an investigation into a number of modelling techniques used to simulate the scattering of electromagnetic radiation from metallic nanoparticle and nanohole structures. These techniques include Mie Theory, T-Matrix, DDA, FDTD and FEM. An introduction is given to the basic underlying theory of each method, along with simulation results obtained for an 80 nm diameter Au sphere in vacuum. The suitability of each technique is considered in terms of its accuracy, computation time and range of geometries to which each method can be applied.

In Chapter 4 the fabrication techniques used to produce single metallic particles such as FIB milling or EBL are described. The excitation conditions for the nanoparticle LSPR are investigated in detail; with particular attention given to the effects of particle size, geometry and aspect ratio on the LSPR frequency. There is also an overview of the dark-field spectroscopy characterization technique, and experimental scattering spectra are compared with simulated data obtained using FEM and T-Matrix techniques.

In Chapter 5, the electromagnetic response of regular arrays of particles is derived through a modification of the single particle response. This is subsequently used to determine the extinction of the array structures. Experimental extinction spectra obtained from structures fabricated by EBL are compared with simulated data. The sensitivity of the optical response to changes in particle size and the surrounding refractive index is explored, and the regimes of particle interactions are studied in closer detail.

In Chapter 6 the electromagnetic properties of arrays of holes with subwavelength periodicity are considered. There is a comparison between the coupling of nanoholes and nanoparticles in periodic arrays. For the range of periodicities studied in this chapter (200 – 250 nm), it is shown that the optical response associated with the nanohole arrays is strongly dependent on the array period, an effect which is attributed to strong LSPR coupling mediated by SPPs associated with the metal film. It is also shown that for the complementary nanoparticle arrays, a minimal shift is observed since SPPs are not supported by this structure.

In Chapter 7 the response of multilayer structures (c.f. Chapter 2) which have been perforated with periodic arrays of holes (c.f. Chapter 6) are considered. It is shown that the optical response exhibits a stop-band in transmission across a wide range of visible frequencies. Further simulations show that the stop-band originates through strong interactions between hole LSPR and Fabry-Perot (FP) resonant modes. The dependence of the spectral position and width of the stop-band is investigated with respect to the cavity spacing and array periodicity.

Chapter 8 presents an investigation into the optical response of metamaterial structures comprised of stacked hole or particle arrays. An alternative explanation to the commonly used electrical circuit formalism is proposed when characterising the response of negative index metamaterials in terms of the hybridization of LSPRs within a multilayer structure. The origin of coupled LSPRs in stacked hole and particle structures is identified, with the anti-symmetric coupled LSPR of both structures being shown to give rise to effective magnetic resonances. For the stacked hole structure, the overlap of the magnetic response with a negative effective permittivity at low frequencies is also shown to facilitate a negative index of refraction.

In Chapter 9 the general conclusions from the thesis are made, and ideas for future studies are suggested.

### **The optical response of continuous metal-dielectric multilayer structures exhibiting Fabry-Perot transmission resonances**

#### **2.1 Introduction**

The etalon first proposed by C. Fabry and A. Perot in 1899 <sup>1</sup>, is well established as an optical transmission resonator. It consists of two parallel and partially reflecting planes separated by a fixed distance, with resonantly enhanced transmission occurring when the wavelength is approximately a half integer multiple of the cavity spacing, it has been utilised in applications ranging from cavity QED <sup>2</sup> to the detection of gravity waves <sup>3</sup>. Historically the Fabry-Perot (FP) resonator consists of only two partially reflective separated planes, however periodic multi-layer arrangements consisting of quarter-wavelength thick dielectric slabs of contrasting refractive indices also demonstrate similar resonant transmission features <sup>4</sup>. The optical response of such a structure exhibits high transmissivity in the pass-bands which are accompanied by stop-bands in reflectivity. The spectral shape of the reflectance / transmittance is governed by the number of periods within the structure, and pass-bands across a narrower frequency range can be achieved by placing two or more of these cavities together to form a series of coupled resonators <sup>5</sup>. With advances in fabrication technology the possibility of investigating more elaborate multilayer structures arose, such as those incorporating metallic layers or containing a high number of periods. In 1939, W. Geffcken <sup>6</sup> fabricated metallo-dielectric thin-film stacks, and observed transmission resonances which were significantly narrower in spectral width than those previously studied in all-dielectric structures, a result of the high reflectivity of the metal layers. Recently, in a structure consisting of multiple periods of metal and dielectric layers <sup>7,8</sup>, it was demonstrated that the resonant transmission may be several orders of magnitude greater than that of a single metal film of the equivalent thickness. Metallo-dielectric structures have been studied extensively in recent years for a number of uses, including non-linear optical applications <sup>9-12</sup> and negative refraction <sup>13,14</sup>.

This chapter starts with a short review section of some of the applications in which multilayer structures find applications such as optical filters or negative refraction. Results of an experimental investigation are then presented for single cavity structures formed from two optically thin Ag layers which enclose a single dielectric layer of MgF<sub>2</sub>.

Structures which comprise multiple cavities are then explored, including the dependence of the spectral position and width of the transmission pass-band on parameters such as metal/dielectric layer thicknesses and the number of periods. At the end of this chapter, it is shown that transmission pass-bands may also be observed in the microwave regime using an equivalent multilayer structure formed using metamaterial elements to replace the metal layers.

Experimental structures studied in this chapter were fabricated using a thermal evaporation technique under vacuum to deposit Ag and MgF<sub>2</sub> layers at a pressure of  $1 \times 10^{-6}$  mbar and a rate of  $5 \text{ \AA s}^{-1}$ . More information about the thermal evaporation fabrication technique can be found in Appendix D of the thesis. Simulated data for multilayer structures was obtained using a recursive Fresnel approach (Appendix A) to determine the complex transmission and reflection coefficients of the structures.

## 2.2 Simulating the optical response of metal-dielectric multilayer structures

It can be shown (in Appendix A) that the amplitude transmission and reflection coefficients of an isotropic planar film having thickness  $l$  are given by Equations 2.1 and 2.2.

$$r = \frac{r_{01} + r_{12} \exp(2ik_x l)}{1 + r_{01} r_{12} \exp(2ik_x l)} \quad 2.1$$

$$t = \frac{t_{01} t_{12} \exp(ik_x l)}{1 + r_{01} r_{12} \exp(2ik_x l)} \quad 2.2$$

Here  $k_x$  represents the wavevector of radiation within the film and  $r_{ij}$  and  $t_{ij}$  are the reflection and transmission amplitude coefficients at the interface between  $i^{\text{th}}$  and  $j^{\text{th}}$  media. A derivation of these coefficients can be found in Appendix A. In order to simulate the optical response of  $N$  layers (illustrated in Figure 2.1), the reflection or transmission coefficients of the entire arrangement are found by recursively applying the formula for the preceding layer. For example, the reflection coefficient associated with the termination layer is first determined using Equation 2.2. This is then substituted in place of  $r_{12}$  when calculating the reflection coefficient of the  $(N-1)^{\text{th}}$  layer etc. Eventually the system is reduced to the problem of a single layer, in which the value of the reflection coefficient which is substituted in place of  $r_{12}$  effectively accounts for the reflection from all previous

layers. Simulated data which is presented in this chapter has been calculated using this recursive technique.

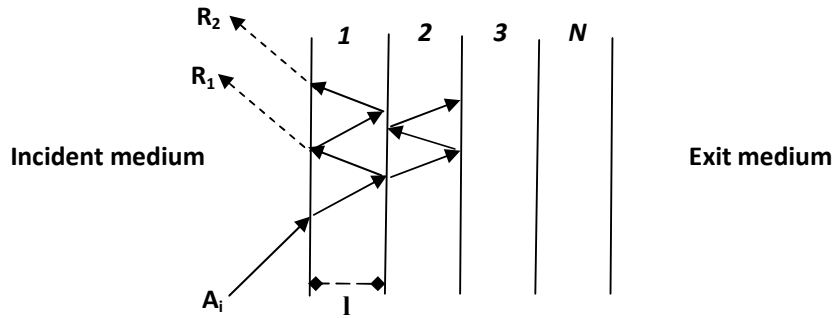


**Figure 2.1:** The transmission and reflection of light in an arrangement formed from  $N$  isotropic layers.

### 2.3 A review of previous studies involving multilayer structures

In this section there will be a short review of previous studies which have utilised multilayer structures for applications including electromagnetic shielding and negative refraction.

#### *Transmission band properties of Ag-MgF<sub>2</sub> multilayer structures:*

It has been shown by Scalora et al.<sup>7</sup> that the transmission band properties of an all-dielectric multilayer structure can be significantly modified by replacing one of the dielectric materials with a metal (such as Ag, Au etc.). In a metal-dielectric arrangement, there is the possibility for visible radiation to resonantly tunnel through the structure with minimal absorption. To demonstrate, in reference 10 a multi layered structure consisting of 2.5 periods of 38 nm Ag / 233 nm MgF<sub>2</sub> was considered. The simulated transmission data from the paper is shown in Figure 2.2, whereby the transmittance magnitude within the pass band regions is significantly larger than a single metal film of the equivalent thickness.

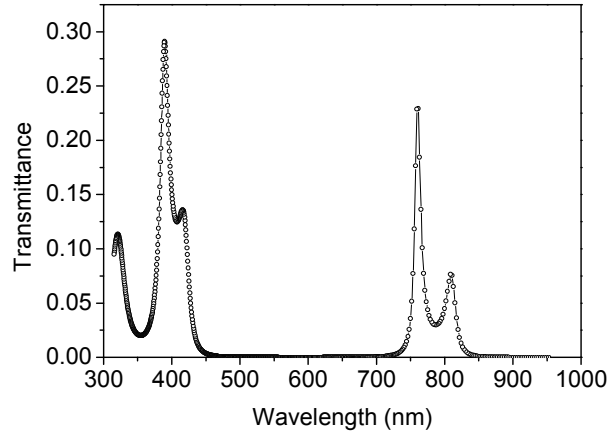


**Figure 2.2:** The simulated transmittance spectrum <sup>10</sup> is shown for a multilayer structure comprised of 2.5 periods of 38 nm Ag and 233 nm MgF<sub>2</sub>. The structure is illuminated at normal incidence in air.

A publication by the same authors <sup>8</sup> also demonstrates some of the advantages of these structures in the microwave regime. Here, simulations of metal-dielectric structures identify a transmission pass band at visible frequencies, a band gap at ultraviolet frequencies, and an almost complete stop-band across infrared, microwave and radio frequencies. The transmission band within the visible region may be suitably optimised to cover the entire visible frequency range by adjusting the thickness of the Ag and MgF<sub>2</sub> layers. This has a number of benefits for electromagnetic shielding applications, such as transparent coatings for aircraft windscreens.

*Effective permittivity, permeability and negative refraction:*

The electric susceptibility  $\chi_e$  of a material relates the bulk polarization per unit volume  $\mathbf{P}$  to the applied electric field  $\mathbf{E}$ , as shown in Equation 2.3. Here  $\varepsilon_0$  represents the permittivity of free space. The electric susceptibility may be used to define the relative permittivity of the medium (Equation 2.4).

$$\mathbf{P} = \varepsilon_0 \chi_e \mathbf{E} \quad 2.3$$

$$\varepsilon = \varepsilon_0 (1 + \chi_e) \quad 2.4$$

Similarly, for non-ferromagnetic materials the magnetic susceptibility  $\chi_m$  of a material

relates the bulk magnetisation per unit volume  $\mathbf{M}$  to the applied magnetic field  $\mathbf{B}$ , as shown in Equation 2.5. The magnetic susceptibility may be used to define the relative permeability of the medium (Equation 2.6). Here  $\mu_0$  represents the permeability of free space.

$$\mathbf{M} = \chi_m \mathbf{H} \quad 2.5$$

$$\mu = \mu_0(1 + \chi_m) \quad 2.6$$

Pendry<sup>15</sup> first proposed that a flat slab of isotropic material having relative  $\epsilon, \mu = -1$  could be used to form a perfect lens, focusing both the near-field and far-field components of a point source. In principle a lens which focuses both the near-field and far-field components would allow for detail to be resolved below the Rayleigh limit (approximately  $0.6 \lambda$ ). Veselago<sup>16</sup> had introduced the term "negative index" to describe such materials having both a negative electric permittivity and a negative magnetic permeability. There are no materials in nature which exhibit these properties, however in recent years a new generation of artificially engineered "metamaterials" have evolved<sup>17-19</sup>. These materials are comprised of sub-wavelength elements (such as wires or loops) that exhibit a strong electric and/or magnetic response on resonance. A metamaterial layer containing a regular arrangement of these sub-wavelength elements behaves as a homogeneous medium with both effective electric permittivity and effective magnetic permeability. An extensive discussion of metamaterial structures which are formed from metallic wires and split rings can be found in Chapter 8.

Pendry considered decoupling the electric and magnetic effects associated with the perfect lens, and showed that for TM polarized radiation a negative permittivity is required, i.e. only the case of  $\epsilon = -1$  needs to be satisfied. This might in principle enable a thin metal film to act as a perfect lens for TM polarised light<sup>13,15,20-21</sup>. The image is formed by negative refraction occurring inside the metal. If the metal is sufficiently thick, and the object sufficiently close (a few tens of nm from the metal surface), incident light may form a first focus inside the metal layer and a second focus outside it, where the object is imaged with features below the diffraction limit. However, in general metals at visible frequencies are highly opaque, making them less desirable for superlensing applications. For example, a 40 nm Ag film will transmit approximately 15% of incident visible light.

One alternative approach towards achieving negative refraction is to consider using multilayer metal-dielectric stacks, since it has been shown that these structures exhibit high transmissivity in the pass band regions. The idea of using multilayers for negative refraction was first proposed by Scalora et al.<sup>13</sup>, and demonstrated experimentally by Zhang et al.<sup>22</sup>. To illustrate negative refraction through a transparent metal lens, Scalora et al. simulated the propagation, and subsequent image formation, of sub-picosecond pulses through an Ag/MgF<sub>2</sub> stack<sup>13</sup>. Figure 2.3 shows simulation ‘snapshots’ of an optical pulse as it passes through an Ag-MgF<sub>2</sub> multilayer stack. The central region of the wave packet appears to be displaced along the positive transverse direction. This shift can only be understood in terms of the negative refraction of the Poynting vector.

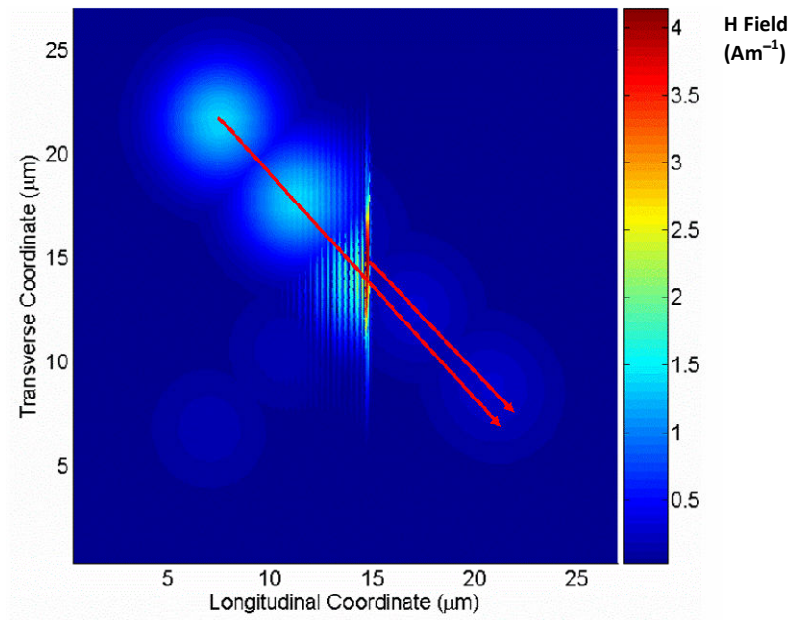


**Figure 2.3** reproduced from reference 13: A Gaussian wave packet (TM polarisation) with carrier wavelength 400 nm is incident at 45 degrees on an Ag-MgF<sub>2</sub> stack. The figure shows several snapshots of magnetic field intensity. The centre of the output pulse is shifted upwards by approximately 266 nm.

When visible radiation which is polarized in a transverse magnetic (TM) configuration is obliquely incident on a metal surface or layer, refraction of the Poynting vector occurs with a negative angle inside the metal layer. Here, the continuity of the normal component of the electric displacement vector (**D**) at the interface between two media with dielectric constants of opposite sign leads to a sign change in the normal component of the electric

field vector. The tangential component of the electric field vector, however, is continuous across the interface. The Poynting vector at the interface between the two media is refracted with a negative angle, as illustrated in Figure 2.4. As has been previously demonstrated, an Ag-MgF<sub>2</sub> multilayer structure exhibits strong resonant transmission features, with minimal reflection or absorption. Even in structures with a high number of periods, these structures exhibit a highly efficient negative refraction process. Numerical simulations have demonstrated negative angles of refraction which approach 45 degrees<sup>13</sup>.

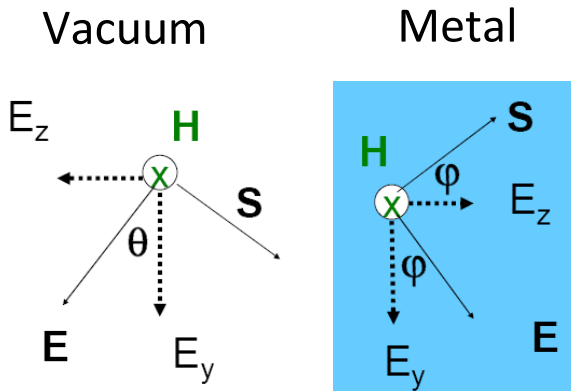


**Figure 2.4** reproduced from reference 13: A TM-polarized beam or pulse is incident from vacuum onto a metal layer at frequencies below the plasma frequency where the real part of the dielectric constant is negative. The preservation of the continuity of the normal component of the electric displacement vector ( $\mathbf{D}$ ) leads to a sign change in the  $E_z$  field component when the dielectric constants have opposite signs.

#### 2.4 Experimental studies of single cavity structures (Ag-MgF<sub>2</sub>-Ag)

In this section the optical constants of the superstrate and substrate media, and those of the metal and dielectric layers will be referred to in terms of their complex refractive index ( $n_r + in_i$ ). The optical response of a single MgF<sub>2</sub> cavity with thickness 140 nm bounded by Ag layers of thickness 20 nm is now discussed. The structure was fabricated on a silica slide ( $n_r = 1.46$ ,  $n_i = 0.00$ ), and is illuminated at normal incidence in air ( $n_r = 1.00$ ,  $n_i = 0.00$ ). The optical constants for Ag and MgF<sub>2</sub> used in the simulation were obtained from reference sources<sup>26</sup>. Figure 2.5 shows the experimental and simulated transmission

spectra obtained for this structure, and the inset schematic shows the layering arrangement in more detail.

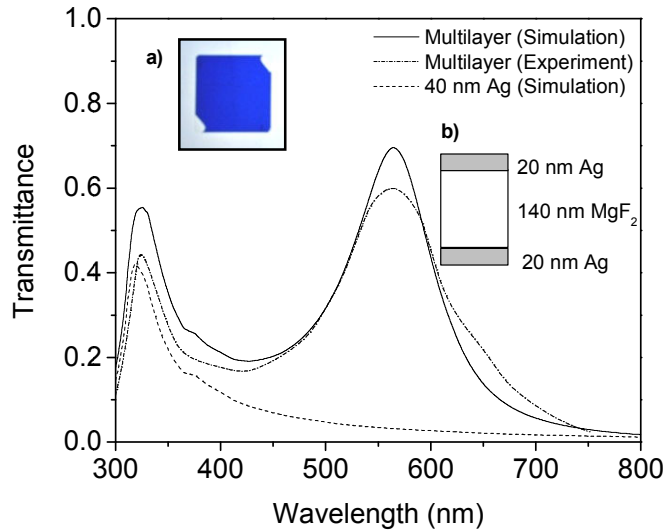


**Figure 2.5:** Experimental and simulated transmittance spectra for a structure consisting of 1.5 periods of 20 nm Ag / 140 nm MgF<sub>2</sub> on a silica slide ( $n_r = 1.46$ ,  $n_i = 0.00$ ), illuminated at normal incidence in air. The dashed line shows the simulated transmittance of a single 40 nm Ag film. Inset (a) shows a colour photograph of the structure viewed in transmission when illuminated with a diffuse white light source (the image has been normalised to the lamp spectrum), and inset (b) shows a schematic of the layering arrangement.

The experimental and simulated transmission spectra for the multilayer structure in Figure 2.6 exhibit distinct maxima at 320 nm and 560 nm. The transmission maxima at 560 nm are attributed to the excitation of standing waves within the dielectric cavity. The Maxwell equations impose the requirement that the tangential E field and its derivative with respect to  $x$  must be continuous at the Ag-MgF<sub>2</sub> interface. The implications of these conditions at this interface are that the fields within the cavity (which are of *sine* or *cosine* functional form) are matched to the evanescent fields inside the metal layers. In Figure 2.6, the time-averaged electric field intensity is shown for a cross section taken perpendicular to the stack at an incident wavelength of 560 nm. This shows the characteristic electric field enhancement that occurs within the dielectric cavity at the resonant frequency, similar to that first observed in the etalon by Fabry and Perot in 1899<sup>1</sup>. One notable observation that can be made is that the magnitude of the transmittance through the cavity structure is

approximately 6 times greater than that of the single 40 nm Ag layer (shown by the dashed line in Figure 2.5). The feature at 320 nm is not related to the cavity response, it is also seen in the dashed curve representing the transmission through a single film comprised of the equivalent thickness of Ag (i.e. 40 nm). In this region of the spectrum the dielectric function of Ag shows a significant reduction in  $\epsilon_i$  (which approaches 0), whilst  $\epsilon_r$  approaches  $-1$ . Using the Fresnel equations at a planar interface between two isotropic media, if the incident medium is air it can be shown that  $T \rightarrow 1.0$  as the permittivity values of the second medium,  $\epsilon_i \rightarrow 0$ ,  $\epsilon_r \rightarrow -1$  respectively.

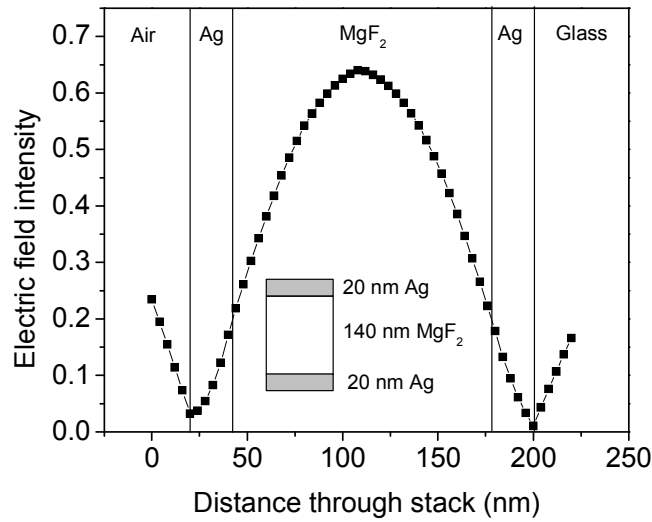


**Figure 2.6:** The time-averaged electric field intensity is shown for a cross section taken perpendicular to the 20 nm Ag / 140 nm MgF<sub>2</sub> / 20 nm Ag stack at an incident wavelength of 560 nm.

Equations 2.7 and 2.8 can be used to determine the resonant wavelength / frequency for the ideal case of quantised standing wave modes between two perfectly reflecting surfaces. In these equations,  $n_r$  is the real component of the refractive index of the medium within the cavity,  $L$  is the cavity length in metres,  $c$  is the speed of light in the medium and  $N$  is the  $N^{\text{th}}$  order resonant mode.

$$\lambda_N = \frac{2n_r L}{N}$$

2.7

$$f_N = \frac{cN}{2n_r L} \quad 2.8$$

It should be noted that in the ideal limit of perfectly conducting films the electromagnetic fields are completely reflected and cannot penetrate the cavity, rendering coupling to the cavity mode impossible. However using Equations 2.7 and 2.8 to consider this hypothetical, ideal scenario predicts a lowest order resonant wavelength of 400 nm. The field distributions in Figure 2.6 clearly show that the resonant mode supported by the cavity is first-order in nature, with penetration of the fields into the bounding Ag layers, due to their finite conductivity. This increases the effective wavelength of the resonant modes which are centred within the dielectric cavity. Thus the resonant wavelength of 560 nm observed in the simulated and experimental data is somewhat larger than predicted by the ideal scenario (400 nm). This will be discussed in more detail below when focusing on multiple cavity structures. Equations 2.7 and 2.8 also show that the resonant wavelengths associated with the Fabry-Perot modes can be tuned by varying the thickness or refractive index of the dielectric cavity. In Figure 2.7 the simulated and experimental transmittance spectra are plotted for two 20 nm Ag layers separated by 140, 180 and 200 nm of MgF<sub>2</sub>. The respective transmittance maxima are observed at incident wavelengths of approximately 560, 660 and 720 nm. As the thickness of MgF<sub>2</sub> is increased, a slight variation is observed in the magnitudes and widths of the Fabry-Perot transmission resonances. This discrepancy arises due to variations in the surface roughness of the MgF<sub>2</sub> and upper Ag layers. In metals, the effects of surface roughness can modify the scattering rate of the conduction electrons, changing the dielectric constants of the material. The degree of surface roughness (and therefore the dielectric properties) of thermally evaporated materials are particularly sensitive to the pressure within the vacuum chamber, and the rate at which the material is deposited. Whilst considerable effort is made to ensure the evaporation conditions are identical for every sample, some small degree of variability is inevitable. More information about the thermal evaporation fabrication technique can be found in Appendix D of the thesis.

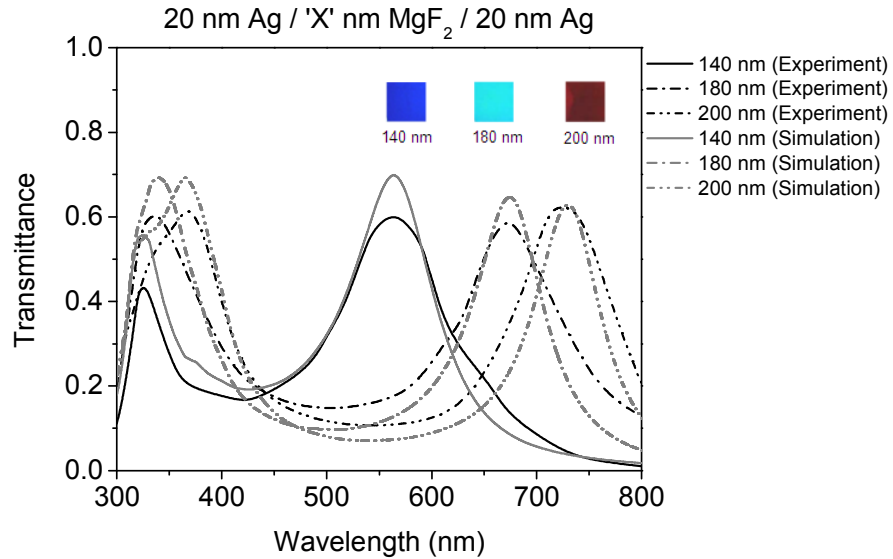


**Figure 2.7:** Simulated and experimental transmittance spectra are shown for two 20 nm Ag layers separated by 140, 180 and 200 nm of MgF<sub>2</sub>. The structure is on a silica slide ( $n_r = 1.46$ ,  $n_i = 0.00$ ) and is illuminated at normal incidence in air. The inset shows colour photographs of the structures viewed in transmission when illuminated with a diffuse white light source (normalised for the lamp spectrum).

### 2.5 Multiple cavity structures (Ag-MgF<sub>2</sub>-Ag-MgF<sub>2</sub>.....)

It is relatively simple during the fabrication process to produce multilayer structures with a very high number of periods. For thermal evaporation chambers fitted with two electrodes it is possible to evaporate both metal and dielectric layers in succession. An electrical switch is used to direct current through each electrode in turn without breaking the vacuum. In multilayer structures with more than one cavity, fields in adjacent cavities may interact, significantly modifying the optical response with respect to a single cavity. In order to study the resonant behaviour of the structure, the assumption is made here that the resonant frequencies occur when the absorbance of the structure is maximal. Figure 2.8 shows the simulated transmittance and absorbance spectra for a structure consisting of 4.5 periods of 20 nm Ag / 110 nm MgF<sub>2</sub>. For simplicity in these simulations it is assumed that the structure is surrounded entirely by glass ( $n_r = 1.52$ ,  $n_i = 0.00$ ).

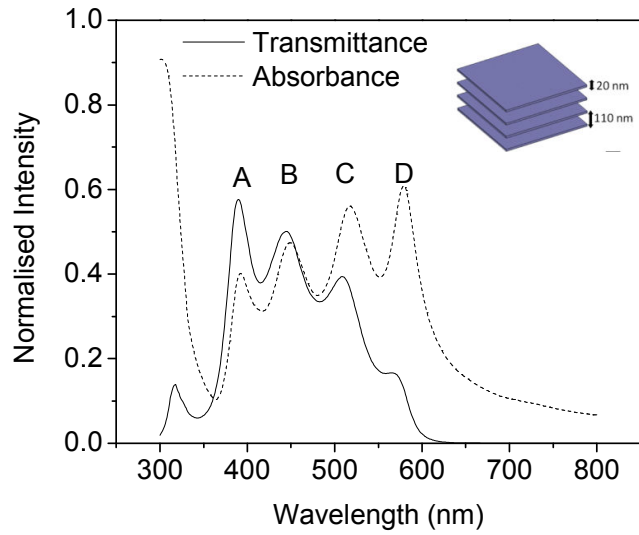


**Figure 2.8:** Simulated transmittance and absorbance spectra for a structure consisting of 4.5 periods of 20 nm Ag / 110 nm MgF<sub>2</sub>. The structure is illuminated at normal incidence and is surrounded by glass ( $n_r = 1.52$ ,  $n_i = 0.00$ ).

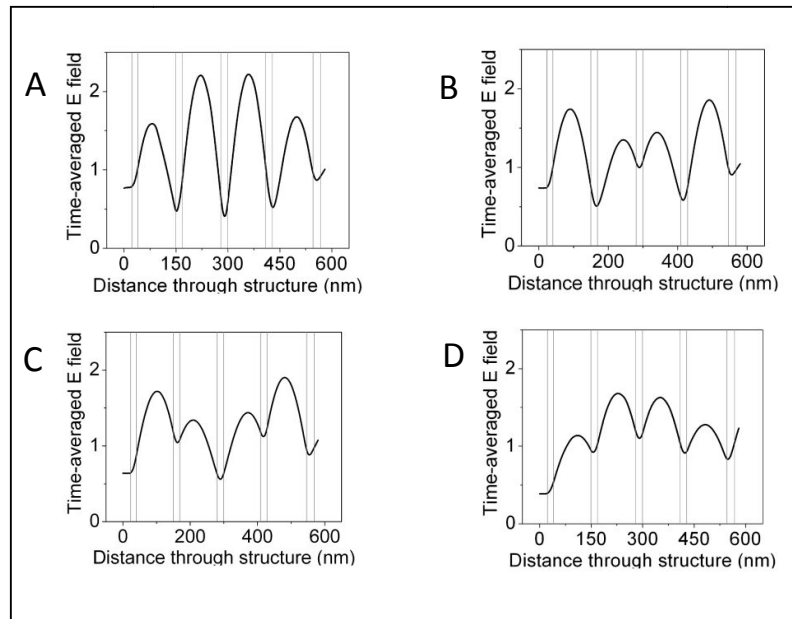


**Figure 2.9:** The time-averaged electric field magnitude is plotted for a cross section taken perpendicular to the multilayer stack at the resonant wavelengths marked A-D in Figure 2.8.

As observed in single cavity structures, the transmittance maximum at 325 nm is due to the dielectric function of Ag. A pass band region in transmittance is observed for incident wavelengths in the range 360 - 600 nm. There are also four distinct transmission maxima located within the pass bands, which decrease in intensity with increase of wavelength. By contrast, the absorption associated with each resonance peak increases in intensity as a function of wavelength. In Figure 2.9, the time-averaged electric field magnitude is plotted for a cross section taken perpendicular to the stack at each of the resonant wavelengths marked from A-D in Figure 2.8. With reference to the field profiles, the differences in the resonant wavelength of each of the modes can now be explained. In resonance A, the electric fields within the metal layer are small, and the majority of the enhanced field exists within the dielectric cavity. In contrast, in resonance D a significant proportion of the electric field extends beyond the dielectric cavity and penetrates into the metal layers. As was identified in the single cavity example, the penetration of the electric fields into the metal layer increases the resonant wavelength of the standing wave oscillation, leading to an 'effective' cavity length which is larger than the optical length of the dielectric cavity. Resonances B and C have 'effective' cavity lengths which lie between those of resonances A and D, since in these resonant modes only pairs of the four cavities oscillate in phase. The field profiles in Figure 2.9 also explain the decrease in magnitude of the resonant transmittance at longer wavelengths. As the resonant wavelength of the cavity modes increases through resonances A-D, the proportion of the electric field within the metal layers also increases. Since the absorption within the medium is proportional to  $\epsilon_i \mathbf{E}^2$ , it is expected that the greatest absorption will occur for the resonant mode which has the largest proportion of the electric field within the Ag layers. This is indeed what is observed in the simulated absorbance spectrum in Figure 2.8. In general, for a multilayer stack surrounded by a homogeneous environment, the number of maxima within each transmission band will be equal to the number of cavities. In Figure 2.10 the number of periods within the multilayer structure is increased and the optical response of a 10.5 period structure of 20 nm Ag \ 100 nm MgF<sub>2</sub> is considered. From a closer inspection of Figures 2.8 and 2.10, it appears that a more rectangular (steeper gradient of the spectrum as the structure makes the transition from being non-transmissive to transmissive) pass band can be achieved by increasing the number of periods. A comparison between Figures 2.8 and 2.10 also suggests the width of the transmission pass band is independent of the number of periods, since the maxima located at the upper and lower band edges do not change in frequency when further periods are added.

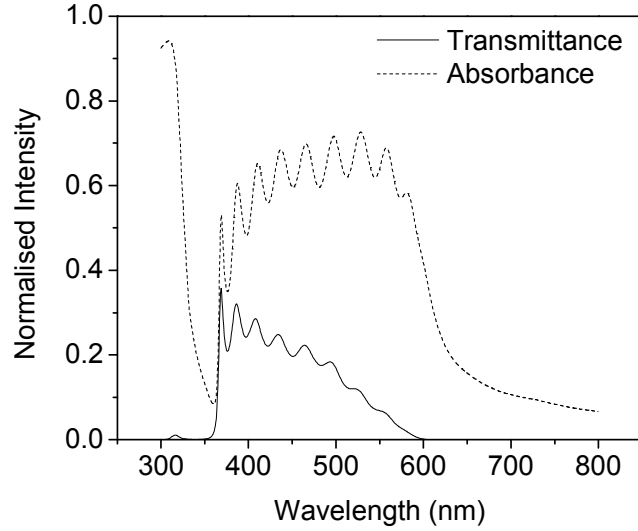


**Figure 2.10:** Simulated transmission and absorbance spectrum of a structure consisting of 10.5 periods of 20 nm Ag / 110 nm MgF<sub>2</sub>. The structure is illuminated at normal incidence and is surrounded by glass  $n_r = 1.52$ ,  $n_i = 0.00$ ).

In order to learn more about the properties of the transmission band, an analytical approach can be used to derive the electric field distributions within an infinite multilayer structure<sup>24</sup>. For simplicity it is assumed that the fields inside the metal layers are purely evanescent and non-oscillatory. The dielectric layers are assumed to have thickness  $a$  and refractive index  $n_{1real}$ , and the metal layers have thickness  $b$  and refractive index  $n_{2imag}$ . The functional of the electric fields within the dielectric region are standing waves originating from the summation of two plane waves which are propagating in opposite directions and are of the form  $\exp(i(n_{1real}kx - \omega t))$  and  $\exp(-i(n_{1real}kx - \omega t))$  respectively. If the time varying components of the waves are neglected, the resulting electric fields within the dielectric layers will have either a *cosine* or *sine* functional form depending on whether the fields are maximal at **a**) the centre of the dielectric cavities (Equation 2.9) or **b**) the dielectric-metal interfaces (Equation 2.10). Within the metal layers, the refractive index is purely imaginary and the wave functions will be centred about  $(a/2 + b/2)$  and have either a *cosh* or *sinh* functional form, depending on whether the fields are maximal at **a**) the centre of the metal layers (Equation 2.11) or **b**) the metal-dielectric interfaces (Equation 2.12).

$$\mathbf{E}_{n1real} = A \cos(n_{1real}k_0x)$$

2.9

$$\mathbf{E}'_{n1real} = A \sin(n_{1real}k_0x) \quad 2.10$$

$$\mathbf{E}_{n2imag} = B \cosh\left(n_{2imag}k_0\left[x - \left(\frac{a}{2} + \frac{b}{2}\right)\right]\right) \quad 2.11$$

$$\mathbf{E}'_{n2imag} = -B \sinh\left(n_{2imag}k_0\left[x - \left(\frac{a}{2} + \frac{b}{2}\right)\right]\right) \quad 2.12$$

Where  $\mathbf{E}_{n1}$ ,  $\mathbf{E}'_{n1}$ , represent the wave functions within the dielectric layers, and  $\mathbf{E}_{n2}$ ,  $\mathbf{E}'_{n2}$  represent the wave functions within the metal layers. A and B represent arbitrary amplitude coefficients. The derivatives of these are therefore:

$$\frac{\partial \mathbf{E}_{n1real}}{\partial x} = -n_{1real}k_0A \sin(n_{1real}k_0x) \quad 2.13$$

$$\frac{\partial \mathbf{E}'_{n1real}}{\partial x} = n_{1real}k_0A \cos(n_{1real}k_0x) \quad 2.14$$

$$\frac{\partial \mathbf{E}_{n2imag}}{\partial x} = n_{2imag}k_0B \sinh\left(n_{2imag}k_0\left[x - \left(\frac{a}{2} + \frac{b}{2}\right)\right]\right) \quad 2.15$$

$$\frac{\partial \mathbf{E}'_{n2imag}}{\partial x} = -n_{2imag}k_0B \cosh\left(n_{2imag}k_0\left[x - \left(\frac{a}{2} + \frac{b}{2}\right)\right]\right) \quad 2.16$$

There is then a series of possible pairings between the electric fields within the metal and those within the dielectric. For example, if those within the dielectric are *cosine*, and those within the metal are *cosh*, Equations 2.9 and 2.10 must be equated at the metal-dielectric boundaries, as must Equations 2.13 and 2.15:

$$A \cos(n_{1real}k_0x) = B \cosh\left(n_{2imag}k_0\left[x - \left(\frac{a}{2} + \frac{b}{2}\right)\right]\right) \quad 2.17$$

$$-n_{1real}k_0A \sin(n_{1real}k_0x) = n_{2imag}k_0B \sinh\left(n_{2imag}k_0\left[x - \left(\frac{a}{2} + \frac{b}{2}\right)\right]\right) \quad 2.18$$

In order to simplify the above expressions, Equation 2.18 can be divided through by 2.17 to leave a single equation.

$$n_{1real} \tan\left(n_{1real}k_o \frac{a}{2}\right) = n_{2imag} \tanh\left(n_{2imag}k_o \frac{b}{2}\right) \quad 2.19$$

This process can then be repeated for all possible combinations (for example *sine* functions matching to *sinh* etc.), to yield three more equations:

$$n_{1real} \tan\left(n_{1real}k_o \frac{a}{2}\right) = n_{2imag} \coth\left(n_{2imag}k_o \frac{b}{2}\right) \quad 2.20$$

$$n_{1real} \cot\left(n_{1real}k_o \frac{a}{2}\right) = -n_{2imag} \tanh\left(n_{2imag}k_o \frac{b}{2}\right) \quad 2.21$$

$$n_{1real} \cot\left(n_{1real}k_o \frac{a}{2}\right) = -n_{2imag} \coth\left(n_{2imag}k_o \frac{b}{2}\right) \quad 2.22$$

From the field profiles in Figure 2.9, one can see that the low frequency band edge occurs when fields in adjacent cavities are in phase and a *cosine* function within the dielectric layers matches to a *cosh* distribution within the metal. Similarly, at the high frequency band edge the fields in adjacent cavities are out of phase and the field in the metal has a *sinh* distribution. The solutions to Equations 2.20 and 2.21 therefore determine the spectral position of the resonances located at the high (2.20) and low (2.21) frequency band edges of the pass-band of the structure respectively. Note that the frequencies of the band edges are dependent upon the thickness and refractive index of the metal / dielectric layers comprising the single unit cell. In a structure consisting of a finite number of periods, *cosine*, *cosh* and *sinh* distribution functions cannot be exactly formed, leading to some deviation from these ideal limits. However as the number of periods is increased, the width of the transmission pass band converges to that of the infinite multilayer structure. This can be seen by comparing Figure 2.8 (a 4.5 period structure) with Figure 2.10 (a 10.5 period structure). In order to demonstrate the accuracy of the previously derived approximation which matches the electric fields within the metal and dielectric regions, Equations 2.19 and 2.20 can be used to determine the frequencies of the band edges of the structure in Figure 2.10 (10.5 periods of 20 nm Ag / 110 nm MgF<sub>2</sub>). If a recursive Fresnel method is used to calculate the simulated transmittance spectrum, the transmission band edges are located at 360 nm and 600 nm respectively. Using reference data <sup>26</sup>, it is assumed here that  $n_{1real}$  (MgF<sub>2</sub>) = 1.39, and  $n_{2imag}$  (Ag) = 1.81 (at  $\lambda = 360$  nm) and 3.80 (at  $\lambda = 600$  nm). These values can be substituted into Equations 2.19 to 2.20, and the subsequent expressions solved numerically for  $k_o$  (shown in Figures 2.16 and 2.17).

$$\tan(7.7 \times 10^{-8} k_0) = 1.29 \coth(3.8 \times 10^{-8} k_0) \quad 2.23$$

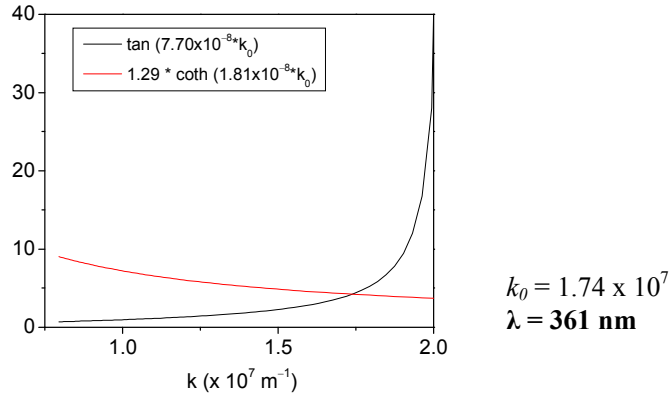


**Figure 2.11:** The high frequency band edge of a multilayer structure formed from a periodic arrangement of Ag and MgF<sub>2</sub> is solved numerically in terms of  $k_0$ .

$$\tan(7.7 \times 10^{-8} k_0) = 2.7 \tanh(3.8 \times 10^{-8} k_0) \quad 2.24$$

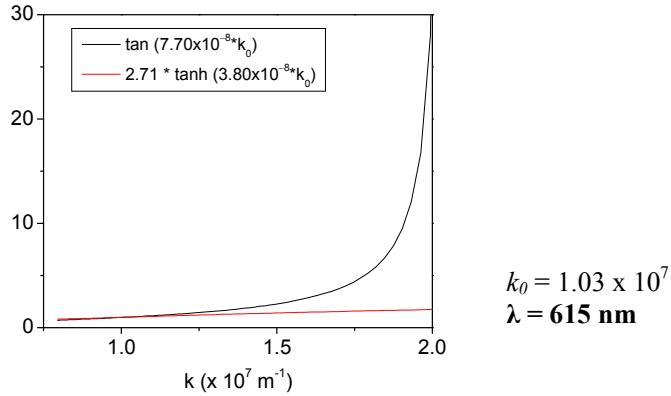


**Figure 2.12:** The low frequency band edge of a multilayer structure formed from a periodic arrangement of Ag and MgF<sub>2</sub> is solved numerically in terms of  $k_0$ .

Figures 2.11 and 2.12 show that the approximation can be used to accurately predict the resonant wavelengths associated with the band edges. This is, in part, due to the assumptions which were made at the outset, particularly that the refractive index of the metal is purely imaginary, with  $n_{2real} = 0$ . For Ag at visible frequencies, the refractive index is not purely imaginary, but is heavily dominated by the imaginary component. For an incident wavelength of 360 nm,  $n_i \approx 10n_r$ , whilst at 600 nm,  $n_i = 30n_r$ <sup>23</sup>. Therefore it may seem surprising that the greatest error between the approximation and the recursive

Fresnel simulation occurs at the low frequency band edge, where the Ag more closely approximates a purely imaginary refractive index. This can be explained by referring to the field profiles in Figure 2.9. Recall that the low frequency band edge corresponds to the fields in adjacent cavities oscillating in phase. At this frequency, a significant proportion of the enhanced field is within the Ag layers, as opposed to the high frequency band edge in which the fields in adjacent cavities oscillate in anti-phase, and the fields within the metal are small. Therefore, any failings in the approximation to correctly account for absorption in the metal will be more evident in the optical response of the structure at the low frequency band edge.

### 2.6 Analogy with the classical example of masses coupled by springs

It is particularly interesting to compare the coupled Fabry-Perot resonances observed in multilayer structures to those of a classical example such as masses which are coupled by springs. Figure 2.13 shows a one-dimensional example of such a system. Here, both masses are separately attached to a rigid wall using springs which have spring constant  $k$ . In addition, a third spring with constant  $k'$  is used to couple the two masses together. In this example, it is assumed that there are no damping forces present, and that the spring constant ( $k'$ ) which couples the two masses is significantly smaller than those connecting the masses to the rigid wall ( $k$ ), ie.  $k' \ll k$ , such that the oscillators are weakly coupled.

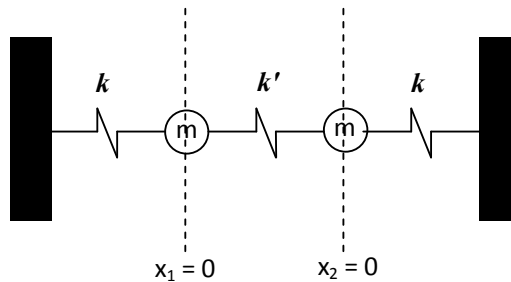


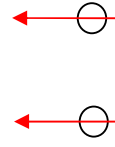
**Figure 2.13:** A one-dimensional classical analogy of two weakly coupled oscillators.

It can be shown that the system of coupled masses exhibits two ‘normal’ resonant modes. These correspond to the masses oscillating either in phase (the symmetric mode) or out of phase (the anti-symmetric mode) respectively.

**The Symmetric mode**

$$x_1 = x_2 = A(\cos(\omega_1 t))$$

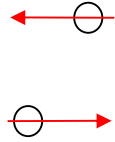
$$\text{Where } \omega_1 = \sqrt{\frac{k}{m}}$$

**The Anti-symmetric mode**

$$x_1 = A(\cos(\omega_2 t))$$

$$x_2 = -A(\cos(\omega_2 t))$$

$$\text{Where } \omega_2 = \sqrt{\frac{k+k'}{m}}$$



From the results presented elsewhere in this chapter, it is known that a multilayer structure which is comprised of two coupled Fabry-Perot cavities has two resonant modes. These can be identified through either transmittance maxima or reflectance minima in the optical response. The resonant field distributions for each of the modes show that the fields in adjacent cavities oscillate either in phase (for the low frequency mode) or out of phase (for the high frequency mode) respectively. The system of coupled masses exhibits identical behaviour, with the high / low frequency modes corresponding to adjacent masses oscillating out of phase / in phase respectively.

## 2.7 Transmittance enhancement through multiple cavity structures

A number of recent publications<sup>7-13</sup> have shown that multilayer structures exhibiting either single or coupled Fabry-Perot cavity resonances can yield enhanced transmission in comparison to a single metal film of the equivalent thickness. An interesting area to investigate is the dependence of the transmittance magnitude on the thickness of the individual metal layers. For example, if a single Ag film with thickness 250 nm is considered – is there an optimum methodology for partitioning the film using resonant dielectric cavities in order to obtain the maximum possible transmission through it? In Figure 2.14, the transmittance, absorbance and reflectance spectra are plotted for various multilayer arrangements in which the thickness of the individual Ag layers is varied, but the total thickness of Ag remains constant (at 250 nm). Each MgF<sub>2</sub> dielectric layer has a fixed thickness of 120 nm, such that the first-order Fabry-Perot modes supported by the structure occur within the visible frequency range. Plot A considers a system of 49 cavities (50 layers of Ag, each 5 nm thick). Plot B is for 24 cavities (25 layers of Ag, each 10 nm

thick). Plot C is for 9 cavities (10 layers of Ag, each 25 nm thick). Plot D is for 4 cavities (5 layers of Ag, each 50 nm thick). Clearly one of the consequences of comparing multilayer stacks in this way is that changing the unit cell of the structure causes the band edges to occur at different frequencies. This is because as the metal layer thickness is reduced, the gradient of the electric field at the dielectric-metal interface also is reduced at the low frequency band edge. This is illustrated for a single section of the multilayer structure in Figure 2.15, where the effective wavelength associated with the oscillation within the dielectric cavities increases as the thickness of the metal layers is reduced from 20 nm to 10 nm. The line shape will also differ between structures, due to the differences in the finite number of periods. However, for the purposes of this comparison the only quantity of interest is the magnitude of the transmission resonances within the first-order pass band.

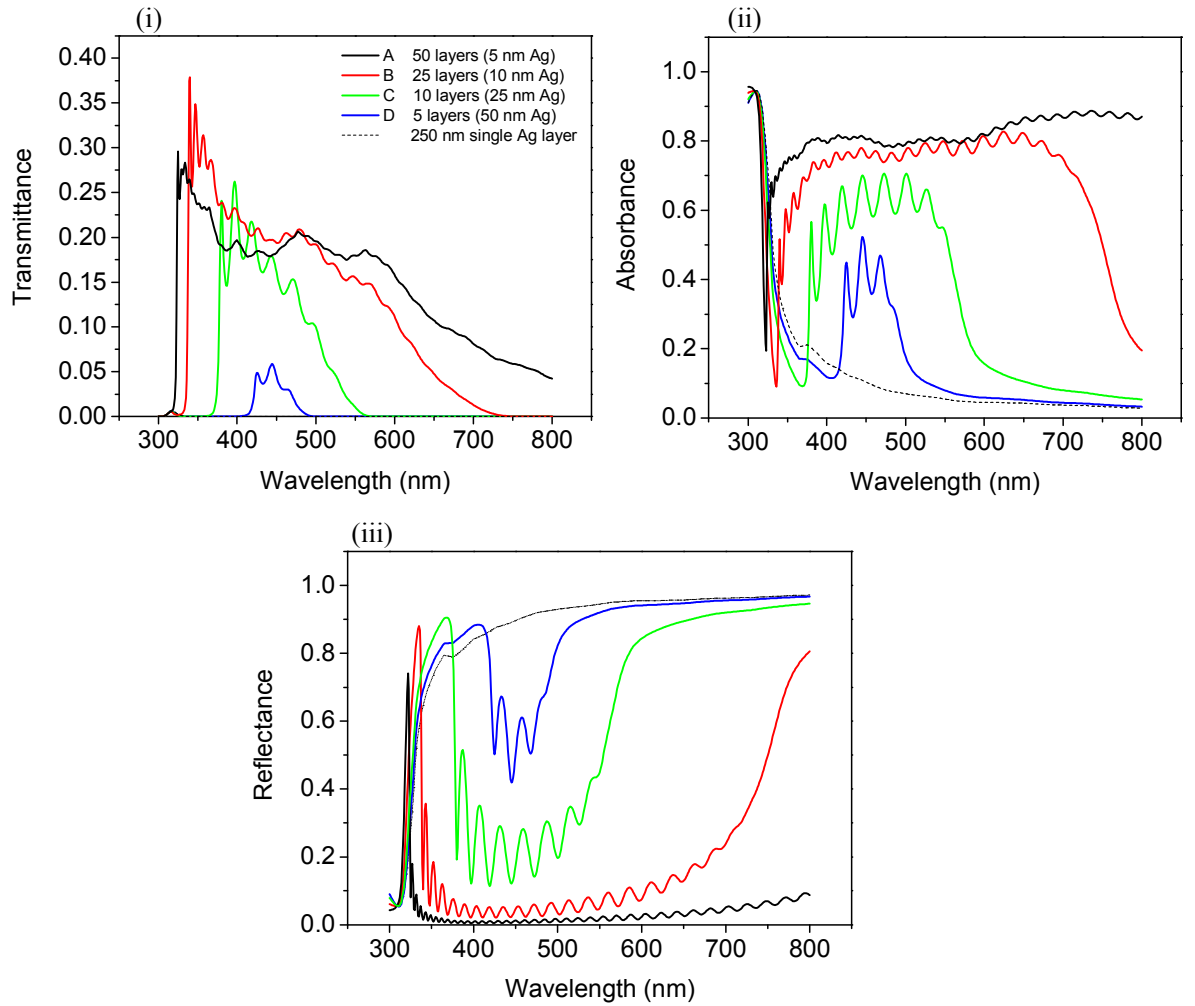


**Figure 2.14:** Simulated transmittance (i), absorbance (ii) and reflectance (iii) spectra for 50 layers of Ag with thickness 5 nm (A), 25 layers of Ag with thickness 10 nm (B), 10 layers of Ag with thickness 25 nm (C) and 5 layers of Ag with thickness 50 nm (D), each separated by 110 nm of MgF<sub>2</sub>. The dashed line is the response of a single layer of 250 nm Ag. The structure is illuminated at normal incidence and is surrounded by glass ( $n_r = 1.52$ ,  $n_i = 0.00$ ).

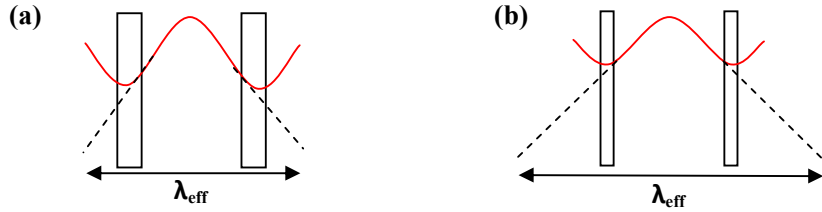


**Figure 2.15:** A diagram showing the electric field distribution for a section (metal-air-metal) of a multilayer structure at the low frequency band edge, where the metal layers have thickness (a) 20 nm and (b) 10 nm.

For thicker layers of Ag (as shown in curve D of Figure 2.14), the first-order transmission band narrows significantly in spectral width. The electromagnetic coupling between adjacent cavities is reduced as the metal layer thickness is increased. The reflectivity of the metal layers also increases as a function of thickness, and reduces the field penetration distance into the stack. The transmission resonance which is conventionally associated with the low frequency band edge (where the fields in the dielectric cavities oscillate in phase and significant field enhancement occurs within the metal layers), is weak and in some cases completely absent since the majority of the incident power is absorbed within the first few metal layers. As the metal layer thickness is decreased, the transmittance magnitude in the pass band region increases, and is greatest for Ag layers with thicknesses in the region 25 nm - 10 nm. The absorbance of the structure also increases as the metal layer thickness is decreased and, perhaps surprisingly, the multilayer structure exhibiting the greatest absorbance is that formed from 5 nm layers. This can be explained through the reduced reflectivity of the thin metal layers, which allows a greater proportion of incident light to penetrate further into the multilayer structure, where it is subsequently transmitted or absorbed. At the cavity resonance condition, there is constructive interference between subsequent reflections in the forward scattered (transmission) direction, and destructive interference between those in the backward scattered (reflection) direction. In Figure 2.16, the time-averaged electric field profiles are shown for structures A-D from Figure 2.14 for a cross-section taken perpendicular to the multilayer stack at the resonant frequency corresponding to the high frequency edge of the first-order transmission band. Since the field distribution at these edges corresponds to fields in all cavities oscillating in anti-phase, the plot has been simplified to show only the field distribution for a single metal layer within the stack.

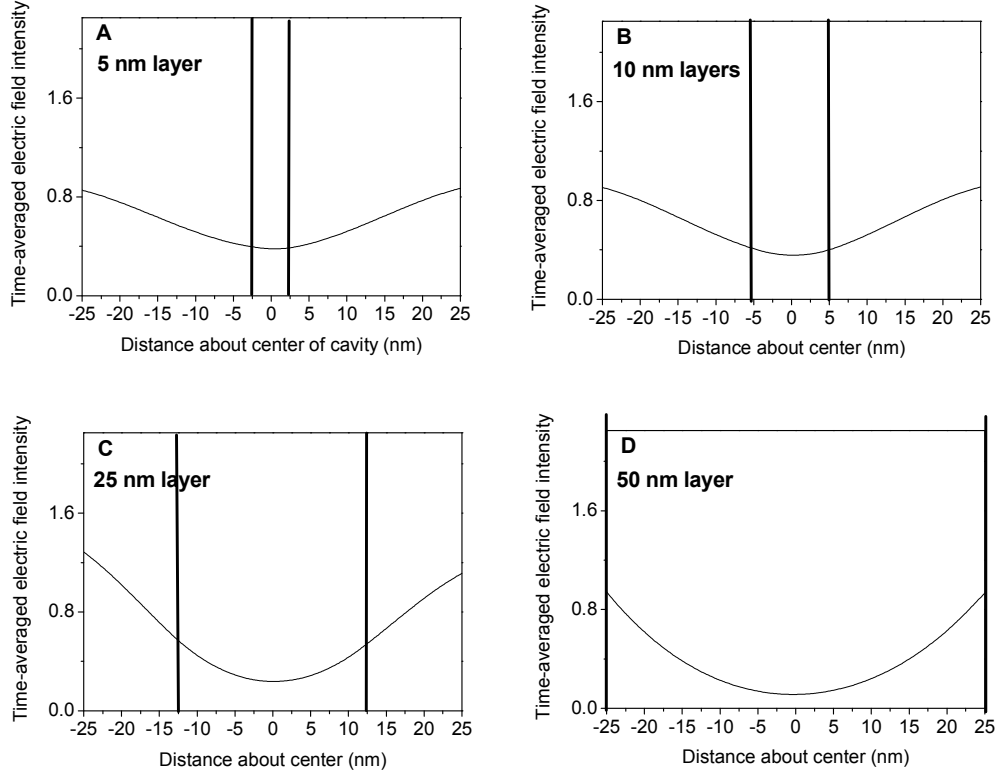


**Figure 2.16:** Time-averaged electric field profiles at the high frequency band edge for the multilayer structures in Figure 2.14 consisting of 5 nm (A), 10 nm (B), 25 nm (C) and 50 nm (D) thick Ag layers separated by 110 nm of  $\text{MgF}_2$ . The structure is illuminated at normal incidence and is surrounded by glass ( $n_r = 1.52$ ,  $n_i = 0.00$ ).

The energy dissipation within the metal layers,  $W$ , in the multilayer structure is proportional to the product of the square of the electric field intensity  $\mathbf{E}^2$  with the imaginary component of the metal permittivity  $\epsilon_i$ . The integrated area under the time-averaged field profiles across the boundaries of the metal layers in Figure 2.16 gives an indication of the absorbance due to a single metal layer within the stack. Clearly the curve which has the smallest integrated area is A, and the largest is D. The electric field will decrease in amplitude between successive metal layers, and a rigorous analysis requires a summation of the integral of the electric field within each layer (Equation 2.25).

$$W \propto \sum_{i=0}^N N_i \int_{-b/2}^{b/2} |\mathbf{E}_i|^2 \epsilon_i \quad 2.25$$

Whilst the absorbance due to an individual 5 nm Ag layer may be small, there is little decay of the electric field within the layer, whereas for a 50 nm Ag layer a steep exponential decay is observed from the interfaces. When the summation in Equation 2.25 is considered over all layers, it is seen that the total absorption from the large number of 5 nm layers far exceeds that from the smaller number of 50 nm layers. Another conclusion that can be made is that the absorbance of the multilayer stack is always limited by that of the equivalent thickness of Ag (shown by the dashed black curve in Figure 2.15). As the layer thicknesses are increased, the absorbance curves of the multilayer structures tend to the single layer response. Again, this is not surprising, since the efficiency of any transmission resonator will always be limited by the intrinsic absorption of its constituent materials. When using metals such as Ag or Au to fabricate multilayer structures, transmission resonances with magnitude unity cannot therefore be observed.

## 2.8 Studies of Fabry-Perot transmission resonances at microwave frequencies

The response of structures comprised of metal and dielectric layers has also been explored at microwave frequencies<sup>25-35</sup>. It is important to note that at these low frequencies, with metal permittivities of the order  $\epsilon = -10^4 + 10^7i$ , the layers are often approximated as perfect conductors<sup>36,37</sup>. As a reference<sup>37</sup>, a single sputtered Au layer was investigated at microwave frequencies. It was found that for short sputtering times the reflectance was low (high transmittance), this was attributed to the low conductivity associated with the disconnected layer of gold particles. For longer sputtering times the fabricated structures consisted of a homogenous metal film, with a thickness of 10 – 20 nm. In these structures the reflectance was found to be close to unity, with little or no transmittance. This is in contrast to the response of continuous metal films at visible frequencies, where partial transmission is observed for Ag films having thicknesses less than 100 nm (refer to Figure 2.5 where the transmission of 40 nm Ag is approximately 5 % for incident wavelengths between 400 – 700 nm).

At microwave frequencies, it is also possible to arrange continuous metal and dielectric layers in a multilayer arrangement such that the dielectric cavity supports Fabry-Perot type resonances<sup>36</sup>. As observed in the optical regime, transmission resonances occur at wavelengths which approximately correspond to half integer multiples of the wavelength within the dielectric medium. However there is a significant difference in the behaviour of

the stack at microwave frequencies, particularly that the transmittance on resonance is very low. For example, a structure comprised of two 20 nm Ag layers separated by 10 nm in vacuum exhibits a series of narrow transmission resonances with magnitude  $\ll 1\%$ , as shown in Figure 2.17.

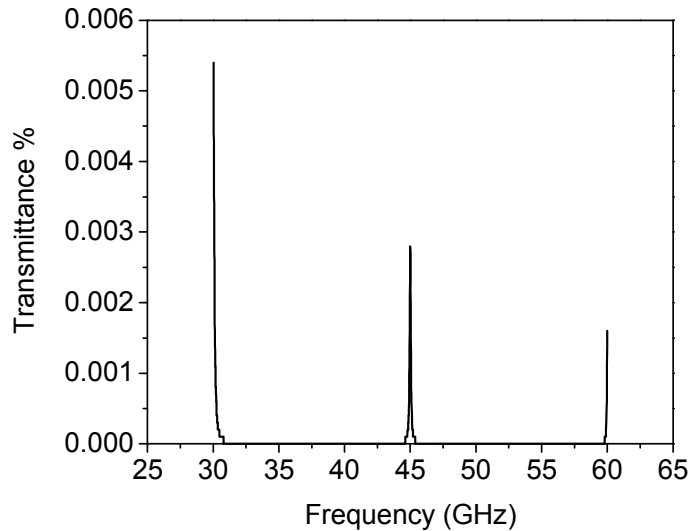


**Figure 2.17:** The simulated transmittance and reflectance spectra are shown for two layers of 20 nm thick Ag ( $\epsilon = -10^4 + 10^7i$ ) separated by 10 nm of vacuum. The sample is illuminated at normal incidence with frequencies ranging from 30 – 60 GHz ( $3.0 - 6.0 \times 10^{10}$  Hz).

The low transmissivity is due to the high impedance mismatch of the metal layers with respect to free space. In a Fabry-Perot resonator, introducing metal layers with a high reflectivity would at first seem a sensible proposition for maximising the field enhancement within the cavity. However another consequence of using high reflectivity layers is that very little field can penetrate into the cavity in the first instance. The response of the multilayer structure is extremely limited by the thickness of the metal layers and the number of periods. Continuous thin metal films are thus impractical to use when attempting to design microwave multilayer stacks which require high transmissivity over a wide band of frequencies. The alternative approach is to engineer a metamaterial structure with electromagnetic properties similar to those of plasmonic metals (eg. Ag, Au) at visible frequencies by patterning a thick metal film with a non-diffracting array of holes or wire grids. Below the cut-off frequency associated with the holes, the structure will support only evanescent waves, and the electromagnetic response can be characterised solely by a real permittivity component which is negative<sup>26,30</sup>.

The technique of using wire grids was first proposed by Bae et al.<sup>26</sup>, and in recent years wire grids and perforated surfaces have attracted considerable attention for a variety of electromagnetic applications<sup>25-35</sup>. Bae et al. used the mesh as an evanescent coupling mechanism to enhance the transmission through a dielectric (Si) plate. The separation between the mesh and the Si plate ( $\lambda/20$ ) was significantly less than that conventionally used in Fabry-Perot transmission experiments ( $\lambda/2$ ). A wave incident on the mesh surface induces evanescent waves which extend above and below the mesh surface. The evanescent waves decay rapidly as a function of distance, with a typical decay length of  $\lambda/20$  from the surface<sup>26</sup>. The decay length is dictated by the size and geometry of the holes. In the presence of a dielectric layer (the Si plate), it was found that coupling between evanescent waves enhanced the transmission through the structure. The transmission enhancement was found to be highly dependent on the cavity spacing, and could be modified by up to 70% across the range 50 – 100  $\mu\text{m}$ . In a second experiment, the structure was also found to behave as a Fabry-Perot cavity at much larger separations. A series of transmission resonances were observed when the cavity spacing was approximately  $\lambda/2$ . An important difference between these resonances and those shown in the example calculation in Figure 2.17 is that the magnitude of the transmission resonances observed by Bae et al. was close to unity. This suggested to us that if continuous metal layers could be substituted with metamaterial layers, various aspects of multilayer optics studied at visible frequencies could also be applied in the microwave regime.

A multilayer stack at microwave frequencies can be fabricated using metallic grid and dielectric layers. The dielectric layers can be fabricated from low loss circuit board such as Nelco NX9255 ( $\epsilon \approx 3 + 0.01i$ ) using a photo lithography technique. An example of the experimental response of a metamaterial-dielectric stack at microwave frequencies is shown in Figure 2.18. This structure was designed and characterised by Butler et al.<sup>29</sup>, and exhibits a series of pass bands corresponding to coupled Fabry-Perot resonances within the dielectric cavities (Figure 2.19).

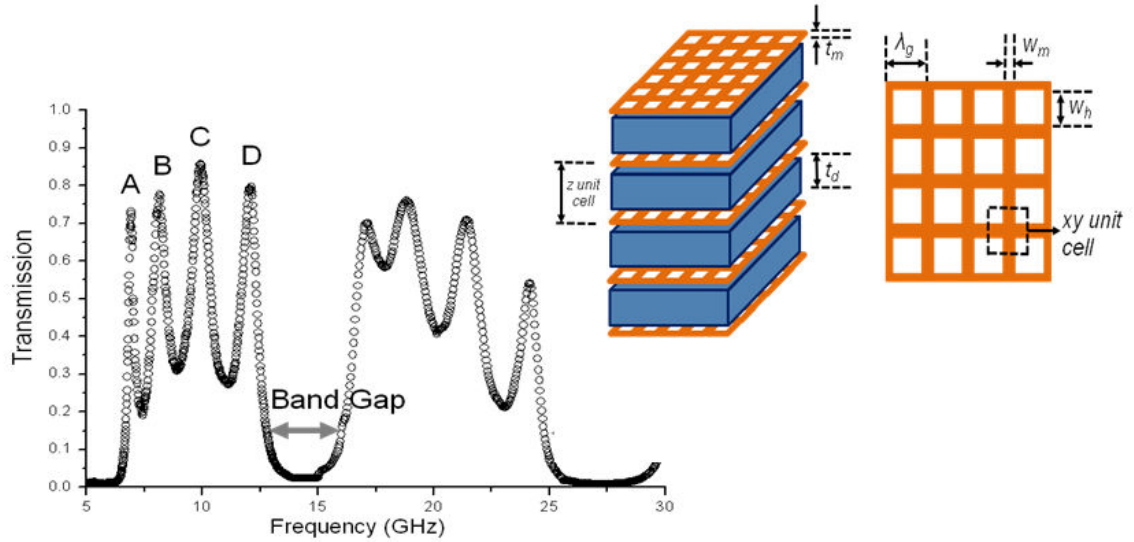


**Figure 2.18** reproduced from reference 29 (Butler *et al.*) : Experimental transmission spectrum of a metamaterial comprising a stack of metallic grid and dielectric layers at microwave frequencies with dielectric cavity thickness ( $t_d$ ) 6.35 mm and metal layer thickness ( $t_m$ ) 18  $\mu\text{m}$ . The inset shows the schematic of the structure and a plan view of the hole geometry, with parameters  $\lambda_g = 5$  mm,  $w_m = 0.15$  mm,  $w_n = 4.85$  mm.

The distribution of the electric fields at each of the resonant frequencies matches that of the metal-dielectric stack at visible frequencies (Figure 2.9). Fabry-Perot resonant modes within the dielectric cavity (*cosine* or *sine* functional form) are coupled through evanescent decaying fields in the metamaterial layers (*cosh* or *sinh* functional form). For the *sinh* case, the fields within the metal are small and the high frequency band edge is in close agreement to that predicted by the ideal Fabry-Perot Equations 2.7 and 2.8. However when the fields in the metallic grid are *cosh*-like, depending on the parameters of the grid layer, the resonant frequency may approach zero. This is explained by similar analogy that of the metal-dielectric structure in Figure 2.15, where the gradient of the electric field at the dielectric-grid interface is reduced as the decay length of the grid layers is decreased. This increases the effective wavelength of the oscillation within the dielectric cavities, lowering the resonant frequency of the structure.

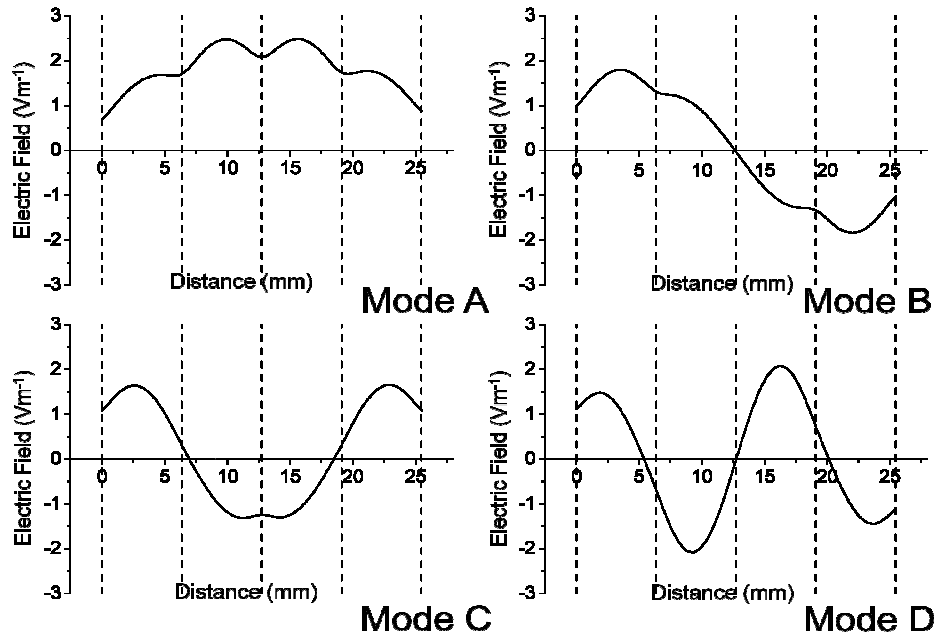


**Figure 2.19** reproduced from reference 29 (Butler et al.): Instantaneous electric-field amplitude distributions as a function of distance perpendicular to the metallic grid-dielectric stack at each of the resonant frequencies marked A-D in Figure 2.18. The vertical dashed lines indicate the positions of the metallic grid layers.

One novel and highly desirable aspect of using the metamaterial structure is that the effective permittivity of the metallic grid layers may be tuned by varying both the thickness of the metal layers and the dimensions of the square hole array. This adds a new degree of tunability, in contrast to metals at visible frequencies where the permittivity of the Ag or Au are fixed. They are material properties and there is no scope for modifying the values of  $\epsilon_r$  or  $\epsilon_i$ . The properties of the transmission band in the visible regime can only be tuned by varying the cavity spacing or the thickness of the metal layers.

By extracting effective parameters of the metallic grid layers<sup>38</sup>, it has been shown that the effective refractive index of the metallic grid layers is almost entirely imaginary ( $n_r \approx 0$ ), meaning that there is very little absorption inside the layers. The maxima in the first order transmission pass band of Figure 2.18 have magnitudes between 70% and 85%. Additional finite element simulations (not shown), have identified that the majority of the absorption in the experimental sample occurs within the dielectric (Nelco NX9255) layers. There are applications where the absorptive properties of the metamaterial structure might

need to be modified. An example could be to minimise the impedance mismatch at an interface with another dielectric. With the metamaterial structure this could be performed easily by filling the regions between the wires with a suitably absorbing dielectric material. Another benefit of the metamaterial structure is that it is also lightweight, since the fractional occupancy of the metal within each unit cell is very low. A lightweight structure having easily modifiable properties is likely to play an important role in microwave and millimetre wave technologies, particularly in structures such as antennas, electromagnetic shielding applications and ‘stealth-like’ absorbing surfaces<sup>30-37</sup>.

## 2.9 Concluding remarks

The work presented in this section represents an original investigation into the optical response of structures formed from periodic arrangements of continuous metal and dielectric layers. It has been shown that a single cavity (metal-dielectric-metal) structure exhibits resonant transmission features equivalent to the Fabry-Perot etalon, whereby transmission maxima are observed at incident wavelengths corresponding to a half integer multiples of the optical cavity length. In multiple cavity structures, the resonant modes of neighbouring cavities may couple, leading to a series of maxima in transmission which are distributed across a band of frequencies (the transmission pass band). The properties of the transmission band can be tuned by varying the thickness of the metal or dielectric layers.

Something which is common to most of the structures presented throughout this chapter is that the metallic layers are continuous (apart from the final section on metallic grids at microwave frequencies). This is particularly important, since the magnitude and spectral width of the observed transmission resonances is highly dependent upon the reflectivity of the metal layers (see appendix A). For example, a layer comprised of non-continuous metallic elements (such as a random arrangement of disconnected metallic particles) will have a reduced conductivity (in comparison to a continuous metal film), and therefore a reduced reflectivity. It is known that noble metallic particles having dimensions  $\ll \lambda$  exhibit localised surface Plasmon resonances (LSPRs) which are quite distinct from the Fabry-Perot resonances presented in this chapter. This chapter serves as a useful prerequisite for Chapters 7 and 8 of the thesis, in which particle arrays and metallic films perforated with arrays of holes are stacked (vertically) to form a metamaterial. Here, the optical response is shown to exhibit resonant features which may be attributed to the excitation of both LSPR and Fabry-Perot modes. There is a much more scope for

optimising the optical response of these structures if the respective modes are first studied, and understood, separately.

## Chapter 3

---

### Techniques used to simulate the scattering of electromagnetic radiation from metallic nanoparticle and metallic nanohole structures

#### 3.1 Introduction

Throughout this thesis simulated data are presented for structures comprised of either metallic particles or metallic films perforated with holes, both as single entities and as part of regular arrays. The simulated data are derived from a variety of computational techniques, some involving commercial software and others which require a degree of programming to solve systems of equations. This chapter includes a discussion of each of the computational techniques used to perform the simulations in subsequent chapters 4-8. The basic underlying theory of each method will be introduced, with an explanation of how each method is implemented. It should be noted that in many cases the theory can be extremely complicated and in some cases entire theses have been dedicated to the study of an individual approach<sup>3</sup>. The final section of this chapter contains a comparison whereby each technique has been used to simulate the scattering from a 80 nm diameter Au sphere in vacuum. The suitability of each technique will be considered in terms of its accuracy, computation time and the range of geometries to which it can be applied. The findings from this Chapter are summarised in table form, it is intended that this may be of use as a reference guide for future calculations.

The simulation techniques which will be compared in this section are **Mie Theory**, the Transition Matrix (**T-Matrix**) method, the Discrete Dipole Approximation (**DDA**), the Finite Element Method (**FEM**) and the Finite Difference Time Domain (**FDTD**) method.

#### 3.2 Mie Theory

*Mie Theory* (**Mie**) is a complete solution of Maxwell equations applicable to the scattering of light by small spherical particles, first proposed by Gustav Mie in 1908<sup>1</sup>. The application of this method requires knowledge of the full solutions to the vectorial form of the wave equations, a derivation is given in *Bohren & Huffman*<sup>2</sup>. However the derivation is lengthy so that here we identify only the main stages of the derivation. This section will consider the scattering of an incident plane wave by a spherical, isotropic and non-

magnetic particle in a non-absorbing isotropic medium. The plane wave must first be expressed in terms of spherical harmonics. The form of the incident electromagnetic wave and its formulation in spherical polar co-ordinates are shown in Equations 3.1 and 3.2.

$$E_i = E_0 e^{ikr \cos \theta} \hat{e}_x \quad 3.1$$

$$\hat{e}_x = \sin \theta \cos \phi \hat{e}_r + \cos \theta \cos \phi \hat{e}_\theta - \sin \phi \hat{e}_\phi \quad 3.2$$

The transformation from Cartesian to spherical polar coordinates which is assumed in Equation 3.2 will now be briefly explained. Figure 3.1 shows a representation of the unit vectors of the spherical polar coordinate system against Cartesian axes, where the vector  $\mathbf{r}$  (which has magnitude  $R$ ) sweeps from the origin to a point P such that  $\theta$  is the polar angle,  $\phi$  is the azimuthal angle and  $\hat{e}_r$ ,  $\hat{e}_\theta$ ,  $\hat{e}_\phi$  represent the radial, polar and azimuthal unit vectors respectively.

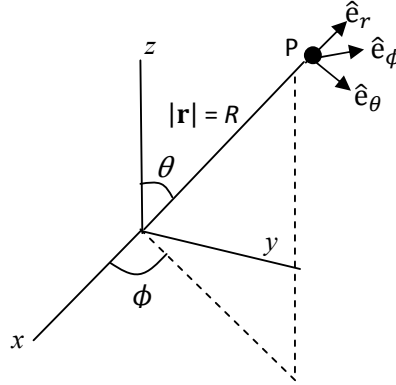


**Figure 3.1:** The unit vectors of the spherical polar coordinate system are represented on Cartesian axes.

The coordinate transformation is achieved by expressing  $\hat{e}_r$ ,  $\hat{e}_\theta$ ,  $\hat{e}_\phi$  as a function of the Cartesian coordinates  $\hat{x}$ ,  $\hat{y}$ ,  $\hat{z}$ . The direction of  $\hat{e}_r$  in Figure 3.1 is parallel to the vector which is swept by increasing  $R$ , whilst  $\theta$  and  $\phi$  are fixed. Similarly,  $\hat{e}_\theta$  is parallel to the vector which is swept by increasing  $\theta$ , whilst  $R$  and  $\phi$  are fixed, and  $\hat{e}_\phi$  is parallel to the vector which is swept by increasing  $\phi$ , whilst  $R$  and  $\theta$  are fixed. A more formal representation is given by Equations 3.3 – 3.5.

$$\hat{e}_r = \frac{1}{\left| \frac{\partial \mathbf{r}}{\partial R} \right|} \left( \frac{\partial \mathbf{r}}{\partial R} \right) \quad 3.3$$

$$\hat{\mathbf{e}}_\theta = \frac{1}{\left|\frac{\partial \mathbf{r}}{\partial \theta}\right|} \left(\frac{\partial \mathbf{r}}{\partial \theta}\right) \quad 3.4$$

$$\hat{\mathbf{e}}_r = \frac{1}{\left|\frac{\partial \mathbf{r}}{\partial \phi}\right|} \left(\frac{\partial \mathbf{r}}{\partial \phi}\right) \quad 3.5$$

From Figure 3.1 it can be shown that:

$$\mathbf{r} = R \sin \theta \cos \phi \hat{\mathbf{x}} + R \sin \theta \sin \phi \hat{\mathbf{y}} + R \cos \theta \hat{\mathbf{z}} \quad 3.6$$

Substituting Equation 3.6 into Equations 3.3 – 3.5 gives:

$$\hat{\mathbf{e}}_r = \sin \theta \cos \phi \hat{\mathbf{x}} + \sin \theta \sin \phi \hat{\mathbf{y}} + \cos \theta \hat{\mathbf{z}} \quad 3.7$$

$$\hat{\mathbf{e}}_\theta = \cos \theta \cos \phi \hat{\mathbf{x}} + \cos \theta \sin \phi \hat{\mathbf{y}} - \sin \theta \hat{\mathbf{z}} \quad 3.8$$

$$\hat{\mathbf{e}}_\phi = -\sin \phi \hat{\mathbf{x}} + \cos \phi \hat{\mathbf{y}} \quad 3.9$$

For an incident wave which has the electric field polarised along the x direction, the solutions corresponding to the Cartesian vector component  $\hat{\mathbf{x}}$  can be extracted and expressed in the form shown in Equation 3.2. A physically realisable time-harmonic electromagnetic field ( $\mathbf{E}, \mathbf{H}$ ) in an isotropic medium must satisfy the wave equation (Equations 3.10 and 3.11). To demonstrate the possible solutions to this equation, a scalar function,  $\psi$ , will be considered for simplicity. The vectorial form of the solution to Equations 3.10 and 3.11 is considerably more involved, however a thorough derivation can be found in the literature<sup>2</sup>. The scalar wave equation in spherical polar coordinates is given in Equation 3.12.

$$\nabla^2 \mathbf{E} + k^2 \mathbf{E} = 0 \quad 3.10$$

$$\nabla^2 \mathbf{H} + k^2 \mathbf{H} = 0 \quad 3.11$$

$$\frac{1}{r^2} \frac{\partial}{\partial r} \left( r^2 \frac{\partial \psi}{\partial r} \right) + \frac{1}{r^2 \sin \theta} \frac{\partial}{\partial \theta} \left( \sin \theta \frac{\partial \psi}{\partial \theta} \right) + \frac{1}{r^2 \sin \theta} \frac{\partial^2 \psi}{\partial \phi^2} + k^2 \psi = 0 \quad 3.12$$

Equation 3.12 may be solved by the separation of variables method, which seeks a solution of the form  $\psi(r, \theta, \phi) = R(r)\Theta(\theta)\Phi(\phi)$ . This yields three separate equations:

$$\frac{d^2 \Phi}{d\phi^2} + m^2 \Phi = 0 \quad \text{a) Azimuthal term} \quad 3.13$$

$$\frac{1}{\sin \theta} \frac{d}{d\theta} \left( \sin \theta \frac{d\Theta}{d\theta} \right) + \left[ n(n+1) - \frac{m^2}{\sin^2 \theta} \right] \Theta = 0 \quad \text{b) Polar term} \quad 3.14$$

$$\frac{d}{dr} \left( r^2 \frac{dR}{dr} \right) + [k^2 r^2 - n(n+1)]R = 0 \quad \text{c) Radial term} \quad 3.15$$

### 3.2a) Azimuthal term:

The solution to the azimuthal element of the wave equation in spherical polar coordinates comprises odd and even terms:

$$\begin{aligned} \Phi_e &= \cos m\phi & \text{Even solutions} & \quad 3.16 \\ \Phi_o &= \sin m\phi & \text{Odd solutions} & \quad 3.17 \end{aligned}$$

### 3.2b) Polar term:

The polar term is the complete form of Legendre's differential equation, which has a series of known solutions. This equation is solved using the method of Frobenius, which uses a trial solution of the form:

$$\theta = \theta^c (a_0 + a_1 \theta^1 + a_2 \theta^2 + \dots) = \theta^c \sum_{n=0}^{\infty} a_n \theta^n \quad 3.18$$

Here,  $a_0, a_1, \dots, a_n$  are constants. The polar term is solved by substituting Equation 3.18, and appropriate expressions for the first and second derivatives of Equation 3.18 with respect to  $\theta$  into Equation 3.14. The solution of Legendre's differential equation using the method of Frobenius can be found in Appendix B. The general solution to the polar term is:

$$y = C_1 P_l^m(\cos \theta) + C_2 Q_l^m(\cos \theta) \quad 3.19$$

There are two solutions to Equation 3.14 since any differential equation with order N must have N linearly independent solutions. Here,  $C_1$  and  $C_2$  are constants,  $P_l^m(\cos \theta)$  and  $Q_l^m(\cos \theta)$  are the associated Legendre functions of first and second kind respectively. In Mie Theory, boundary conditions require that the solutions to the wave equation must be finite between  $\theta = 0$  and  $\theta = \pi$  (or  $x = 0$  and 1 in the case of  $P_l^m(x)$  and  $Q_l^m(x)$ ). In this instance, the Legendre functions of second kind are not valid solutions, since they diverge to infinity at  $\theta = 0$ . The only physically meaningful terms which contribute to the solution of the wave equation arise from  $P_l^m(\cos \theta)$ .

**3.2c) Radial term:**

The radial element of the solution to the wave equation in Equation 3.15 can be rearranged by introducing two new variables,  $\rho$  and  $Z$ , such that:

$$\rho = kr \text{ and } Z = R\sqrt{\rho}$$

$$\rho \frac{d}{d\rho} \left( \rho \frac{dZ}{d\rho} \right) + \left[ \rho^2 - \left( n + \frac{1}{2} \right)^2 \right] = 0 \quad 3.20$$

Equation 3.20 is a form of Bessel's differential equation. As shown previously with Legendre's differential equation, this may also be solved using the method of Frobenius, an example for Bessel's equation is shown in Appendix C. There are two possible solutions to Equation 3.13, termed Bessel functions of the first (Equation 3.21) and second (Equation 3.22) kind respectively.

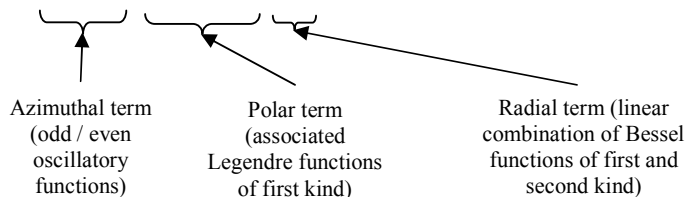
$$j_n(\rho) = \sqrt{\frac{\pi}{2\rho}} J_{n+\frac{1}{2}}(\rho) \quad 3.21$$

$$y_n(\rho) = \sqrt{\frac{\pi}{2\rho}} J_{n+\frac{1}{2}}(\rho) \quad 3.22$$

Here, the Bessel functions of the second kind ( $y_n$ ) also diverge at  $\rho = 0$ , however unlike the Legendre functions of the second kind, these solutions are not disregarded. This is because, whilst the Bessel functions of the second kind diverge to infinity at  $r = 0$ , they may be used to describe solutions outside the sphere, where  $r > 0$  and their value is finite. The  $y_n$  terms may be used to evaluate the incident / scattered field distributions in the regions outside of the sphere, where  $\rho > 0$  and the value of  $y_n$  is finite. As demonstrated with the polar term, the complete solution to Equation 3.20 may contain any linear combination of  $j_n$  and  $y_n$  terms. For reasons which are unknown, this is sometimes referred to in the literature as “the Bessel function of third kind”. It should be stressed that this is not a third solution to Bessel's differential equation; there is no such solution, though additional solutions may arise though a linear combination of the solutions of first and second kind. The complete solution of the scalar wave equation in spherical polar coordinates may now be expressed as:

$$\psi_e = \cos m\phi P_l^m(\cos \theta) z_n \quad \text{Even solutions} \quad 3.23$$

$$\psi_o = \sin m\phi P_l^m(\cos \theta) z_n \quad \text{Odd solutions} \quad 3.24$$



The azimuthal and polar terms within Equations 3.23 and 3.24 represent the angular distribution  $(\theta, \phi)$  of the scattered field at a constant, arbitrary distance from the centre of the sphere. The normal modes of the electromagnetic field may be expressed in terms of the integer values which are assigned to  $l$  and  $m$ . The first few normal modes are shown in Figure 3.2, where the scalar spherical harmonics are plotted for  $l = 1$  to 5 and  $m = 1$  to  $l$  where  $\theta$  is varied from 0 to  $90^\circ$  and  $\phi$  is varied from 0 to  $360^\circ$ . As the value of  $l$  is increased, an increasing number of nodes and antinodes are observed in the angular distribution of the electromagnetic fields. The increase in the number of nodes / anti-nodes as a function of  $l$  is equivalent to the increasing number of surface charge density maxima / minima which are observed in the higher order (multipole) resonances of metallic nanoparticles.

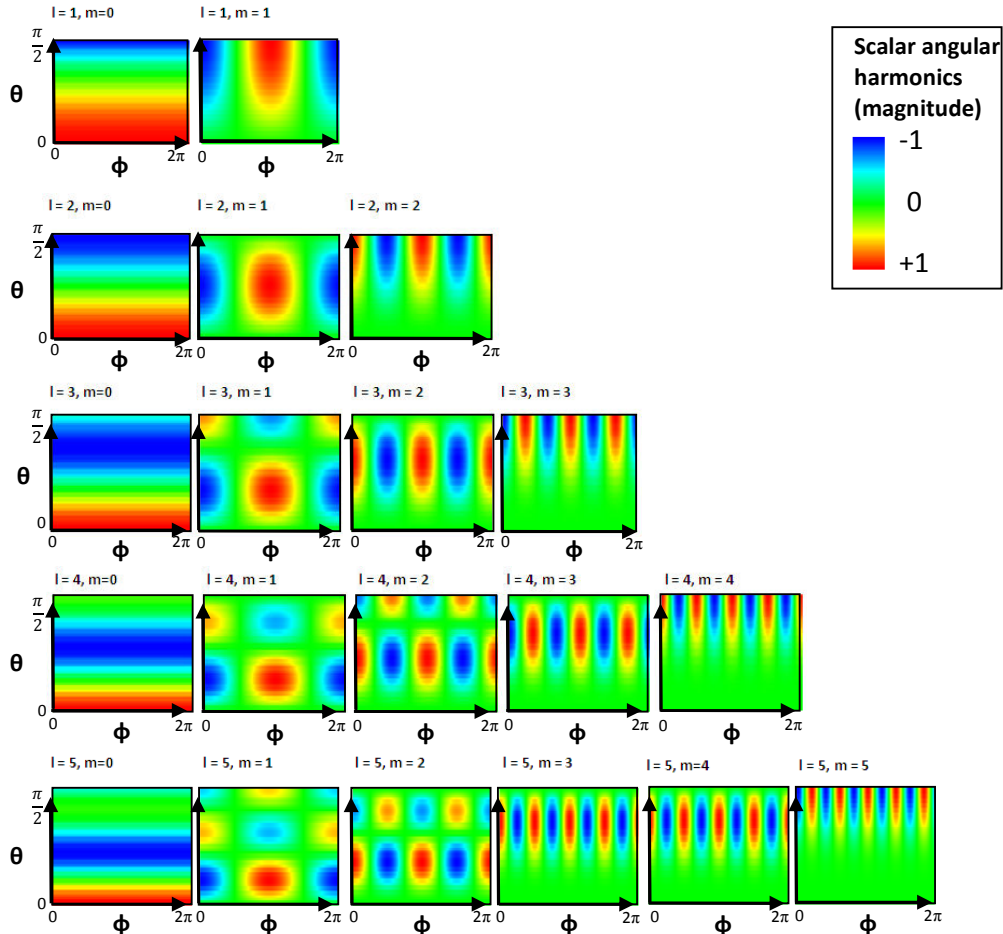


**Figure 3.2:** The scalar spherical harmonics are shown for  $l = 1$  to 5 and  $m = 1$  to  $l$  where  $\theta$  is varied from 0 to  $90^\circ$  and  $\phi$  is varied from 0 to  $360^\circ$ . The colour scale represents the

magnitude of the product of the azimuthal and polar solutions to Equation 3.12, which have been normalised to the same scale (-1 to +1).

This derivation has only considered the solution to the scalar form of the wave equation in spherical polar coordinates. However, Mie Theory requires the application of these principles in vectorial form, such that  $\mathbf{E}$  and  $\mathbf{H}$  of the incident and scattered fields may be accurately described. The vector solution to the wave equation introduces two vector quantities, termed  $\mathbf{M}$  and  $\mathbf{N}$ , which obey the same relations as  $\mathbf{E}$  and  $\mathbf{H}$  for an electromagnetic wave. Firstly, both  $\mathbf{M}$  and  $\mathbf{N}$  must satisfy the wave equation. Secondly, the curl of  $\mathbf{M}$  must be proportional to  $\mathbf{N}$ , and thirdly, the curl of  $\mathbf{N}$  must be proportional to  $\mathbf{M}$ . The process of converting the incident plane wave into a series of vector spherical harmonics is rather lengthy, however the result is summarised in Equation 3.25.

$$\mathbf{E}_i = \mathbf{E}_0 \sum_{n=1}^{\infty} i^n \frac{2n+1}{n(n+1)} \left( \mathbf{M}_{o1n}^{(1)} - i\mathbf{N}_{e1n}^{(1)} \right) \quad 3.25$$

Here  $\mathbf{M}_{o1n}$  and  $\mathbf{N}_{e1n}$  represent the spatial distribution of the vector spherical harmonics in terms of the spherical polar coordinate unit vectors ( $\hat{\mathbf{e}}_r, \hat{\mathbf{e}}_\theta, \hat{\mathbf{e}}_\phi$ ). In Equation 3.25, the subscript terms of the vector spherical harmonics,  $o1n$  and  $e1n$  arise because  $l=1$  for the case of an incident plane wave. The ‘ $o$ ’ and ‘ $e$ ’ parts of the subscript refer to odd and even solutions respectively. If the incident electric field is specified by Equation 3.25, then the corresponding magnetic field may be specified by the curl of this quantity:

$$\mathbf{H}_i = -\frac{k}{\omega\mu} \mathbf{E}_0 \sum_{n=1}^{\infty} i^n \frac{2n+1}{n(n+1)} \left( \mathbf{M}_{e1n}^{(1)} - i\mathbf{N}_{o1n}^{(1)} \right) \quad 3.26$$

The internal field ( $\mathbf{E}_i, \mathbf{H}_i$ ) and the scattered field ( $\mathbf{E}_s, \mathbf{H}_s$ ) may also be expanded into vector spherical harmonics using the same approach. At the boundary between the sphere and the surrounding medium, the incident, scattered and internal fields are matched and conditions are imposed such that:

$$(\mathbf{E}_i + \mathbf{E}_s - \mathbf{E}_1) \wedge \hat{\mathbf{e}}_r = (\mathbf{H}_i + \mathbf{H}_s - \mathbf{H}_1) \wedge \hat{\mathbf{e}}_r = 0 \quad 3.27$$

The full expression for the electric and magnetic fields scattered by the sphere is given by:

$$\mathbf{E}_s = \sum_{n=1}^{\infty} \mathbf{E}_n \left( i a_n \mathbf{N}_{e1n}^{(2)} - b_n \mathbf{M}_{o1n}^{(2)} \right) \quad 3.28$$

$$\mathbf{H}_s = \frac{k}{\omega\mu} \sum_{n=1}^{\infty} \mathbf{E}_n \left( i b_n \mathbf{N}_{o1n}^{(2)} + a_n \mathbf{M}_{e1n}^{(2)} \right) \quad 3.29$$

Where  $\mathbf{E}_n = i^n E_0 \frac{(2n+1)}{n(n+1)}$  and  $n$  is the integer corresponding to the spherical vectorial harmonic of interest.

The terms  $a_n$ , and  $b_n$  in Equations 3.28 and 3.29 determine the scattering coefficients, and depend on the complex refractive index  $m$ , and size to wavelength ratio  $x$  of the sphere. A better physical understanding of the spherical vectorial functions can be gleaned by plotting the distributions of the vector harmonic solutions within the region of the particle. The electric field distributions shown in Figure 3.3 were published in Mie's original paper <sup>1</sup> and represent the 'normal modes' of the particle. This figure shows the vector field lines (corresponding to the electric field) for a cross section taken through the centre of the sphere lying perpendicular to the incident wave vector. For every 'nth' vector harmonic solution, there are two distinct types of mode <sup>2</sup>. In one mode there is no radial magnetic field component (the transverse magnetic mode), and in another there is no radial electric field component (the transverse electric mode). The field lines show the surface confinement of free charges at equally spaced distances around about the circumferential region of the sphere. These distributions represent the excitation of localised surface plasmon resonances which are dipolar, quadrupolar and octupolar in nature. There will be a more detailed discussion on this topic in subsequent chapters.

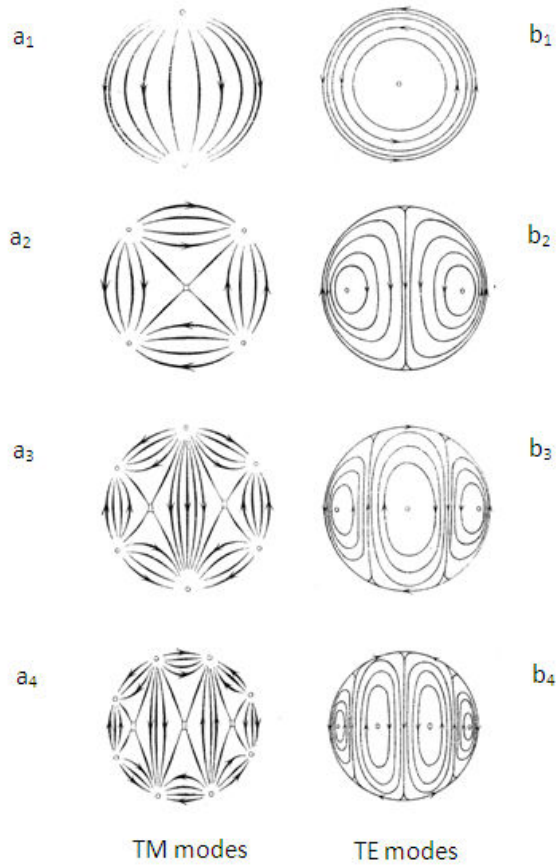


**Figure 3.3:** Electric field patterns (viewed in cross section) showing the normal modes of a sphere as proposed by Mie in 1908 <sup>1</sup>.

It is possible to use software such as MATLAB <sup>4</sup>, Mathematica <sup>5</sup> or Maple <sup>6</sup> to explicitly solve for the scattered electric and magnetic fields. Mie Theory can also be extended to consider other spherical cases such as concentric shells or dielectric particles with metallic coatings <sup>1</sup>. It should be noted that when calculating the scattering from single metallic particles, the scattering cross section  $C_{sca}$  is often cited. The scattering cross section is determined by integrating the scattered electric field over a spherical surface in the far field and normalising it to the incident irradiance, as shown in Equation 3.30. The scattering efficiency  $Q_{sca}$  is also sometimes cited, this is calculated by dividing the scattering cross section  $C_{sca}$  by the cross sectional area of the scatterer as projected onto a plane lying perpendicular to the plane of incidence.

$$C_{sca} = \frac{k}{|\mathbf{E}_i|^2} \int_{dS} \mathbf{E}_{scattered}(\mathbf{r}') \cdot \mathbf{E}_{scattered}^*(\mathbf{r}') \hat{\mathbf{r}} dS \quad 3.30$$

$$Q_{sca} = \frac{C_{sca}}{\pi a^2} \quad 3.31$$

### 3.3 The ‘T-Matrix’ method

The T-Matrix method is an approach used to compute the Transition Matrix. The Transition Matrix is a linear operator relating the coefficients of the incident and scattered electromagnetic fields for simple geometries such as spheres, cylinders or cuboids, and is exact. The manner in which this method is applied has a number of similarities to Mie Theory, and in some ways it is a more general form of Mie Theory. It also requires the expansion of the incident and scattered fields into a series of vectorial harmonics. Indeed, Equations 3.28 and 3.29 can also be assumed to be valid in describing the scattered fields from a non-spherical object. The linearity the Maxwell equations enable the coefficients of the incident and scattered fields to be related by a Transition Matrix (the **T-Matrix**):

$$\begin{bmatrix} a_n^{scattered} \\ b_n^{scattered} \end{bmatrix} = \begin{bmatrix} T_{11} & T_{12} \\ T_{21} & T_{22} \end{bmatrix} \begin{bmatrix} a_n^{incident} \\ b_n^{incident} \end{bmatrix} \quad 3.32$$

The ‘T’ terms in Equations 3.32 correspond to elements of the T-matrix,  $a_n^{scattered}$  and  $b_n^{scattered}$  are the coefficients of the scattered field (From Equation 3.28) and  $a_n^{incident}$  and  $b_n^{incident}$  are the coefficients of the incident field. The elements of the T-Matrix depend only on the size parameters and refractive index of the scattering particle, and the refractive index of the surrounding medium. For non-spherical particles, it is also dependent upon the orientation of the particle with respect to the incident wave vector and polarisation<sup>7-10</sup>. In computing the T-Matrix, the Maxwell equations are solved for boundary conditions specific to the particle geometry, and subsequently this allows the eigenmodes of the structure to be determined. The Transition Matrix therefore is an eigenmodal solution and does not explicitly depend on incident angle. Once computed, the T-Matrix method can be used to calculate any light scattering of interest<sup>9</sup>, either cross-sections or scattering matrix elements. Similar to Mie Theory, the integral in Equation 3.30 can be used to evaluate the electromagnetic field across the full range of scattering

angles. Through a suitable modification of the boundary conditions, it is also possible to use this approach to consider arbitrarily shaped scattering objects. However this is difficult to implement, and is not widely studied, since the number of matrix elements increases significantly for arbitrary shapes, leading to an increase in the computation time. There are several freely available T-Matrix codes which operate on Unix systems<sup>11</sup>. A general review of the T-matrix method can be found in the paper by M. I. Mishchenko et al.<sup>3,10</sup>.

### 3.4 The Discrete Dipole Approximation (DDA)

The *Discrete Dipole Approximation (DDA)*, or as it's sometimes referred to, the 'coupled dipole' approximation involves replacing each particle by an assembly of finite cubical elements. Each of these elements is considered sufficiently small that only dipole interactions with an applied electromagnetic field and with induced fields in other elements need to be considered. This reduces the solution of Maxwell's equations to an algebraic problem of many coupled dipoles<sup>12</sup>. Each of the dipoles within a continuous assembly acquires dipole moments in response to both the external electric field, and the electric fields due to neighbouring dipoles. The polarisability of an individual dipole can be approximated using the Clausius-Mossotti relation<sup>15-16</sup>. This is given in Equation 3.33 where it is assumed that the inclusion has permittivity  $\epsilon_p$ , and the surrounding dielectric has permittivity  $\epsilon = 1 + 0i$ :

$$\alpha_{CM} = \frac{3d^3}{4\pi} \left( \frac{\epsilon_m - 1}{\epsilon_m + 2} \right) \quad 3.33$$

The radiated field of an individual dipole may be approximated by<sup>15</sup>:

$$\mathbf{E}_{\text{dipole}} = \frac{e}{4\pi\epsilon} \frac{i\omega d}{c} \left[ \frac{\omega^2}{c^2 d} \hat{\mathbf{r}} \wedge \mathbf{p} \wedge \hat{\mathbf{r}} + \left( \frac{1}{d^3} - \frac{i\omega}{cd^2} \right) [3(\hat{\mathbf{r}} \cdot \mathbf{p})\hat{\mathbf{r}} - \mathbf{p}] \right] \quad 3.34$$

Here  $\hat{\mathbf{r}}$  is unit vector associated with a vector  $\mathbf{r}$  which is taken from the dipole to the point at which the field is sampled,  $d$  is the distance to the sampling point,  $\mathbf{p}$  is the vector associated with the induced dipole moment,  $\omega$  is the angular frequency of the scattered radiation and  $\epsilon$  is the permittivity of the surrounding medium. In solving for the scattering characteristics of the continuous distribution, each particle in the array has induced dipole

$\mathbf{P}_i = \alpha_i \mathbf{E}_{\text{local}}$ , where  $\mathbf{E}_{\text{local}}$  is the electric field at  $\mathbf{r}_i$  due to the incident wave ( $\mathbf{E}_{\text{inc},i}$ ), plus a contribution  $\mathbf{E}_j$  from all other dipoles ( $j$ ), given in Equation 3.35:

$$\mathbf{E}_{\text{local}} = \mathbf{E}_{\text{inc},i} + \sum_{\substack{j=1 \\ i \neq j}} \mathbf{E}_j \quad 3.35$$

Equation 3.35 can be written in matrix form, in which the interaction matrix ( $\mathbf{A}_{ij}$ ) is used to describe the radiative coupling between dipoles:

$$\mathbf{A}\mathbf{P} = \mathbf{E}_{\text{inc}} \quad 3.36$$

$$\mathbf{A}_{ij} = \frac{e^{ikr_{ij}}}{r_{ij}} \left[ k^2 (\hat{\mathbf{r}} \otimes \hat{\mathbf{r}} - \mathbf{I}) + \frac{ikr_{ij} - 1}{r_{ij}^2} (3\hat{\mathbf{r}} \otimes \hat{\mathbf{r}} - \mathbf{I}) \right] \quad 3.37$$

As with the other computation methods which are described in this chapter, once the scattered electric field associated with the collection of dipoles has been determined, the scattering cross section  $C_{\text{sca}}$  can be calculated by performing the integral in Equation 3.30. The most computationally demanding part of this method occurs during the matrix solving phase. Very efficient methods for solving the DDA equations have been developed using fast-fourier-transform and complex-conjugate gradient methods, and as a result it is possible to use thousands of dipoles for routine calculations<sup>10</sup>. Software such as DDSCAT is an example of free software which can be compiled using a Unix system<sup>11</sup>.

### 3.5 Finite Element Method (FEM)

*Finite Element Modelling (FEM)* divides up the problem space into many smaller regions which are very often ‘tetrahedra’, with the field inside each region being described by a local function. Since the tetrahedra have flat faces they cannot exactly represent the surface of a sphere for example, but by using enough of them a sufficiently accurate polyhedral approximation is possible<sup>18</sup>. The values of vector field quantities such as  $\mathbf{E}$  or  $\mathbf{H}$  associated with each element are determined by interpolating values at vertices and midpoints of the tetrahedra. The ‘Whitney tetrahedron’ first proposed by Nedelec in 1980 is shown in Figure 3.4 and is an example of a vector finite element configuration which is commonly utilised<sup>19</sup>.

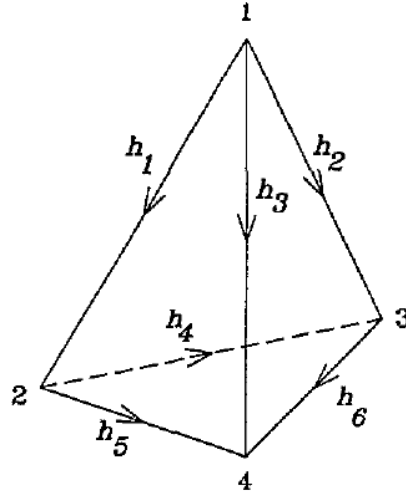


**Figure 3.4:** The Whitney tetrahedron – an example of a vector finite element.

The vector field  $\mathbf{X}$  inside the element shown in Figure 3.4 is specified by Equation 3.38, where  $v_i$  are vector basis functions which are linear functions of the coordinates  $x, y, z$  inside the element:

$$\mathbf{X}(x, y, z) = \sum_{i=1}^6 h_i v_i(x, y, z) \quad 3.38$$

In Figure 3.2,  $h_1 \dots h_6$  represent the edges of the tetrahedron, and are not directly related to the components of the vector  $\mathbf{X}$ . In order to make  $\mathbf{X}$  tangentially continuous across an edge which is shared between two tetrahedra, it is only necessary to equate the tangential components of  $\mathbf{X}$  for two adjacent edges (with a change of sign if the gradients of the chosen edges are of opposite sign). In the Whitney tetrahedron there is one degree of freedom per edge, and the resulting field  $\mathbf{X}$  is tangentially conserved across the edges and faces of adjacent elements. The normal component of  $\mathbf{X}$  is often discontinuous at the edges and faces of two adjacent tetrahedra. In order to relate the normal components of  $\mathbf{X}$  of two neighbouring tetrahedra a weighted residual method is used. This seeks to minimise the average difference of the residual errors between the normal component of  $\mathbf{X}$  across all edges / faces of a particular element. In determining the unknown vector quantities of each element the unknowns are expressed through a series of linear simultaneous equations, which may be written in matrix form (Equation 3.39), where  $[u]$  represents the column vector of unknowns.

$$[S][u] = [b] \quad 3.39$$

More formally, the matrices of unknowns are derived from the Maxwell equations. To briefly show the advantages of using a matrix representation, consider the following example of the two Maxwell equations below which are expressed in differential form:

$$\nabla \cdot \mathbf{E} = \frac{\rho}{\varepsilon_0} \quad 3.40$$

$$\nabla \wedge \mathbf{B} = \frac{\partial \mathbf{E}}{\partial t} + \mathbf{J} \quad 3.41$$

These may be written explicitly as:

$$\frac{\partial B_z}{\partial y} - \frac{\partial B_y}{\partial z} - \frac{\partial E_x}{\partial t} = \rho \frac{dx}{d\tau} \quad 3.42$$

$$\frac{\partial B_x}{\partial z} - \frac{\partial B_z}{\partial x} - \frac{\partial E_y}{\partial t} = \rho \frac{dy}{d\tau} \quad 3.43$$

$$\frac{\partial B_y}{\partial x} - \frac{\partial B_x}{\partial y} - \frac{\partial E_z}{\partial t} = \rho \frac{dz}{d\tau} \quad 3.44$$

$$-\frac{\partial E_x}{\partial x} - \frac{\partial E_y}{\partial y} - \frac{\partial E_z}{\partial z} = \rho \frac{dt}{d\tau} \quad 3.45$$

If the three components of the current density  $\mathbf{J}$  and the charge density  $\rho$  are combined into a single four vector, such that each component is the incremental charge per unit volume multiplied by the respective component of the four velocity of the charge, the result is:

$$J_x = \rho \frac{dx}{d\tau} \quad J_y = \rho \frac{dy}{d\tau} \quad J_z = \rho \frac{dz}{d\tau} \quad J_t = \rho \frac{dt}{d\tau} \quad 3.46 - 3.49$$

Here,  $\tau$  represents the diffusion time of the charges. If the partial derivatives on the left hand side of the differential equations (Equations 3.42 – 3.45) are arranged according to their denominators ( $x, y, z, t$ ) then the equations can be expressed as:

$$\sum_{\mu=1}^4 \frac{\partial \mathbf{P}_{\mu\nu}}{\partial x^\mu} = \rho \frac{dx^\nu}{d\tau} \quad 3.50$$

$$\text{Where } x^1, x^2, x^3, x^4 = x, y, z, t \text{ and } \mathbf{P} = \begin{bmatrix} 0 & B_z & -B_y & -E_x \\ -B_z & 0 & B_x & -E_y \\ B_y & -B_x & 0 & -E_z \\ E_x & E_y & E_z & 0 \end{bmatrix}$$

Thus by considering two of the Maxwell equations it is possible to combine both the  $\mathbf{E}$  and  $\mathbf{B}$  fields within a single matrix. In applying the matrix representation of the Maxwell

equations directly to the finite element method, Equation 3.38 is used to define  $\mathbf{E}$  and  $\mathbf{B}$  for each tetrahedron.  $\mathbf{E}$  may be expressed in terms of edge elements of the Whitney tetrahedron  $\mathbf{W}_i^1$  ( $i = 1 \dots N_e$ ) and  $\mathbf{B}$  in terms of face elements  $\mathbf{W}_i^2$ , ( $i = 1 \dots N_f$ ), as shown in Equations 3.51 and 3.52<sup>20</sup>.

$$\mathbf{E} = \sum_{i=1}^{N_e} a_i \mathbf{W}_i^1 \quad 3.51$$

$$\mathbf{B} = \sum_{i=1}^{N_f} b_i \mathbf{W}_i^2 \quad 3.52$$

Here  $N_e$  and  $N_f$  represent the number of interior edges and faces of each element respectively, whilst  $a_i$  and  $b_i$  are unknown quantities. The array of unknown quantities are denoted as column vectors, (i.e. in the form  $[\mathbf{E}] = [a_1, a_2 \dots a_{N_e}]^T$  and  $[\mathbf{B}] = [b_1, b_2 \dots b_{N_f}]^T$ ), and these may also be coupled to the unknown quantities of adjacent elements. This is because when considering tetrahedra which share an edge, the tangential component of  $\mathbf{E}$  must be conserved. Similarly, for any tetrahedra which share a face, the normal component of  $\mathbf{B}$  must be conserved. In the absence of surface charges or currents the field quantities within the tetrahedral elements must also satisfy Equations 3.53 – 3.54. The reasons for this are discussed in more detail in Chapter 4.

$$[\mathbf{D}] = [\varepsilon][\mathbf{E}] \quad 3.53$$

$$[\mathbf{H}] = [\mu^{-1}][\mathbf{B}] \quad 3.54$$

The column vectors  $[\mathbf{D}] = [c_1, c_2 \dots c_{N_e}]^T$  and  $[\mathbf{H}] = [d_1, d_2 \dots d_{N_f}]^T$  represent the electric flux density and magnetic flux intensity respectively. The individual elements (row  $i$ , column  $j$ ) of the permittivity  $[\varepsilon]$  and inverse permeability  $[\mu^{-1}]$  matrices are given by the integrals:

$$[\varepsilon]_{i,j} = \int_{\Omega} \mathbf{W}_i^1(\varepsilon(\mathbf{r})) \mathbf{W}_j^1 d\Omega \quad 3.55$$

$$[\mu^{-1}]_{i,j} = \int_{\Omega} \mathbf{W}_i^2(\mu^{-1}(\mathbf{r})) \mathbf{W}_j^2 d\Omega \quad 3.56$$

The  $\Omega$  term in Equations 3.55 – 4.56 defines the computational domain over which the integral is performed (i.e. for a three dimensional simulation it is the volume of the tetrahedron), and  $\varepsilon$  and  $\mu$  are the complex permittivity tensors at location  $\mathbf{r}$ . Once  $\mathbf{E}, \mathbf{B}, \mathbf{D}$  and  $\mathbf{H}$  have been expressed as column vectors of coupled unknowns they may be

substituted into the Maxwell equations and solved using matrix algebra. The matrices which are solved in finite element simulations have extremely large dimensions but are very sparse. A number of optimisation techniques are therefore used in order to increase the computation speed. These numerical methods are beyond the scope of the present study, but techniques include the conjugate gradient and incomplete Choleski-gradient methods amongst others <sup>21</sup>.

It is possible to assess the accuracy of the numerical solution by comparing results from a sequence of successively refined meshes. The solutions of equations often have geometric features such as localized regions of high gradient. In this case it is more economical to refine the mesh selectively, (i.e., only where these high gradients occur). The adaptive refinement procedure generates a sequence of solutions on successively finer meshes, at each stage selecting and refining those elements at which the gradient of E or H is largest between adjacent elements. In practice, the process is terminated when the gradient of the fields between adjacent tetrahedra is below a preset limit, or if the number of elements are such that the computation time for the simulation exceeds a preset limit (both of these limits are specified by the user). HFSS <sup>22</sup>, and FEMLab / Comsol <sup>23</sup> are examples of commercial FEM modelling software, and there are also packages which are freely available such as OOFEM <sup>24</sup> and FFEP <sup>25</sup>.

### **3.6 Finite Difference Time Domain (FDTD)**

*Finite Difference Time Domain (FDTD)* computations are not entirely dissimilar to FEM in that they also generate a mesh which subdivides the problem space. Maxwell's equations are discretised in both space and time, using centered finite differences on a uniform Cartesian grid. There are several methods used for discretisation, the most common being the Yee scheme. Figure 3.5 shows Yee's original configuration for the location of the electric and magnetic field vector components on a unit cell <sup>26,27</sup>.

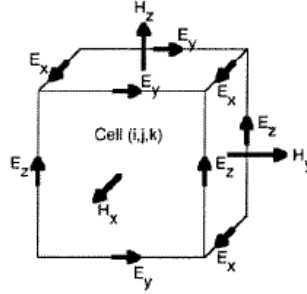


**Figure 3.5:** The Cartesian grid configuration proposed by Yee in 1966.

In considering the interaction of incident electromagnetic radiation with a metallic particle, the differential form of the wave equation is solved at two instants in time, separated by a small interval  $\delta t$ <sup>28</sup>. The mesh is successively refined to increase numerical accuracy using an adaptive process in the same formalism as in the FEM methods. In FDTD simulations the excitation source is a pulse as opposed to a plane wave. This has some benefits, particularly that a broadband output can be obtained with a single execution of the program (by taking a Fourier transform). Examples of commercial FDTD software include Lumerical Solutions<sup>29</sup> and Remcom Xfdtd<sup>30</sup>. MEEP is an FDTD source code which is freely available<sup>31</sup>.

### 3.7 Suitability of each method and example calculations to simulate the scattering response of an 80 nm diameter Au sphere in vacuum

*Computations were performed on a Dell Vostro 200 personal computer, having a dual-core processor (each with a clock speed of 2.19 GHz), 2 Gb of RAM and 250 Gb of available hard drive space.*

Mie theory is the preferred choice for simulating metallic spheres since it constitutes an ‘almost exact’ solution for the scattered electromagnetic radiation from spherical geometries. Unlike DDA, FEM or FDTD methods the accuracy of the Mie Theory solution does not depend on resolution-limited parameters such as the inter-dipole spacing or element length. As previously discussed, the scattered field can be represented as a summation of spherical vectorial harmonics. If this summation was performed over an infinite number of harmonics it would represent an exact solution for the case of the interaction between a sphere and a plane polarised wave. In practice however, the summation is truncated at a finite number of terms, and the accuracy of the solution will

therefore depend on the truncation order. The T-Matrix approach can also be used to simulate spherical particles, since for a spherical scattering particle the solutions simplify to those which are applied using Mie Theory. Both the Mie Theory and T-Matrix methods can be used to compute the scattered field faster than the other approaches, with the computation time being proportional to  $(r / \lambda)$ , where  $r$  is the sphere radius and  $\lambda$  is the incident wavelength. However, for spheres with radii less than  $1\mu\text{m}$  being evaluated at visible frequencies, the computation time is extremely rapid and the dependence on the size of the sphere is often unnoticed. To evaluate the scattering efficiency,  $Q_{sca}$  (the ratio of the total scattered power to incident power), for a 80 nm diameter Au sphere at one particular frequency takes approximately  $1.0 \times 10^{-3}$  seconds for both Mie Theory and T-Matrix methods (using the hardware specified at the beginning of this section).

If the particle under consideration is non-spherical, but has planar symmetry, or is symmetric about an axis, it is possible to use the T-Matrix method to compute the scattering characteristics. The majority of T-Matrix codes contain embedded routines which are specifically adapted to match the boundary conditions relating the internal, incident and scattered fields for various geometries such as spheres, cylinders, cones and rectangular multilayer slabs. As with Mie Theory, the computation time scales according to the ratio between the particle size and the incident wavelength. The field expansions used to form the  $T$ -matrix are truncated at a particular number of elements, this is proportional to  $r^4$  (where  $r$  is the radius of a sphere whose volume is equal to that of the scattering particle)<sup>3</sup>. This can introduce rounding errors, which may be significant for sufficiently elongated or flattened objects. Mischenko has conducted an extensive study into the effects of particle size on the convergence of the solutions which are derived from the T-Matrix method<sup>3</sup>.

The DDA approach can also be utilised to evaluate the scattering properties of homogenous non spherical particles which are axisymmetric or those which possess other planes of symmetry. The fundamental concept of this approach is that a solid particle is replaced by an array of  $N$  point dipoles on a lattice which has a significantly smaller spacing than the wavelength of the incident radiation. Collectively the positions of the dipoles retain the original shape<sup>9</sup>. The computation time is therefore heavily dependent on the inter-dipole spacing and the total number of dipoles used to replicate the original scattering object. For example, the time taken to evaluate  $Q_{sca}$  for an 80 nm diameter Au

sphere with an inter-dipole spacing of 3 nm takes approximately 48 seconds for one particular frequency. This is significantly longer than the Mie Theory solution above, which takes only  $10^{-3}$  seconds per frequency. If the inter-dipole spacing is increased to 4 nm the computation time is halved to 24 seconds. The limiting factor which governs the ability of the algorithm to solve a particular scattering problem is dependent upon a combination of both the CPU speed and RAM of the workstation concerned. The RAM requirement, as specified by the program, is stated in Equation 3.57 below where  $N_x$ ,  $N_y$ , and  $N_z$  are the number of dipoles distributed across the scattering particle in the  $x$ ,  $y$  and  $z$  directions respectively.

$$\text{Minimum RAM} = (1690 + 0.764(N_x \times N_y \times N_z)) \times 10^3 \text{ bytes} \quad \mathbf{3.57}$$

For example, Equation 3.57 can be used to show that in order to simulate a cuboid having side length 80 nm using an inter-dipole spacing of 1 nm, a minimum of 0.5 Gb of RAM is required. Whilst the DDA solution converges to the equivalent Mie theory result as the inter-dipole spacing approaches zero, a compromise between the accuracy and computation time is required. There is thus a significant disadvantage in terms of computation time associated with DDA as opposed to using the more rapid T-Matrix approach. However, DDA is often the preferred method for evaluating arbitrarily shaped scattering objects, as one can specify a series of dipole locations in tabulated form.

For many particle or sample geometries, the previously described techniques (Mie Theory, the T-Matrix method and the DDA method) are not suitable for simulating the scattering response. Examples of such structures include infinite arrays of metallic particles, arrangements of metallic nanoparticles exhibiting multipolar resonances and nanoholes in metallic films. In order to simulate these structures, it is necessary to use either FEM or FDTD approaches. Both methods can be used to distinguish between the incident and scattered fields within the problem space. A typical simulation for an 80 nm diameter Au sphere in vacuum consists of a spherical unit cell with ‘radiation’ boundaries at the surface. These boundaries are used to model open problems that allow waves to radiate infinitely far into space. The wave is absorbed at the radiation boundary, essentially ballooning the boundary infinitely far away from the structure. The accuracy of the approximation depends on the distance between the boundary and the object from which the radiation emanates<sup>7</sup>. In both FEM and FDTD methods the scattered field may be computed once E

or  $\mathbf{H}$  has been determined inside each volume element. The total scattered power is determined by integrating the normal component of the Poynting vector with respect to the surface normal of the bounding sphere, as shown earlier in Equation 3.30. This is normalised to obtain the Scattering Efficiency  $Q_{sca}$  by dividing by the total incident flux for a sphere of equal volume.

A convergence test can be used in both the FEM and FDTD methods to check the suitability of the mesh, and to avoid regions of instability. It should be noted that there is a significant difference between using FEM and FDTD methods to simulate structures across the visible frequency range. Since the FDTD method is solved in the time-domain, a pulse is used as the incident excitation source to obtain a broadband frequency output. Dispersion information must therefore be specified over a much wider range of frequencies than simply the range of interest. Therefore, the permittivity of metallic structures must be approximated using any suitable frequency dependent permittivity model (e.g. using Drude model parameters), as opposed to experimental values, which may not necessarily cover the required range. Whilst both the FEM and FDTD approaches can solve for arbitrarily shaped particles, they are the most time consuming of all approaches considered. The time taken to evaluate  $Q_{sca}$  using FEM for an 80 nm diameter Au sphere at one particular frequency takes approximately 144 seconds (using a mesh with minimum element length 3 nm). As with the DDA method, a compromise has to be made between mesh accuracy and computation time for FEM and FDTD techniques. When using an FDTD method, the simulation takes approximately 180 minutes (using a minimum element length of 3 nm) to cover the visible frequency range. The difference in computation time between these two approaches can vary quite significantly depending on how many frequency points are required. For example, if only 5 frequency points are required, FEM (12 minutes) is more rapid than FDTD (180 minutes). Conversely, if 100 frequency points are required, FEM (240 minutes) is slower than FDTD (180 minutes).

In considering the effects of workstation specification, the computation time for FEM and FDTD approaches is limited by hierarchical order, CPU speed, RAM and hard drive space. The computation time which is required to solve matrix elements for each tetrahedron is heavily dependent on CPU speed, and a near 1:1 correspondence between the CPU speed and computation time is observed. The software utilises RAM as a temporary storage area for the rapid reading / writing of matrix elements associated with tetrahedra in which the vector field quantities are being solved. Once the field quantities for a particular

tetrahedron have been determined, they are written permanently to disk. Problems can occur if RAM is limited, since the hard drive is then used as ‘virtual RAM’. This considerably lengthens the computation time as the read/write speed of the hard drive is significantly slower than the RAM module. Most commercial software vendors provide diagnostic utility software which can be used to check machine specification and advise of suitability before running a particular type of model.

### **Results obtained for simulating an 80 nm Au sphere in vacuum:**

For the Mie Theory, T-Matrix, DDA and FEM simulation techniques the Au permittivity values were obtained from Johnson & Christy<sup>32</sup>. Figure 3.6 shows the real and imaginary components of the Au permittivity as a function of wavelength. Figure 3.7 shows the simulated  $Q_{sca}$  values as a function of frequency for an 80 nm diameter Au sphere in vacuum using **Mie Theory** (equations in MATLAB), **T-Matrix** (a Fortran code written by T. Wriedt<sup>11</sup>), **DDA** (DDSCAT<sup>14</sup>), **FEM** (Ansoft HFSS<sup>21</sup>) and **FDTD** (Lumerical<sup>22</sup>) techniques. The FEM simulation used approximately 40000 elements with a minimum element length of 3.11 nm. The DDA and FDTD approaches used 3.00 nm inter-dipole spacing and element length respectively. For each of the simulation techniques in this comparison, the scattering efficiency  $Q_{sca}$  curves exhibit maxima at 525 nm which are associated with excitation of the localised surface plasmon resonance (LSPR) of the structure. When the diameter of the sphere is significantly smaller than the incident wavelength, the electrostatic approximation can be used to show that dipolar LSPR occurs when  $\text{Re}(\epsilon_{metal}) = -2$ . In scattering particles of finite size, such as the 80 nm diameter sphere considered here, the resonant condition is red-shifted slightly due to dynamic depolarisation effects. LSPRs and dynamic depolarisation effects are considered in more detail in Chapter 4 of the thesis.

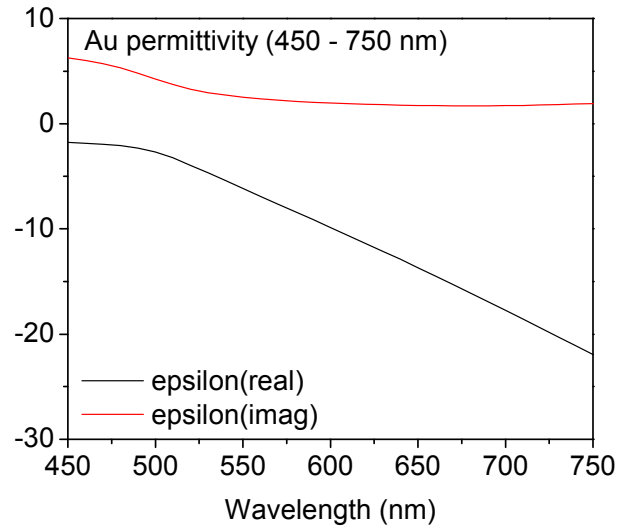


**Figure 3.6:** The real and imaginary components of the permittivity are shown for Au for wavelengths in the range 400 – 750 nm. Permittivity values were obtained from reference data, published by Johnson & Christy<sup>32</sup>.

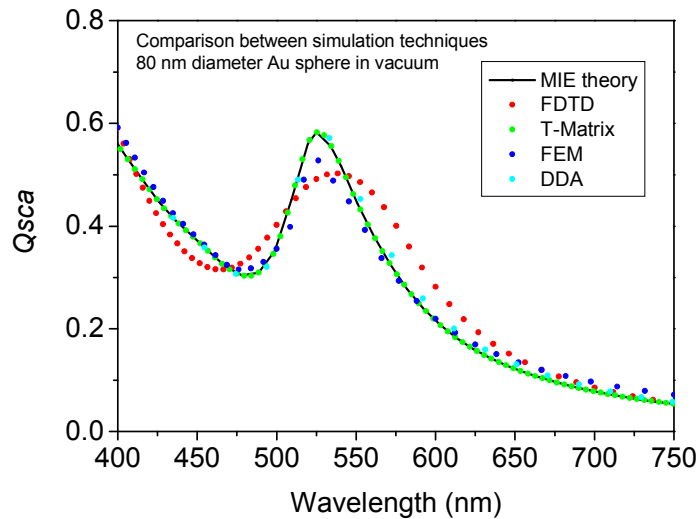


**Figure 3.7:**  $Q_{sca}$  plotted as a function of frequency for an 80 nm diameter Au sphere in vacuum, based upon simulated data obtained using Mie Theory (black), FDTD with an element length of 3.00 nm (red), T-Matrix (green), FEM with an element length of 3.11 nm (blue) and DDA with an interdipole spacing of 3.00 nm (cyan) methods. For the Mie Theory, T-Matrix, DDA and FEM simulation techniques the Au permittivity values were

obtained from Johnson & Christy<sup>32</sup>. For the FDTD method a Drude model was used to calculate permittivity values ( $\omega_p = 1.3 \times 10^{16} \text{ s}^{-1}$  and  $\gamma = 5.0 \times 10^{13} \text{ s}^{-1}$ ).

The Mie Theory and T-Matrix methods both give good agreement across the frequency range shown here. This is to be expected, since both methods use an equivalent approach to calculate the scattered field distribution. The Mie Theory and T-Matrix methods are probably best described as ‘almost exact’; the reasoning for this will now be explained. Both methods impose boundary conditions at the surface of the particle which match the spherical vectorial wave functions of the incident, scattered and internal fields. During the computation routine, the field expansions for both approaches are truncated at a particular number of elements (which is proportional to  $r^4$ ). This can introduce rounding errors, however unlike other methods such as DDA / FEM / FDTD, the Mie Theory and T-Matrix methods are not resolution limited. The scattering efficiency curves which have been presented in Figure 3.7 for the FEM and DDA techniques have comparable resolution, in which the values of the inter-dipole spacing and element length are 3.00 nm and 3.11 nm respectively. As has already been discussed, the numerical accuracy of the techniques depends on the resolution of these parameters. However, a compromise has to be made which takes into account the computation time of the simulation and the specification of the available hardware. The curves presented in Figure 3.7 represent the optimum resolution which can be achieved within these constraints. The maximum error using the FEM technique occurs at resonance. The scattering behaviour on resonance is strongly determined by the resonant field enhancement that occurs at the surface of the metallic sphere. Any resolution limited factors are likely to lead to errors in the field matching conditions at the surface, and therefore this lead to discrepancies in comparison with the scattering response of the exact Mie Theory solution. The sources of maximum error when using the DDA technique occur at the resonant frequency (for the reasons previously described) but also at longer wavelengths away from the resonant frequency. This discrepancy has also been observed in other DDA simulations of dielectric particles where the ratio of the particle size to the incident wavelength approaches zero<sup>14</sup>. Its origins are known to arise from the mathematical technique of the DDA method, but unlike the error at the resonant frequency a physical explanation for this discrepancy is less straightforward. The discrepancy between the FDTD method relative to the other approaches is somewhat unavoidable and occurs through the use of permittivity values based on Drude parameters. Data which has been simulated using the Mie Theory, T-

Matrix, FEM and DDA approaches assumes values of the permittivity are derived from experimental data (Johnson and Christy<sup>32</sup>).

Figures 3.8 and 3.9 show simulated  $Q_{sca}$  obtained using an exact Mie Theory solution compared with those obtained using DDA and FEM approaches respectively. In each figure, the element length and inter-dipole spacing have been varied to determine the relative error in  $Q_{sca}$  compared to the exact Mie Theory solution, this is shown in the inset. In the limit that either the mesh element length or inter-dipole spacing approach zero,  $Q_{sca}$  is found to approach the exact Mie solution. In order to purely investigate the role of FDTD mesh element size, a different comparison is considered in Figure 3.10 in which permittivity values based on Drude parameters are used for both FDTD and Mie Theory. Here, simulated  $Q_{sca}$  from an FDTD simulation has been directly compared against Mie Theory using Drude model parameters ( $\omega_p = 1.3 \times 10^{16} \text{ s}^{-1}$  and  $\gamma = 5.0 \times 10^{13} \text{ s}^{-1}$ ) for an 80 nm diameter Au sphere in vacuum. As the mesh element length approaches zero, the simulated values of  $Q_{sca}$  from the FDTD method are also shown to approach the equivalent Mie Theory solution.

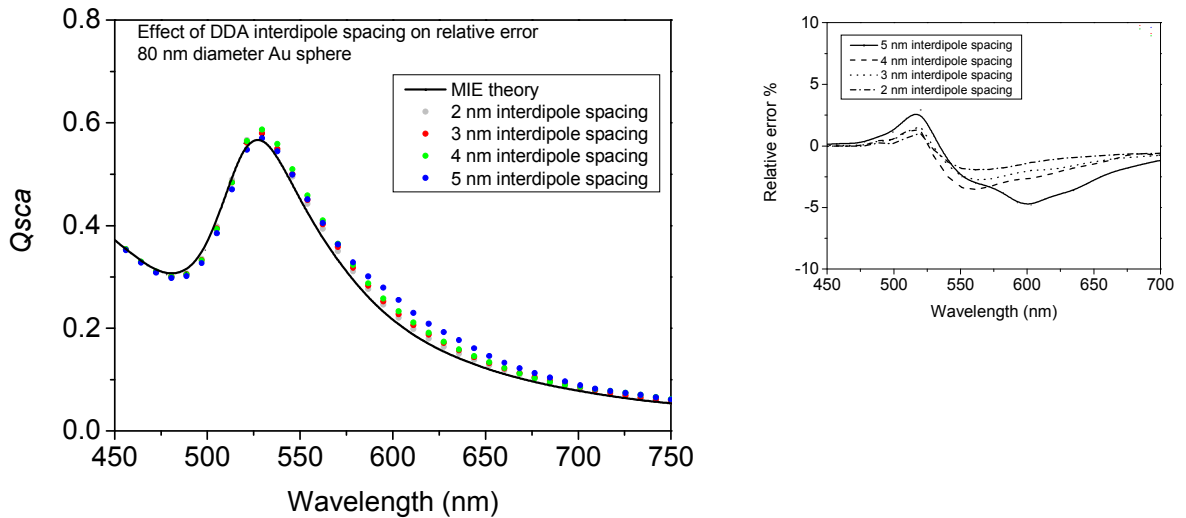


**Figure 3.8:** Mie vs DDA:  $Q_{sca}$  simulated using Mie Theory for a 80 nm Au sphere in vacuum is directly compared with that obtained using the DDA method. The coloured data points show the effect of varying the inter-dipole spacing across a 2 nm to 5 nm range. *Inset* – relative error is plotted as a function of wavelength for different mesh sizes.

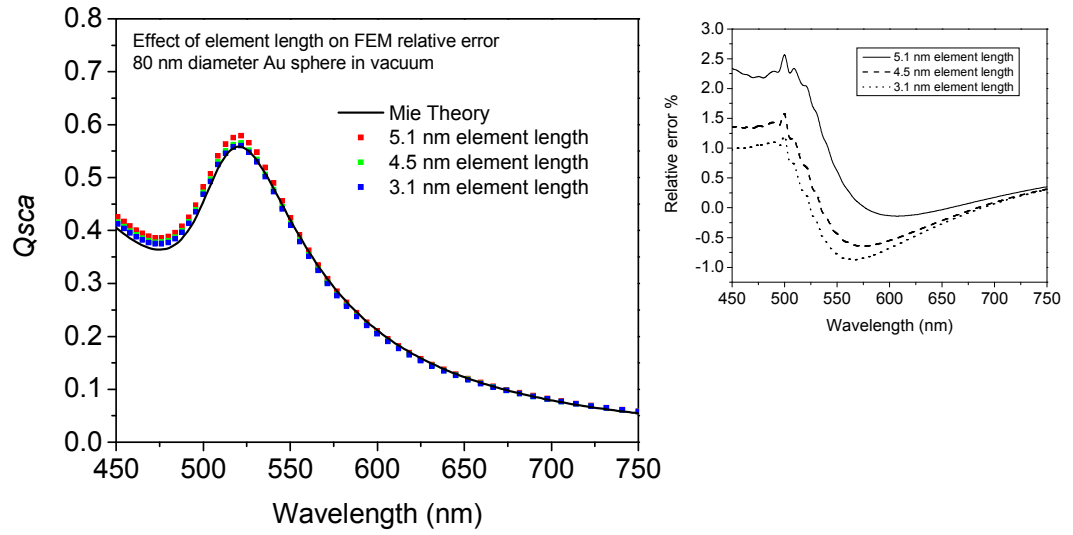


**Figure 3.9:** Mie vs FEM:  $Q_{sca}$  simulated using Mie Theory for a 80 nm Au sphere in vacuum is directly compared with that obtained using a FEM approach. The coloured data points show the effect of varying the mesh element length. *Inset* – relative error is plotted as a function of wavelength for different mesh sizes.

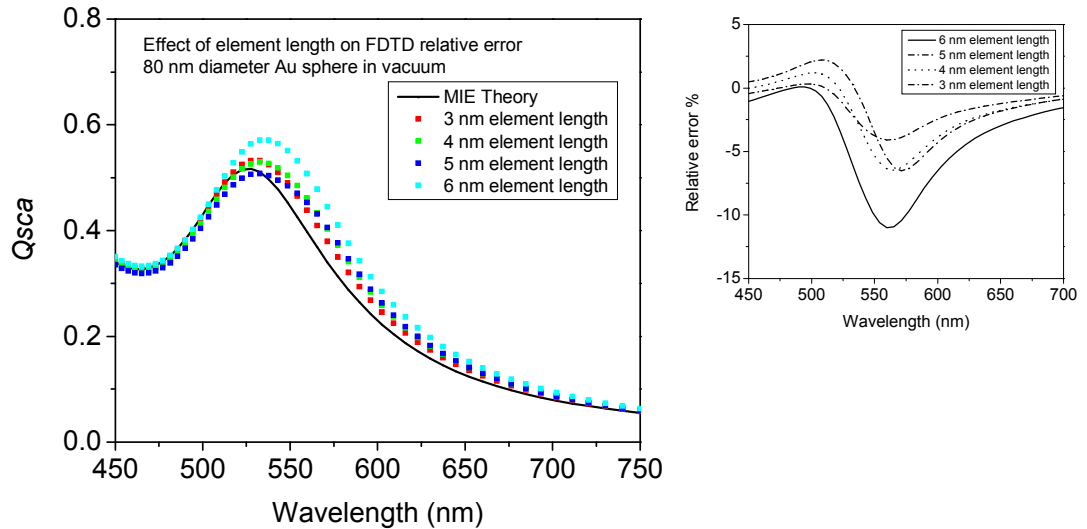


**Figure 3.10:**  $Q_{sca}$  simulated using Mie Theory for a 80 nm diameter Au sphere in vacuum is directly compared with that obtained using the FDTD method. A Drude model ( $\omega_p = 1.3 \times 10^{16} \text{ s}^{-1}$  and  $\gamma = 5.0 \times 10^{13} \text{ s}^{-1}$ ) is used to calculate Au permittivity values for both

models. The coloured data points show the effect of varying mesh element length. *Inset* – relative error is plotted as a function of wavelength for different mesh sizes.

### 3.8 Concluding remarks and the evaluation of each technique.

This chapter contains a comparison of five computational techniques commonly used to simulate the scattering of light by small metallic particles. The suitability of each technique has been considered in terms of computation time and the types of geometries to which it can be applied. For the case of an 80 nm diameter Au sphere in vacuum, the simulated scattering efficiency  $Q_{sca}$  data from an exact Mie scattering solution has been compared with that obtained from the other methods. These other methods have been shown to converge to the Mie Theory solution when parameters which govern the resolution of the simulation (such as element length or inter-dipole spacing) approach zero. There are many factors which must be considered when choosing a computational technique to simulate particle scattering, and the significant advantages and disadvantages are summarised in Table 1.

In Chapters 4 and 5 of the thesis, the optical response of metallic nanoparticle structures is considered. In simulating the structures in these chapters, we have referred to Table 1 below as a reference guide in order to select the appropriate technique. For example, single metallic cylinders and metallic rods in Chapters 4 and 5 have been simulated using the T-Matrix method, since the boundary conditions which are imposed at the surface of the scattering particle may be specified relatively easily using cylindrical or spherical polar coordinates. For these geometries, the T-Matrix method is the preferred choice since it also computes the scattered field in the least time compared to the other approaches. Conversely, the scattering response of periodic metallic nanoparticle arrays may not be computed using Mie Theory, T-Matrix or DDA methods. The solution of the electromagnetic fields in both the Mie Theory and T-Matrix methods does not account for interactions between particles, and whilst the DDA method can be used to simulate the response of more than one particle, the computation time scales rapidly with the number of particles, such that many experimental scenarios cannot be accurately replicated using the current hardware specification. The author's preferred choice for periodic arrays containing a large number of particles (more than 20) is FEM, since periodic boundary

conditions can be specified at the edges of the unit cell. The computation time for FEM simulations of particle arrays is significantly reduced in comparison to the other techniques

Another area in which FEM simulations are utilised is presented in Chapters 6-8, where the optical response of metallic films perforated with periodic arrays of nanoholes is discussed. These structures can only be simulated using FEM or FDTD techniques. Mie Theory and T-Matrix methods are not suitable for the same reasons as described previously for particles (the boundary conditions do not consider interactions between adjacent scatterers). The DDA method is also unsuitable, since the metallic films are continuous and therefore an infinite number of dipoles would be required to accurately determine the scattered field distribution for these structures.

Method	Computation Time for Au sphere with radius $\ll \lambda$	Advantages	Disadvantages
<b>Mie Theory</b>	<i>Rapid</i> – A few milliseconds per individual frequency	<ul style="list-style-type: none"> <li>• Rapid computation time.</li> <li>• Can also be applied to scattering from multilayered spheres and concentric coatings.</li> </ul>	<ul style="list-style-type: none"> <li>• Applicable only to spherically symmetric particles.</li> <li>• Not possible to include a substrate interaction, therefore difficult to replicate many experiments.</li> </ul>
<b>T-Matrix</b>	<i>Rapid</i> – A few milliseconds - per individual frequency.	<ul style="list-style-type: none"> <li>• Rapid computation time.</li> <li>• Wide range of geometries supported.</li> <li>• Also possible to include a substrate interaction</li> </ul>	<ul style="list-style-type: none"> <li>• Computations are numerically unstable for elongated or flattened objects. (the matrices are truncated during computation– rounding errors become significant and accumulate rapidly)</li> </ul>
<b>DDA</b>	<i>Moderate</i> – depends on number of dipoles, and separation. Typically 50s per individual frequency.	<ul style="list-style-type: none"> <li>• Can be used to evaluate any arbitrary shaped particle by specifying a dipole position list.</li> </ul>	<ul style="list-style-type: none"> <li>• Convergence criterion: <math> n kd &lt; 1</math>  <math>n</math> = complex refractive index  <math>k</math> = wavevector  <math>d</math> = inter-dipole separation            (Not possible to solve for high aspect ratio elongated particles or large refractive indices)</li> </ul>
<b>FEM</b>	<i>Lengthy</i> – A compromise is made against element length, typically 150s per individual frequency with 3nm element length. 100 points across the visible frequency range takes approximately 4 hours.	<ul style="list-style-type: none"> <li>• Can be used to evaluate scattering parameters from any arbitrary shaped particle.</li> </ul>	<ul style="list-style-type: none"> <li>• Computation time is lengthy.</li> </ul>
<b>FDTD</b>	<i>Lengthy</i> – A compromise is made against element length. A broadband response is computed across a wide frequency range, typically taking 2-3 hours to cover visible frequencies.	<ul style="list-style-type: none"> <li>• Can be used to evaluate scattering parameters from any arbitrary shaped particle.</li> </ul>	<ul style="list-style-type: none"> <li>• In FDTD a pulse is used as the excitation source. Permittivity values have to be specified over much wider frequency range than just the range of interest. Drude model is not an accurate representation of experimental data.</li> <li>• Computation time is lengthy.</li> </ul>

**Table 3.1:** Comparison of computation time, advantages and disadvantages of five commonly used computational techniques used to simulate light scattering from metallic nanoparticle and nanohole structures. Computations were performed on a Dell Vostro 200 personal computer, having a dual-core processor (each with a clock speed of 2.19 GHz), 2 Gb of RAM and 250 Gb of available hard drive space).

### The scattering of electromagnetic radiation from metallic nanoparticles

#### 4.1 Introduction

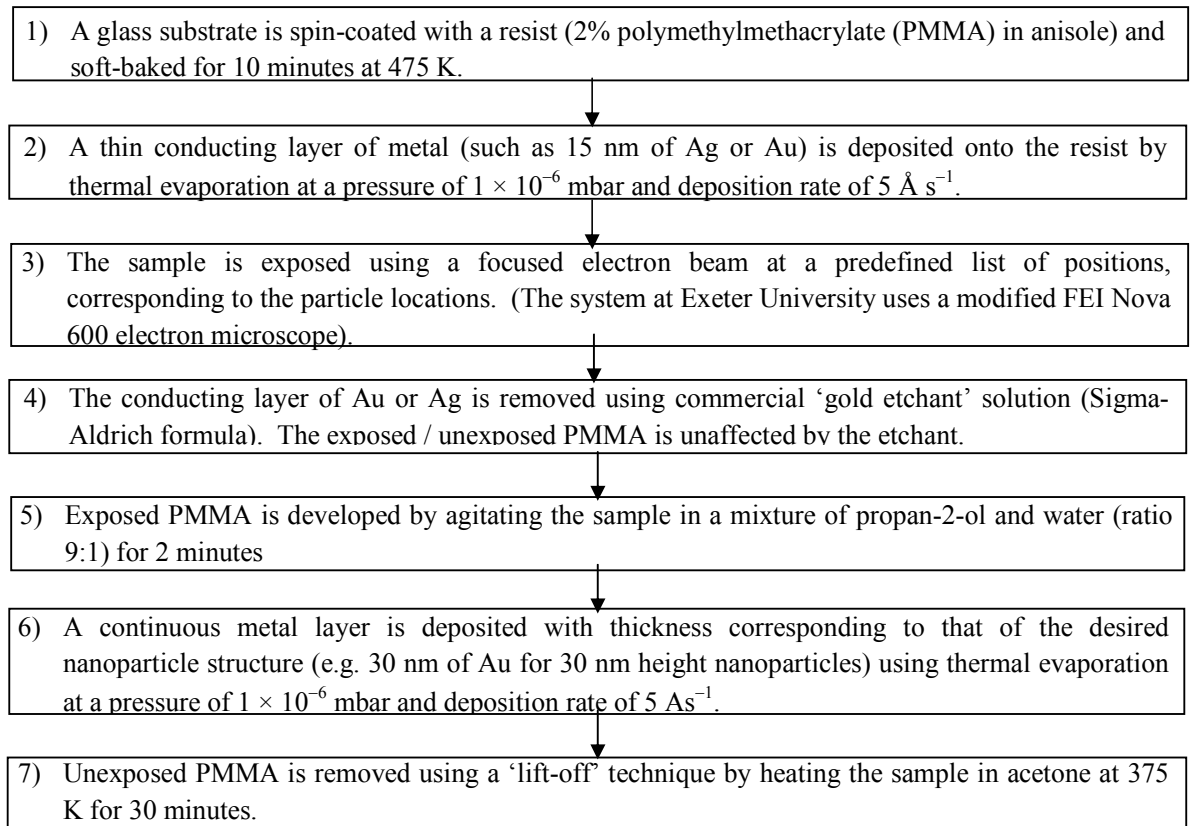
In Chapter 2 the response of multilayer structures comprised of continuous metal and dielectric layers was discussed. In these structures it is essential that the metallic layers are continuous in order to provide a high reflectivity interface and facilitate the coupling between *cos* or *sin* type wave functions in adjacent dielectric cavities. In metallic structures that are non-continuous, such as particles, different types of electromagnetic modes can be supported. For example, it is known that when a noble metal nanoparticle (with dimensions  $\ll \lambda$ ) is illuminated with visible light of appropriate frequency, the spatially confined conduction electrons undergo a coherent oscillation, known as a localised surface plasmon resonance (LSPR)<sup>1</sup>. The excitation of a LSPR is accompanied by significant field enhancement in the vicinity of the particle, particularly at the interfaces between the metal and the surrounding medium, and incident light is scattered strongly by oscillating electric charges within the nanoparticle. In a small particle, all charges within it oscillate collectively in phase, such that the particle itself behaves as an individual dipole oscillator. When the size of the particle is such that it can no longer be considered to be significantly smaller than the incident wavelength, the retardation of the incident electromagnetic field leads to an inhomogeneous polarization across the particle and multipolar charge distributions (quadrupolar, octupolar etc..) can be observed. This has significant implications on the magnitude and angular distribution of the scattered field at frequencies corresponding to higher-order multipolar LSPRs<sup>2</sup>. The scattering properties of nanoparticles have been exploited in stained glass windows for hundreds of years<sup>3</sup>, and with recent advances in fabrication technology now allowing finer control over structural dimensions, many other applications have since been proposed. The significant field enhancement that occurs in the vicinity of the particle renders the LSPR frequency highly sensitive to the particle environment, a property which has been utilized in applications such as optical filters<sup>4</sup>, bio-sensing<sup>5-7</sup> and surfaced enhanced Raman spectroscopy<sup>8,9</sup>.

This chapter contains an introduction to fabrication techniques used to produce single metallic particles, such as Focused Ion Beam (FIB) milling and Electron Beam Lithography (EBL). The excitation conditions for the nanoparticle LSPR will then be investigated in detail; with particular attention given to the effects of particle size,

geometry and aspect ratio on the LSPR frequency. There will be an overview of the dark-field spectroscopy optical characterization technique, which is a novel technique used to measure only the light which is scattered by the particle. Experimental scattering spectra will be compared with simulated data obtained using FEM and T-Matrix techniques. The results of simulations which investigate the angular response of multipolar resonances in large particles and particle clusters will be discussed with relevance to display applications.

#### 4.2 Fabrication of metallic nanostructures using Focused Ion Beam (FIB) milling and Electron Beam Lithography (EBL) techniques

Experimental nanoparticle structures presented throughout this chapter were fabricated using an EBL technique, the main stages of which are described in the flowchart below. These stages are also illustrated in Figure 4.1, which shows a series of cross-sections taken perpendicular to the substrate.



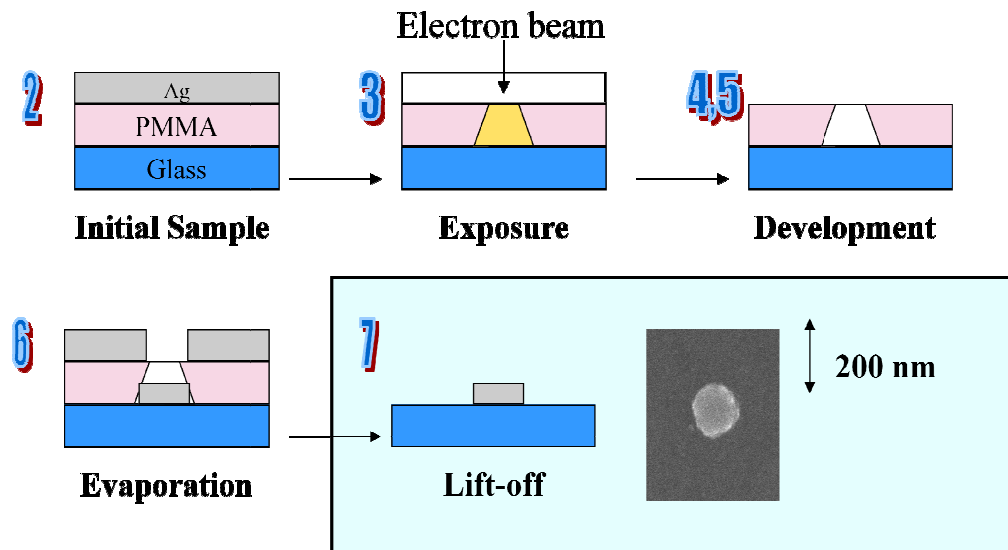


**Figure 4.1:** The main stages of an electron beam lithography process used to fabricate Au nanoparticles. The SEM image shows a single Au nanoparticle with diameter 90 nm and height 20 nm.

There are several crucial steps which must be carefully negotiated in order to fabricate a satisfactory sample. The thickness of the PMMA layer needs to be such that it can accommodate the thickness of the metal layer required for the nanoparticle structure. For example, if the PMMA layer is only 50 nm thick, the maximum thickness of metal that may be deposited is 50 nm. The thickness of PMMA which is deposited is related to the concentration of the solution and the speed of rotation of the resist spinner, a relationship (concentration / spin speed / thickness) provided by the chemical manufacturers. Figure 4.2 shows an example spin speed / thickness curve for PMMA of varying concentrations<sup>10</sup>. When using A2 (2%) PMMA, a spin speed of 1500 – 2000 rpm is required in order to deposit a layer with thickness 100 nm.

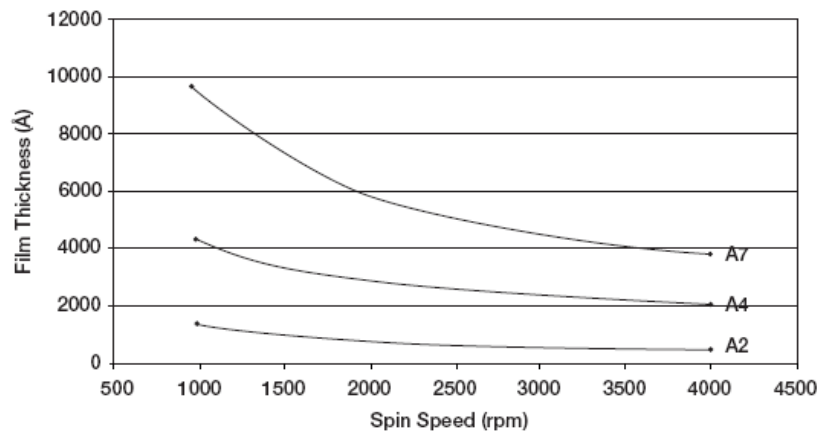


**Figure 4.2:** Spin speed curves for A2 (2%), A4 (4%) and A7 (7%) concentrations of PMMA dissolved in anisole.

Another important factor is the dose, which is a product of the electron beam current, and the speed at which the beam rasters the surface. If the dose is too large, the final particles will be larger than desired. However if the dose is too small the resist is only partially exposed and the process may yield no particles at all. The point spread function associated with the intensity distribution of the electron beam leads to a slightly tapered exposure channel, as opposed to one with perfectly straight edges. This becomes more pronounced as a function of depth, and during the metal deposition stage it is essential that the centres of the evaporation filament and the exposure region are aligned to avoid distortion of the particle shape.

FIB milling is a somewhat less sophisticated approach to fabrication, and requires fewer stages. A continuous metal layer for the desired nanoparticle structure (e.g. 30 nm of Au for nanoparticles with height 30 nm) is first deposited using thermal evaporation. A focused beam of ions from a gallium source is then used to sputter atoms from the metal surface. The ion beam is steered to a predefined list of positions corresponding to areas where material is to be removed (the inverse of the particle locations). Figure 4.3 shows a schematic representation of the material removal process, with SEM images showing examples of single holes and particles fabricated using this method. In general FIB milling is not the preferred method for fabricating particle structures, since the Gallium ions are strongly scattered by surfaces with any degree of roughness (such as metal layers), leading to undesired removal of material in adjacent locations.

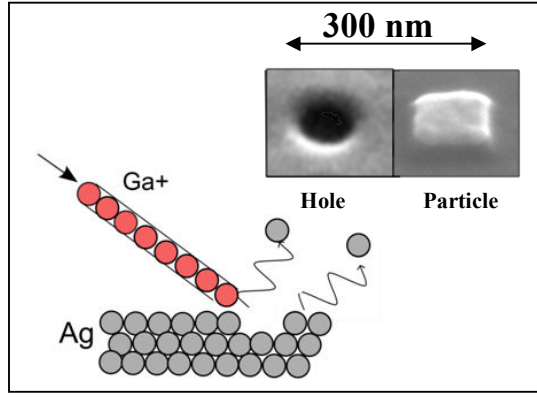


**Figure 4.3:** Schematic representation of the material removal process. The inset shows SEM images of a cylindrical hole with 90 nm diameter and 20 nm depth and a square particle with 90 nm side length and 20 nm depth fabricated using FIB milling.

### 4.3 The electromagnetic response of small metallic particles

The scattering response of small metallic nanoparticles is often calculated using the electrostatic approximation, which considers the sphere as an ideal dipole (two opposite charges in the limiting case where the distance between them approaches zero)<sup>11</sup>. In a moment we will discuss why this assumption may be considered valid. In a material with finite conductivity, the Maxwell equations can be used to show that free charge density can be considered to be zero (Equations 4.1 - 4.3).

$$\nabla \cdot \mathbf{D} = \rho_{free} \quad 4.1$$

$$\nabla \cdot (\epsilon \mathbf{E}) = \rho_{free} \quad 4.2$$

$$\nabla \cdot \mathbf{J} = \nabla \cdot (\sigma \mathbf{E}) = -\frac{\partial \rho_{free}}{\partial t} \quad 4.3$$

Equating  $\nabla \cdot \mathbf{E}$  from both sides gives:

$$\frac{\partial \rho_{free}}{\partial t} + \frac{\sigma}{\epsilon} \rho_{free} = 0 \quad 4.4$$

At the interface between two media (termed 1 and 2), the Maxwell equations impose the following boundary conditions:

$$(\mathbf{D}_2 - \mathbf{D}_1) \cdot \hat{\mathbf{n}} = \rho_{surface}$$

A discontinuity in the normal component of  $\mathbf{D}$  yields a surface charge

4.5

$(\mathbf{E}_2 - \mathbf{E}_1) \cdot \hat{n} = 0$	The tangential component of $\mathbf{E}$ is conserved	4.6
$(\mathbf{H}_2 - \mathbf{H}_1) \cdot \hat{n} = J_{surface}$	A discontinuity in the tangential component of $\mathbf{H}$ yields a surface current	4.7
$(\mathbf{B}_2 - \mathbf{B}_1) \cdot \hat{n} = 0$	The normal component of $\mathbf{B}$ is conserved	4.8

Therefore, if a homogeneous sphere with radius  $a$  and permittivity  $\varepsilon_1$  is placed in a medium of different permittivity  $\varepsilon_2$  in which there is a static electric field, a charge will be induced on its surface. The uniform electric field in the surrounding medium will also be distorted. The electric fields inside ( $\mathbf{E}_{inside}$ ) and outside ( $\mathbf{E}_{outside}$ ) the sphere can be calculated from the scalar potentials ( $\Phi_{inside}$  and  $\Phi_{outside}$ ), and at large distances away from the sphere the assumption is made that the electric field is the unperturbed applied field (Equation 4.11).

$$\mathbf{E}_{inside} = -\nabla\Phi_{inside} \quad 4.9$$

$$\mathbf{E}_{outside} = -\nabla\Phi_{outside} \quad 4.10$$

$$\lim_{r \rightarrow \infty} \Phi_{outside} = -E_0 r \cos \theta = -E_0 z \quad 4.11$$

The electric field inside the sphere is related to the unbalanced charge density ( $\rho_{unbalanced}$ ) through the divergence of the electric field:

$$\nabla \cdot \mathbf{E} = \frac{\rho_{unbalanced}}{\varepsilon_0} \quad 4.12$$

As shown in Equation 4.9, the electric field is defined as the negative gradient of the potential. Equations 4.12 and 4.11 may be combined, forming a direct relationship between the potential and the charge density, also known as Poisson's equation (Equation 4.13). If the unbalanced charge density is equal to zero, this reduces to Laplace's equation (Equation 4.14).

$$\nabla \cdot \nabla\Phi = \nabla^2\Phi = -\frac{\rho_{unbalanced}}{\varepsilon_0} \quad 4.13$$

$$\nabla^2\Phi = 0 \quad 4.14$$

In order to determine the potential inside and outside of the sphere, Laplace's equation must be solved in spherical polar co-ordinates. It is assumed that since the sphere is

symmetric about the  $z$  axis, variations in the azimuthal angle ( $\phi$ ) may be neglected. The form of Laplace's equation which is solved is therefore:

$$\frac{1}{r^2} \frac{\partial^2}{\partial r^2} (r^2 \Phi) + \frac{1}{r \sin \theta} \frac{\partial}{\partial \theta} \left( \sin \theta \frac{d\Phi}{d\theta} \right) = 0 \quad 4.15$$

Equation 4.15 may be solved using the separation of variables method by letting  $\Phi = R\Theta$ , where  $R(r)$  represents a function of radial distance ' $r$ ' and  $\Theta(\theta)$  a function of elevation angle ' $\theta$ '. An example of using the separation of variables method has already been given in Chapter 2 (section 2.1), and in Appendix B so the final solutions will be shown without workings. The solutions to  $R$  and  $\Theta$  are:

$$R = a_1 r^m + a_2 r^{-m-1} \quad 4.16$$

$$\Theta = \frac{1}{2^m} \left( \frac{d}{d(\cos \theta)} \right)^m ((\cos \theta)^2 - 1)^m = P_m(\cos \theta) \quad 4.17$$

Here  $a_1$  and  $a_2$  are constants,  $m$  is an integer and  $\theta$  is the polar angle as defined by the spherical polar coordinate system. At infinity the potential is equal to that of the unperturbed applied field (given by Equation 4.11). The solution for the potential outside the sphere is therefore constructed such that the perturbation to the applied field due to the sphere vanishes as  $r \rightarrow \infty$ .

$$\Phi_{outside} = \sum_{m=0}^{\infty} b_m \left( \frac{a}{r} \right)^{m+1} P_m(\cos \theta) - E_0 r \cos \theta \quad 4.18$$

Within the sphere, as  $r \rightarrow 0$  the solution must be finite:

$$\Phi_{inside} = \sum_{m=0}^{\infty} c_m \left( \frac{a}{r} \right)^m P_m(\cos \theta) \quad 4.19$$

In Equations 4.18 and 4.19, the radius of the dielectric sphere is represented by  $a$ . At the boundary between the sphere and the surrounding medium,  $\Phi_{outside} = \Phi_{inside}$ . By equating Equations 4.18 and 4.19, and imposing the continuity of the normal component of the electric displacement vector  $\mathbf{D}$  at the interface, the coefficients  $b_m$  and  $c_m$  can be determined.

$$\varepsilon_1 \left( \frac{\partial \Phi_{inside}}{\partial r} \right) = \varepsilon_2 \left( \frac{\partial \Phi_{outside}}{\partial r} \right) \quad 4.20$$

The general solution of Laplace's equation has angular solutions which are equivalent to the spherical harmonics which were identified in the Mie Theory derivation contained within Chapter 3. Here,  $m$  represents an integer which corresponds to the angular harmonic of interest (e.g.  $m = 1$  is the dipole contribution,  $m = 2$  the quadrupole etc.). For a small sphere which obeys the electrostatic approximation, only the dipole term is the significant contributor to the potential both inside and outside of the sphere. The coefficients  $b_1$  and  $c_1$  are given by:

$$b_1 = E_0 a \left( \frac{\varepsilon_1 - \varepsilon_2}{\varepsilon_1 + 2\varepsilon_2} \right) \quad 4.21$$

$$c_1 = E_0 a \left( \frac{3\varepsilon_2}{\varepsilon_1 + 2\varepsilon_2} \right) \quad 4.22$$

With knowledge of these weighting coefficients, the potential inside and outside of the sphere can be expressed as:

$$\Phi_{inside} = -\frac{3\varepsilon_2}{\varepsilon_1 + 2\varepsilon_2} E_0 r \cos \theta \quad 4.23$$

$$\Phi_{outside} = -E_0 r \cos \theta + E_0 a^3 \frac{\varepsilon_1 - \varepsilon_2}{\varepsilon_1 + 2\varepsilon_2} \frac{\cos \theta}{r^2} \quad 4.24$$

Since we have assumed that the dipole term is dominant in the series of angular harmonics associated with a small sphere, a direct analogy can be made between the electrostatic potential outside the sphere, and that of a dipole formed from two equal and opposite point charges  $\pm q$ , separated by a distance  $d$ :

$$\Phi = \frac{qd \cos \theta}{4\pi\varepsilon_m r^2} \quad 4.25$$

The electric field outside the sphere can be considered as the superposition of the applied field and the field of an ideal dipole<sup>11</sup>. The polarisation ( $\mathbf{p}$ ) and therefore the polarisability ( $\alpha$ ) of the sphere may be expressed as:

$$\mathbf{p} = 4\pi a^3 \frac{\epsilon_1 - \epsilon_2}{\epsilon_1 + 2\epsilon_2} \mathbf{E}_0 \quad 4.26$$

$$\alpha = 4\pi a^3 \frac{\epsilon_1 - \epsilon_2}{\epsilon_1 + 2\epsilon_2} \quad 4.27$$

When considering illumination of the sphere with visible light, the applied field is not static but is an incident electromagnetic wave which has temporal and spatial variation. However if the sphere is small compared to the wavelength of the oscillation (i.e. the size parameter,  $ka \ll 1$ ), the equations can still be used to approximate the polarisability. This is because at any instant of the oscillation the incident field is approximately uniform across the sphere<sup>11</sup>. An important point to note is that the field inside the sphere will not be uniform unless the imaginary component of the refractive index is zero, a condition not satisfied by metals at visible frequencies. Therefore the electrostatic approximation for metal particles is never a completely accurate description of the scattered or internal fields. It does however provide a useful insight into the excitation conditions of the dipolar LSPR modes. The LSPR frequency occurs when a metallic particle has maximum polarisability<sup>1</sup>. This is because the intensity of the scattered radiation is proportional to the dipole moment which is induced across the nanoparticle by the application of the incident electromagnetic field. Since the polarisability is defined as the ratio of the induced dipole moment to the applied electric field, it is reasonable to expect maximum scattering and absorption of incident light to occur at the maximum polarisability condition. From an inspection of Equation 4.27 it can be inferred that a numerical pole in the real part of the polarisability occurs when  $\epsilon_1 = -2\epsilon_2$ . In vacuum, this corresponds to a metal with a real permittivity value of  $-2$ , a value found for metals such as Ag or Au within the visible region. In Figure 4.4, the real and imaginary components of the polarisability (Equations 4.28 and 4.29) are plotted for 60 nm diameter Ag spheres. This is compared against the scattering efficiency ( $Q_{sca}$ ). In both structures the maxima occur at similar wavelengths, corroborating the relationship between polarisability and the frequency of the LSPR. The small difference of approximately 15 nm that exists between the spectral positions of the maxima for the imaginary component of the polarisability ( $\alpha$ )

and the scattering efficiency ( $Q_{sca}$ ) arises due to the limitations of the electrostatic approximation. This discrepancy is more severe for large particles having dimensions which are comparable to the incident wavelength, as will be discussed later.

$$\alpha_{real} = 4\pi a^3 \left( \frac{\epsilon_r^2 + \epsilon_i^2 + \epsilon_r - 2}{\epsilon_r^2 + \epsilon_i^2 + 4\epsilon_r + 4} \right) \quad 4.28$$

$$\alpha_{imag} = 4\pi a^3 \left( \frac{3\epsilon_i}{\epsilon_r^2 + \epsilon_i^2 + 4\epsilon_r + 4} \right) \quad 4.29$$

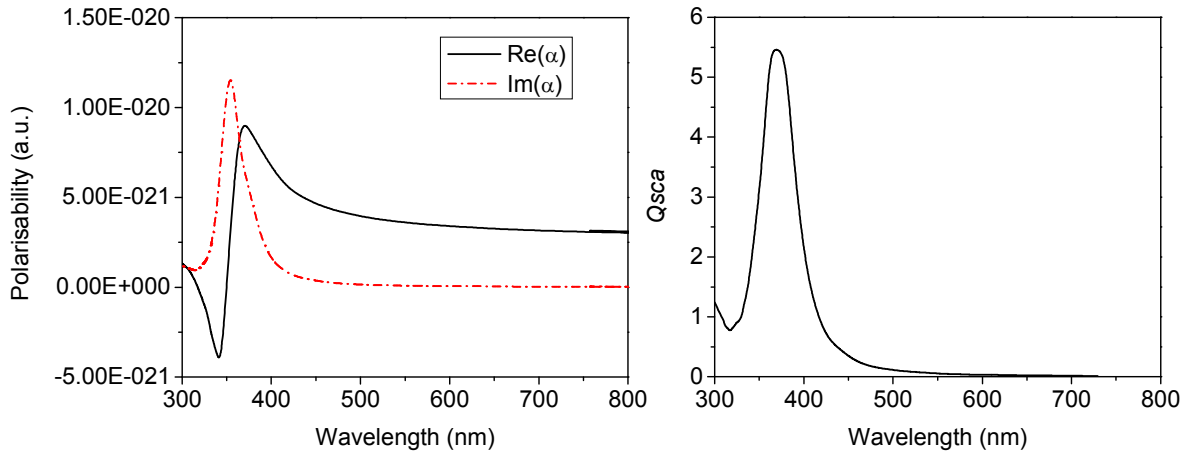


**Figure 4.4:** The real and imaginary components of the polarisability are plotted for a 60 nm diameter Ag sphere (left) in vacuum. This is compared against the scattering efficiency ( $Q_{sca}$ ) which has been simulated using Mie Theory (right).

The previous derivation considered the resonance condition for spheres  $\ll \lambda$ . This can also be extended to non-spherical geometries. The principle of solving scalar potentials inside and outside the inclusion remains the same, with the exception that there is now more scope for geometrical adaptation. An ellipsoid for example (shown in Figure 4.5), has three semi-axes with lengths  $a$ ,  $b$  and  $c$  respectively, and Laplace's equations are best solved using ellipsoidal coordinates.

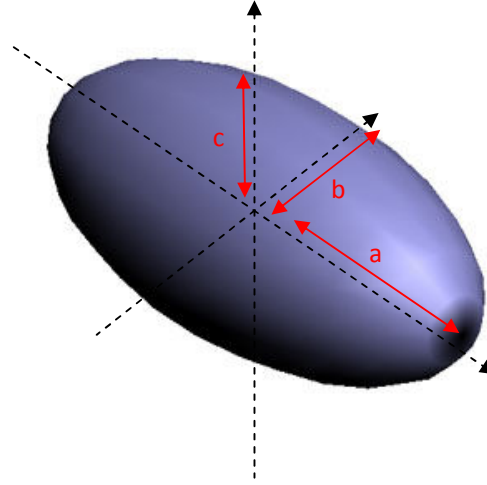


**Figure 4.5:** Schematic of an ellipsoidal particle, showing the axes of symmetry and the semi axis lengths  $a$ ,  $b$  and  $c$ .

By solving Laplace's equation in ellipsoidal coordinates, it can be shown<sup>11, 12</sup> that the diagonal components of the polarisability tensor for the electric field parallel to each of the principal axes of an ellipsoid is given by:

$$\alpha_i = 4\pi abc \frac{\varepsilon_1 - \varepsilon_2}{3\varepsilon_2 + 3L_i(\varepsilon_1 - \varepsilon_2)} \quad 4.30$$

Where  $i = a, b, c$  and  $L_i$  is a dimensionless quantity specified by:

$$L_i = \frac{abc}{2} \int_0^\infty \frac{dq}{(i^2 + q)((q + a^2)(q + b^2)(q + c^2))^{0.5}} \quad 4.31$$

The  $L_i$  elements are referred to in the literature as 'geometrical shape factors' or 'depolarisation factors'. These are numerical quantities that are purely real, and depend on the surface curvature (and therefore the relative lengths of the semi-axes) of the ellipsoid. The functional form of the denominator is such that its sum of elements over all axes is always equal to unity. A sphere for example has  $L = 1/3$  for all axes, whilst a prolate spheroid with ratios of  $a/b$  and  $a/c$  of 5 has shape factors of approximately 0.055 (for the long axis) and 0.472 (for the short axes). Figure 4.6 shows how the shape factor along a

single axis  $L_a$ , varies as length  $a$  is fixed and other two lengths  $b$  and  $c$  are varied equally with  $b = c$ .

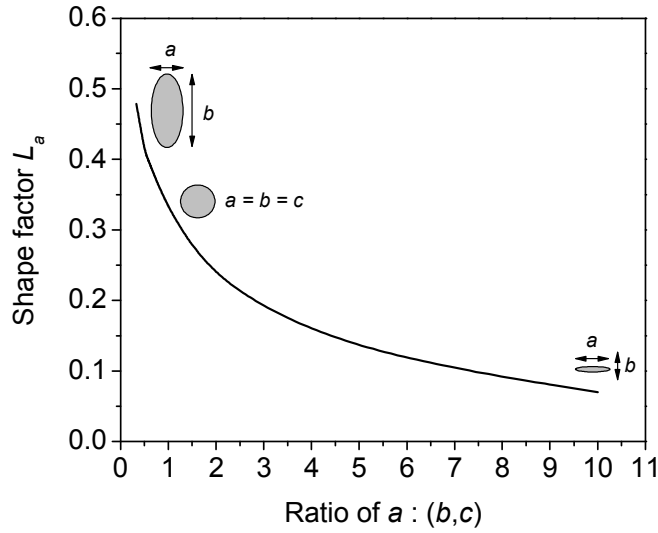


**Figure 4.6:** Using Equation 4.31, the shape factor  $L_a$  is plotted against the ratio of  $a : (b,c)$  for an ellipsoid in which length  $a$  is fixed and lengths  $b,c$  are increased such that  $b = c$ .

For lengths where  $a < b,c$  the shape factor  $L_a$  increases and is asymptotic towards unity for a rod with infinite length. At  $a = b = c$ ,  $L_a$  passes through 0.333, the expected shape factor for a sphere. As  $b,c$  are decreased such that  $a > b,c$ ,  $L_a$  decreases and is asymptotic to zero for an infinitely narrow rod. It is therefore evident that any disc-like structure with  $a < b,c$  and  $b = c$  will have two resonant frequencies. These are associated with polarisability maxima arising from the geometrical resonances of the short axis and long axes. Equations 4.32 and 4.33 show the general form of the real and imaginary parts of the polarisability for a non-spherical scatterer.  $L_i$  represents the shape factor for the axis parallel to the incident electric field. These expressions can be derived by simplifying Equation 4.30, and will reduce to the spherical case (Equations 4.28 and 4.29) when  $L_i = 1/3$ .

$$\alpha_{real} = \frac{4\pi a^3}{3} \left( \frac{\epsilon_r + L_i \epsilon_r^2 + L_i \epsilon_i^2 - 2L_i \epsilon_r + L_i - 1}{1 + 2L_i \epsilon_r - 2L_i + L_i^2 \epsilon_r^2 - 2L_i \epsilon_r + L_i^2 \epsilon_i^2 + L_i^2} \right) \quad 4.32$$

$$\alpha_{imag} = \frac{4\pi a^3}{3} \left( \frac{\epsilon_i}{1 + 2L_i \epsilon_r - 2L_i + L_i^2 \epsilon_r^2 - 2L_i \epsilon_r + L_i^2 \epsilon_i^2 + L_i^2} \right) \quad 4.33$$

Figure 4.7 shows the real and imaginary components for  $\mathbf{E}$  polarised along the long and short axes of an Ag rod ellipsoid with dimensions  $30 \text{ nm} \times 30 \text{ nm} \times 80 \text{ nm}$ . This is compared with the simulated scattering efficiency obtained using a T-Matrix approach for incident light polarised parallel to the long and short axes of the rod. A comparison of the two plots shows a discrepancy between the maxima associated with the long axis resonance. The maximum of the real part of the polarisability occurs for an incident wavelength of 475 nm, however the scattering efficiency maximum is around 510 nm. The phase of the incident wave cannot be considered uniform across the entire length of the rod. For a rod length of 80 nm the electrostatic approximation is beginning to fail, and the effects of dynamic depolarisation<sup>13,14</sup> must be included to correctly determine the LSPR frequency for long axis.

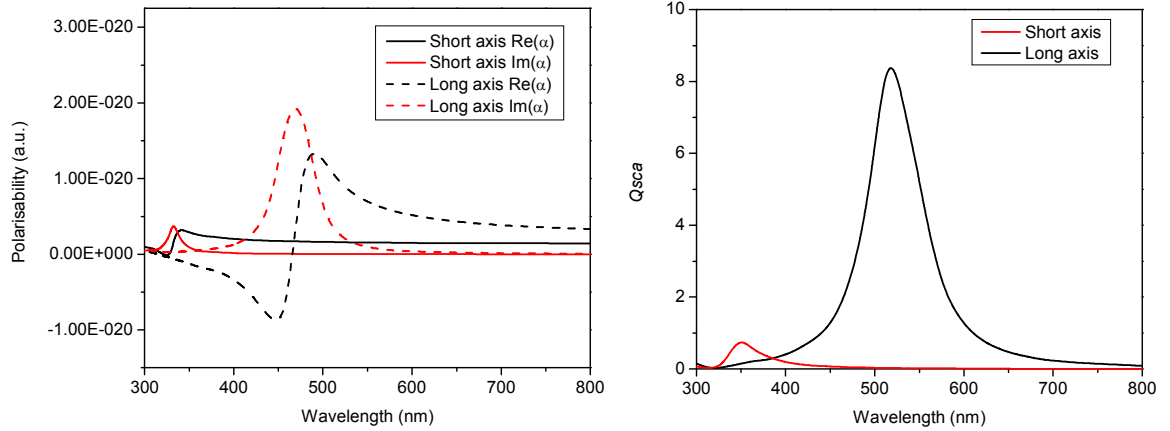


**Figure 4.7:** The real and imaginary components of the polarisability are plotted as a function of wavelength for the incident electric field polarised parallel to the long and short axes of an Ag rod with dimensions  $30 \text{ nm} \times 80 \text{ nm} \times 80 \text{ nm}$  (left). A T-Matrix method has been used to simulate the scattering efficiency of the rod illuminated with light polarised along the long and short axes (right).

#### 4.4 Optical characterisation using dark-field spectroscopy

In this section the optical characterisation of cylindrical Au particles fabricated by EBL will be considered. Figure 4.8 shows a SEM image of nanoparticles which are typically 35 nm height, and have diameters ranging from 45 nm to 160 nm.

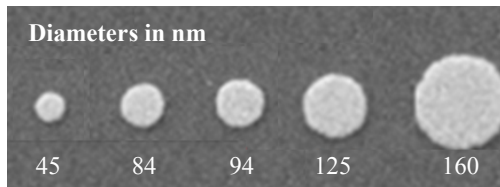


**Figure 4.8:** An SEM image showing an example of cylindrical Au nanoparticles fabricated by EBL. These particles have height 35 nm and diameters ranging from 45 nm to 160 nm. *Note:* On the sample the particles are separated by 2  $\mu\text{m}$  but the images have been merged for visualisation.

One method for determining the optical transmission and extinction characteristics of a structure (for example a planar Ag film) is to use bright field spectroscopy. This illuminates the sample at near normal incidence with a collimated white light source, with an objective being used to focus the collected light onto a spectrometer. However, this technique is not suitable for studying the scattering response of single nanoparticles, since the size of the incident beam is significantly larger than the particle diameter. Only a small proportion of the collected light will be due to light scattering from the particle, and deconvolving the response is extremely difficult. A possible solution to this problem is to use spatial modulation spectroscopy. A lens is used to focus the incident beam to a spot size of a few tens of  $\mu\text{m}$ , and the optical stage is forced into oscillation (using a motor) in a plane which lies perpendicular to the incident wave vector. It has been shown that with suitable mathematical analysis the modulated element of the transmitted power can be used to extract the extinction cross section of the single particle<sup>15</sup>.

Another technique which characterises the optical response of single particles is dark field spectroscopy. A schematic of the apparatus is shown in Figure 4.9. The arrangement differs from bright field spectroscopy in a number of ways. The incident beam is partially blocked using an opaque circular disc, such that light can only pass around the edge of the disc. A ring-like pattern of illumination is brought to a tight focus at the surface of the

sample. Beyond the sample, an objective with a high numerical aperture (1.25) is used to collect the scattered light and pass it to a spectrometer. To minimise reflections at the substrate-air interface, an oil immersion objective is used in conjunction with refractive index matching liquid having parameters equal to that of the substrate ( $n_r = 1.52$ ,  $n_i = 0.00$ ). An advantage of using dark field spectroscopy is that the collected light consists of only that which is scattered by the particle. This is because the incident angle is sufficiently large that the unscattered light is beyond the collection angle of the objective. Figure 4.10 shows a photograph of scattering from Au nanoparticles viewed using a dark-field microscope. The nanoparticles are identical to those illustrated in Figure 4.8, with height 35 nm and diameters ranging from 45 nm to 160 nm. When obtaining spectroscopic measurements, the particles are spaced by a minimum distance of 2  $\mu\text{m}$  to avoid the scattering response of a single particle being modified by electromagnetic near field coupling from adjacent particles.

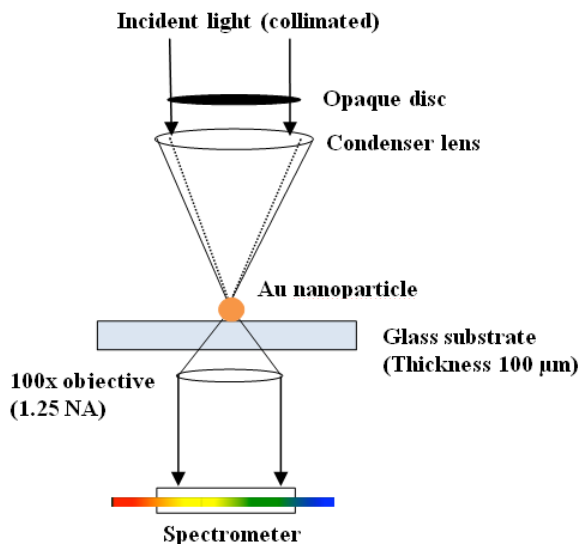


**Figure 4.9:** Schematic illustrating the experimental configuration for dark-field spectroscopy.



**Figure 4.10:** CCD image obtained from a dark field microscope used to observe scattering from Au discs with height 35 nm and diameters ranging from 45 nm to 160 nm. The image has been normalised to the lamp spectrum.

In order to obtain a scattering spectrum from the dark field images, light from the objective is passed to a spectrometer. This uses a diffraction grating to disperse the scattered light into its constituent wavelengths across several rows of pixels on a CCD. A mechanical shutter is used to select the region of the image corresponding to the nanoparticle locations, and imaging software records the intensity on each pixel of the CCD. Figure 4.11 shows the experimental scattering spectra obtained for the Au discs shown in Figure 4.8. This is compared against scattering cross section data which has been simulated using a T-Matrix method, with wavelength dependent  $\epsilon$  parameters for Au taken from reference data published by Johnson & Christy<sup>16</sup>. In (c) of Figure 4.11, the resonant wavelengths of simulated and experimental scattering spectra have also been compared, and show reasonable agreement, with a maximum discrepancy of  $\approx 15$  nm in resonant wavelength between the two datasets.

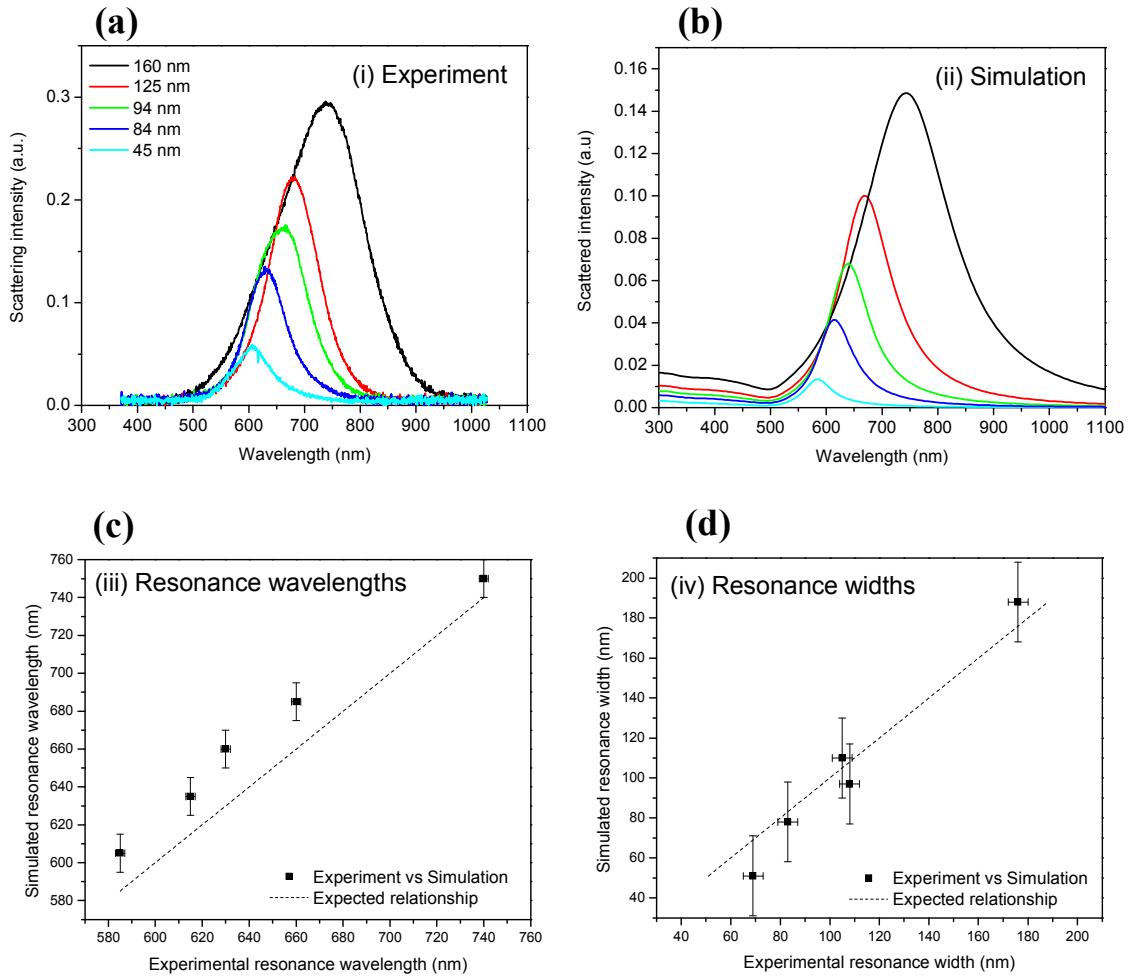


**Figure 4.11:** Dark field scattering spectra (a) of Au discs with height 35 nm and diameters ranging from 45 to 160 nm are compared with simulated spectra (b) obtained using a T-Matrix method. In (c) the resonant wavelengths and widths (d) from the experimental and simulated scattering spectra are compared.

In considering the most likely origin of the discrepancy between the simulated and experimental resonant wavelengths, it is assumed in the simulation that all particles are cylindrical. However, as discussed previously, the EBL fabrication process is such that the exposure regions are slightly rounded / tapered at the edges. The experimental Au particles are therefore slightly ellipsoidal in shape, and by considering the shape factor of this modified “slightly ellipsoidal” geometry it is found that the resonant frequency is increased when compared to a perfect cylinder. Both the experimental and simulated scattering curves in Figure 4.11 exhibit a red shift in the LSPR wavelength as the diameter of the disk is increased. The electrostatic approximation can be used to show that for light polarised

parallel to the diameter of the disk, as the diameter of the disk is increased the shape factor  $L_i$  decreases and the condition at which maximum polarisability occurs is red-shifted (Figure 4.6). In addition, the electrostatic approximation begins to fail when the effects of dynamic depolarisation are significant. If the size of the disc is such that the incident field cannot be considered uniform across long axes of the structure, the resonant wavelength is further red-shifted beyond that which is predicted by the electrostatic approximation. Another observation which can be made is that the width of the resonance increases with the diameter of the disc (inset (d) of Figure 4.11). This is primarily due to the radiative decay mechanism of the LSPR. The energy relaxation of a LSPR comprises both a non-radiative decay process with time constant  $\tau_{nr}$  and a radiative decay process with time constant  $\tau_r$ . The non-radiative decay channel considers losses which occur when oscillating electrons lose their energy through inelastic scattering to single electron excitations. The non-radiative loss can be related to the dielectric constants of the metal, and in metals such as Ag and Au it is found to be highly dependent upon the spectral overlap of the LSPR with the interband absorption edge<sup>1</sup>. The radiative decay channel corresponds to the loss of energy through the emission of electromagnetic radiation. For metal nanoparticles with diameters below 30 nm, the energy relaxation is dominated by non-radiative decay processes, however for larger diameters the radiative element is found to be the most significant contributor to energy loss, as it is proportional to the number of electrons within the scattering particle. The radiative damping rate, for the simple case of a sphere, is given by Equation 4.34<sup>17</sup>.

$$\frac{1}{\tau_r} = \frac{2\omega_p^4}{9c^3} \frac{\sqrt{\epsilon_1}}{1 + 2\epsilon_1} r_0^3 \quad 4.34$$

Here  $\tau_r$  is the dephasing time associated with the radiative decay mechanism, which represents the time required for the electrons to return to their unperturbed state.  $\omega_p$  and  $\epsilon_1$  represent the plasma frequency and real component of the permittivity of the surrounding medium,  $c$  is the speed of light in vacuum and  $r_0$  is the radius of the sphere. This expression can in principle be generalised to include other geometries such as the disk-like structure in Figure 4.11, however deriving an analytical formulation for the resonance width is particularly complex and beyond the scope of the present study. In general, as the size of the scatterer (and number of electrons with the particle) is increased, the resonance width will also increase as a result of the shorter dephasing time. In inset (d) of Figure

4.11, the resonance widths of the simulated and experimental scattering spectra are compared and show reasonable agreement.

#### 4.5 The angular response of the multipolar LSPR modes

The majority of liquid crystal display devices operate by selectively transmitting a specified range of wavelengths / polarisation configurations that are incident from a diffuse source of white-light illumination located behind the cell. This can be a disadvantage, particularly when the device is illuminated from the front with ambient light, such as when attempting to view the device in bright sunlight. Another difficulty is that whilst the alignment of molecules within a liquid crystal cell can be readily switched with an applied electric field, there are very few electro-optical effects which give rise to a strong coloured reflection. A possible solution to both of these problems is to investigate the hosting of metallic nanoparticles within a liquid crystal cell. As has already been shown, metallic nanoparticles exhibit geometrical resonances that give rise to strong scattering at visible frequencies. The ideal behaviour for a display application would be a step-like scattering response with two switchable states, one in which there is maximum scattering and another in which there is little or no scattering (shown in Figure 4.12). The maximum scattering state would need to have a broadly flat response over a viewing angle range of  $\pm 45$  degrees. From a display perspective this is a fundamental requirement as the response in the maximum scattering phase must not change significantly when the illumination angle  $\theta$  or the scattering angle  $\phi$  deviates from normal incidence.

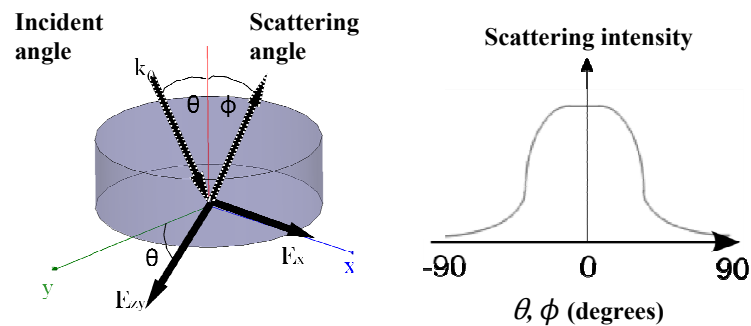


**Figure 4.12:** Desired scattering response of a nanoparticle which could be hosted within a liquid crystal cell. In the diagram,  $\theta$  represents the illumination angle of the incident beam which is polarized either parallel ( $E_{zy}$ ) or perpendicular ( $E_x$ ) to the plane of angular variation and  $\phi$  represents the scattering angle of the radiated field.

For particles significantly smaller than the incident wavelength, the electrostatic approximation can be applied and the response of the nanoparticle can be approximated to a dipole. It can be shown that the angular distribution of the radiated power emitted by a dipole illuminated with radiation having an electric field  $\mathbf{E}$  which is linearly polarised along the dipole axis is of the form <sup>12</sup>:

$$\frac{dP}{d\Omega} = \frac{c^2}{32\pi^2} \sqrt{\frac{\mu_0}{\epsilon_0}} k^4 |\mathbf{p}|^2 \sin^2 \phi \quad 4.35$$

Here,  $\mathbf{p}$  represents the dipole moment and  $c$  is the angle between the unit vectors of the dipole moment and the wave vector of the radiated field,  $P$  is the radiated power and  $\Omega$  represents the solid angle. An initial inspection of Equation 4.35 suggests that a small nanoparticle will exhibit a scattering intensity which follows a  $\sin^2 \phi$  or  $\cos^2 \phi$  dependence. In Figure 4.13 a T-Matrix method has been used to simulate the scattering efficiency of an Ag cylinder with height 25 nm and diameter 80 nm. The cylinder is illuminated at various angles of incidence for light polarised both parallel (a) and perpendicular (b) to the plane of incidence. (For planar structures these polarisation states would be termed Transverse Magnetic (TM) and Transverse Electric (TE) respectively, however this terminology cannot be applied for the case of a single particle.) In graph (c) of Figure 4.13 the magnitude of the  $Q_{sca}$  maxima from (a) have been normalised such that  $Q_{sca}(\theta = 0^\circ) = 1.0$ , and these values have been plotted against a  $\cos^2 \theta$  function. The scattering intensity for A clearly follows a  $\cos^2 \theta$  dependence as a function of illumination angle  $\theta$ , whereas for (b) there is no angular dependence. This is because in (a) the incident polarisation is such that as the angle of incidence is varied, the electric field changes from being parallel to the long axis to that of the short axis. The polarisability maximum of the short axis is considerably smaller than that of the long axis (by a factor of approximately 100). This is due to the aspect ratio of the particle, as shown in the earlier analysis, and in Figure 4.7. Therefore a drastic reduction in scattering intensity occurs as the alignment of the electric field is varied between the two axes. In contrast, as the incident angle  $\theta$  is varied in (b), the electric field always remains in the plane of the disc, and therefore no variation in scattering intensity is observed.

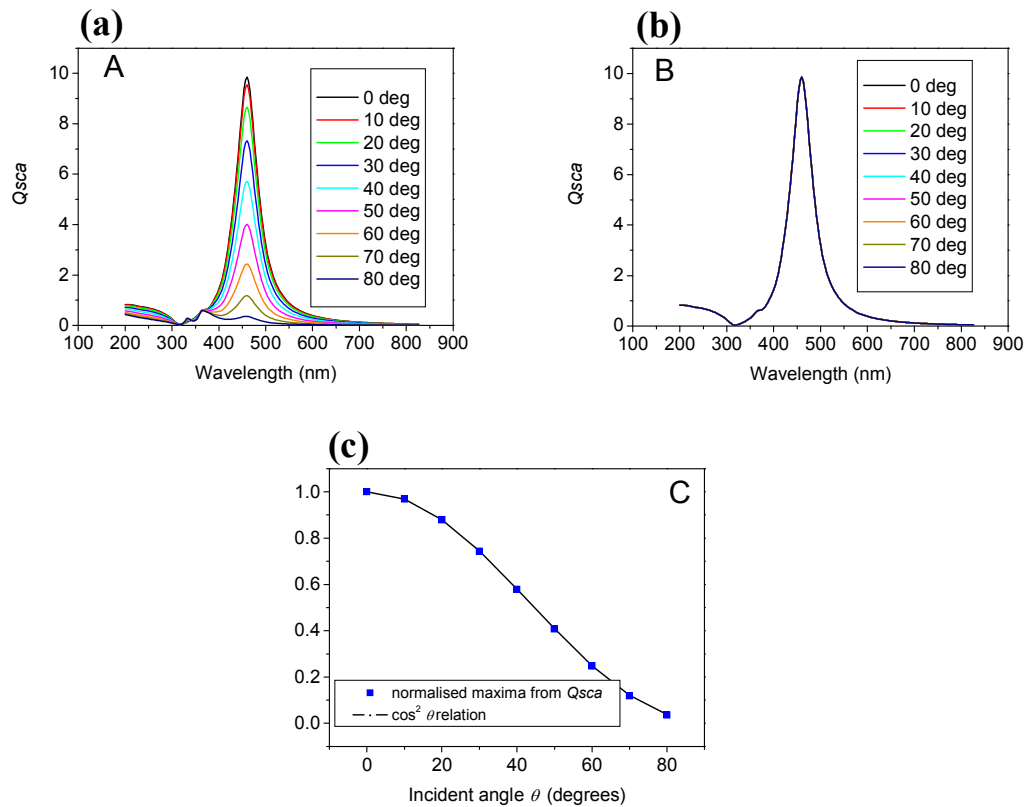


**Figure 4.13:** The scattering efficiency of an Ag disc with height 25 nm and diameter 80 nm has been simulated using a T-Matrix method for light incident at various illumination angles  $\theta$  ranging from 0 to 80 degrees. The incident beam is polarised parallel (a) and perpendicular (b) to the plane of angular variation. In the lower graph (c) the magnitude of the maxima from the scattering efficiency curves in (c) have been normalised to 1, and are plotted against a  $\cos^2 \theta$  function.

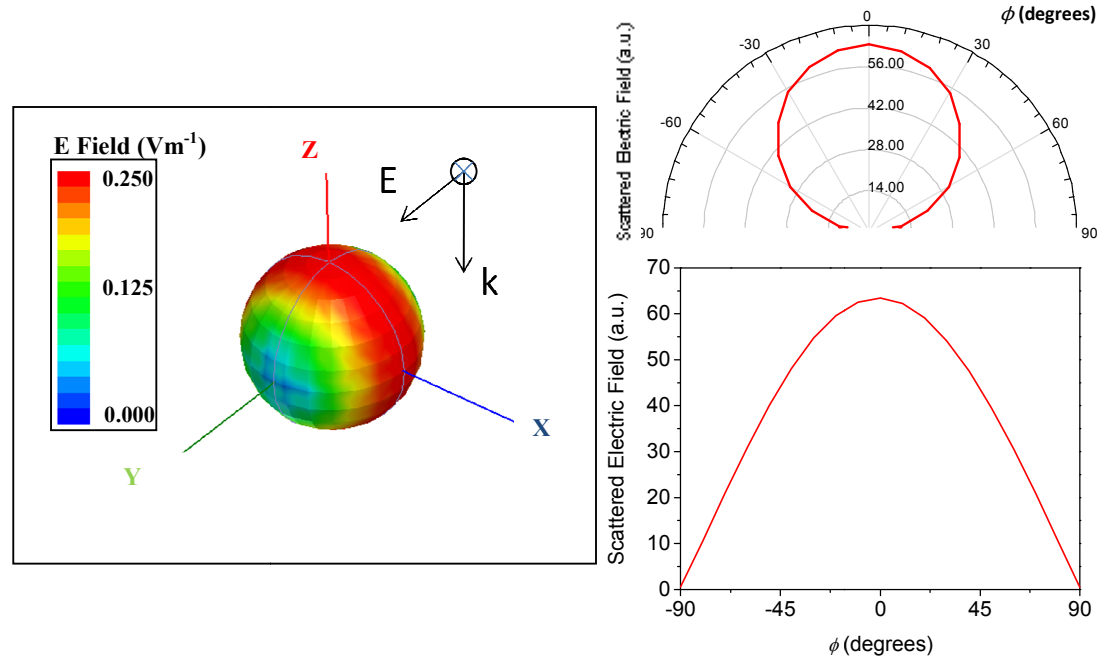


**Figure 4.14:** The scattered electric field distribution from the Ag disc has been simulated using a FEM technique and has been projected onto a spherical surface in the far field. A polar plot of the radiated field in the upper half space is shown for a cross section through the YZ plane. The electric field intensity has been plotted as a function of the scattering angle  $\phi$ .

Figure 4.14 shows the far field radiation pattern of the disc (projected onto a spherical shell) for light incident at normal incidence at the resonant wavelength corresponding to the dipolar LSPR. A polar plot of the radiated field in the upper half space is shown for a cross section through the XZ plane, and the electric field intensity has been plotted as a function of scattering angle  $\phi$ . It is shown that, as predicted by Equation 4.35, the radiated field also follows a  $\cos\phi$  angular dependence (or  $\cos^2\phi$  for radiated power). Small nanoparticles such as flat cylindrical discs or spheres are thus clearly not suitable for display purposes. This is because the apparent transition between the maximum and minimum scattering arrangement occurs over a wide range of angles, which in terms of a display will lead to a reduction in the contrast ratio. There appears to be two approaches for modifying the angular response of the scattered field such that it is not governed by the dipolar term. One approach is to consider the response of higher-order multipolar modes that may be supported by larger metallic nanoparticles (those having dimensions  $\approx \lambda$ ). The

distribution of the radiated power from a quadrupole for example, does not explicitly follow a  $\cos^2 \phi$  angular dependence <sup>12</sup>:

$$\frac{dP}{d\Omega} = \frac{c^2 k^6}{512\pi^2} \sqrt{\frac{\mu_0}{\epsilon_0}} Q_0^2 \sin^2 \phi \cos^2 \phi \quad 4.36$$

The terms in Equation 4.36 have the same definition as those in Equation 4.35.  $Q_0^2$  represents a constant which is determined from the diagonal components of the quadrupole moment tensor.

A second approach is to investigate placing several nanoparticles in close proximity. In this instance, electromagnetic coupling between particles can significantly modify their charge distributions and LSPR properties. For example, it has been shown that when two or more nanoparticles are brought within a few tens of nm of each other, plasmon hybridization can occur. In this instance, two distinct resonant modes are observed which are associated with the symmetric and anti-symmetric distribution of charge across the particle arrangement <sup>18</sup>. A diagram showing the instantaneous charge and field distributions of the two resonant modes at arbitrary phase of the incident wave is shown in Figure 4.15. This is illustrated for a cross section taken through the centre of the particles, where the incident wave vector  $\mathbf{k}$  and electric field  $\mathbf{E}$  are polarised in the configuration shown. The vector arrows represent the direction of the electric field inside the particles, with the + and – symbols indicating regions of positive and negative charge respectively.

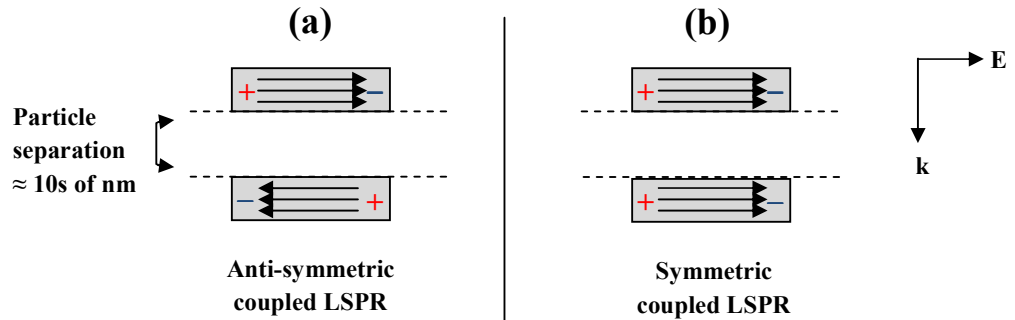


**Figure 4.15:** The instantaneous charge and field distributions are illustrated for two metallic nanoparticles which interact through the overlap of their resonant electromagnetic fields. Plasmon hybridisation can occur in particles separated by distances which are a few

10s of nm in vacuum, resulting in two coupled LSPRs associated with the anti-symmetric (a) and symmetric (b) distribution of charge across the structure.

The topic of coupled LSPRs in hole and particle arrays will be discussed extensively in Chapter 8, with relevance to electromagnetic metamaterial applications which exhibit a negative index of refraction. Towards the end of the present chapter, the response of the anti-symmetric and symmetric coupled LSPRs will also be discussed in terms of their incident angle  $\theta$  and scattering angle  $\phi$  responses. It has been shown by Grigorenko et al. that the anti-symmetric coupled LSPR is favoured in tapered pairs of nanorods<sup>18</sup>. This has particular relevance to display applications, since it has already been identified that charge distributions which resemble a quadrupole (two dipoles in anti-phase) may offer an improved incident angle  $\theta$  and scattering angle  $\phi$  response in comparison to the dipolar LSPR which is excited in small metal nanoparticles.

Small nanoparticles only support dipolar LSPRs, since the incident field is approximately uniform across the structure and so the conduction electrons oscillate collectively in phase with the electric field. However, when the particle size is comparable to, or larger than, the incident wavelength it is possible for higher order multipolar modes to be observed. In order to consider the existence of dipolar and quadrupolar modes, the scattered electric field must be expanded such that it contains the first and second terms in the solution to Laplace's equation. Previously we have shown that Equations 4.18 and 4.19 can be used to express the potential inside and outside of a dielectric sphere as a series of angular harmonics. If the series is expanded to terms up to and including  $m = 2$ , the electric field outside the sphere may be calculated using Equations 4.9 and 4.10 and subsequently expressed as a linear sum of dipole and quadrupole elements. This scattered field expansion is shown in Equation 4.37 as a function of the Cartesian coordinates  $x$ ,  $y$ ,  $z$ . Here,  $r$  is the modulus of the vector from the origin to the point at which the electric field is sampled. It is assumed that the sphere has radius  $r_0$ , complex permittivity  $\epsilon_l$  and is surrounded by vacuum.

$$\begin{aligned}
 \mathbf{E}_{\text{sca}} = E_0 \hat{x} + ikE_0(x\hat{x} + z\hat{z}) - \alpha E_0 \left[ \frac{\hat{x}}{r^3} - \frac{3x}{r^5}(x\hat{x} + y\hat{y} + z\hat{z}) \right] & \quad 4.37 \\
 - \beta E_0 \left[ \frac{x\hat{x} + z\hat{z}}{r^5} - \frac{5z}{r^7}(x^2\hat{x} + y^2\hat{y} + xz\hat{z}) \right] & \\
 \text{Dipolar term} & \quad \text{Quadrupolar term}
 \end{aligned}$$

The dipolar polarisability term  $\alpha$  is that given previously in Equation 4.27. The quadrupolar polarisability term is given by  $\beta$ , where:

$$\beta = \gamma r_0^5 \quad 4.38$$

$$\gamma = \frac{\varepsilon_1 - 1}{\varepsilon_1 + \frac{3}{2}} \quad 4.39$$

A fundamental difference between the quadrupole and dipole polarisability terms is the factor in the denominator. In the quadrupole term there is a factor of  $3/2$ , however in the dipole term this factor is  $2$ . The implications of this are that in addition to the dipole contribution, a singularity occurs in  $\beta$  when  $\varepsilon_l = -3/2$ , this corresponds to the resonant condition for the quadrupolar mode in the electrostatic limit. This analysis can be further extended to higher orders by increasing the number of terms in the series expansion for the potential inside and outside of the sphere (Equations 4.18 and 4.19). It is important to note that the electrostatic approximation does not consider the effects of dynamic depolarisation which occur in structures in which the ratio of the particle size to the incident wavelength is large<sup>13,14</sup>. Here we have used the electrostatic approximation purely to give a physical insight for the simple case of dipolar and quadrupolar excitations of a sphere, without wishing to become too involved in mathematical detail. In Figure 4.16, Mie Theory has been used to simulate the scattering efficiency of a 200 nm diameter Ag sphere in vacuum. The scattering spectrum shows several maxima corresponding to multipolar resonances. A finite element method has been used to simulate the electric field distributions at the resonant frequencies corresponding to multipolar excitations for a cross section taken through the centre of the sphere. This cross section is for a plane which lies perpendicular

to the incident wave vector. Note that these field distributions are identical to those shown in Figure 3.1 (Chapter 3) which represents the normal modes of a spherical particle as proposed by Mie in 1908<sup>19</sup>.

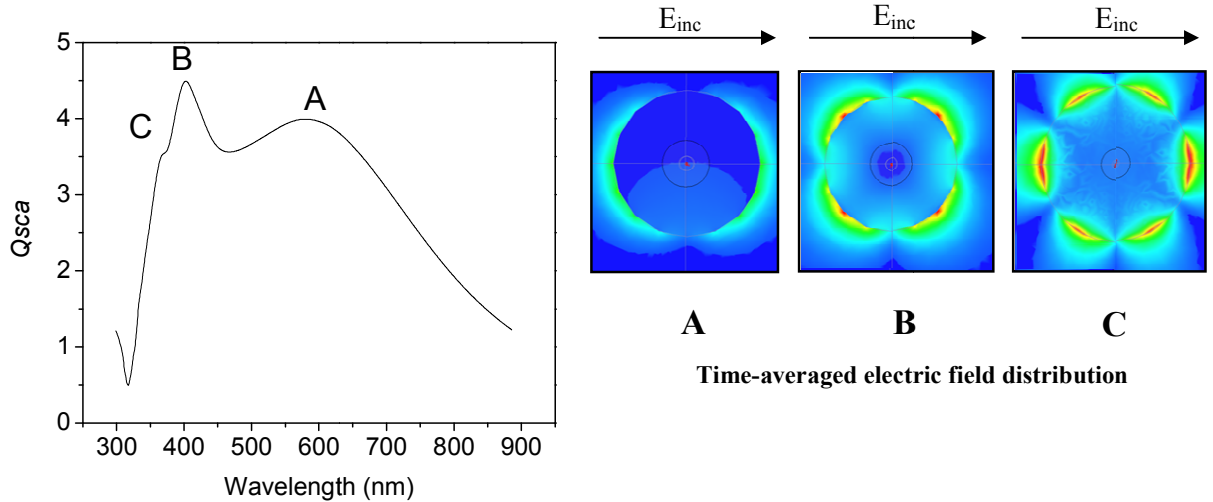


**Figure 4.16:** The scattering efficiency of a 200 nm diameter Ag sphere in vacuum has been simulated using Mie Theory, with light incident at 45 degrees. A FEM technique has been used to simulate the time-averaged electric field distributions for a cross section taken through the centre of the sphere at the resonant frequencies labelled A, B and C (intensity scales are arbitrary). The incident electric field is polarised along the direction shown by the arrow above the figures.

Figure 4.17 shows the far field radiation pattern of the disc (projected onto a spherical shell) for light incident at normal incidence at the resonant wavelength corresponding to the quadrupolar LSPR (feature B). A polar plot of the radiated field is shown for a cross section through the XZ plane and the electric field intensity has been plotted as a function of scattering angle  $\phi$ . Perhaps surprisingly, the majority of the radiated power appears to be forward scattered. This is not what would be expected from Equation 4.36, which suggests that a quadrupole should radiate uniformly across four ‘lobed’ regions that are symmetric with respect to the incident wave vector.

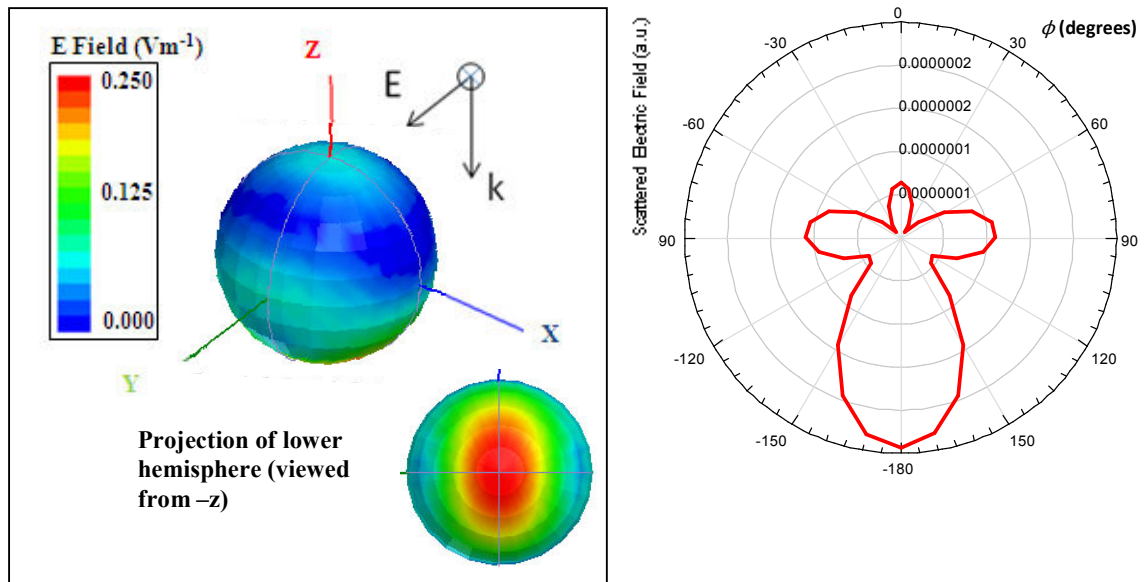


**Figure 4.17:** The scattered electric field distribution from a 200 nm diameter Ag sphere has been simulated using a FEM technique at the resonant frequency corresponding to the quadrupolar LSPR, and has been projected onto a spherical surface in the far field. A polar plot of the radiated field is shown on a polar plot as a function of the scattering angle  $\phi$  for a cross section through the YZ plane.

In order to further elucidate the origins of the apparent forward scattering behaviour, we now consider the effect of interference between the radiated fields associated with the dipolar and quadrupolar modes. As Figure 4.16 shows, the maximum associated with the quadrupolar mode at B is superimposed on a much broader feature arising from the dipolar contribution at A which is off-resonance at B. If it is assumed that an oscillating dipole emits spherical waves of the form shown in Equation 4.40, the spatial representation of the field distribution at  $t = 0$  will be that of diagram (a) in Figure 4.18. Here, the dipole is placed at the origin and oscillates in a plane which is perpendicular to the page. In the spatial field representations in Figure 4.18, the position of the dipole is represented by a solid black circle, however it should be noted that this is purely for illustration since it is assumed to be a point source. The red and blue colours correspond to regions of positive and negative amplitude of the electric field  $\mathbf{E}$  respectively, and the radiated fields from the dipole in forward and back scattering directions are in phase.

$$\psi = \frac{1}{r} (\cos (kr - \omega t)) \quad 4.40$$

Similarly, the quadrupolar term can be approximated as two dipoles which are separated by a distance  $\lambda/2$  along the y direction and oscillate out of phase. One dipole emits spherical waves of the form given by Equation 4.41, and the other that of Equation 4.42.

$$\psi = \frac{1}{r} (\cos (kr - \omega t + \pi/4)) \quad 4.41$$

$$\psi = \frac{1}{r} (\cos (kr - \omega t - \pi/4)) \quad 4.42$$

The field distribution of the two dipoles at  $t = 0$  is shown in diagram (b) in Figure 4.18, where the dipoles are separated by  $\lambda/2$  along the y direction and are arranged to be symmetrical about the origin. The quadrupolar term alone will give rise to both forward and back scattering, as would be expected from the earlier analysis of Equation 4.36. However, the important point to note is that the forward and back scattered waves are out of phase with respect to each other. The scattering response of the sphere at a given wavelength will be a superposition of contributions from both dipolar and quadrupolar excitations, and the resulting field distribution will involve a weighted sum of the two. For the purposes of a simple discussion, it will be assumed here that the intensities of the dipole and quadrupole radiated fields are equal, such that the two plots can be summed. In this instance the result is diagram (c) of Figure 4.18. It should be noted that this assumption may not necessarily be valid for all scenarios, a thorough analysis would require each contribution to be appropriately weighted by the  $b_2$  and  $c_2$  coefficients obtained from the rigorous solution of Laplace's equation. In the upper half plane, the dipole and quadrupole terms interfere destructively and there is little or no back scattering in the radiated fields. In contrast, the waves in the lower half plane interfere constructively, leading to strong forward scattering. The conclusion therefore is that in a large metallic nanoparticle the radiated fields of the quadrupolar mode (or any other higher order mode for that matter) cannot be observed in isolation. In order for metallic nanoparticle structures to be utilised in a new generation of liquid crystal display devices, a fundamental requirement is that they must exhibit a strong back scattering response at visible frequencies. The final part of this chapter contains an investigation into alternative

approaches which may be used to modify the scattering response, including placing nanoparticles in close proximity to each other such that electromagnetic coupling between particles may modify the LSPR.

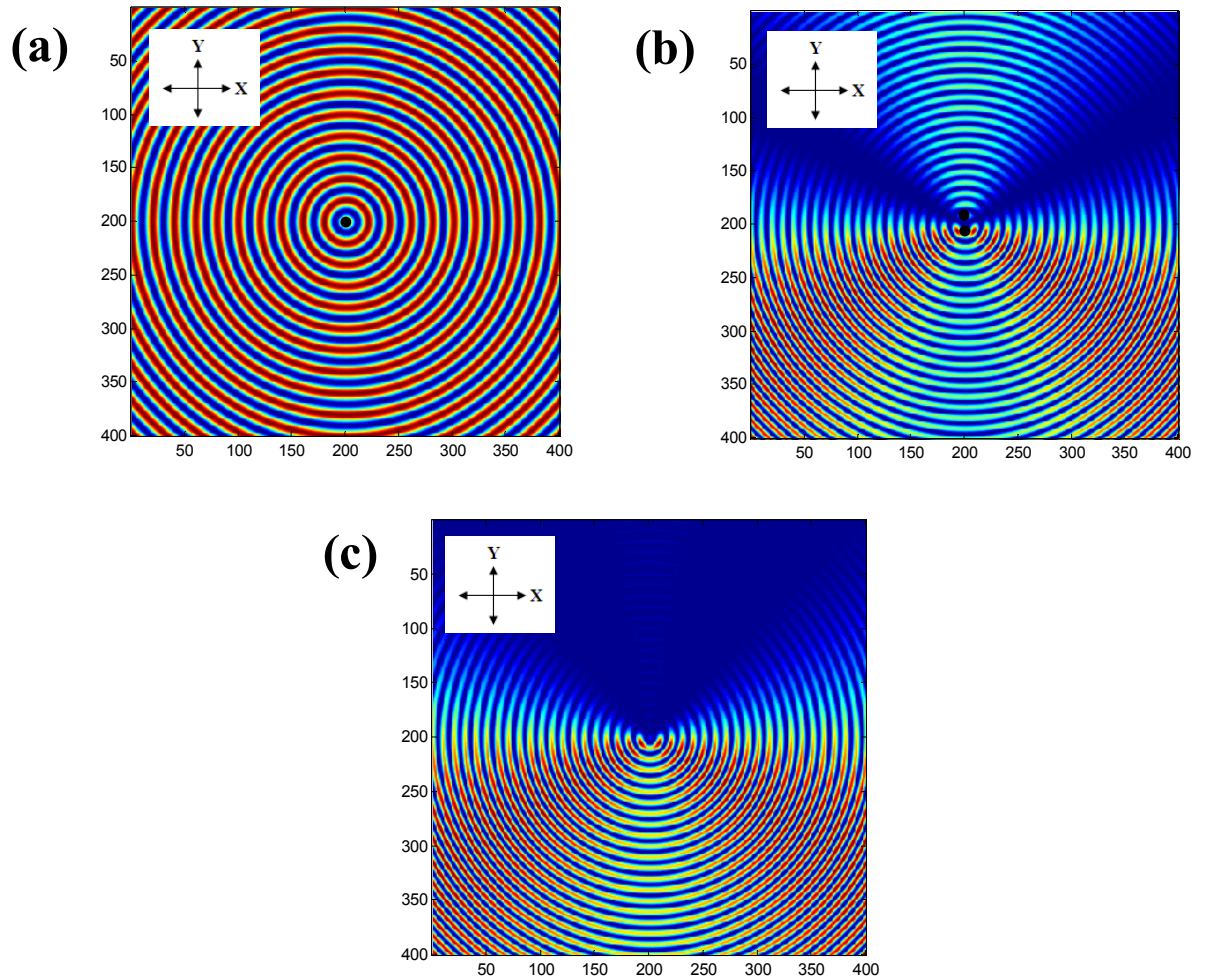


**Figure 4.18:** The instantaneous field distribution is shown for a point dipole emitting a spherical wave (a), two point dipoles separated by  $\lambda/2$  (along the y direction) emitting spherical waves which are out of phase by  $\pi$  radians (b), and (c) the sum of (a) and (b).

#### 4.6 Arrangements of nanorods

It has been shown by Grigorenko et al. using closely spaced pairs of tapered nanorods that the interaction between particles introduces a splitting of the single particle LSPR into symmetric and anti-symmetric branches<sup>18</sup>. Giessen et al. have since made similar observations for pairs of stacked cylindrical discs<sup>20</sup>. At the frequency of the symmetric

resonance, the electrons in neighbouring particles move in phase, behaving as an oscillating dipole. However at the anti-symmetric resonance the electrons in neighbouring particles are out of phase such that the oscillating dipoles cancel. The response of the structure is determined by the oscillating dipole which is induced by the incident magnetic field, and the oscillating quadrupole which is induced by the incident electric field<sup>18</sup>. A diagram of the field and charge distributions associated with the symmetric and antisymmetric modes is shown in Figure 4.15. The response of the anti-symmetric branch of the coupled LSPR has particular relevance in the design of electromagnetic metamaterials<sup>21-24</sup>, however as has been discussed previously, the radiated field associated with the quadrupole response is also important for display applications. It can be shown that the response of a single Ag nanorod may be modified by placing additional nanorods at distances 20 nm above and below it. At these small separations, the coupling between particles is facilitated by the overlap of the electromagnetic fields which emanate from the ends of the rods in the regions between the particles<sup>25</sup>.

First consider the response of a single Ag nanorod having dimensions 80 nm length, 30 nm width and 25 nm height respectively, which is illuminated in the configuration shown in (a). The angle of incidence  $\theta$  is varied from 0 to 90 degrees in 15 degree increments with the incident electric field is polarised in the plane of angular variation. Graph (b) of Figure 4.19 shows the scattering efficiency plotted as a function of wavelength. For illumination at normal incidence (0 degrees), the electric field is polarised parallel to the long axis of the rod, whilst for an incident angle of 90 degrees the electric field is polarised parallel to the short axis. The maxima at 575 nm are attributed to excitation of the dipolar LSPR which is associated with the long axis, as discussed in Section 4.3. In graph (c) of Figure 4.19, the magnitude of the scattering efficiency maxima are plotted as a function of incident angle  $\theta$  and are compared against a normalised  $\cos^2\theta$  function. There is reasonable agreement between the two curves, as would be expected for small particles whose response can be approximated using the electrostatic polarisability expression in Equation 4.30.

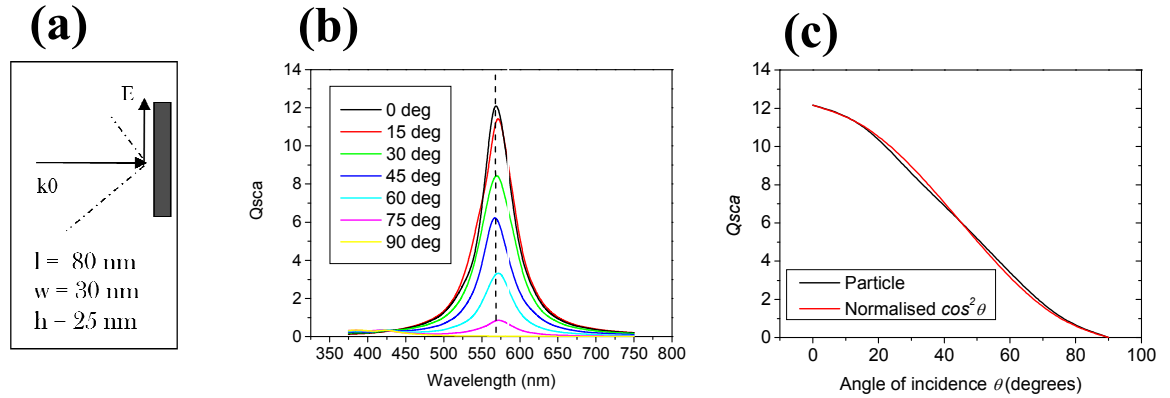


**Figure 4.19:** A FEM technique is used to simulate the optical response of an Ag nanorod in vacuum having dimensions length 80 nm, width 30 nm and height 25 nm respectively. The rod is illuminated in the configuration shown in (a). The angle of incidence  $\theta$  is varied from 0 to 90 degrees in 15 degree increments, and the scattering efficiency is plotted as a function of wavelength in (b). In (c) the magnitude of the  $Q_{sca}$  maxima at 575 nm are plotted as a function of incident angle  $\theta$  and are shown against a normalised  $\cos^2 \theta$  function.

In an arrangement of three metallic rods which are separated by a few tens of nm, it is known that the LSPR frequencies of the individual rods are reduced by near field electromagnetic coupling between particles<sup>11</sup>. Pinchuk et al.<sup>26</sup> have previously investigated the response of linear chains formed from Ag spheroids, in which the resonant frequencies were derived for spheroids located at different positions along the chain. For three identical spheroids, it was found that the two outer spheroids exhibited equal resonant frequencies, whilst that of the centre spheroid occurred at a frequency which was slightly reduced in comparison to the outer spheroids. The difference in resonant frequencies was attributed to the variable strength of near-field electromagnetic coupling along the chain. Here, we apply a similar principle using a linear chain of three metallic rods (Figure 4.20). In this structure, it is shown that the two outer rods are influenced by electromagnetic fields from one nearest neighbour (the centre rod), whilst the centre rod is influenced by electromagnetic fields from two nearest neighbours (the two outer rods). This is particularly significant, since the frequency of the scattered radiation at the LSPR frequency is generated in proportion to the dipole moment which is induced by the incident electromagnetic field. In Figure 4.20 the red arrows represent the direction of the induced dipole moment across the particles, whilst the blue arrows represent the direction of the induced dipole moment between particles. Note that in this particle configuration, the

induced and near-field contributions oppose each other. This leads to a reduction in the restoring force associated with the induced charges, and a decrease in the resonant frequency of the LSPR.

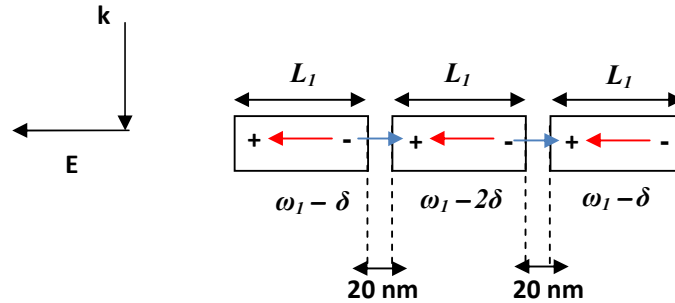


**Figure 4.20:** Diagram showing three identical metallic rods separated by 20 nm in a linear chain, the resonant frequencies are shown below each rod. The red arrows represent the direction of the induced dipole moment across the particles, whilst the blue arrows represent the direction of the induced dipole moment between particles. In the left of the figure, the direction of the incident wave vector and the polarisation of the incident electric field are shown.

Here  $\omega_1$  represents the resonant frequency of a single rod having length  $L_1$ , and  $\delta$  is the perturbation of the resonant frequency of a single rod due to near field electromagnetic coupling. Although the three rods are identical, assuming the magnitude of  $\delta$  is equal along the chain, Figure 4.20 shows that at normal incidence this structure should exhibit two resonant frequencies. One frequency is associated with the LSPR of the two outer rods, equal to  $\omega_1 - \delta$ , and another frequency of  $\omega_1 - 2\delta$  is associated with the LSPR of the centre rod. These interactions are of particular importance in the design of particle structures which may be utilised in display applications. The optical response of the structure in Figure 4.20 is governed by the magnitude of the electric field enhancement at the ends of the rods, and the separation between them<sup>26</sup>. At illumination angles away from normal incidence, the magnitude of the field enhancement at the end of the rods decreases, leading to a reduction in  $\delta$ . As the value of  $\delta$  approaches zero, the individual resonances of the rods will be recovered ( $\omega_1$ ). From a display perspective this does not constitute the ideal spectral response, since as the illumination angle is increased, two maxima (at frequencies  $\omega_1 - 2\delta$  and  $\omega_1 - \delta$ ) will merge to form a single maximum at frequency  $\omega_1$ . This is unlikely to yield a scattering response with high contrast.

However, the inverse response may be of benefit, i.e. if a single maximum occurring at normal incidence were to separate into two maxima having different resonant frequencies as the illumination angle is increased. This can be achieved by reducing the length of the centre rod. Consider the arrangement in Figure 4.21, where the outer and centre rods have lengths  $L_1$  and  $L_2$  and resonant frequencies  $\omega_2$  and  $\omega_1$  respectively. From the polarisability expression previously derived in Equation 4.30, it can be shown that for incident radiation which has the electric field polarised along the long axis of the rod, the LSPR frequency increases as the length of the rod is decreased (i.e.  $\omega$  and  $L$  are inversely proportional). Since  $L_2 < L_1$ , the resonant frequencies of the single rods follow the relationship  $\omega_2 > \omega_1$ .

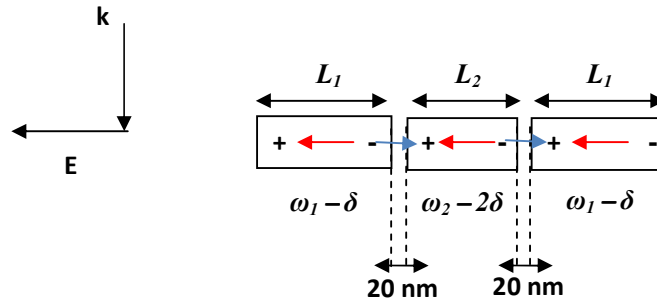


**Figure 4.21:** Diagram showing three metallic rods separated by 20 nm in a linear arrangement, the resonant frequencies are shown below each rod. The outer rods have length  $L_1$  and the centre rod has length  $L_2$ . The red arrows represent the direction of the induced dipole moment across the particles, whilst the blue arrows represent the direction of the induced dipole moment between particle. In the left of the figure, the direction of the incident wave vector and the polarisation direction of the incident electric field are shown.

As demonstrated for the triple rod arrangement in Figure 4.20, the near field electromagnetic coupling between rods leads to a red shift in the LSPR frequencies, this additional shift is again denoted by  $\delta$ . For a suitable optimisation of  $L_2$ , it is possible that all rods in the chain may exhibit a single resonant frequency at normal incidence. This requires the condition that:

$$\omega_1 - \delta = \omega_2 - 2\delta \quad 4.43$$

**i.e.**  $\omega_2 - \omega_1 = \delta \quad 4.44$

When the difference between  $\omega_2$  and  $\omega_1$  is equal to the red-shift in frequency arising from near-field electromagnetic coupling, a single resonant frequency is observed. At illumination angles away from normal incidence, the strength of electromagnetic coupling is reduced, and the optical response exhibits two resonant frequencies ( $\omega_1$  and  $\omega_2$ ). Using FEM simulations, it is possible to demonstrate these interactions by computing the scattering response of an arrangement of three Ag rods. In the simulation, the outer rods have length 80 nm, whilst the centre rod has length 60 nm. The heights and widths of all rods in the simulation were 25 nm and 30 nm respectively, as shown in inset (a) of Figure 4.22. In inset (b) of Figure 4.22, the scattering efficiency ( $Q_{sca}$ ) is plotted for illumination angles ranging between 0 and 90 degrees for light which is polarised in the plane of angular variation. As expected from the earlier analysis, the structure exhibits a single maximum in scattering efficiency at normal incidence, and as the incident angle is increased two maxima are evident. The distribution of the scattering intensity in inset (c) of Figure 4.22 is significantly narrower than a  $\cos^2\theta$  functional dependence. Figure 4.23 shows the time-averaged electric field distribution at the resonant frequency for a cross section taken through the centre of the structure. There is a significant overlap of the enhanced electric field from adjacent rods, particularly in the vacuum regions between the particles, providing further evidence of electromagnetic coupling between particles.

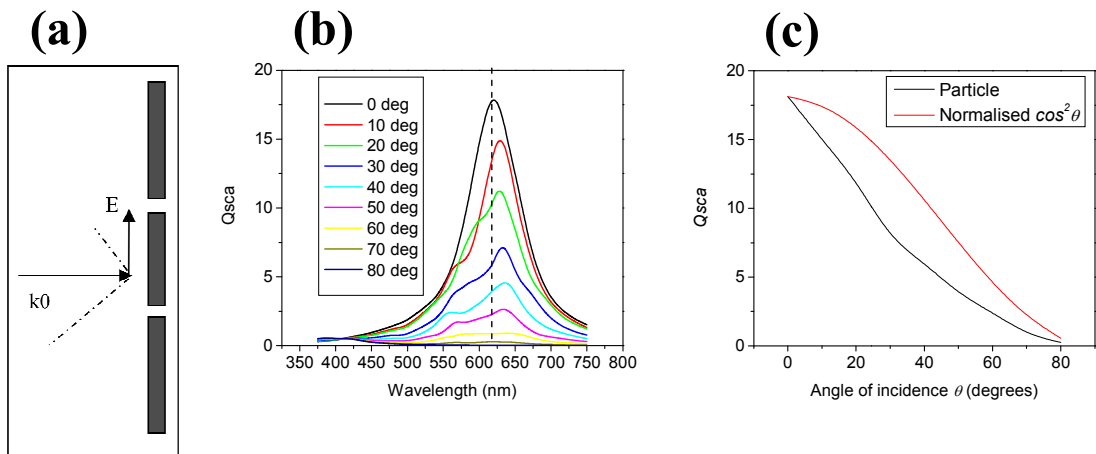


**Figure 4.22:** A FEM technique is used to simulate the optical response of three Ag nanorods in vacuum. The central rod has length 60 nm, width 30 nm and height 25 nm. The upper and lower rods have length 80 nm, width 30 nm and height 25 nm. The rods are separated by 20 nm and are illuminated in the configuration shown in (a). The angle of incidence  $\theta$  is varied from 0 to 90 degrees, and the scattering efficiency is plotted as a

function of wavelength in (b). In (c) the magnitude of the  $Q_{sca}$  maxima at 615 nm are plotted as a function of incident angle and are shown against a normalised  $\cos^2 \theta$  function.

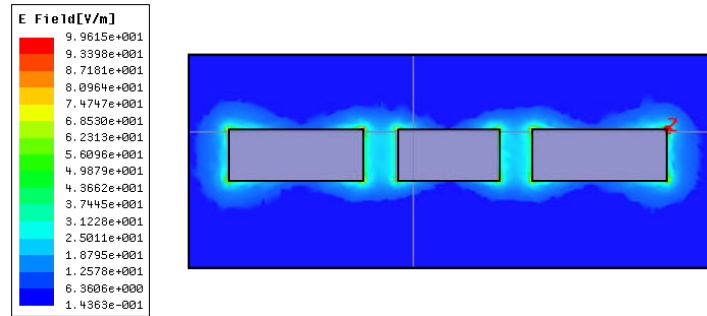


**Figure 4.23:** The time-averaged electric field distribution is shown for a cross section through the centre of the rods, which is shown for a plane lying perpendicular to the incident wave vector.

The incident angle  $\theta$  response exhibited by the triple rod arrangement in Figure 4.22 is promising for display requirements. One of the fundamental aims of the project is to identify structures exhibiting an incident angle response which is steeper than the  $\cos^2 \theta$  dependence of small metallic nanoparticles (having dimensions  $\ll \lambda$ ). In order to quantitatively describe the angular response, the scattering efficiency ( $Q_{sca}$ ) values in Figure 4.22 may be plotted as a function of incident angle, and subsequently fitted using a  $\cos^n$  functional form (where  $n$  is the fitted parameter) for each wavelength. In Figure 4.24 the function  $f(\theta) = \cos^n \theta$  is plotted as function of incident angle, where  $n$  is varied from 2.0 to 6.0, and  $\theta$  is varied from  $0^\circ$  to  $90^\circ$ . As the value of  $n$  is increased, the gradient of  $f(\theta)$  at  $f(\theta) = 0.5$  increases, whilst the range of angles which are covered by the minimum scattering phase also increases. To illustrate, when  $n = 2.0$ ,  $f(\theta) \approx 0$  for incident angles between  $80^\circ$  and  $90^\circ$ , however when  $n = 6.0$ ,  $f(\theta) \approx 0$  for incident angles between  $60^\circ$  and  $90^\circ$ . In Figure 4.25, the values of  $\theta$  at  $f(\theta) = 0.5$  (inset a) and the gradient of  $f(\theta)$  at  $f(\theta) = 0.5$  (inset b) are shown for  $n = 2.0$  to  $n = 6.0$ , where it may be observed that the gradient of  $f(\theta)$  has increased by a factor of approximately 1.5 across this range.

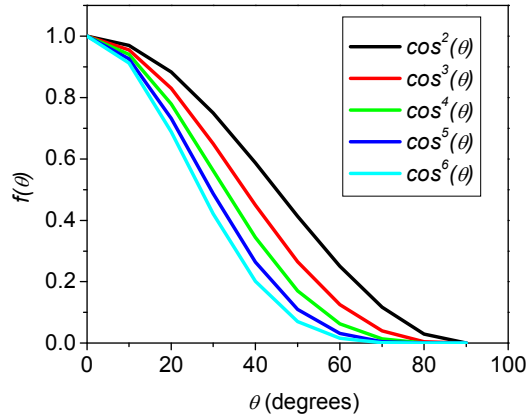


**Figure 4.24:** Several  $\cos^n \theta$  functions are plotted as a function of  $\theta$ , where  $n$  is varied from 2.0 to 6.0 and  $\theta$  is varied from  $0^\circ$  to  $90^\circ$ .

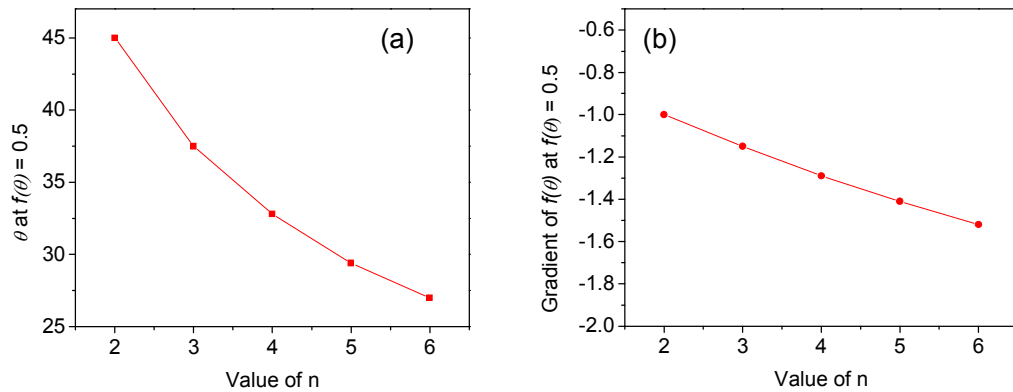


**Figure 4.25:** The values of  $\theta$  at  $f(\theta) = 0.5$  (a) and the gradient of  $f(\theta)$  at  $f(\theta) = 0.5$  (b) are plotted as function of  $n$ .

Metallic nanoparticles which are hosted within a liquid crystal display device may be subjected to a range of illumination and orientation angles. In order for the scattering response to exhibit a high contrast between the regimes of maximum and minimum scattering intensity, the gradient of the incident angle response should be as large as possible. As discussed in the introduction to Section 4.5, the ideal transition would resemble an almost step-like function, such that a change in incident angle of  $0^\circ - 1^\circ$  is sufficient to completely switch the scattering intensity response from being maximal to minimal. In order to demonstrate the suitability of the  $\cos^n \theta$  fitting procedure, it is first applied to the scattering data obtained for the single Ag rod in Figure 4.19. In inset (a) of Figure 4.26 the scattering efficiency ( $Q_{sca}$ ) is plotted as a function of incident angle and wavelength. The  $Q_{sca}$  enhancement which is observed for incident wavelengths at

approximately 575 nm corresponds to excitation of the dipolar LSPR. In order to fit a  $\cos^n\theta$  function to the angular response, the scattering efficiency ( $Q_{sca}$ ) is plotted as a function of incident angle, for each wavelength in the simulation. This creates a large number of plots (typically 100) which are similar to those shown in inset (c) of Figure 4.22. A macro is then executed which normalises the scattering efficiency curves and fits the values to a suitable  $\cos^n\theta$  function. The fitting routine was performed using commercial Origin software which utilises an algorithm based upon a singular value decomposition technique<sup>27</sup>. Following the execution of the macro, the fitted values of  $n$  are extracted as a tabulated dataset and are plotted as a function of incident wavelength, shown in inset (b) of Figure 4.26.

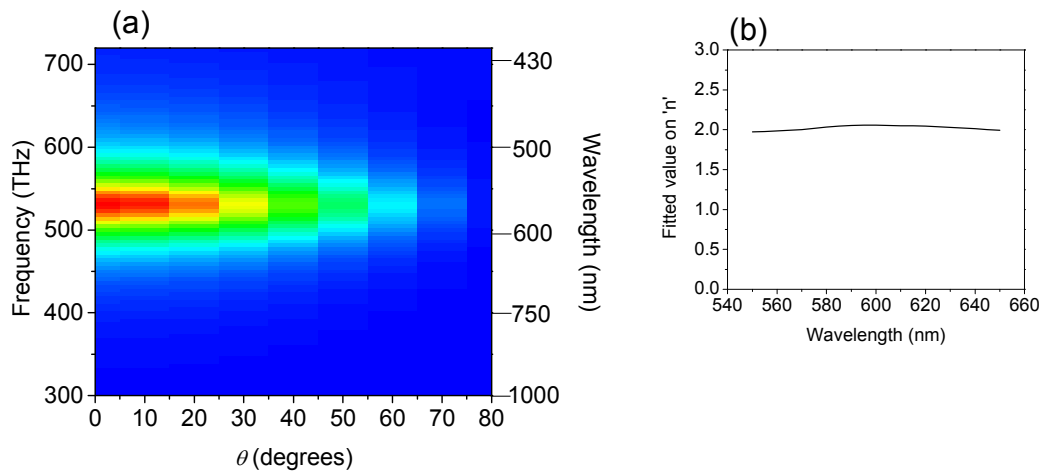


**Figure 4.26:** In (a), the scattering efficiency of a single Ag rod (80 nm length, 30 nm width, 25 nm height) is plotted as a function of incident angle  $\theta$  and wavelength. At each wavelength, the angular response is fitted to a  $\cos^n\theta$  function, and in (b) the fitted value of  $n$  is plotted as a function of incident wavelength.

For incident wavelengths between 550 nm and 650 nm, the fitted value of  $n$  falls within the range 1.98 to 2.02. This is in good agreement with the expected scattering response for a small metallic nanoparticle which may be described using the electrostatic approximation (shown previously in Figure 4.13), and the scattering intensity follows a  $\cos^2\theta$  dependence with respect to incident angle. It is only possible to fit wavelengths which are centred about the LSPR wavelength using this procedure, since outside this range the structure is off-resonance and the scattering intensity is weak. The numerical errors due to rounding and the finite resolution of the simulation are significant for weak scattering intensities, this introduces numerical noise which may reduce the accuracy of the fitted parameters. In inset (a) of Figure 4.27, the scattering efficiency ( $Q_{sca}$ ) is plotted as a function of incident

angle and wavelength for the triple Ag rod structure in Figure 4.22, and in (b) the fitted values are plotted as a function of the incident wavelength. The dashed line represents the spectral position of the single scattering efficiency maximum which is observed at normal incidence. The scattering response at 615 nm may be fitted using a  $\cos^{5.01}\theta$  functional form, this appears to be in agreement with the angular response data in inset (c) of Figure 4.22, where it was previously shown that the angular response at 615 nm was significantly narrower than a  $\cos^2\theta$  functional dependence.

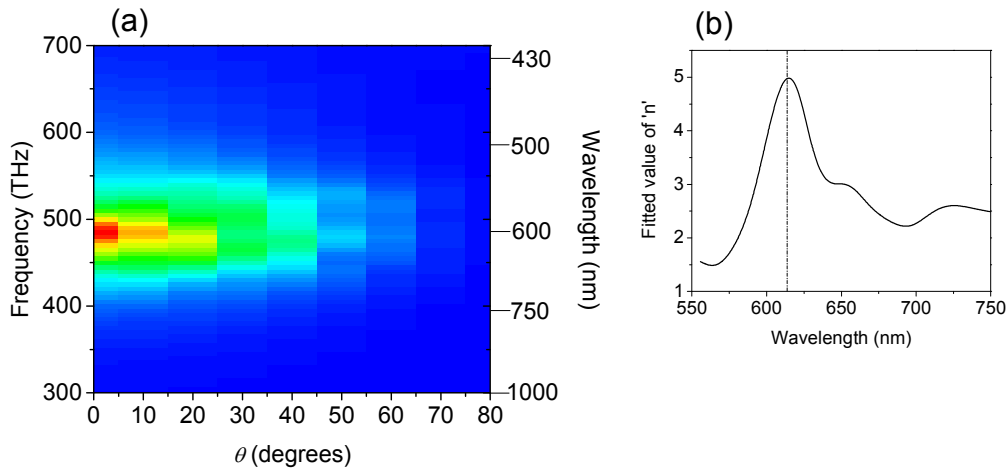


**Figure 4.27:** In (a), the scattering efficiency of an arrangement of three Ag rods (from Figure 4.22) is plotted as a function of incident angle  $\theta$  and wavelength. At each wavelength, the angular response is fitted to a  $\cos^n\theta$  function, and in (b) the fitted value of  $n$  is plotted as a function of incident wavelength. The dashed line represents the spectral position of the single scattering efficiency maximum which is observed at normal incidence.

The scattering response of the 200 nm diameter Ag sphere which was previously shown in Figure 4.17 was understood by considering the interference between the radiated fields arising from dipolar and quadrupolar excitations. In the upper half plane, it was shown that the radiated fields associated with the dipole and quadrupole LSPRs interfere destructively such that is negligible back scattering from the structure. In order to be of use in display applications, the triple rod arrangement must scatter a significant proportion of the illuminating radiation towards the observer. In Figure 4.28, the far field radiation pattern of the triple rod arrangement in Figure 4.22 is shown at the resonant wavelength (projected onto a spherical surface) for light which is incident at normal incidence. A polar

plot of the radiated field is shown for a cross section through the XZ plane, and the electric field intensity has been plotted as a function of scattering angle  $\phi$ . The intensity profile shows equal intensities of forward and back scattered radiation, exhibiting a number of similarities with that of the dipolar field distribution for a single Ag disc in Figure 4.14. This response is extremely promising in terms of the display criteria, and a possible area for future study could include the optimisation of the structure such that forward scattered radiation is minimised and the back-scattered radiation preferentially enhanced.

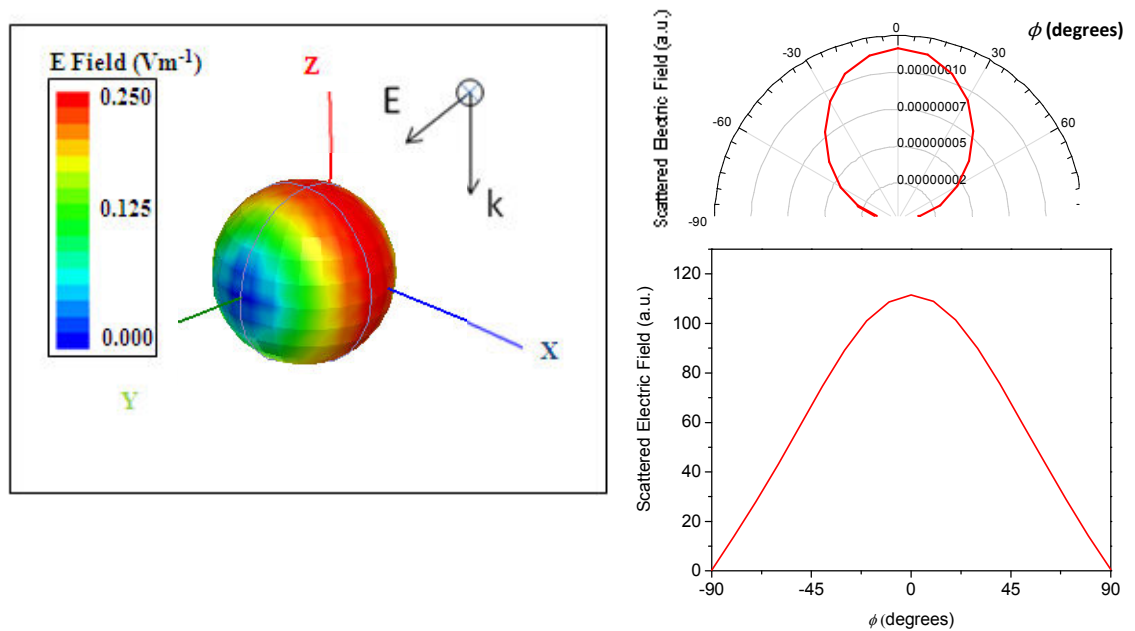


**Figure 4.28:** The scattered electric field distribution for the arrangement of three Ag rods in Figure 4.22 has been simulated using a FEM technique and has been projected onto a spherical surface in the far field. A polar plot of the radiated field in the upper half space is shown for a cross section through the YZ plane. The electric field intensity has been plotted as a function the scattering angle  $\phi$ .

#### 4.7 Concluding remarks and implications for the remainder of the thesis

This chapter contains an investigation into a number of approaches used to modify the scattering response of metallic nanoparticles, in terms of both the incident angle  $\theta$  response and the distribution of the scattered field  $\phi$ . A synopsis of the conclusions is given in Table 4.1, but is also summarised briefly here. In one approach, the size of the particles was increased such that higher order multipolar modes were excited. This proved to be the least effective option, since the incident angle response was considerably

broadened in comparison to a small metallic nanoparticle, and the scattering response was primarily in the forward direction. The alternative approach considered placing several particles in close proximity, a regime in which near-field electromagnetic coupling can modify the properties of the LSPR. In this arrangement, the optical response is highly sensitive to the effects of near-field electromagnetic coupling between adjacent rods. With a suitable optimisation of particle geometry, it has been shown that it is possible to modify both the incident angle and scattering angle response significantly in comparison to the  $\cos^2\theta$  and  $\cos^2\phi$  dependence which is predicted for small particles described by the electrostatic approximation. These findings have particular relevance in the development of new generations of liquid crystal displays, where we have shown that the angular response may be fitted using a much steeper  $\cos^5\theta$  functional form, and suggests that this is a promising area in which to conduct further research.

Whilst investigations throughout this chapter have shown that the properties of the LSPR may be modified by near-field interactions between two or more particles, electromagnetic coupling is also observed in regular arrays of nanoparticles. Here, in addition to near-field coupling, interactions which are associated with the regular lattice spacing of the array may also occur. Chapter 5 presents experimental and simulated studies of the optical response of periodic nanoparticle arrays, and contains an extensive discussion regarding the various regimes of particle interactions. The electromagnetic coupling between particles in periodic arrays is also particularly significant in the studies of negative index metamaterials which are presented in Chapter 8. When particle arrays are stacked vertically, it is shown that plasmon hybridization similar to that of single particles in Section 4.5 may be observed, and the metamaterial structure exhibits an effective magnetic permeability at the resonant frequency of the anti-symmetric coupled LSPR.

<b>Structure</b>	<b>How does the scattering intensity vary as a function of the incident angle (<math>\theta</math>)?</b>	<b>How does the scattering intensity vary as a function of scattering angle (<math>\phi</math>)?</b>
<b>Small discs (size <math>\ll \lambda</math>)</b>	The intensity response follows a $\cos^2\theta$ dependence as predicted by the electrostatic approximation.	The intensity response follows a $\cos^2\phi$ dependence as predicted by the electrostatic approximation.
<b>Large discs (size <math>\approx \lambda</math>)</b>	The intensity response is broader than $\cos^2\theta$ , due to the interference between the radiated fields from quadrupolar and dipole resonances	The intensity response is narrower than a $\cos^2\phi$ function (it is proportional to $\cos^2\phi\sin^2\phi$ ). However it may be solely forward scattering, there is no back scattering if there is destructive interference between the radiated fields from quadrupolar and dipolar resonances.
<b>Clusters of rods (individual rod size <math>\ll \lambda</math>)</b>	The intensity response is narrower than $\cos^2\theta$ due to near field interactions between rods modifying the response of the single particle LSPR.	The intensity response is slightly narrower than $\cos^2\phi$ and is equal in intensity for the forward and back scattering directions.

**Table 4.1:** A summary of the angular response characteristics evaluating the behaviour of the scattering intensity as a function of the incident ( $\theta$ ) and scattering angle ( $\phi$ ).

### The optical response of metallic nanoparticles arranged in periodic arrays

#### 5.1 Introduction

Chapter 4 contained an investigation into the optical response of single metallic particles and arrangements of a few metallic particles separated by tens of nm. It was shown that a single particle exhibited a LSPR which was dependent on the size and shape of the particle, in addition to its permittivity and that of the surrounding medium. In arrangements of two or more particles, the properties of the LSPR were also be modified by near-field interactions. Furthermore, it was shown that the optical response of the structures could be well characterised using a dark-field spectroscopy technique. Bright-field spectroscopy is not suitable for the characterisation of single particles, since the scattered light has a much smaller intensity than that which is directly transmitted. However, when nanoparticles are arranged into regular arrays (such as a square lattice) with a greater cross sectional area, a significant proportion of the incident light may be scattered or absorbed. It is then possible to use bright-field spectroscopy to determine the extinction of the arrays. In regular arrays of particles, there are a number of regimes in which interactions between particles may occur. For example, when the periodicity of the array is sufficiently small (when the separation between the edges of particles in adjacent unit cells is a few tens of nm), near field interactions can decrease the dipolar restoring force that is experienced by electrons within individual particles, and red-shift the LSPR to lower frequencies<sup>1-3</sup>. Conversely, in arrays where the periodicity is comparable to the incident wavelength, light may be diffracted at frequencies in the vicinity of the LSPR, and there is the possibility for coherent electromagnetic field interactions. Light that is scattered so as to propagate in the plane of the particles will undergo multiple scattering from the regularly spaced metallic particles. It has been shown by Augu   et al. that a dramatic enhancement in optical extinction may be observed when the wavelength of the scattered light is in the same spectral region as the LSPR<sup>4</sup>. Regular arrays of nanoparticles have been utilised extensively for a number of applications including optical waveguides<sup>5-8</sup>, biosensing<sup>9-11</sup> and surface enhanced Raman spectroscopy (SERS)<sup>12</sup>.

This chapter contains a derivation of the electromagnetic response of regular arrays of particles through a treatment based on the modification of the single particle response.

This will subsequently be used to determine the extinction of the array structures. Experimental extinction spectra obtained from structures fabricated by electron beam lithography will be compared with model data which has been simulated using a finite element method. The sensitivity of the optical response to changes in particle size and the surrounding refractive index will be explored, and the regimes of particle interactions will also be studied in closer detail.

## 5.2 Modification of the single particle response in regular arrays

The polarisability of an ellipsoid has been previously derived for the case of illumination at normal incidence with the electric field polarised along each of its principal axes. Recall from Chapter 3 that the  $L_i$  terms are geometrical shape factors that depend on the relative lengths of the semi-axes of the ellipsoid  $a, b, c$  (Equation 5.1) and  $\varepsilon_1, \varepsilon_2$  are the permittivities of the particle and the surrounding medium respectively.

$$\alpha_i = 4\pi abc \frac{\varepsilon_1 - \varepsilon_2}{3\varepsilon_2 + 3L_i(\varepsilon_1 - \varepsilon_2)} \quad 5.1$$

The polarisability in Equation 5.1 is valid for a single particle which obeys the electrostatic approximation, requiring that  $a, b, c \ll \lambda$ . When the particle is illuminated with an electromagnetic wave, the oscillation of charges across it causes a scattered wave to be re-radiated in proportion to the induced dipole moment. In an array of particles, the net field experienced by each individual particle is the sum of the incident field in addition to the scattered field from neighbouring particles. If it is assumed that the dimensions of the particles are significantly smaller than the incident wavelength, the coupled dipole approximation may be used to determine the scattering response. Recall from Chapter 3 (Section 3.4) that the net field at each dipole is the sum of the incident field, plus the radiation which is scattered by neighbouring dipoles. The field radiated by a dipole located at the origin may be approximated by:

$$\mathbf{E}_{\text{dipole}} = \frac{e \frac{i\omega d}{c}}{4\pi\varepsilon_0} \left[ \frac{\omega^2}{c^2 d} \hat{\mathbf{r}} \wedge \mathbf{p} \wedge \hat{\mathbf{r}} + \left( \frac{1}{d^3} - \frac{i\omega}{cd^2} \right) [3(\hat{\mathbf{r}} \cdot \mathbf{p})\hat{\mathbf{r}} - \mathbf{p}] \right] \quad 5.2$$

Here  $\hat{\mathbf{r}}$  is unit vector associated with a vector  $\mathbf{r}$  which is taken from the origin to the point at which the field is sampled (having magnitude  $d$ ),  $\mathbf{p}$  is the vector associated with the induced dipole moment,  $\omega$  is the angular frequency of the scattered radiation and  $\varepsilon_0$  is the permittivity of free space. In solving for the scattering characteristics of the continuous

distribution, each particle in the array has an induced dipole  $\mathbf{p}_i = \alpha_i \mathbf{E}_{\text{local}}$ , where  $\mathbf{E}_{\text{local}}$  is the electric field at  $\mathbf{r}_i$  due to the incident wave ( $\mathbf{E}_{\text{inc},i}$ ), plus a contribution  $\mathbf{E}_j$  from all other induced dipoles  $\mathbf{p}_j$ , given in Equation 5.3<sup>13</sup>. The interaction matrix ( $\mathbf{A}_{ij}$ ) characterises the sum of the retarded fields from all other dipoles, hence the summation in Equation 5.3 is performed over all  $j$ , with the exception of  $i = j$ .

$$\mathbf{E}_{\text{local}} = \mathbf{E}_{\text{inc},i} - \sum_{\substack{j=1 \\ i \neq j}}^N \mathbf{A}_{ij} \mathbf{p}_j \quad 5.3$$

$$\mathbf{A}_{ij} \mathbf{p}_j = k^2 e^{ikr_{ij}} \left( \frac{\hat{\mathbf{p}}_j \left( \mathbf{r}_{ij} \wedge \left( \mathbf{r}_{ij} \wedge \mathbf{p}_j \right) \right)}{r_{ij}^3} \right) + e^{ikr_{ij}} (1 - ikr_{ij}) \left( \frac{r_{ij}^2 \mathbf{p}_j - 3\hat{\mathbf{p}}_j \left( \mathbf{r}_{ij} \cdot \mathbf{p}_j \right)}{r_{ij}^5} \right)$$

where  $i = 1, 2, \dots, N$ ,  $j = 1, 2, \dots, N$  and  $i \neq j$ . 5.4

In Equation 5.4,  $\mathbf{r}_{ij}$  and  $\mathbf{p}_j$  represent the positions and induced dipoles of each particle within the array respectively. The  $\hat{\mathbf{p}}_j$  terms represent the projection along the unit vector of the dipole moment  $\mathbf{p}_j$ . For an infinite array of dipoles, it has been shown by Schatz et al.<sup>13</sup> that it is possible to generate an analytical solution to Equation 5.3 when the incident wave vector is perpendicular to the plane of the array by assuming that the induced polarisation in each array element is the same. Schatz et al. showed that the polarisation of each particle is given by:

$$\mathbf{P} = \frac{\alpha \mathbf{E}_{\text{inc}}}{1 - \alpha S} \quad 5.5$$

Here,  $\mathbf{E}_{\text{inc}}$  represents the incident electric field vector,  $\alpha$  is the polarisability of the particle (which for small particles is given by the electrostatic approximation in Equation 5.1), and  $S$  is the array factor which represents the contribution from neighbouring particles. The array factor is equal to the summation term (including the minus sign) given in Equation 5.3. Often in the literature, the polarisation of each particle is expressed in terms of an effective polarisability  $\alpha^*$ :

$$\mathbf{P} = \alpha^* \mathbf{E}_{\text{inc}} \quad 5.6$$

$$\alpha^* = \frac{1}{\frac{1}{\alpha} - S} \quad 5.7$$

Consider an individual dipole  $i$ , which is positioned within an infinite square array of dipoles  $j$ , as shown in Figure 5.1. When the array is illuminated at normal incidence, all dipoles are aligned in the same direction. For simplicity it is assumed that each dipole has a unit dipole moment  $\mathbf{p}_i, \mathbf{p}_j = 1$ .

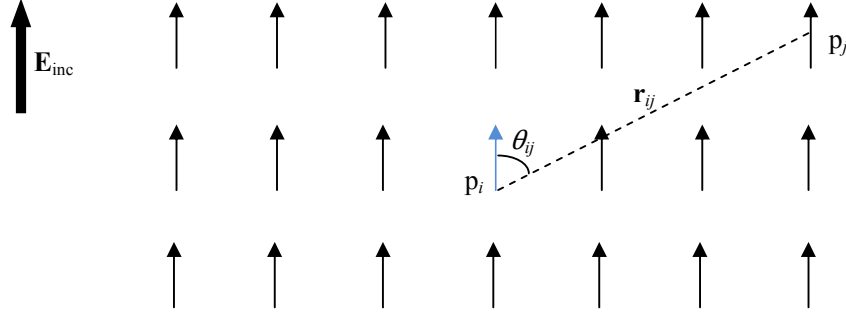


**Figure 5.1:** An individual dipole  $i$  is positioned within an infinite square array of identical dipoles  $j$ . The local electric field at the origin is a sum of the incident electric field plus the retarded fields from all other dipoles.

To calculate the array factor for the structure in Figure 5.1, we refer to Equation 5.4 and note that the scalar and vector products may be simplified. Since it is assumed that  $\mathbf{p}_j$  is equal to unity, this term vanishes from the solution.

$$\mathbf{r}_{ij} \wedge (\mathbf{r}_{ij} \wedge \mathbf{p}_j) = -r_{ij}^2 \sin \theta_{ij} \quad 5.8$$

$$\mathbf{r}_{ij} (\mathbf{r}_{ij} \cdot \mathbf{p}_j) = r_{ij}^2 \cos \theta_{ij} \quad 5.9$$

Here  $\theta_{ij}$  represents the angle between  $\mathbf{r}_{ij}$  and the polarization direction of the induced dipole  $\mathbf{p}_j$ . However the terms in Equation 5.4 refer to the projection of the scalar and vector products along the unit dipole moment vector  $\hat{\mathbf{p}}_j$ . This introduces an additional  $\sin \theta_{ij}$  term into Equation 5.8 and an additional  $\cos \theta_{ij}$  term into Equation 5.9, such that:

$$\hat{\mathbf{p}}_j \left( \mathbf{r}_{ij} \wedge (\mathbf{r}_{ij} \wedge \mathbf{p}_j) \right) = -r_{ij}^2 \sin^2 \theta_{ij} \quad 5.10$$

$$\hat{\mathbf{p}}_j \left( \mathbf{r}_{ij} (\mathbf{r}_{ij} \cdot \mathbf{p}_j) \right) = r_{ij}^2 \cos^2 \theta_{ij} \quad 5.11$$

Substituting Equations 5.10 – 5.11 into the expression for the array factor yields:

$$S = - \sum_{dipoles} k^2 e^{ikr_{ij}} \left( \frac{-r_{ij}^2 \sin^2 \theta_{ij}}{r_{ij}^3} \right) + e^{ikr_{ij}} (1 - ikr_{ij}) \left( \frac{[r_{ij}^2 - 3r_{ij}^2 \cos^2 \theta_{ij}]}{r_{ij}^5} \right) \quad 5.12$$

This can be simplified to the expression which is often found in the literature (Equation 5.13).

$$S = e^{ikr_{ij}} \sum_{dipoles} \left( \frac{k^2 \sin^2 \theta_{ij}}{r_{ij}} \right) + \left( \frac{(1 - ikr_{ij})(3 \cos^2 \theta - 1)}{r_{ij}^3} \right) \quad 5.13$$

Once the interactions from adjacent particles have been considered, the scattered field distributions and optical cross sections are computed in an identical manner to the DDA simulation technique in Chapter 3. Whilst here the interactions between particles have been described through an effective polarisability which is derived from the coupled dipole approximation, other mesh-based simulation techniques such as FEM and FDTD (in which the electric and magnetic fields are directly solved in matrix form) use a different approach. In FEM and FDTD simulation techniques, periodic boundary conditions are imposed which require that the magnitude and direction of the fields at a point on an assigned boundary must exactly match the fields at a corresponding point on a second assigned boundary. These boundary pairs (termed ‘Master’ and ‘Slave’ respectively) are assigned to planar surfaces at the edge of the unit cell <sup>14</sup>. Figure 5.2 shows the configuration which is used in Ansoft HFSS (a commercial finite element package) to simulate an infinite square array of metallic cylinders. Notice the two pairs of Master / Slave boundaries which impose periodic boundary conditions along both the  $x$  and  $y$  directions.

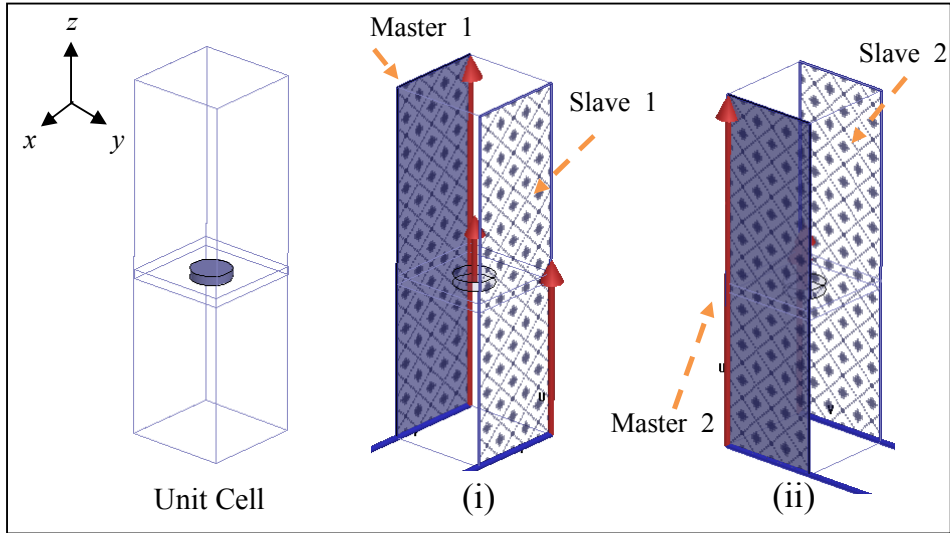


**Figure 5.2:** When using an FEM approach to simulate infinite arrays of particles, periodic boundary conditions are imposed along  $x$  (i) and  $y$  (ii) directions.

For the case of illumination at angles away from normal incidence, the periodic boundary conditions must be modified. A phase difference is introduced between the fields at identical points on paired boundaries in order to account for the difference in optical path length across the unit cell. The magnitude of the phase difference is calculated from the frequency and incident angle of the illuminating radiation. Once the scattered field distribution has been calculated, the extinction of the array can be determined. When using a DDA approach, the optical cross sections associated with each unit cell are either calculated directly, or can be numerically integrated from the scattered field<sup>15</sup>. The diagram in Figure 5.3 shows the scattering of an incident plane wave by an individual nanoparticle. Here it is assumed that the scattered electric and magnetic fields are comprised of spherical waves of the form shown in Equations 5.14 and 5.15.

$$\mathbf{E}'_{\text{scattered}}(\mathbf{r}) = \frac{e^{ikr}}{r} \mathbf{E}_{\text{scattered}}(\hat{\mathbf{r}}) \quad 5.14$$

$$\mathbf{H}'_{\text{scattered}}(\mathbf{r}) = \sqrt{\frac{\epsilon_0}{\mu_0}} \frac{e^{ikr}}{r} (\hat{\mathbf{r}} \wedge \mathbf{E}_{\text{scattered}}(\hat{\mathbf{r}})) \quad 5.15$$

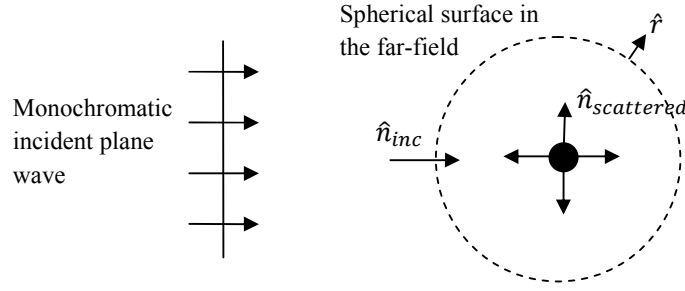


**Figure 5.3:** The scattering of an incident plane wave by a small metallic nanoparticle.

The total scattered power  $W_{sca}$  is defined by Equation 5.16, where the normal component of time averaged Poynting vector corresponding to the scattered field is integrated over a spherical surface in the far-field. This expression may be simplified by substituting in Equations 5.14 and 5.15, to yield an expression for the total scattered power in terms of the scattered electric field (Equation 5.18).

$$W_{sca} = r^2 \int_S \langle \mathbf{S}_{scattered}(\mathbf{r}) \rangle \hat{\mathbf{r}} dS \quad 5.16$$

$$\text{where } \langle \mathbf{S}_{scattered}(\mathbf{r}) \rangle = \frac{1}{2} \text{Re}[\mathbf{E}'_{scattered}(\mathbf{r}) \wedge [\mathbf{H}'_{scattered}(\mathbf{r})]^*]$$

$$W_{sca} = r^2 \int_S \frac{1}{2} \text{Re} \left[ \frac{e^{ikr}}{r} \mathbf{E}_{scattered}(\hat{\mathbf{r}}) \wedge \sqrt{\frac{\epsilon}{\mu}} \frac{e^{-ikr}}{r} (\hat{\mathbf{r}} \wedge \mathbf{E}_{scattered}^*(\hat{\mathbf{r}})) \right] \hat{\mathbf{r}} dS \quad 5.17$$

$$W_{sca} = \frac{1}{2} \sqrt{\frac{\epsilon}{\mu}} \int_S [\mathbf{E}_{scattered}(\hat{\mathbf{r}}) \cdot (\mathbf{E}_{scattered}^*(\hat{\mathbf{r}}))] \hat{\mathbf{r}} dS \quad 5.18$$

Here  $k$  is the incident wavevector, and  $\epsilon$ ,  $\mu$  represent the complex permittivity and permeability of the scattering medium respectively. The scattering cross section ( $C_{sca}$ ) is defined as the integral of the normal component of the square of the scattered electric field over a spherical surface in the far-field, which is normalised to the incident irradiance. The relationship between the total scattered power and the scattering cross section is given by Equation 5.19.

$$C_{sca} = \frac{W_{sca}}{\frac{1}{2} \sqrt{\frac{\epsilon}{\mu}} |\mathbf{E}_{inc}(r)|^2} = \frac{k}{|\mathbf{E}_{inc}(r)|^2} \int_S [\mathbf{E}_{scattered}(\hat{\mathbf{r}}) \cdot (\mathbf{E}_{scattered}^*(\hat{\mathbf{r}}))] \hat{\mathbf{r}} dS \quad 5.19$$

The rate of dissipation of energy inside the particle due to ohmic loss is given by the time average of the energy density inside the scattering medium:

$$W_{abs} = \langle u \rangle = \frac{1}{T} \int_0^T u(t) dt \quad 5.20$$

$$\langle u \rangle = \omega (\varepsilon_{imag} (\mathbf{E}_{total})^2 + \mu_{imag} (\mathbf{H}_{total})^2) \quad 5.21$$

The  $\varepsilon_{imag}$  and  $\mu_{imag}$  terms in Equation 5.21 represent the imaginary components of the relative permittivity and permeability of the scattering medium respectively. For the structures which are discussed in this chapter,  $\mu_{imag} = 0$ , and so in subsequent calculations this term is neglected. The absorption cross section is determined by normalising the integrated value of the time averaged energy density over the particle volume by the incident irradiance (Equation 5.22).

$$C_{abs} = \frac{k \varepsilon_{imag}}{|\mathbf{E}_{inc}(\mathbf{r})|^2} \int_V (\mathbf{E}_{total}(\hat{\mathbf{r}}) \cdot \mathbf{E}_{total}^*(\hat{\mathbf{r}})) d^3r \quad 5.22$$

Once any two of the three optical cross sections ( $C_{sca}$ ,  $C_{abs}$ ,  $C_{ext}$ ) are known, the unknown optical cross section can be determined using the relationship  $C_{ext} = C_{sca} + C_{abs}$ . The extinction cross section is the sum of the scattering and absorption cross sections, which when multiplied by the incident irradiance gives the total monochromatic power which is removed from the incident light by the combined effects of scattering and absorption. When determining the optical response of an infinite array, the definitions for the optical cross sections must be interpreted with some caution. This is because  $C_{sca}$  is calculated by integrating the scattered field over all azimuthal and polar scattering angles. When considering the reflectance of an infinite array, only the back scattering radiation is of interest, and so the limits of the integral in Equation 5.23 must be modified.  $C_{sca}$  is no longer calculated, but rather the differential scattering cross section has to be integrated over a specific range of angles in spherical polar co-ordinates ( $\theta$  is integrated over  $0^\circ$  to  $+90^\circ$  and  $\phi$  is integrated over  $0^\circ - 360^\circ$ ), to give a cross section which is sometimes termed  $C_{sca-bk}$  in the literature. The result of this calculation can be divided by the square of the periodicity to obtain the reflection coefficient (Equation 5.23).

$$R = \frac{C_{sca-bk}}{d^2} = \int_0^{2\pi} \int_0^{\frac{\pi}{2}} \mathbf{E}_{scattered}(\mathbf{r}') \cdot \mathbf{E}_{scattered}^*(\mathbf{r}') \sin \phi d\theta d\phi \quad 5.23$$

Similarly, when calculating the extinction the experimentally obtained spectrum must take into account light which has been forward scattered by the particle ( $C_{sca-fs}$ ). The extinction in logarithmic form is often used when characterising arrays<sup>16,17</sup> and is given by:

$$Extinction = -\log\left(\frac{C_{ext}}{d^2} - \frac{C_{sca-fs}}{d^2}\right) \quad 5.24$$

In some reference sources it is sometimes assumed that  $C_{ext}$  takes the form  $C_{ext} = C_{sca-bk} + C_{abs}$ , and so in this case Equation 5.24 may be quoted using only the first term in the logarithmic expression. An important point to note is that Equations 5.23 and 5.24 are only valid for arrays which are non-diffracting (zeroth-order for frequencies in the vicinity of particle LSPRs). If incident light is diffracted by a periodic structure, the transmittance or reflectance associated with an individual diffracted order should be calculated by integrating the differential scattering cross section (DSCS) across the appropriate range of scattering angles. Simply integrating the DSCS across all angles will calculate the total reflection / extinction of the structure due to all real (propagating) diffracted orders. Since the calculations are performed across a spherical surface at which a far-field transformation has been applied (see below), it is assumed that the amplitude of any possible evanescent diffracted orders are small, such that they do not contribute to the optical response in the far-field.

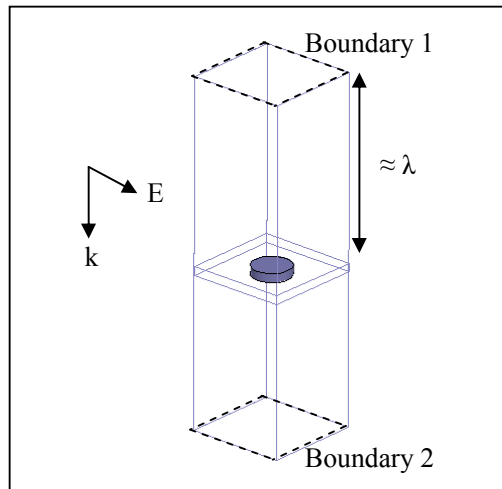


**Figure 5.4:** The electric field distributions at the upper and lower boundaries of the unit cell are used to determine the transmission and reflection coefficients of the structure.

In a finite element simulation of a periodic structure, the electric field distribution can also be integrated using Equations 5.19 and 5.22, but this is not strictly necessary. A more efficient approach is to use a far-field transformation which can be applied at the upper and lower boundaries of the unit cell, illustrated in the diagram in Figure 5.4. For example, the far-field transformation of fields on the transmission side of the structure can be derived from the Fraunhofer diffraction formula <sup>18</sup>:

$$\mathbf{E}(k_x, k_y) \propto \int_{-\infty}^{\infty} \int_{-\infty}^{\infty} \exp[-i(k_x x + k_y y)] S(x, y) \mathbf{E}(x, y) dx dy \quad 5.25$$

where  $\mathbf{E}(k_x, k_y)$  is the far field electric field distribution in terms of the spatial components of the  $\mathbf{k}$  vector,  $x$  and  $y$  represent positional co-ordinates on the upper boundary,  $S(x, y)$  is the array factor from Equation 5.13 and  $\mathbf{E}(x, y)$  represents the electric field distribution on the upper boundary. The far-field radiation is simply a Fourier transform of the scattered light, and can be simplified to:

$$\mathbf{E}(k_x, k_y) \propto \mathcal{F}[S(x, y)\mathbf{E}(x, y)] \quad 5.26$$

To determine the transmission and reflection coefficients of the structure from the electric fields in a finite element model, the scattered power must be normalised by the incident irradiance. In determining the reflectance, the integration in Equation 5.23 is performed for the scattered fields across boundary 1 of the unit cell in Figure 5.4. This is normalised by the equivalent calculation for an empty unit cell having the same dimensions. Similarly for the transmittance, the integral is performed for the fields across boundary 2, and the normalisation process from boundary 1 is repeated.

As with the DDA/CDA method, this approach is only valid in the absence of diffraction. If the incident light is diffracted, a separate method is required which expands the scattered fields into a series of propagating modes, allowing individual diffracted orders to be determined. The power in each order can be extracted using a method proposed by Wu et al. <sup>19</sup>, however this is rather lengthy and beyond the scope of the work discussed in this chapter.

### 5.3 Effects of particle size variation in nanoparticle arrays fabricated by EBL

The optical response of experimental nanoparticle array structures will now be discussed, with particular attention being paid to the effects of size variation. Square arrays of cylindrical Au particles fabricated by EBL (a technique introduced in Chapter 4) were characterised using bright-field spectroscopy. A diagram of the experimental apparatus is shown in Figure 5.5.

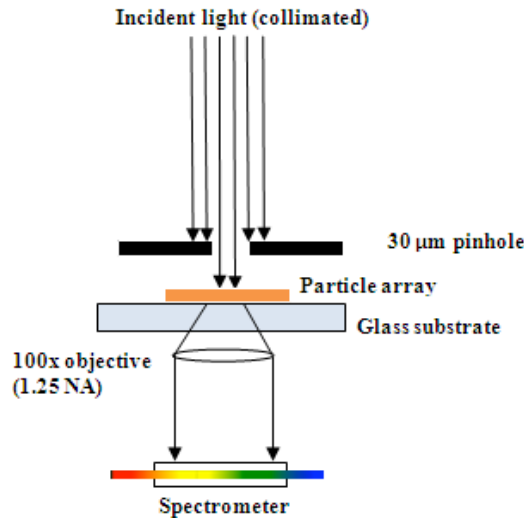


**Figure 5.5:** A diagram of the experimental apparatus for characterising the optical response of particle arrays using bright-field spectroscopy.

The arrays were fabricated on a glass ( $n_r = 1.52$ ,  $n_i = 0.00$ ) substrate, and index-matched to an oil immersion objective ( $n_r = 1.52$ ,  $n_i = 0.00$ ). The sample was illuminated at normal incidence in air. A 100x objective was used to collect the transmitted light and pass it to a spectrometer. Simulations of the structures were performed using a finite element method in which permittivity values for Au were taken from reference data<sup>20</sup>. Each array was  $10 \mu\text{m} \times 10 \mu\text{m}$  in dimension, with periodicity 300 nm. The height of the cylindrical particles was  $35 \pm 2$  nm, and the mean diameters ranged from 72 nm to 130 nm. The effects of size and positional disorder cannot be incorporated within the simulation, and so imaging software was used to determine the mean particle dimensions from a sampled area of  $10 \times 10$  particles. SEM images of  $3 \times 3$  particles from each of the arrays are shown in Figure 5.6, and in Figure 5.7 the experimental and simulated extinction spectra of the structures are compared.

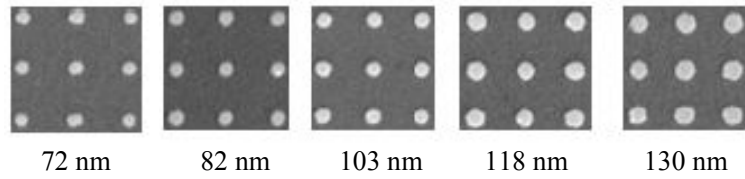


**Figure 5.6:** SEM images of sections of gold nanoparticle arrays with height 35 nm, periodicity 300 nm and mean diameters ranging from 72 nm to 130 nm.

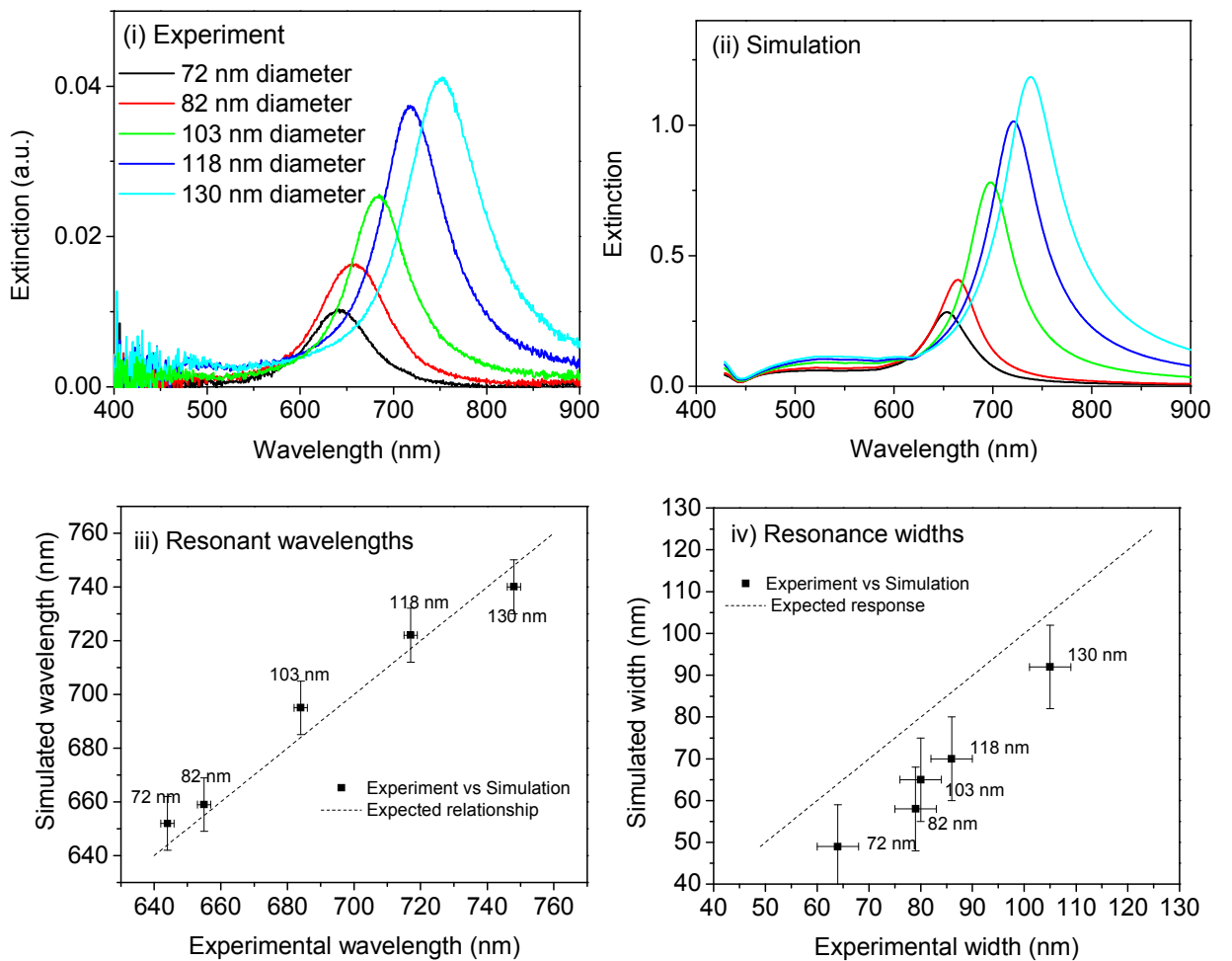


**Figure 5.7:** The experimental (i) and simulated (ii) extinction spectra are compared for regular arrays of nanoparticles with 300 nm periodicity and particle diameters ranging from 72 nm to 130 nm. The simulated and experimental resonant wavelengths (iii) and widths (iv) are also compared. The discs are illuminated at normal incidence, and are surrounded by a medium with refractive index  $n_r = 1.52$ ,  $n_i = 0.00$ .

In Figure 5.7 it is evident that the resonant frequency increases approximately linearly as a function of particle diameter. This behaviour can be explained by referring to the single particle response, and more specifically the polarisability relationship in Equation 5.1. For larger diameters, there is a reduction in the shape factor  $L_i$  associated with the component of the incident electric field which is polarised parallel to the diameter of the disc. This means that for larger discs, the condition whereby the real component of the polarisability is maximised occurs at longer wavelengths. The widths of the resonances in the simulated and experimental data follow a similar trend as the size of the particles is increased; however there is a discrepancy between their magnitudes, which is typically 15 – 20 nm outside permitted error boundaries. This discrepancy is attributed to the effects of inhomogeneous broadening due to variations in particle size and shape across the nanoparticle arrays, an artefact of the fabrication technique which cannot be incorporated into the finite element simulations. The overall increase in the resonance widths of larger discs in both the experimental and simulated data can be explained in terms of the radiative decay process (discussed for single particles in Chapter 4). In metallic discs having diameters greater than 35 nm, the greatest contribution to energy loss is through a radiative decay mechanism. The radiative damping rate is proportional to the number of electrons within the scattering particle, hence larger nanoparticles will exhibit an increased radiative damping rate, which leads to an increase in the width of the LSPR.

For arrays of small particles with periodicities in the range 250 nm – 350 nm such as those with 72 and 82 nm particle diameters in Figure 5.7, the optical response is similar to that of the isolated particle, an observation previously made by Haynes et al <sup>17</sup>. This is because the separation between particles is sufficiently large that near-field electromagnetic coupling is weak, since the decay length of the LSPR is a few tens of nm and there is only weak overlap of the resonant electromagnetic fields between particles in adjacent unit cells. The periodicity is also sufficiently small that the structure can be considered non-diffracting for frequencies in the vicinity of LSPRs, and it is not possible for constructive interference to occur between coherent scattering events across the array. Figure 5.8 shows the simulated extinction cross section for discs with 35 nm height and diameters ranging from 72 nm to 130 nm, surrounded by a medium with refractive index  $n_r = 1.52$ ,  $n_i = 0.00$ . The resonant wavelengths from the single particle extinction are plotted against those for the experimental arrays. The difference in resonant wavelengths arises from the long-range coupling between particles. This is more significant for larger particles which

exhibit a greater scattering intensity, and leads to a blue-shift in the array response in comparison to the single particle LSPR wavelength.

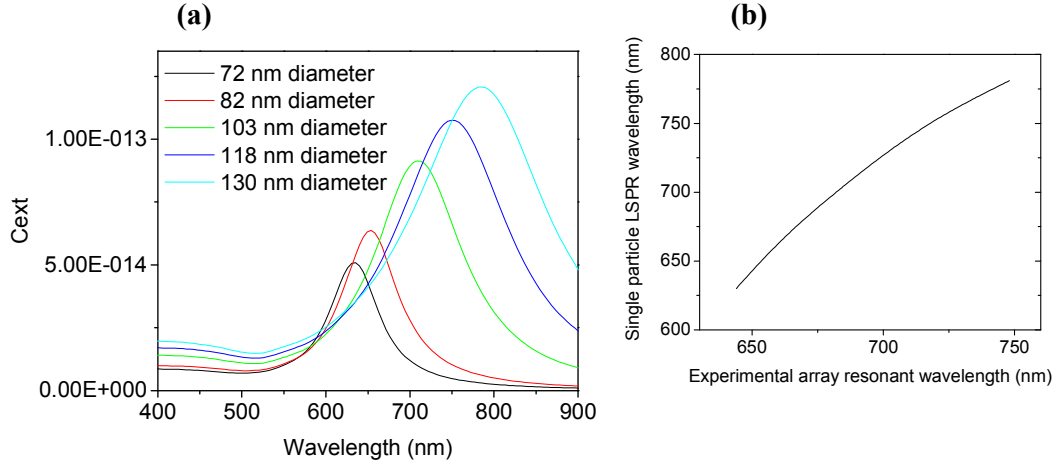


**Figure 5.8:** The simulated extinction cross section  $C_{ext}$  is shown in (a) for individual discs having height 35 nm and diameters ranging from 72 to 130 nm. In (b), the resonant wavelengths from the single particle simulations are plotted against those determined from the experimental extinction spectra of the arrays. The discs are illuminated at normal incidence, and the surrounding medium has refractive index  $n_r = 1.52$ ,  $n_i = 0.00$ .

#### 5.4 Refractive index sensitivity of nanoparticle arrays

It is well known that at the LSPR frequency there is significant enhancement and confinement of the resonant electromagnetic fields in the vicinity of the particles<sup>1</sup>. The LSPR is particularly sensitive to changes in both the local and bulk refractive index of the surrounding medium. The sensitivity of the single particle LSPR to bulk changes can be determined directly using the polarisability expression from Equation 5.1. Recall that for a small sphere which is described by the electrostatic approximation (in Section 4.3), that the LSPR condition is satisfied when a numerical pole occurs in the real part of the polarisability of the scattering particle, as shown in Equation 5.27.

$$\varepsilon_{metal}^* = -2\varepsilon_{medium} \quad 5.27$$

Here  $\varepsilon_{medium}$  is the permittivity of the surrounding medium and  $\varepsilon_{metal}^*$  represents the permittivity of the scattering particle at the LSPR wavelength. If it is assumed that the

surrounding medium has a refractive index which is entirely real ( $n_{1real}$ ), Equation 5.27 may be written as:

$$\varepsilon_{metal}^* = -2n_{1real}^2 \quad 5.28$$

The sensitivity of the LSPR is dependent on both the gradient of  $\varepsilon_{metal}$  at the resonant wavelength and the refractive index of the surrounding medium  $n_{1real}$ . Equation 5.28 may be rearranged in terms of  $\lambda^*$ :

$$\frac{d\varepsilon_{metal}^*}{dn} = -4n_{1real} \quad 5.29$$

$$\frac{d\varepsilon_{metal}^*}{dn} = \frac{2\varepsilon_{metal}^*}{n_{1real}} \quad 5.30$$

$$\frac{d\lambda^*}{dn} = \frac{2\varepsilon_{metal}^*}{n_{1real} \left( \frac{d\varepsilon(\lambda)}{d\lambda} \right)} \quad 5.31$$

If the dielectric function  $\varepsilon(\lambda)$  is approximated using a lossless Drude model ( $\omega_p = 1.3 \times 10^{16} \text{ s}^{-1}$  for Au),  $d\lambda/dn$  may be calculated for various incident wavelengths and surrounding media. In (a) of Figure 5.9,  $d\lambda/dn$  is plotted for incident wavelengths in the range 300 – 1000 nm, with  $n_{1real}$  varied between 1.5 and 4.5. The dashed arrows represent the wavelengths at which the resonant condition in Equation 5.28 is satisfied. In (b) and (c) the values of  $\varepsilon_{metal}$  at the resonant condition and the LSPR wavelength are plotted as a function of  $n_{1real}$ . It can be observed that as refractive index of the surrounding medium is increased, the LSPR condition in Equation 5.28 is red-shifted to longer wavelengths, where the gradient of  $d\lambda/dn$  is greater. As the refractive index of the surrounding medium ( $n_{1real}$ ) is increased from 1.5 to 4.5, the value of  $d\lambda/dn$  at the resonant frequency increases from 350 to 390 nm respectively.

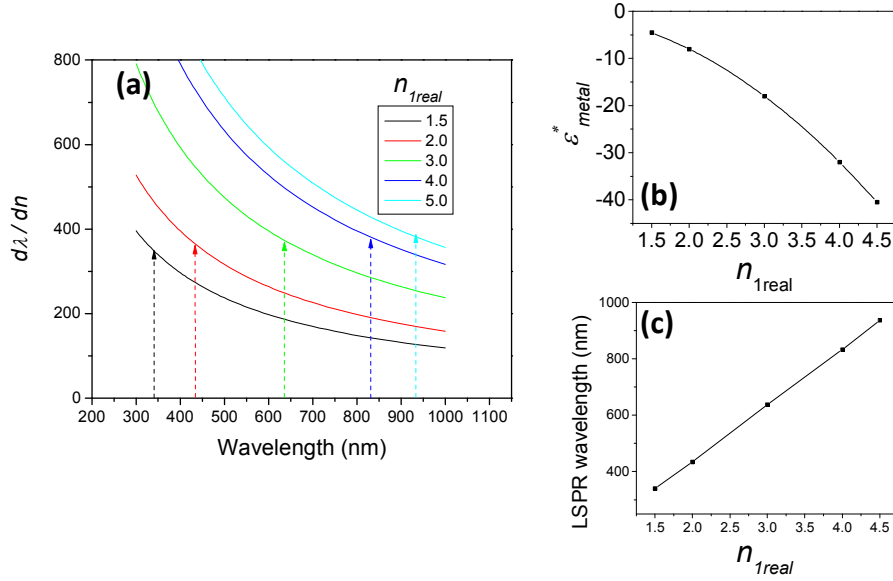


**Figure 5.9:** In (a) the calculated values of  $d\lambda/dn$  from Equation 5.31 are shown for incident wavelengths across the range 300 – 1000 nm, and  $n_{1real}$  varying between 1.5 and 4.5. The dashed arrows represent the wavelengths at which the resonant condition in Equation 5.28 is satisfied. In (b) and (c) the values of  $\epsilon_{metal}$  at the resonant condition and the LSPR wavelength are plotted as a function of  $n_{1real}$ . The scattering particle is an Au sphere with dimensions  $\ll \lambda$ , the permittivity values have been obtained using a lossless Drude model ( $\omega_p = 1.3 \times 10^{16} \text{ s}^{-1}$ ).

For particles arranged in regular arrays, the bulk refractive index sensitivity is also governed by the polarisability of the individual particles. Periodic arrays offer the additional benefit of large area coverage, allowing techniques such as bright-field spectroscopy to be used to characterise the optical response. Furthermore, interactions between particles in periodic arrays can lead to additional regions of field enhancement which may further improve the refractive index sensitivity in comparison to the single nanoparticle structure. For arrays in which there is a substrate, determination of the response is considerably more involved, since the polarisability expression in Equation 5.1 is only valid for a particle surrounded by a homogeneous medium. The effect of the substrate can be incorporated using a multiple scattering method, as shown by several authors<sup>21,22</sup>. This approach requires the incident and scattered fields to be expanded into spherical vector harmonics for each scattering particle, all scattering events can then be summed to give the response of the plane. Following this process, the scattered fields are transformed back into a plane wave representation such that the scattering matrices of

consecutive layers can be combined. Here, the presence of the substrate has simply been incorporated into the design of the finite element simulations. It is possible to use these simulations to investigate in greater detail the effect of varying the superstrate refractive index, enabling the bulk refractive index sensitivity of the structure to be determined. Figure 5.10 shows the simulated extinction spectra for arrays of particles in which the superstrate refractive index is varied from  $n_r = 1.0$  to 2.0. The relationship between the superstrate refractive index and the resonant wavelength is non-linear, but can be fitted with a polynomial (shown in Figure 5.10). In sensing applications it is often preferable to quote sensitivity in terms of a wavelength shift in nm per refractive index unit (RIU) change. This information is obtained using the gradient of the fitted polynomial at the refractive index which is equal to that of the substrate ( $n_r = 1.5$ ). From Figure 5.10, it can be deduced that  $d\lambda/dn \approx 179$  nm at  $n = 1.50$ .

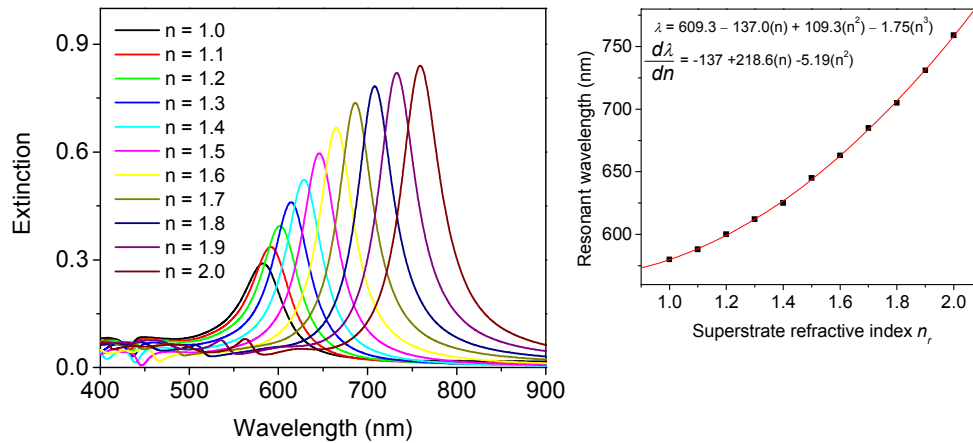


**Figure 5.10:** Simulated extinction spectra are shown for arrays of cylindrical Au nanoparticles with height 35 nm, diameter 90 nm and periodicity 300 nm. The refractive index of the glass ( $n_r = 1.52$ ,  $n_i = 0.00$ ) substrate is fixed whilst the refractive index of the superstrate is varied from  $n_r = 1.0$  to 2.0.

In Figure 5.11, the time-averaged electric field distribution is shown at the resonant frequency for a cross section taken perpendicular to the substrate for the case of a homogenous surrounding medium with refractive index  $n_r = 1.52$ ,  $n_i = 0.00$ . The field distribution exhibits characteristics which are typical of particle LSPRs<sup>1</sup>, notably that it is dipolar in nature and regions of enhancement are concentrated at the surface of the particle. These regions of enhancement occur at the corners of the disc, along the direction in which the incident electric field is polarised. It is well known that the local refractive index

sensitivity of the LSPR is greatest in the regions where significant field enhancement occurs. The local change in the refractive index will lead to a modification in the propagation constant associated with charge density oscillations which are propagating along the direction in which the incident electric field is polarised. This modification is dependent on the overlap of the resonant electromagnetic fields which are associated with the eigenmodes of the particle (as demonstrated using Mie Theory in Section 3.2) and the effective refractive index of the outer layers. With this knowledge, it is possible to investigate alternative configurations in which the refractive index sensitivity of the array can either be enhanced or reduced. For example, the sensitivity can be reduced by embedding the particles into the substrate, such that the superstrate medium is in contact only with the upper surface of the particle. Figure 5.12 shows the simulated extinction spectra for an array of Au cylinders (35 nm height, 90 nm diameter, 300 nm periodicity) embedded in a glass substrate with the superstrate refractive index being varied across the range  $n_r = 1.0$  to 2.0. From Figure 5.12, it can be deduced that  $d\lambda/dn \approx 112$  nm at  $n_r = 1.50$ . This represents a reduction in sensitivity when compared to the particles on a substrate in Figure 5.10 for which  $d\lambda/dn \approx 179$  nm at  $n_r = 1.50$ .

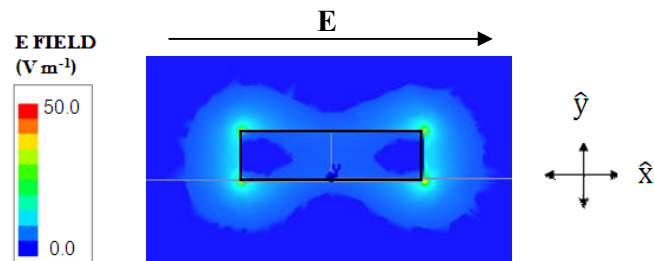


**Figure 5.11:** The time-averaged electric field distribution is shown at the resonant frequency for a cross section through the particle, taken perpendicular to the substrate. The arrow above the field profile represents the direction of the incident electric field. The arrow above the field profile represents the polarisation direction of the incident electric field.

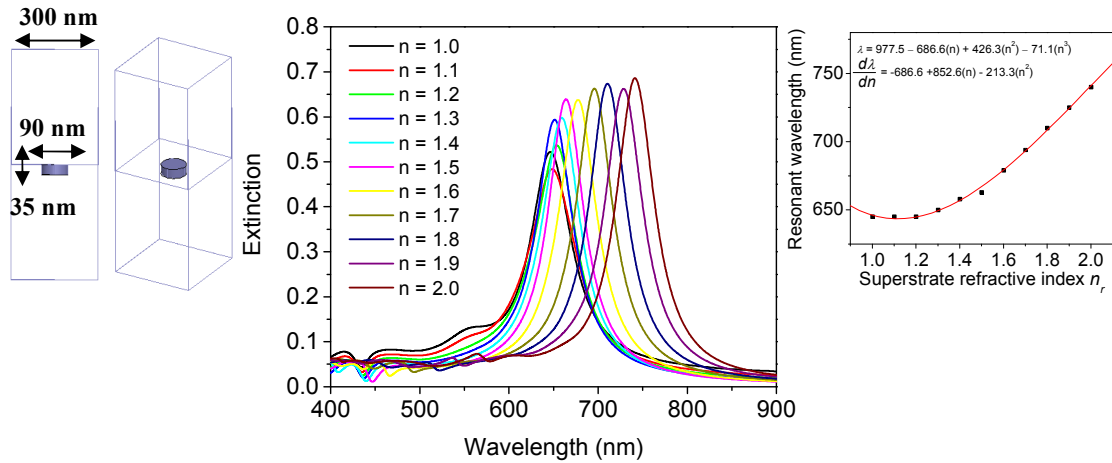


**Figure 5.12:** The simulated extinction spectra are shown for an array of Au cylinders with 35 nm height, 90 nm diameter and 300 nm periodicity embedded in a glass ( $n_r = 1.52$ ,  $n_i = 0.00$ ) substrate, with the superstrate refractive index being varied across the range  $n_r = 1.0$  to 2.0.

Conversely, the refractive index sensitivity can also be increased by placing the particle on a dielectric ‘plinth’ above the substrate (Figure 5.13). Previously, the region of field enhancement which occurred below the particle was inside the substrate, whereas in this alternative configuration the resonant field distribution extends both into the dielectric plinth and the superstrate medium. It is therefore expected that the structure will exhibit a greater sensitivity to changes in the refractive index of the superstrate medium. In Figure 5.13 the simulated extinction spectra are shown for arrays of Au cylinders in which the particles are raised on a glass plinth with height 20 nm, and the superstrate refractive index is varied from  $n_r = 1.0$  to 2.0. From Figure 5.13, it can be deduced that  $d\lambda/dn \approx 300$  nm at  $n_r = 1.50$ . This represents an increase in sensitivity when compared to the particles on a substrate in Figure 5.10 for which  $d\lambda/dn \approx 179$  nm at  $n_r = 1.50$ .

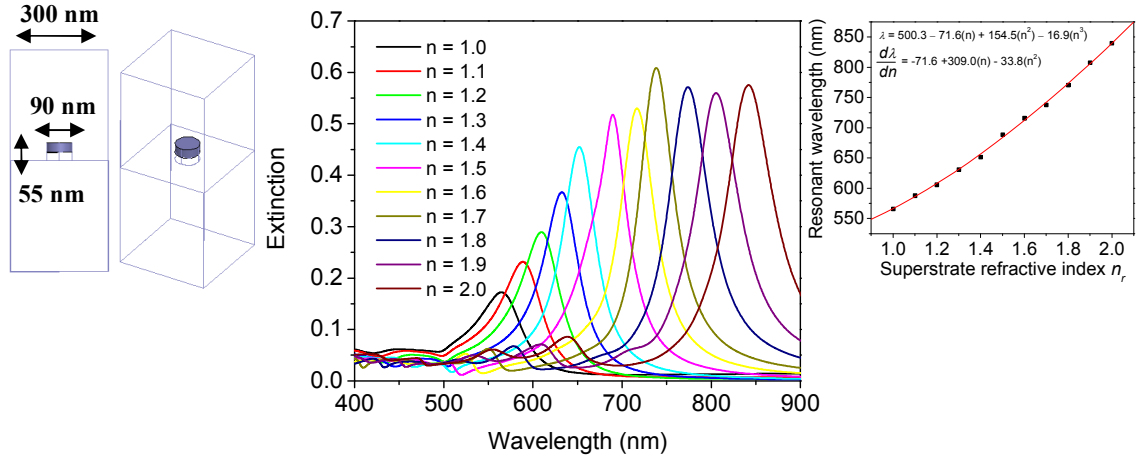


**Figure 5.13:** The simulated extinction spectra are shown for an array of Au cylinders with 35 nm height, 90 nm diameter and 300 nm periodicity raised on a glass ( $n_r = 1.52$ ,  $n_i = 0.00$ ) ‘plinth’ of thickness 20 nm, with the superstrate refractive index being varied across the range  $n_r = 1.0$  to 2.0.

### 5.5 Periodicity regimes in which particles may interact

Previously the periodicity of the experimentally fabricated arrays was such that the optical response was typically governed by that of the isolated particle structure. However by modifying the periodicity of the array it is possible to explore different regimes of particle interactions. This can be understood in greater detail by referring to the expression for the array factor  $S$  which was derived at the beginning of the chapter:

$$S = e^{ikd} \sum_{particles} \left( \frac{k^2 \sin^2 \theta}{d} \right) + \left( \frac{(1 - ikd)(3 \cos^2 \theta - 1)}{d^3} \right) \quad 5.32$$

where  $d$  represents the lattice spacing associated with a regular array of particles and  $\theta$  represents the azimuthal angle between the  $i^{\text{th}}$  and  $j^{\text{th}}$  particles which are lying in a plane which is parallel to the substrate.

For a regular square array with lattice spacing  $d$ , the array factor is a sum of two terms, one of which is dependent on  $1/d$ , and the other  $1/d^3$ . Each of these terms has an additional dependence on  $d$ , in particular the  $e^{ikd}$  dependence of both terms (which is a measure of

retardation between particles) and leads to both terms having complex contributions to  $S$ <sup>17</sup>. As a simplification however, one can regard the  $1/d^3$  term as contributing to short-range interactions, and the  $1/d$  term as contributing to long-range interactions. The regimes of particle interactions in arrays can be divided into three categories, and these will be briefly considered in turn.

- **1)** Where the lattice spacing is such that the separation between particles is a few tens of nm, the  $1/d^3$  term is dominant.
- **2)** Where the lattice spacing is greater than tens of nm, but less than the incident wavelength, the  $1/d$  term is dominant.
- **3)** Where the lattice spacing is comparable to the incident wavelength, the  $1/d$  term is dominant. However, there is the additional possibility for coherent interactions to arise when light is scattered in the plane of the array.

### **Regime 1: Where the effects of near field interactions dominate**

Figure 5.14 shows the simulated extinction spectra for arrays of Au cylinders (90 nm diameter, 35 nm height) in which the periodicity of the array is increased from 100 nm to 175 nm in increments of 25 nm. As the periodicity is increased, it can be observed that the resonant wavelength is blue-shifted to shorter wavelengths. In Figure 5.15 the time-averaged electric field distribution is shown at the resonant frequency for a cross section taken parallel to the substrate for a periodicity of 100 nm. There is evidence of strong inter-particle coupling, and field enhancement can be observed between the particles along the direction in which the incident electric field is polarised. The electromagnetic fields from neighbouring particles reduce the restoring force associated with dipole moment which is induced by the illuminating radiation. The diagram in Figure 5.16 identifies the near-field interactions between Au cylinders for a section of  $3 \times 3$  of particles within the infinite array. The cross section is taken through the plane of the substrate, such that the array is viewed from above. The red arrows represent the direction of the induced dipole moment across the particles, whilst the blue arrows represent the direction of the induced dipole moment between particles. Note that in this particle configuration, there is significant near-field coupling along the direction which is parallel to the polarisation of the incident electric field, such that two vectors are aligned in opposite directions. This leads to a reduction in the restoring force associated with the induced dipole moments, and a decrease in the resonant frequency of the LSPR.

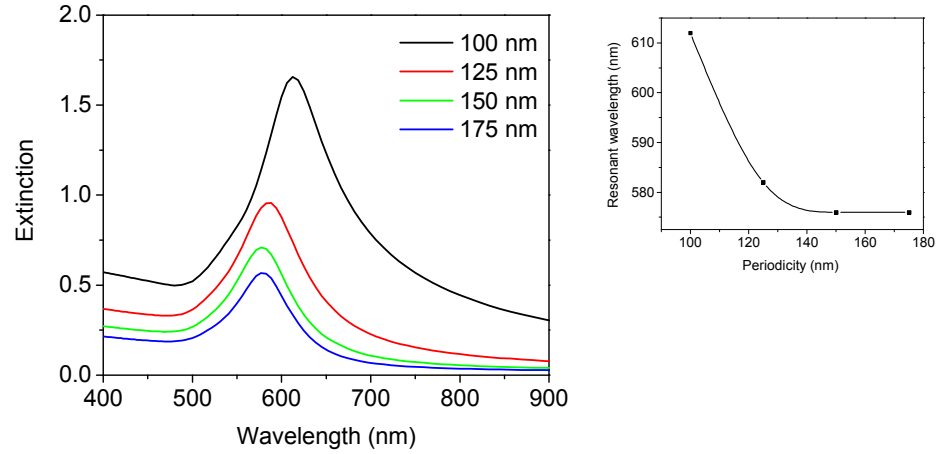


**Figure 5.14:** The simulated extinction spectra are shown for arrays of Au cylinders (90 nm diameter, 35 nm height) in which the periodicity of the arrays has been varied from 100 nm to 175 nm in increments of 25 nm. The arrays are illuminated at normal incidence in air on a glass ( $n_r = 1.52$ ,  $n_i = 0.00$ ) substrate.

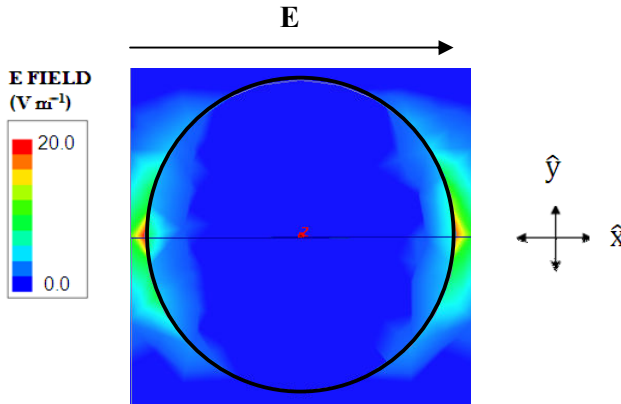


**Figure 5.15:** The time-averaged electric field distribution is shown for a cross section taken parallel to the substrate at the resonant frequency for a periodicity of 100 nm. The arrow above the field profile represents the polarisation of the incident electric field along the line of the unit vector  $\hat{x}$ .

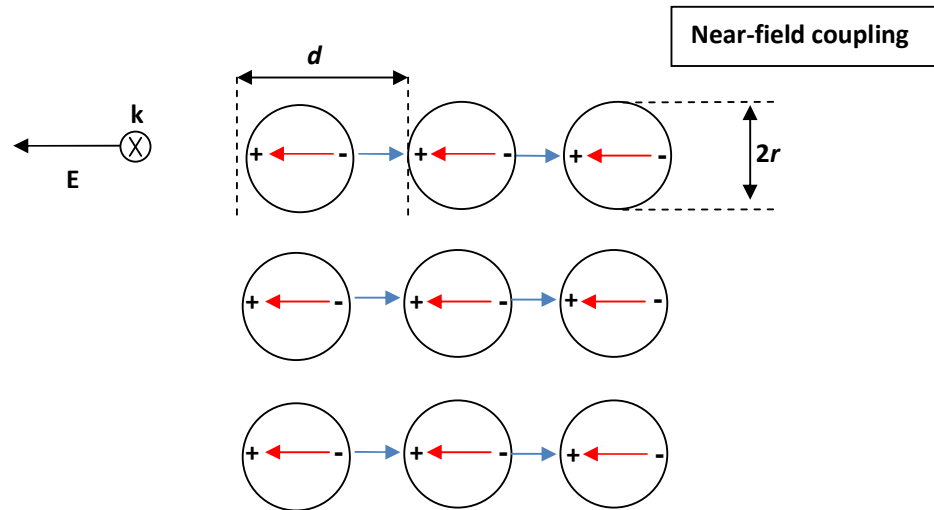


**Figure 5.16:** Plan view of a  $3 \times 3$  array of nanoparticles with radius  $r$  and periodicity  $d$ . The red arrows represent the direction of the induced dipole moment across the particles, whilst the blue arrows represent the direction of the induced dipole moment between particles. In the left of the figure, the direction of the incident wave vector and the polarisation of the incident electric field are shown.

**Regime 2: Where the lattice spacing is greater than tens of nm but smaller than the incident wavelength**

In Figure 5.17 the periodicity of the array in the simulations is further increased from 200 nm to 400 nm in 25 nm increments. The observed shift in wavelength is significantly smaller, with the resonant wavelength red-shifting slightly as the periodicity is increased. At these separations, the  $1/d$  term from Equation 5.32 becomes the dominant contributor to the array factor  $S$ . The particles can be thought of as interacting through radiative dipolar interactions, in which the scattered fields from adjacent dipoles constructively interfere. This phenomenon has also been discussed in the work of Lamprecht et al <sup>23</sup>. When the periodicity is smaller than the incident wavelength, the diffracted orders associated with the structure are evanescent. The radiated fields from neighbouring particles are superimposed with their respective phase shifts (which are dependent on the periodicity of the array), leading to an enhancement of the local fields in the plane of the array and a blue-shift in comparison to the single particle response. The diagram in Figure 5.18 identifies the radiative coupling between Au cylinders for a section of  $3 \times 3$  of particles within the infinite array. This is shown for a cross section which is taken for a plane which is parallel to the substrate, such that the array is viewed from above. The red arrows

represent the direction of the induced dipole moment across the particles, whilst the blue arrows represent the direction of the radiated electric field. Since the direction of the emitted radiation from a dipole is perpendicular to the direction along which it oscillates, the radiative coupling occurs between rows which are perpendicular to the polarisation direction of the incident electric field. Note that the arrows of both the induced dipole moment and radiated field are aligned parallel, this leads to an increase in the restoring force associated with the induced dipole moment and the resonant frequency for scattering.

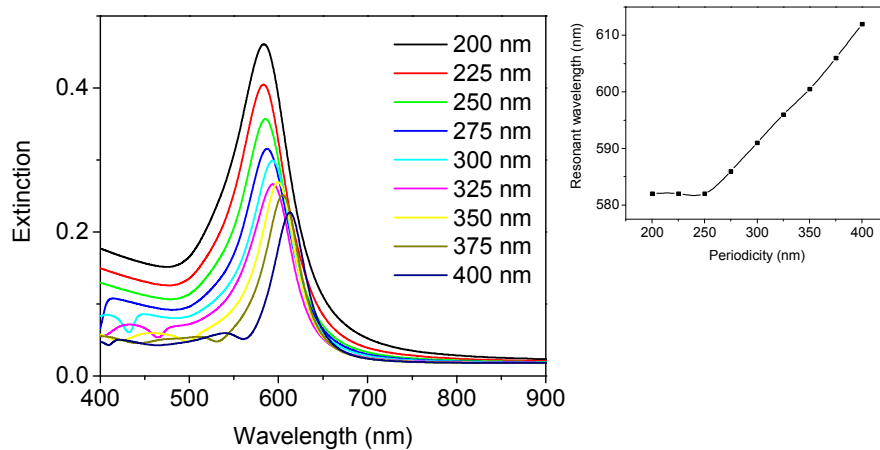


**Figure 5.17:** The simulated extinction spectra are shown for arrays of Au cylinders (90 nm diameter, 35 nm height) in which the periodicity of the arrays has been varied from 200 nm to 400 nm in increments of 25 nm. The arrays are illuminated at normal incidence in air on a glass ( $n_r = 1.52$ ,  $n_i = 0.00$ ) substrate.

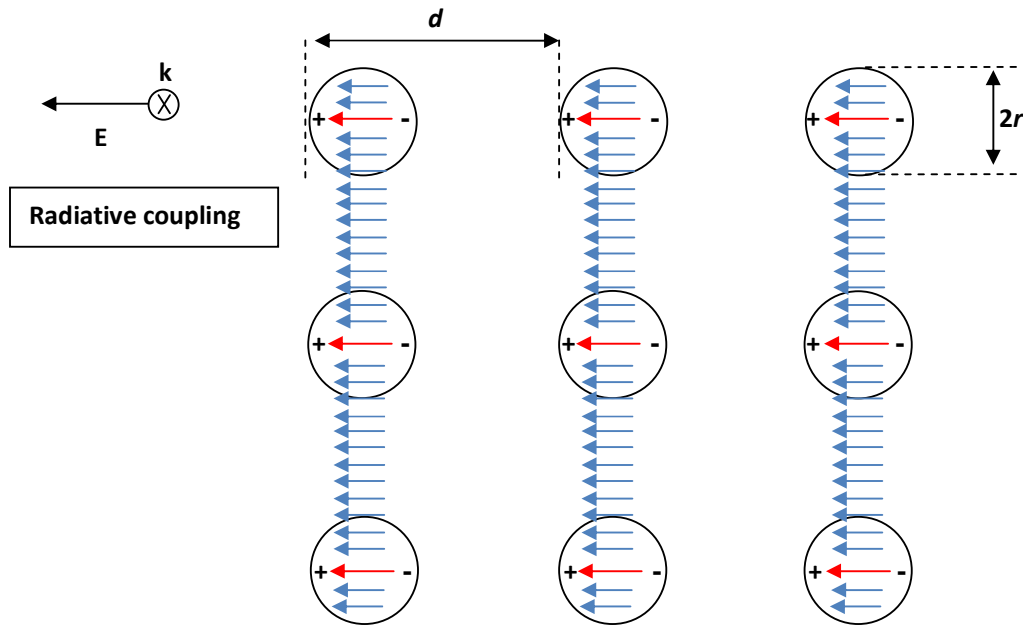


**Figure 5.18:** Plan view of a  $3 \times 3$  array of nanoparticles with radius  $r$  and periodicity  $d$ . The red arrows represent the direction of the induced dipole moment across the particles, whilst the blue arrows represent the direction of the radiated electric field. In the left of the figure, the direction of the incident wave vector and the polarisation of the incident electric field are shown.

**Regime 3: Where the periodicity is comparable to or greater than the incident wavelength.**

If the periodicity is further increased, the  $1/d$  term remains dominant and the resonant frequency oscillates weakly as a function of periodicity, depending on the interference condition between the radiated fields. The single particle response is recovered in the limit that  $d \rightarrow \infty$ . In addition to this, the effects of retardation (or dynamic depolarisation) are also significant in determining the magnitude of the polarisability in arrays such as these which have periodicities which are comparable to the incident wavelength. Another important factor is that for some periodicities the extinction minima associated with the diffraction of incident radiation are observed in the same spectral region as the LSPR. Narrow spectral features have been observed in work investigating rectangular Au nanorods in which the periodicity is diffracting for frequencies in the vicinity of LSPRs<sup>16</sup>. It has been predicted by Zou and Schatz<sup>24</sup> that when the imaginary part of the array factor  $S$  is negative it is possible for the radiative damping mechanism associated with the isolated particle to be minimised or even cancelled by the diffractive coupling between

particles. This leads to significant improvements in the quality factor in comparison to the single particle response. The extinction cross section can be obtained from the imaginary component of the effective polarisability, using the optical theorem<sup>1</sup>:

$$\sigma_{ext} \propto k \text{Im}(\alpha)$$

5.33

A maximum in extinction can be found when the denominator in the real part of Equation 5.33 is minimised. The intensity of the extinction peak is dependent upon the imaginary component of the array factor  $S$ . When the diffraction edge is on the high energy side of the LSPR frequency, the diffractive coupling between particles is weak as the permitted diffracted orders are of higher energy than the LSPR. However, when the diffraction edge is on the lower energy side of the LSPR, a sharp and intense peak is found on the long wavelength tail of the main resonance. The sharp peak which occurs closest to the diffraction edge was found to be more intense for particles with a high aspect ratio<sup>16</sup>. The diffractive coupling between particles is dependent on the overlap between the propagating field and the mode associated with the LSPR. In Figure 5.19, the extinction from arrays of rectangular Au particles (35 nm height, 85 nm width, 123 nm length) is shown with periodicities ranging from 480 nm to 560 nm, surrounded by a medium with refractive index  $n_r = 1.52$ ,  $n_i = 0.00$ . The data in Figure 5.19 was provided by Auguie et al.<sup>16</sup>

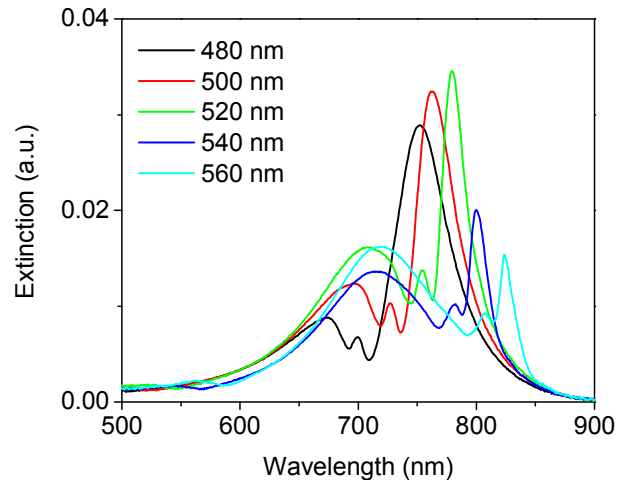


**Figure 5.19:** Experimental extinction spectra published by Auguie et al.<sup>16</sup> are shown for square arrays of rectangular Au nanoparticles (35 nm height, 85 nm width, 123 nm length), with periodicities ranging from 480 to 560 nm. The surrounding medium has refractive

index  $n_r = 1.52$ ,  $n_i = 0.00$ . The incident electric field is polarised along the long axis of the particles.

Other studies<sup>25,26</sup> have also investigated this type of coupling in particle pairs in which the excitation of the anti-symmetric mode (sometimes termed the ‘dark mode’) is typified by evanescent field enhancement between particles, in addition to reduced scattering and radiation damping when compared to the symmetric (or ‘bright’) mode.

## 5.6 Concluding remarks

Previously Chapter 4 contained an investigation into the optical response associated with LSPRs in single metallic nanoparticles. Here, these studies have been extended to consider the modification of the single particle LSPR when particles are incorporated into periodic arrays. This modification to the optical response has been explained by analogy to the coupled dipole approximation, in which each of the particles within the array is modelled as a point dipole which has an effective polarisability. It is shown that the effective polarisability is dependent on the geometry and periodicity of the array. A method has been also described for obtaining the extinction of an infinite array using the optical cross sections derived from single particle experiments or simulations. It is well known that the resonant field distribution associated with the LSPR is particularly sensitive to the refractive index of the surrounding medium. Here, the refractive index sensitivity of the optical response has been explored, with simulations investigating different geometries which may be used to either increase or decrease the refractive index sensitivity of the arrays. The regimes of electromagnetic coupling between particles in regular arrays have also been investigated. The strength of these interactions has been shown to be highly dependent on the periodicity of the array, and can be separated into three main regimes of short-range, long-range and coherent interactions.

The remaining chapters (Chapters 6 - 9) are concerned with the optical response of metallic films perforated with arrays of nanoholes, structures which are complementary to those presented here. In Chapter 6, it will be shown that a single perforation in an optically thin metallic film may exhibit a localized resonance (a hole LSPR) which is associated with induced dipole moments in the vicinity of the metal film surrounding the hole. The LSPRs of nanoholes have a number of similarities to the LSPRs of metallic nanoparticle structures, and are quite distinct from the enhanced transmission resonances observed in optically thick perforated metal films<sup>27</sup>. The study of the interactions between LSPRs in

particle arrays presented in this chapter serves as a useful pre-requisite for the investigation of nanohole arrays in Chapter 6.

### **The optical response of metallic films perforated with periodic arrays of subwavelength holes**

#### **6.1 Introduction**

The previous chapter contained an investigation into the optical response of metallic nanoparticles arranged in regular arrays. In this chapter the response of the complementary structure will be discussed, a metallic film perforated with arrays of subwavelength holes. Much interest has surrounded the recent demonstration of enhanced transmission through optically thick metal films which have been perforated with two-dimensional arrays of subwavelength holes<sup>1-5</sup>. This enhancement has been attributed to the excitation and subsequent coupling of surface plasmon-polariton (SPP) modes across the metal film. In these structures, transmission maxima are observed for wavelengths which are approximately equal to the periodicity of the array. With suitable optimization of the array periodicity, this enhancement can be observed across any desired frequency regime within the electromagnetic spectrum (visible, IR, THz or GHz domain)<sup>6</sup>. Recently it has been shown that holes in thin metal films can also exhibit localised resonances which are observed at visible frequencies for metallic structures, analogous to the so-called particle plasmon widely investigated in metallic nanoparticles<sup>6-8</sup> (and extensively discussed throughout Chapter 4 of this thesis). The work of Kall et al.<sup>9-12</sup> further investigates these “hole plasmons” (hole LSPRs) and provides evidence that these localised modes can also couple to SPPs associated with the metal film. It is thought that interactions between hole LSPRs and SPPs gives rise to strong inter-hole coupling, an effect which has been observed for a thin gold film perforated with a random arrangement of nanoholes<sup>11</sup>.

In this chapter the electromagnetic properties of these ‘hole plasmons’ will be investigated as part of a regular array with subwavelength periodicity. It is shown that the hole LSPR is highly sensitive to the periodicity of the array, and exhibits field enhancement within the hole. There will also be a comparison between the coupling of nanoholes and nanoparticles in non-diffracting regular arrays. For the range of periodicities studied here (200 – 250 nm), it is shown that the spectral position of the transmittance minimum associated with the nanohole arrays varies with array period, an effect which is attributed to strong LSPR coupling mediated by SPPs associated with the metal film. For the

complementary nanoparticle arrays, a minimal shift is observed since SPPs are not supported by this structure.

## 6.2 Enhanced transmission through optically thick metal films perforated with periodic arrays of holes

One of the most significant discoveries involving hole arrays was that of Ebbesen et al. in 1998<sup>1</sup>. In these structures substantially enhanced transmission was observed when light was incident on an optically thick metal film which was perforated with periodic arrays of nanoholes, such that the periodicity of the holes facilitated grating coupling to SPP modes supported by the metal film. Consider an infinite square array of holes with periodicity  $d$  formed from an optically thick film of Ag (permittivity  $\epsilon_{Ag}$ ), and surrounded by a medium with permittivity  $\epsilon_I$  (as illustrated in Figure 6.1).

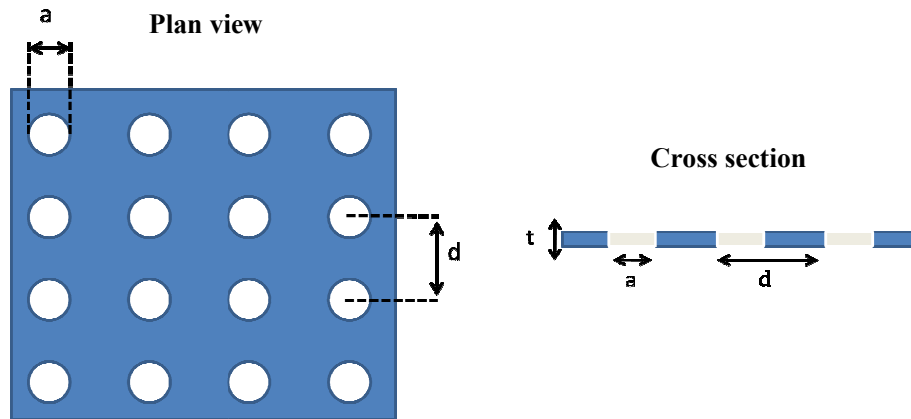


**Figure 6.1:** A metal film with thickness  $t$  is perforated with a square array of cylindrical holes having diameter  $a$  and square periodicity  $d$ . The diagrams show the structure as viewed from above (left) and in cross section (right).

In order to understand the origin of the transmission resonances in this structure, an appropriate starting point is to refer to the dispersion relation for an air / Ag planar interface with the dielectric function of the Ag being described by a Drude model, this is shown in (a) of Figure 6.2. The dashed black line represents the light line, and the blue shaded area define the region over which freely propagating light may radiatively couple to the structure, whilst the solid red curve represents the SPP dispersion which is based upon the Drude model. For small  $\mathbf{k}$ , the dispersion curve is parallel to the light line, whereas for large  $\mathbf{k}$  the asymptotic limit is dependent on the plasma frequency of the metal ( $\omega_p/0.7071$ ).

It is well known that one cannot excite an SPP at a planar metal-air interface simply by illuminating from the air side, since the wave vector of the SPP which is parallel to the interface is greater than that of the incident radiation. An appropriate mechanism is therefore required to match the momentum of the incident light to the parallel momentum component of the SPP. One approach is to periodically corrugate the metal surface to form a diffraction grating<sup>13</sup>. A photon incident upon a one dimensional grating (a monograting) can be scattered by subtracting or adding an integer multiple of the grating vector  $\mathbf{k}_g (=2\pi/d)$ , where  $d$  is the grating pitch. This results in a back-folding of the light line at the Brillouin zone boundary, such that  $2n$  lines cross the  $y$  axis at  $\mathbf{k} = 0$  which correspond to the  $\pm n^{\text{th}}$  diffracted orders of the grating ((b) in Figure 6.2).

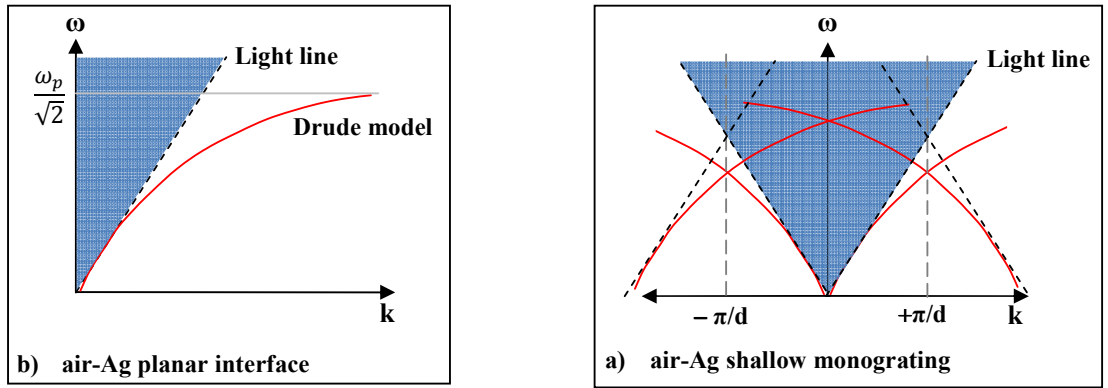


**Figure 6.2:** Schematic representations of the dispersion relations are shown for (a) an air - Ag planar interface and (b) an air-Ag shallow monograting. The red lines represent the SPP dispersion curves, and dashed black lines are the diffracted and non-diffracted light lines. It is assumed that the dielectric function of the Ag may be described using a Drude model.

It is possible for a hole array such as that presented in Figure 6.1 to act as a grating in two dimensions, imparting integer wave vector components of  $(2\pi n_x / d)$  and  $(2\pi n_y / d)$  along  $x$  and  $y$  directions respectively. These components represent the lattice vectors of the square array, with  $n_x$  and  $n_y$  being the mode indices. The excitation of SPPs by allowed grating orders occurs when the condition in Equation 6.1 is satisfied<sup>1,13</sup>.

$$\mathbf{k}_0 \sin \theta \pm n_x \mathbf{G}_x + n_y \mathbf{G}_y = \mathbf{k}_{\text{SPP}} \quad 6.1$$

$$\mathbf{G}_x = \mathbf{G}_y = \frac{2\pi}{d} \quad 6.2$$

where  $\mathbf{k}_0$  is the wave vector of the incident radiation, and  $\mathbf{k}_{SPP}$  is the wave vector associated with the SPP as defined in Equation 6.3. At normal incidence, it follows that SPP excitation can occur for incident wavelengths which satisfy Equation 6.4.

$$k_{SPP} = \frac{\omega}{c} \left( \frac{\epsilon_1 \epsilon_{Ag}}{\epsilon_1 + \epsilon_{Ag}} \right)^{\frac{1}{2}} \quad 6.3$$

$$\lambda_{SPP} = \frac{d}{\sqrt{n_x^2 + n_y^2}} \sqrt{\frac{\epsilon_1 \epsilon_{Ag}}{\epsilon_1 + \epsilon_{Ag}}} \quad 6.4$$

Figure 6.3 shows the simulated zeroth-order transmission spectrum obtained using a finite element method for a 200 nm thick Ag film perforated with an infinite array of cylindrical holes with diameter 150 nm and periodicity 600 nm (one of the original structures proposed by Ebbessen et al. <sup>1</sup>). Simulations are for a glass ( $n_r = 1.52$ ,  $n_i = 0.00$ ) substrate, with illumination at normal incidence in air. Permittivity values for Ag were taken from reference data <sup>14</sup>. The transmittance maximum occurring at 320 nm is not of particular interest here, since it arises from the Ag permittivity values across this range. The permittivity of Ag may be decomposed into contributions from free ( $\epsilon_f$ ) and bound ( $\epsilon_b$ ) electrons. The  $d$ -band associated with the bound Ag electrons is approximately 4eV below the Fermi energy. For photons with energy  $\approx 4$ eV (320 nm), the interband transition of electrons between  $4d \rightarrow 5s$  orbitals occurs. This leads to an increase in magnitude of  $\epsilon_{imaginary}$ , and  $\epsilon_{real}$  passes through zero. For an optically thin metal layer the reflectivity approaches zero, whilst the transmission and absorption both increase. In Figure 6.3, additional transmission maxima can also be observed at longer wavelengths. At these wavelengths it was found that the transmission efficiency divided by the fractional occupancy of the holes was greater than 2, implying that twice as much light is transmitted than directly impinges on the holes.

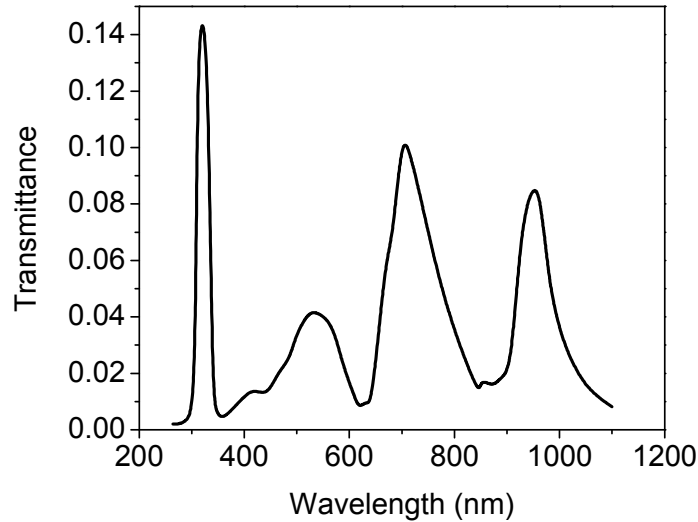


**Figure 6.3:** The simulated zeroth-order transmittance spectrum is shown for a 200 nm thick Ag film perforated with an array of cylindrical holes with diameter 150 nm and periodicity 600 nm. The sample is illuminated at normal incidence in air, and is situated on a glass ( $n_r = 1.52$ ,  $n_i = 0.00$ ) substrate.

Previously, the diffraction of light through small holes in perfect conductors had been approximated by H. A. Bethe<sup>15</sup>. It was expected that any observed transmittance would be strongly inhibited with a dependence which is proportional to  $(d/2\lambda)^4$  for holes obeying the condition  $d \ll \lambda$ . The mechanism giving rise to the enhanced transmission in these diffracting arrays has been the subject of considerable debate in recent years. The work of Barnes et al.<sup>16</sup> has discussed mechanisms in which the role of diffraction is essential in order to facilitate coupling between incident light and SPP modes. Three possible scenarios have been proposed whereby enhanced transmission may be observed<sup>16</sup>:

- i) Incident light couples to an SPP mode supported by the surface facing the incident light. The field enhancement at the surface which is associated with the SPP mode increases the probability of transmission through the holes, where the field is scattered by the periodic array to produce visible light.
- ii) Incident light cannot couple to an SPP mode on the incident face; instead matching conditions allow light that is weakly transmitted through the array to couple to an SPP mode on the exit interface, which can then scatter into transmitted light.
- iii) Processes i) and ii) may occur simultaneously.

The maximum observed at approximately 700 nm in Figure 6.3 can be attributed to the coupling of the 1<sup>st</sup> diffracted order associated with the two dimensional periodicity of holes to an SPP mode confined to the air-metal interface. Similarly, the transmittance maximum at approximately 1000 nm is attributed to the coupling to SPPs via the 1st diffracted order associated with the metal-substrate interface. The authors also found that the results were identical regardless of whether the illuminating radiation impinges on the air-metal or the metal-glass interface<sup>17</sup>. These conclusions can be verified by examination of the resonant field distribution at the resonant frequency corresponding to the 1<sup>st</sup> diffracted order at the air-metal interface (shown in Figure 6.4). Here, the time-averaged electric field distribution is shown for a cross section taken parallel to the upper metallic surface and through the centre of the structure, for an incident wavelength of 700 nm. The bright ‘bands’ of electric field intensity identify periodic enhancement across the metal surface, which is also concentrated around the rim of the nanoholes. To further illustrate the importance of the grating coupling mechanism in the role of enhanced transmission, in Figure 6.5 the transmission spectrum for a slightly different hole array is shown, in which the metal film thickness and hole diameters are identical to those of Figure 6.3, however the periodicity has been increased to 900 nm. As expected, the two transmission maxima observed in Figure 6.3 are red-shifted to longer wavelengths in accordance with the 1<sup>st</sup> diffracted order at the air-metal and metal-air interfaces occurring at lower frequencies.

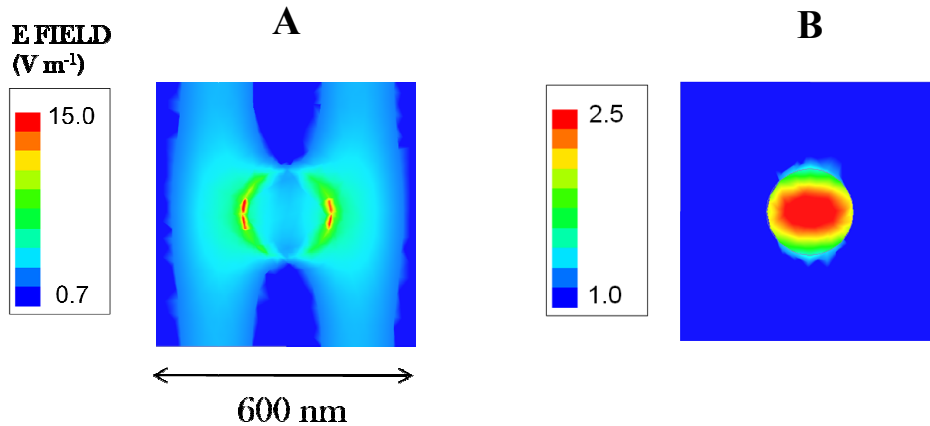


**Figure 6.4:** The time-averaged electric field distribution is shown for the structure in Figure 6.3. A cross section is taken parallel to the upper metal surface (a) and through the centre of the structure (b). The sample is illuminated at normal incidence with an incident wavelength of 700 nm.

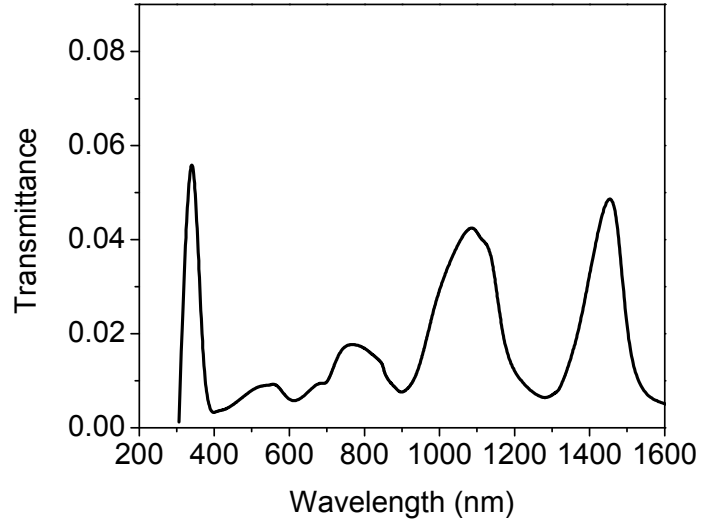


**Figure 6.5:** The simulated zeroth-order transmittance spectrum is shown for a 200 nm thick Ag film perforated with an array of cylindrical holes with diameter 150 nm and periodicity 900 nm. The sample is illuminated at normal incidence in air, and is situated on a glass ( $n_r = 1.52$ ,  $n_i = 0.00$ ) substrate.

### 6.3 Localised resonances of nanometric holes in thin metal films

A localised optical response associated with a single nanohole has recently been reported<sup>11,18</sup>. It has been suggested that such a response arises from dipole moments induced about the rim of the hole by an incident electromagnetic field in a manner analogous to that more widely studied in metallic nanoparticles<sup>6-8</sup>. As has been identified in the previous two chapters, localised dipolar resonances are often characterised using the electrostatic polarisability approximation (Equation 6.5).

$$\alpha_i = 4\pi abc \frac{\varepsilon_1 - \varepsilon_2}{3\varepsilon_2 + 3L_i(\varepsilon_1 - \varepsilon_2)} \quad 6.5$$

Equation 6.5 describes the polarisability  $\alpha$  of a small inclusion with permittivity  $\varepsilon_1$  surrounded by a medium  $\varepsilon_2$ , governed by geometrical shape factors along each of the principal axes of the inclusion ( $L_i$ ). By considering a lossless Drude model for the permittivity for the metal, given by  $\varepsilon_{\text{drude}} = 1 - \omega_p^2/\omega^2$ , where  $\omega_p$  is the metal plasma frequency, one can evaluate the polarisability of both particles and holes by considering ( $\varepsilon_l$

$= \varepsilon_{drude}$ ,  $\varepsilon_2 = 1$ ) and  $(\varepsilon_2 = 1, \varepsilon_I = \varepsilon_{drude})$ , respectively. By, finding the frequency at which the denominator of Eq. 6.5 is zero, it is straightforward to evaluate the resonant frequency of the localized response. Doing so, one predicts a resonant frequency of  $\omega_p \sqrt{L}$  for particles and  $\omega_p \sqrt{1-L}$  for holes. For prolate spheroids with eccentricity approaching zero, in which the incident electric field is polarized perpendicular to the rotational axis,  $L_x = L_y = 1/2$  <sup>19,20</sup>. Eq. 6.5 therefore predicts identical resonant frequencies for prolate metal spheroids and prolate voids within a metal as the eccentricity approaches zero, both amounting to  $\omega_p/\sqrt{2}$ . For Au, with  $\omega_p = 1.37 \times 10^{16} \text{ s}^{-1}$  <sup>20</sup>, this corresponds to a resonant wavelength of 194 nm, i.e. in the ultraviolet spectral range. The dimensions of the particles and holes discussed thus far in this thesis are such that their length cannot be considered infinite, in fact the nanoparticles discussed in Chapters 4 and 5 are more oblate. On increasing the eccentricity of the inclusion, L is lowered. For isotropic geometries such as a sphere,  $L_x = L_y = L_z = 1/3$  <sup>21</sup> such that the resonant frequency of a spherical particle in vacuum shifts to  $\omega_p/\sqrt{3}$ , while that of a spherical void in a metal is  $\omega_p \sqrt{2/3}$ . Whilst increasing the eccentricity of a metal particle can shift its dipolar resonance towards the visible spectral region <sup>22</sup>, the associated response for a void in a metal shifts to very high frequencies in the far UV spectral region <sup>23</sup>. A number of other authors have also noted this discrepancy <sup>9-12,18</sup>, including those which have measured the scattering response of single nanoholes <sup>11,18</sup>. In this instance, both the experimental and simulated data clearly show a single resonance at visible frequencies for the isolated nanoholes. Figure 6.6 shows a typical example of experimental dark field scattering spectra for single nanoholes of various diameters perforating a 20 nm thick Au film <sup>11</sup>. The maxima in scattering intensity occur within the visible frequency range and exhibit a distinct red-shift in resonant wavelength as the diameter of the nanoholes is increased, which is also accompanied by spectral broadening. It was shown by Wannemacher <sup>24</sup>, that scattering from nanoholes with diameters 50 – 100 nm in optically thin Ag films was resonantly enhanced in the blue-green spectral range due to LSPR excitation. The resonant wavelength was also found to red-shift with increasing diameter, in agreement with that shown in Figure 6.6.

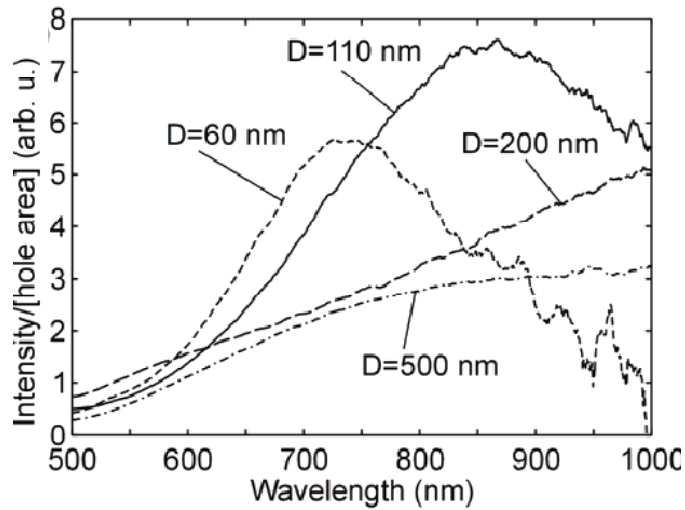


**Figure 6.6** reproduced from reference 11: The dark field scattering intensity is shown for nanoholes with diameters ranging from 60 nm to 500 nm, fabricated from a 20 nm thick Au film. The samples are fabricated on a glass ( $n_r = 1.52$ ,  $n_i = 0.00$ ) substrate and are illuminated at normal incidence in air.

A major failing of the electrostatic approximation embodied by Equation 6.5 is the inability to properly take into account the presence of the flat metallic surfaces at the entrance and exit of the hole sample. The presence of these interfaces means that the dipolar excitation of the hole can decay non-radiatively to SPPs, giving rise to an additional loss mechanism and a considerable red-shift in the frequency of the hole resonance from that predicted by Equation 6.5<sup>10-12,18</sup>.

#### 6.4 Comparison between the optical response of metallic nanoparticle and nanohole arrays

In this section there will be a comparison between the simulated and experimental transmittance spectra of hole and particle arrays. Structures were fabricated using focused ion-beam milling (FIB) for the hole arrays and electron-beam lithography (EBL) for the particle arrays (using a modified FEI Nova 600 system). For both the holes and particles, a glass substrate ( $n_r = 1.52$ ,  $n_i = 0.00$ ) was used, on which gold (Au) films of thickness  $20 \pm 2$  nm were deposited by thermal evaporation (at a rate of  $5 \text{ \AA s}^{-1}$  and in a pressure of  $1 \times 10^{-6}$  mbar). FIB milling was used to produce square arrays of circular holes with periodicities of 200 nm, 225 nm and 250 nm; the arrays were  $8 \text{ \mu m}$  on a side. Arrays of circular nanoparticles were fabricated using EBL following the procedure described in Chapter 4. The insets in Figure 6.7 show scanning electron microscope images of both

nm diameter hole and particle arrays, each with a periodicity of 200 nm. For this choice of period, diffraction is not possible for frequencies in the vicinity of the LSPRs. Bright-field transmission spectra were obtained by illuminating the sample with a collimated beam of light from a tungsten filament source at normal incidence. An objective (100 $\times$ ) was used to collect the light and pass it to a spectrometer. The optical responses of the arrays were simulated using a commercial finite element package (Ansoft HFSS)<sup>25</sup> with a mesh size of 4.5 nm. Permittivity values for gold were taken from reference data<sup>26</sup>.

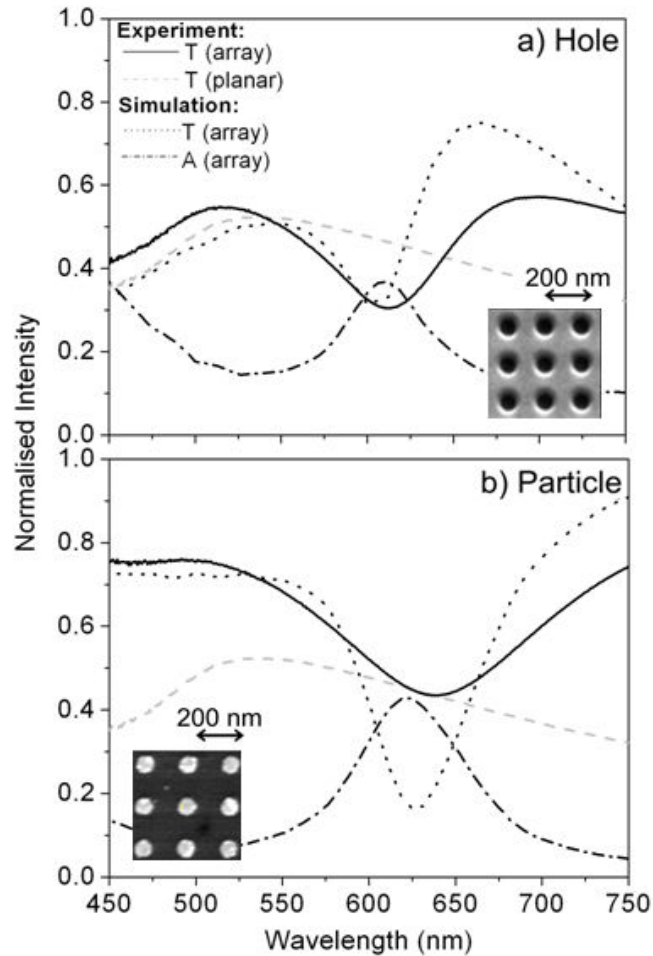


**Figure 6.7:** Experimental transmittance spectra are compared against simulated transmittance and absorbance spectra obtained for 8  $\mu\text{m}$  square arrays of 90 nm diameter holes in a (a) 20 nm thick Au film and (b) 90 nm diameter, 20 nm height cylindrical Au particles with periodicity 200 nm, illuminated at normal incidence in air. The dashed gray curve in both (a) and (b) shows the experimental transmittance spectrum obtained from a 20 nm Au film illuminated at normal incidence in air.

Figure 6.7 shows a comparison between experimental and simulated transmittance spectra for square arrays with period 200 nm for 90 nm diameter cylindrical holes (Figure 6.7(a)) and 90 nm diameter cylindrical particles (Figure 6.7(b)). Also shown in Figure 6.7 are simulated absorbance spectra for these two structures, together with the measured transmittance of 20 nm thick planar gold film (on glass) for comparison. The film thickness is chosen such that holes and particles of similar radii would have LSPR modes in the same spectral region. For both nanoparticle and nanohole arrays, transmittance minima are observed at  $\sim 600$  nm. These minima are attributed to the excitation of LSPRs associated with the particles and holes. It should be noted that in the hole structures discussed here we do not expect coupling to SPP modes associated with the Au surfaces through a radiative diffraction mechanism<sup>13,27</sup> since the periodicity of the array is significantly smaller than the incident wavelength. This has been verified by calculating the frequency dependent in-plane wavevector  $k_{sp}(\omega)$  for a SPP on a 20 nm thick Au film on glass<sup>13</sup> and determining the solutions to the coupling condition for normal incidence,  $k_{sp} \pm G = 0$ , where  $G$  are the grating vectors associated with a 200 nm period bigrating. Doing this, a lowest frequency solution is predicted at 376 nm, well outside the wavelength range studied here. Diffractive coupling to SPPs is therefore not expected to contribute to the optical response in the wavelength range studied here (400 – 800 nm).

Confirmation of this interpretation comes from referring to the (simulated) absorbance spectra: the spectra show clear maxima that are linked to the transmittance minima, something that is expected when resonant modes are excited, as the enhanced fields associated with the modes lead to a greater absorption in the metal<sup>16</sup>. As expected, the minima in the transmittance of the hole arrays exhibit a shape typical of a Fano resonance, more easily seen when one compares the hole array transmittance spectra with those of the planar film. For both nanoparticle and nanohole arrays there are two channels for transmission, direct transmission (a continuum), and transmission based on coupling by scattering both into and out of the LSPRs; it is interference between these two transmission routes that leads to the Fano response<sup>30</sup>.

### 6.5 Inter-hole coupling and effect of periodicity

To understand the optical response of the nanoparticle and nanohole arrays better, a number of simulations were carried out to determine the scattered electric field distribution for each of the structures. Similarities between the hole and particle resonant modes can be

seen in Figure 6.8, where the scattered electric field distributions are plotted at the appropriate resonant frequencies. From Figures 6.8(a) and 6.8(b) it can be deduced that both structures exhibit a largely dipolar electric field distribution. For the hole resonance, significant field enhancement occurs inside the hole and around the rim, while the highest field intensity for the particle can be found in a ‘lobed’ region outside the particle. It can also be observed that the instantaneous electric field vectors inside the particle and hole are aligned in opposite directions. This substantiates the earlier assertion that the resonances in the hole and particle arrays are complementary.

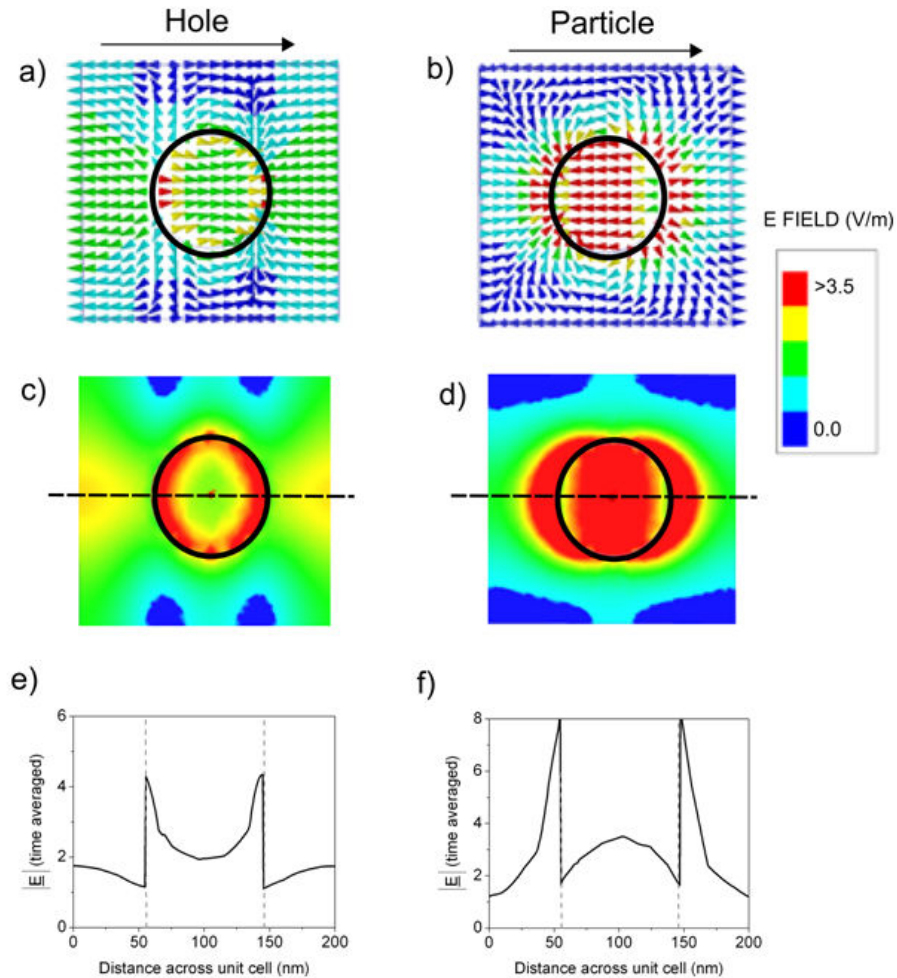


**Figure 6.8:** Field profiles are shown at the absorbance maximum of the hole and particle array structures. The upper profiles show the instantaneous scattered electric field vector for (a) the hole and (b) the particle arrays, taken at the same instant in phase for each structure. The arrows above (a) and (b) indicate the vector of the incident electric field. The centre plots show the time-averaged scattered electric field profiles for (c) the hole and (d) the particle. In (e) and (f), a line plot has been taken through the centre of the

structures along the dashed line shown in (c) and (d), and the time-averaged electric field magnitude is shown as a function of position across the unit cell.

Interestingly, for the nanohole array, it can be observed in Figures 6.8(c) and 6.8(e) that there is significant field enhancement at the metal-air interface in the regions between the holes, which is absent for the particle array (Figures 6.8(d) and 6.8(f)). This observation is consistent with the demonstration of the excitation of SPPs of the metal film in the vicinity of nanoholes<sup>29</sup>. Of particular importance in the present case will be the nearly symmetric (with respect to surface charge distributions) SPP mode. This is the only bound SPP mode that such a thin metal film may support when flanked by different refractive index media (as is the situation here)<sup>30</sup>. The field enhancement between the holes in Figures 6.8(c) and 6.8(e) suggests that even in the non-diffracting arrays, nearly symmetric SPPs supported by the metal film may play an important role in determining the optical response. For instance, the presence of the flat metallic film connecting adjacent holes could provide an additional coupling mechanism between the LSPRs of nanoholes, one mediated by nearly symmetric SPPs. It is the excitation of SPPs through scattering that enables the LSPR modes of adjacent nanoholes to interact sufficiently such that a spectral shift in their response occurs.

It is well known that when metallic nanoparticles are formed into an array the LSPRs that they support may be modified due to electromagnetic coupling between the particles,<sup>10,31-33</sup> as has been extensively discussed throughout Chapter 5. This coupling has previously been studied for particles, where Haynes et al.<sup>10</sup> found a small but observable blue-shift in the resonant frequency when the period is decreased from 500 nm to 250 nm. These same authors also suggested that the blue-shift would cease for periods somewhat less than 250 nm. The presence of the air-metal and metal-substrate interfaces in our hole arrays obviously constitute a major difference to particle arrays, which allows the localized resonances of nanoholes to couple not only to incident light but also to SPPs. Figure 6.9 shows the experimental and simulated transmittance spectra for 90 nm diameter hole arrays and for 90 nm diameter particle arrays for three different periods of 200, 225, and 250 nm. For the particle arrays, the change in resonant wavelength is very small over this range of periods (in agreement with Haynes et al.<sup>10</sup>) and this is also seen in the simulated data. In contrast, the resonant transmission for the hole array is much more sensitive to the period of the structure: an increase in the period of the hole structure by 50 nm leads to a red-shift of the transmittance minimum by approximately 60 nm. This result is consistent with the

blue-shift of the LSPR noted by Kall and co-workers<sup>11</sup> on increasing the hole density in irregular hole arrays.

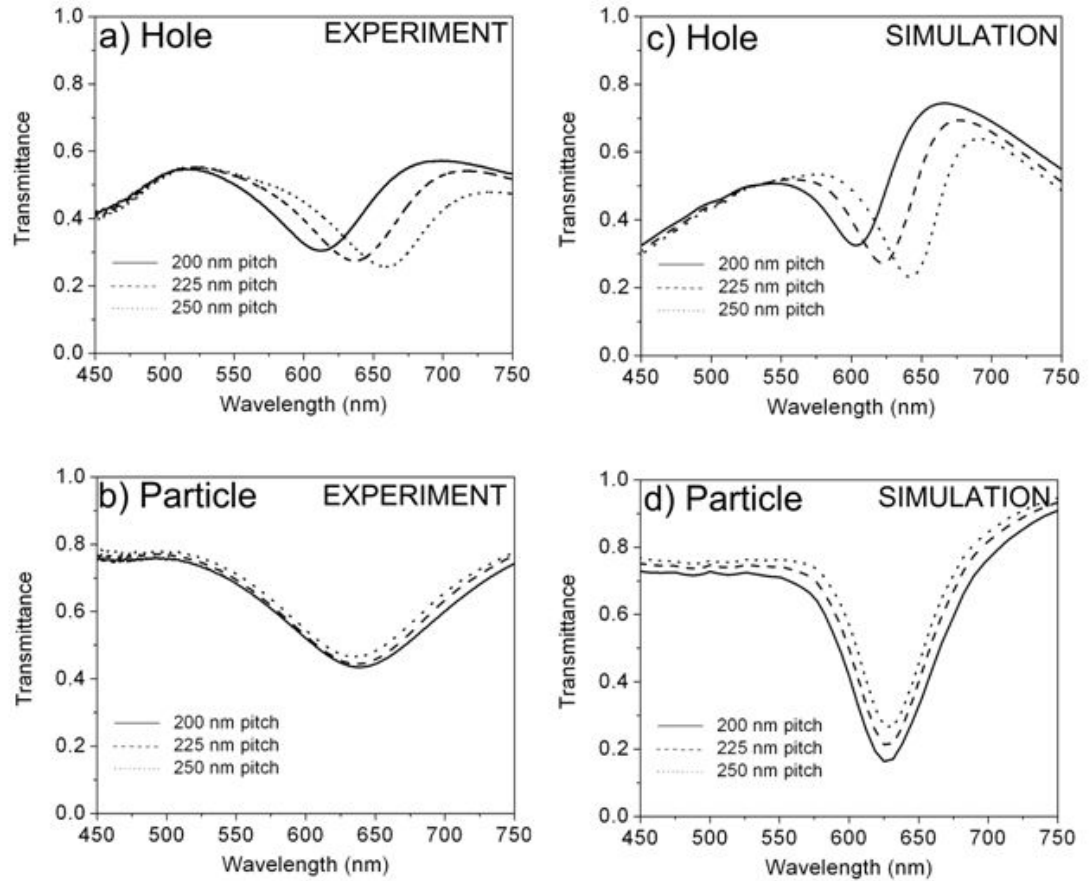


**Figure 6.9:** Comparison between experimental and simulated transmission spectra for 90 nm diameter hole ((a) and (c)) and particle ((b) and (d)) arrays with periodicity 200, 225 and 250 nm.

In addition to modifying LSPR frequencies, it should be noted that the excitation of symmetric SPPs supported by the metal film in nanohole ensembles will give rise to several other effects. First, because of the sensitivity of the optical response of the LSPRs to interhole separation, any small variations in periodicity will contribute to inhomogeneous broadening. It is thus not surprising that a random ensemble of holes<sup>11</sup> exhibits a considerably broader spectral response than the periodic arrays studied here. Moreover, the delocalisation of the electric field in SPP modes means that, in general, one

may expect to observe weaker local-field enhancements for the LSPR of nanoholes compared to the complementary nanoparticle structures.

## 6.6 Variations in hole size and geometry

This section investigates the effects of hole size and shape on the optical response of the hole LSPR. In Figure 6.10 the experimental and simulated transmittance spectra are plotted for hole arrays with periodicity 250 nm and diameters ranging from 70 nm to 100 nm. Somewhat counter-intuitively, however, increasing the diameter of the holes decreases the magnitude of the transmittance minimum. This effect is easiest to explain using Fano's 'coupled channel' approach<sup>28</sup>, which considers a resonance as arising from the interference between two contributions, a resonant and non-resonant element. The shape of the Fano resonance is determined by the ratio of the relative amplitudes of the directly transmitted and reradiated light, which is strongly dependent on the degree of coupling to the localised mode. In varying the hole diameter, the relative amplitudes of both the directly transmitted light and that which interacts with the coupled hole LSPR are modified. Although there is qualitative agreement between the resonant frequencies of the simulated and experimental data, there is a significant difference between the lineshapes off-resonance. In particular the gradient of the transmittance in the simulated data is much steeper. This discrepancy is attributed to differences between the permittivities of Au film used in the experiment and the reference values used for the simulation. The data used for Au in the simulation was that of Johnson and Christy<sup>26</sup>, in which the authors determined permittivity values for planar Au films having thicknesses typically 2-3 times greater than those studied here. In thin metallic films, it is known that the effects of surface scattering can lead to effective permittivity values somewhat different to those obtained for bulk media. This is corroborated by referring to the dashed gray curves of Figure 6.10, in which the simulated and experimental transmittance spectra of the 20 nm planar Au film are shown. The discrepancy is also evident in the lineshape of the planar films, suggesting that it originates through a difference in permittivity values.

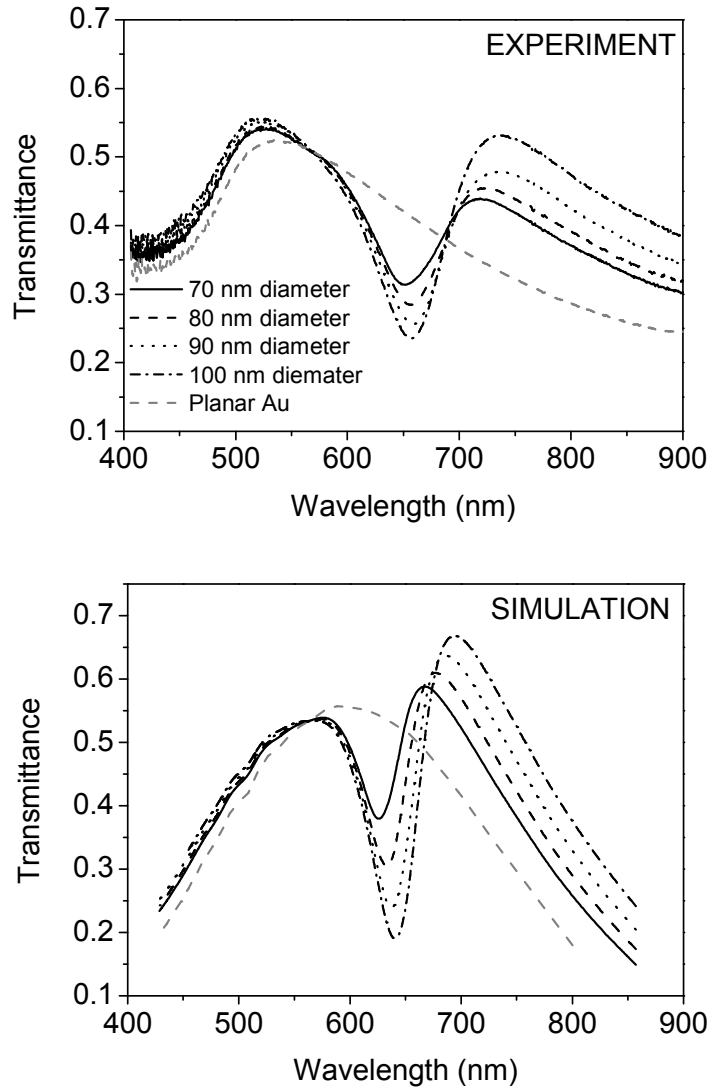


**Figure 6.10:** The experimental (left) and simulated (right) transmittance spectra are shown for hole arrays with periodicity 250 nm and hole diameters ranging from 70 nm to 100 nm. The arrays are on a glass ( $n_r = 1.52$ ,  $n_i = 0.00$ ) substrate, and are illuminated at normal incidence in air. The dashed gray curves show the experimental and simulated data for a planar Au film with thickness 20 nm.

Another interesting area for investigation is the effect of hole geometry on the optical response. Numerical simulations have been performed for an array of rectangular holes with square periodicity 200 nm and dimensions 45 nm  $\times$  90 nm. The previous section contained a discussion of structures comprised of cylindrical holes, whereby the axial symmetry leads to an independent polarisation response at normal incidence. For rectangular holes, the optical response varies according to the direction along which the

incident electric field is polarised. For simplicity, only the two extreme cases of light polarised along either the long or short axes of the hole will be considered. Figure 6.11 shows the simulated transmittance spectra for the incident electric field polarised along the long and short axes of the rectangular hole array, compared with that for an array of 70 nm diameter cylindrical holes (having a comparable cross sectional area). It can be seen that for light polarised along the short axis of the hole, coupling to the localised mode is stronger when compared to the 70 nm diameter cylindrical holes. The field profiles in the inset of Figure 6.11 illustrate the time-averaged electric field distribution at the resonant frequencies for the rectangular hole. The intensity of the LSPR associated with the short axis is larger in magnitude and occurs at a longer wavelength than that of the long axis. This behaviour is the inverse of what would be expected for a rectangular metallic nanoparticle, where the polarisability is larger for the long axis resonance, which also occurs at a longer wavelength than the short axis resonance. This behaviour can also be understood by referring to the reciprocal polarisability considerations discussed in Section 6.3. This explanation also predicts that both long and short axes resonances for the hole should lie in the UV spectral region, but as has already been identified the hole LSPRs may couple to SPPs associated with the flat metallic surfaces. This additional energy loss mechanism red-shifts the resonant frequencies of the hole LSPRs into the visible region, such that hole and particle LSPRs can be observed across a similar range of frequencies. The simulation results in Figure 6.11 suggest that an interesting area to conduct future research would be to fabricate experimental samples with different hole geometries. It is relatively simple to achieve this using an identical procedure of focused ion beam milling as used for the arrays of circular holes. Furthermore, simulations show that the field enhancement within the rectangular holes is larger than that of the circular holes (by a factor of 2-3), which may have interesting consequences for the refractive index sensitivity of the structure.

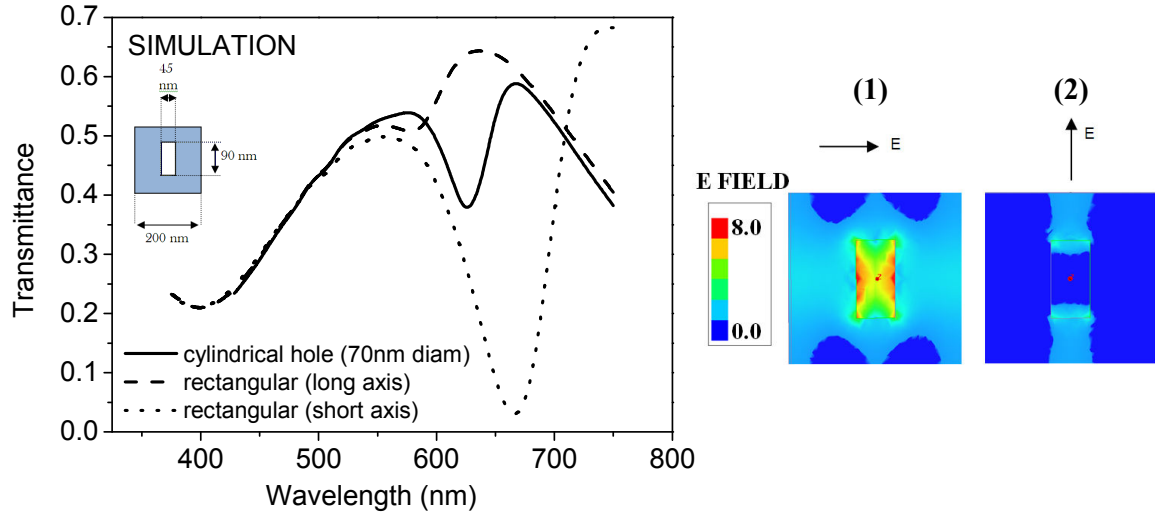


**Figure 6.11:** The simulated transmittance spectra are shown for hole arrays with periodicity 200 nm. The solid black line represents the simulated transmittance for arrays of 70 nm diameter cylindrical holes. The dashed and dash-dot lines represent the simulated transmittance of rectangular holes with dimensions 45 nm  $\times$  90 nm illuminated with light having the electric field polarised along the long (dashed) and short (dash-dot) axes. The arrays are on a glass substrate ( $n_r = 1.52$ ,  $n_i = 0.00$ ), and are illuminated at normal incidence in air.

### 6.7 Possible applications

The suitability of utilising a configuration which exhibits a localised resonance for possible sensing<sup>34-36</sup> and/or non-linear optical applications has attracted significant interest. It is well established that LSPRs have several desirable properties, including narrow resonances and strong field enhancement in the vicinity of the particle. In Figure 6.8 it has already been shown that a hole LSPR can exhibit significant field enhancement inside the hole. Other authors have proposed using single holes in a plasmon enhanced sensor<sup>22</sup>. By comparing the field profiles for hole and particle in Figure 6.6, it is evident that the field localisation of the hole is weaker than that of the corresponding particle, suggesting that particles may be more suitable for applications where field localisation is important, such as surface enhanced Raman scattering (SERS). However, the weaker confinement of field for holes may be viewed as a compromise, as the interaction between hole LSPRs renders the optical response highly sensitive to changes in interhole distance, making them a

possible candidate for use in such applications where tunability of the localised resonance is useful. For this purpose, the regular arrays studied here have the distinct advantage of low inhomogeneous broadening compared to random arrays. Furthermore, from a practical perspective, it is easier to engineer hole array structures via a single process of focused ion beam milling as opposed to particle array structures of similar dimensions which require several stages of electron beam lithography.

### 6.12 Concluding remarks

In this section the optical response of metallic films which have been perforated with arrays of subwavelength holes has been considered. In optically thick metal films perforated with periodic arrays of holes, it has been shown that maxima in transmission are observed. The origins of these maxima have been attributed to SPP modes supported by the metal film, in which the periodicity of the holes excites these modes through a grating coupling mechanism. Furthermore, it has been shown that nanometric holes in optically thin metal films support a different type of resonant mode which is localised. A comparison has been made between the behaviour of nanoparticles and nanoholes in non-diffracting arrays and it has been shown that the spectral position of the transmittance minimum associated with the nanohole arrays varies with array period, an effect which is attributed to strong LSPR coupling mediated by SPPs associated with the metal film. However for the complementary particle arrays there is no such shift since this structure does not support SPPs.

In the next two chapters, the nanohole arrays presented throughout this chapter are stacked (vertically) to form different types of metamaterials. In Chapter 7, quarter wavelength thick dielectric layers are used to periodically separate the perforated metallic layers, forming a series of coupled Fabry-Perot cavities similar to those studied in Chapter 2. It is perhaps not surprising that this structure should exhibit optical characteristics which are typical of both Fabry-Perot modes and hole LSPRs. Somewhat unexpectedly, however, the strong interaction between these two resonant modes leads to the observation of a transmission stop band across a wide range of visible frequencies. The spectral position and width of the stop band may independently be tuned by modifying the resonant frequency of the hole LSPR (as shown in this chapter) or the transmission band characteristics of the multilayer stack (as shown in Chapter 2). Furthermore, in Chapter 8 we demonstrate that when the spacing between two hole array layers is reduced to a few tens of nm (such that

the frequencies of the Fabry-Perot transmission resonances are outside of the visible frequency range), hybridization of the hole LSPR modes may occur. As the spacing between layers is decreased below 60 nm, two resonant modes are observed, one is blue shifted to frequencies above the single hole LSPR (the symmetric mode) whilst the other is red-shifted below it (the anti-symmetric mode). Electromagnetic metamaterials which are formed from stacked hole arrays exhibit an effective magnetic response at the resonant frequency of the anti-symmetric coupled LSPR. We show that the interactions between hole LSPRs provides an alternative explanation to the electrical circuit analogy in describing the effective negative index of refraction which is associated with perforated metamaterials.

### Interactions between Fabry-Perot and nanohole resonances in metallo-dielectric plasmonic nanostructures

#### 7.1 Introduction

Whilst the Fabry-Perot (FP) type resonance discussed in Chapter 2 is one example of an electromagnetic mode that is supported by a periodic nano-structure, many others exist. For example, in Chapter 6 the response of metallic films perforated with periodic arrays of subwavelength holes was considered, in which different types of resonant modes may also be supported including localized surface plasmon resonances (LSPRs) similar to those studied in metallic nanoparticle structures<sup>1-4</sup>. For arrays of nanoholes with a sufficiently short periodicity that they are non-diffracting (i.e. zeroth order for frequencies in the vicinity of LSPRs), the electromagnetic coupling between holes leads to a significant modification of the optical response when compared to an isolated hole<sup>5</sup>. In this chapter an investigation will be conducted into the response of multilayer structures (such as those discussed in Chapter 2) which have been perforated with periodic arrays of holes (similar to those in Chapter 6). It is perhaps not surprising that the optical response exhibits both LSPRs and FP-type transmission resonances. However, the optical response also exhibits some unusual characteristics; notably a stop-band in transmission occurring across a wide range of visible frequencies. The stop-band is centred at the LSPR frequency observed for a single layer of holes, and is accompanied by significant absorption. Further numerical simulations identify a shift in frequency of the FP modes as a result of strong interactions between LSPR and FP modes. This interaction is also observed in the simulated dispersion of the modes. The effects of hole diameter, the number of layers in the stacked arrangement and the permittivity of the metal layers on the optical response of the structure will be considered. It is also shown that the spectral width and centre frequency of the stop-band can be tuned by varying the cavity spacing and array periodicity, making these structures useful in optical filter applications. Variant structures in which the metallic layers are not continuous but rather have a “fishnet” structure, not so dissimilar to the structures examined here, are also being keenly pursued as electromagnetic metamaterials<sup>6-8</sup>.

## 7.2 The response of a single metallic layer perforated with a periodic array of holes

Consider the optical response of a planar Ag film with thickness 20 nm (shown in Figure 7.1), which is subsequently perforated with an infinite square array of cylindrical holes having diameter 60 nm and periodicity 150 nm (as shown in the inset of Figure 7.1). The structure is simulated using commercial finite element software (HFSS from Ansoft Corporation)<sup>9</sup>, with a mesh size of 4.5 nm, and is illuminated at normal incidence. The surrounding medium is glass ( $n_r = 1.52$ ,  $n_i = 0.00$ ) and is assumed to be non dispersive over the frequency range of interest, whilst the permittivity values for Ag were taken from reference data<sup>10</sup>. The perforated structure in Figure 7.1 shows a distinct transmittance minimum for incident light of approximately 545 THz ( $\lambda_{\text{vac}} = 550$  nm). At a similar frequency, the absorbance spectrum also shows a clear maximum which is linked to the transmittance minimum. We attribute these transmittance minima / absorbance maxima to the coupling of incident light to dipolar LSPR modes associated with holes in the array, in a manner analogous to that of LSPRs in metallic nanoparticles<sup>1-5</sup>, as discussed previously in Chapter 6. The hole array structure discussed here is slightly different to the hole array structures presented in Chapter 6. For reasons which will become evident later, the regular periodicity of the structures discussed here is 150 nm such that the LSPR associated with the nanoholes occurs for light incident with frequency 545 THz ( $\lambda_{\text{vac}} = 550$  nm). To allow the frequency of the hole LSPR to be tuned across a wider range of visible frequencies, the metallic layers in the simulations are Ag as opposed to the experiments and simulations in Chapter 6 which used Au. Au is not appropriate for observing resonant frequencies in the blue region of the visible spectrum.

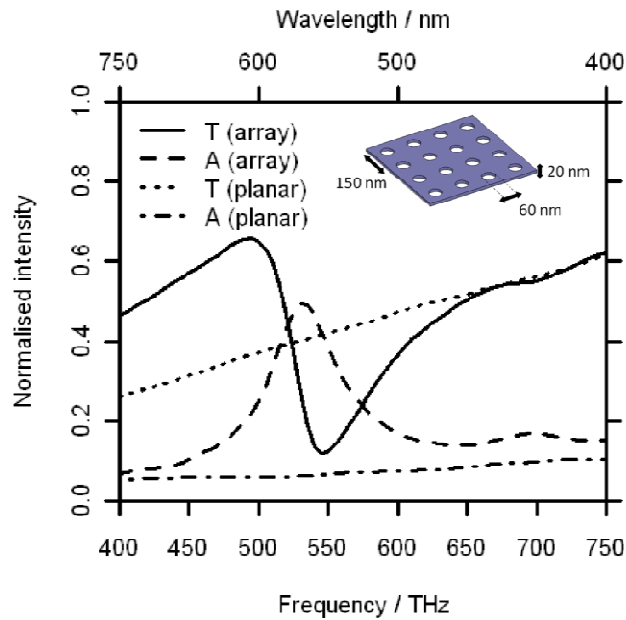


**Figure 7.1:** Simulated transmittance (T) and absorbance (A) spectra at normal incidence for a planar Ag layer (20 nm thickness) perforated with an infinite square array of 60 nm diameter cylindrical holes with periodicity 150 nm (shown in the inset). The surrounding medium has refractive index ( $n_r = 1.52$ ,  $n_i = 0.00$ ).

### 7.3 The response of a multilayer stack comprised of 5.5 periods of (20 nm Ag - 110 nm glass)

In Figure 7.2 the results from a recursive Fresnel technique (Appendix A) are presented which show the simulated optical response of a periodic structure consisting of five planar Ag layers (thickness 20 nm) separated by 110 nm of glass, illuminated at normal incidence with a glass surrounding medium ( $n_r = 1.52$ ,  $n_i = 0.00$ ). The transmittance and absorbance spectra show the four first-order resonant FP modes of the structure, and a partial transmission (pass-band) region for frequencies in the range 475 THz – 750 THz ( $\lambda_{\text{vac}} = 630 \text{ nm} - 400 \text{ nm}$ ). As discussed elsewhere<sup>11</sup>, and in Chapter 2, the width of the pass-band region is known to be independent of the number of layers, and is determined only by the metal and cavity thicknesses forming the unit cell. The pass-band region originates from a resonant tunneling mechanism associated with the evanescent fields in the Ag layers coupling to cavity resonances in the glass layers. In the inset of Figure 7.2, the time-averaged electric field magnitude is plotted as function of position for a cross section taken perpendicular to the metal-glass interfaces. The differences between the resonant

frequencies of the band edges can be explained by reference to the field distributions and the finite conductivity of the Ag layers. At the high frequency band edge (the FP mode at 660 THz ( $\lambda_{\text{vac}} = 454$  nm)), fields in adjacent cavities oscillate out of phase and the majority of the field enhancement occurs within the cavity region. A small amount of the oscillation occurs within the metal layer, with the nodes corresponding to the lowest order resonant mode occurring slightly inside the metal, not at the interface as would be expected for a perfect conductor. This modifies the resonant frequency of the low frequency band edge such that it is red-shifted in comparison to that predicted using a perfect conductor for the metal layers. At the low frequency band edge (the FP mode at 440 THz ( $\lambda_{\text{vac}} = 680$  nm)), fields in adjacent cavities oscillate in phase and a significant proportion of the oscillating field is within the Ag layers. The effective wavelength of this oscillation extends significantly beyond the Ag-glass interfaces such that the wavelength of the lowest order resonant mode is longer than that predicted using the physical size and refractive index of the cavity in the Fabry-Perot equations (refer to Chapter 2 for a detailed derivation). The vertical dashed line in Figure 7.2 illustrates the resonant frequency for a single layer of 20 nm Ag perforated with a square array of holes having diameter 60 nm and periodicity 150 nm.

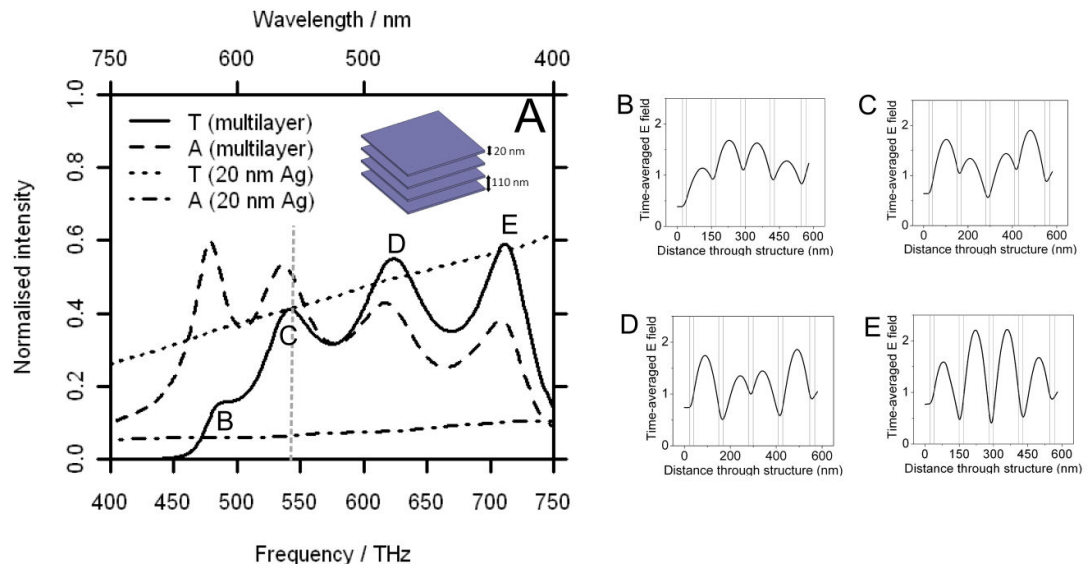


**Figure 7.2:** Simulated transmittance (T) and absorbance (A) spectrum at normal incidence for a single Ag layer (20 nm thickness) and a multi-layer structure consisting of 5 layers of 20 nm Ag separated by 110 nm (A). The surrounding medium has refractive index  $n_r =$

1.52,  $n_i = 0.00$ . The grey line illustrates the resonant frequency for a single layer of 20 nm Ag perforated with holes having diameter 60 nm and periodicity 150 nm. The inset figures (B-E) show the time-averaged electric field magnitude at the resonant frequencies of the FP modes for a cross section taken perpendicular to the stack.

#### 7.4 Multi-layer structures perforated with periodic arrays of subwavelength holes

In this section structures which incorporate features from those in sections 7.1-7.2 will be considered. In Figure 7.3, the simulated transmittance and absorbance spectrum is plotted for a planar structure consisting of 5 layers of Ag with thickness 20 nm separated by 110 nm, perforated with an infinite array of cylindrical holes with 60 nm diameter and 150 nm periodicity. The positioning of the layers is such that holes in adjacent layers are aligned to be directly above each other.

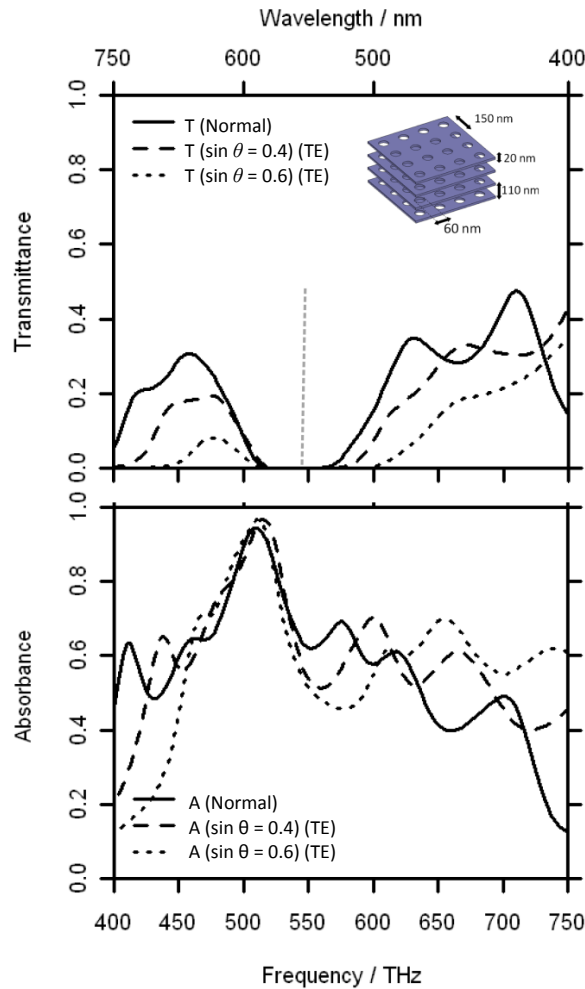


**Figure 7.3:** Simulated transmittance (T) and absorbance (A) spectra for a planar structure consisting of 5 layers of Ag with thickness 20 nm separated by 110 nm, perforated with an

infinite square array of cylindrical holes with 60 nm diameter and 150 nm periodicity. The surrounding medium has refractive index  $n_r = 1.52$ ,  $n_i = 0.00$ . The solid line corresponds to illumination at normal incidence, the dashed and dotted lines correspond to illumination with TE polarized light at angles  $23.5^\circ$  ( $\sin \theta = 0.4$ ) and  $36.9^\circ$  ( $\sin \theta = 0.6$ ) respectively. The grey line at 545 THz represents the resonant frequency for a single layer of Ag perforated with an identical array of holes (Figure 7.1).

There are a number of spectral features which immediately suggest interactions between LSPR and FP modes. As with the planar structure, a series of transmittance maxima are observed in Figure 7.3. However, at normal incidence these are separated by a stop-band centred around 540 THz ( $\lambda_{\text{vac}} = 555$  nm). It is possible to identify similarities between the nature of the stop band and the optical characteristics of the LSPR for the single layer of holes in Figure 7.1. The centre frequency of the stop-band in Figure 7.3 is in close agreement with the LSPR observed for the single layer of holes. The width of the stop-band is also similar to that of the transmittance minima / absorbance maxima which are attributed to the coupling of incident light to LSPRs in the single layer of holes. In comparison with the planar multilayer structure, a shift in frequency of the FP modes is observed, which is dependent on the relative frequencies of both the individual FP modes and the LSPR of the hole.

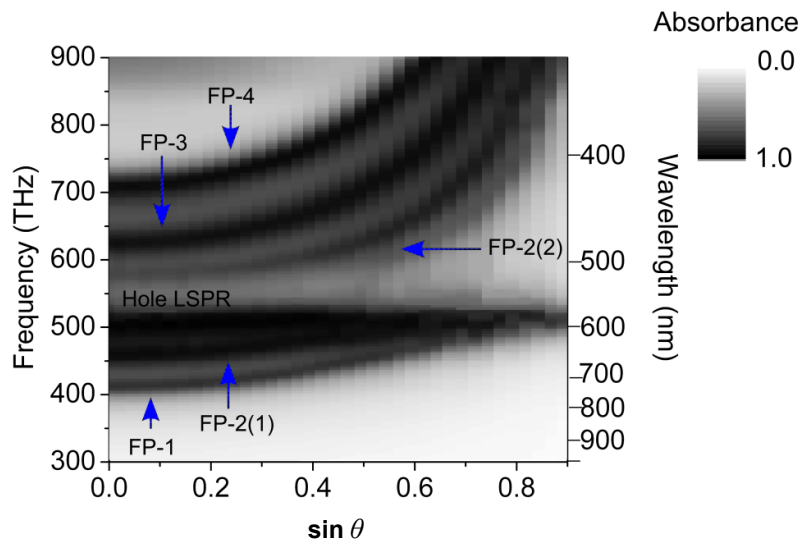


**Figure 7.4:** Contour plot showing the magnitude of the simulated absorbance as a function of frequency and  $\sin \theta$  (where  $\theta$  is the incident angle) for TE polarized light illuminating the structure in Figure 7.3.

In Figure 7.4, the magnitude of the simulated absorbance has been plotted as a function of frequency and incident angle ( $\sin \theta$ ) in order to map the simulated dispersion of the modes supported by the structure. This is shown for the case of transverse electric (TE) polarized light. The dispersion of the mode associated with the LSPR in Figure 7.4 shows a relatively flat-band at a frequency of 510 THz ( $\lambda_{\text{vac}} = 588 \text{ nm}$ ) with absorption close to unity. The response of the structure in Figures 7.3 and 7.4 has been characterized in terms of the incident radiation having Transverse Electric (TE) polarization, where the incident electric field is polarized perpendicular to the plane of angular variation. A stop-band in transmission is also observed across the same frequency range when the structure is illuminated with Transverse Magnetic (TM) polarized radiation, with the modes dispersing in a similar manner as a function of incident angle. The only difference between illuminating the structure with TE and TM polarized radiation lies in the resonant frequencies of the FP modes as a result of their dispersion. Therefore to avoid confusion, any subsequent discussion in this section assumes illumination with TE polarized light. A note should also be made here regarding the spectral form of the resonances in absorption and transmission, as seen in Figures 7.1-7.4, as this will be important when discussing the stop-band in transmission. Unsurprisingly, both the FP resonances and the LSPR hole resonance are identified by resonant absorption features (Figure 7.4). However, the fields associated with the FP modes are localized within the cavity, resulting in a higher than off-resonance field strength on the transmission side of the structure (see Figures 7.2(a) and (b)). Thus resonant transmission peaks (just as from standard FP etalons) are observed upon their excitation. Conversely, the resonance associated with the holes is a highly localized mode confined to the metal film, resulting in an increase in absorption and decrease in transmission. Simplistically, the form of the transmission curves in Figure 7.3 can now readily be understood as resulting from FP-type transmission maxima distributed across the frequency range, with a transmission minimum at 550 THz ( $\lambda_{\text{vac}} = 545 \text{ nm}$ ) arising from the LSPR hole resonance. However, a more complete understanding can be gleaned from investigating the dispersion of the modes in Figure 7.4.

Whilst the three higher frequency modes above the horizontal LSPR disperse as a function of angle in a manner consistent with them being FP type modes, there is a clear interaction between the LSPR and the modes occurring at a lower frequency than the LSPR. Closer inspection of Figure 7.4 shows that the resonance associated with the hole is situated amongst what appears to be five FP modes. Given that the structure consists of only four cavities, from the analysis of multi-layer structures one would expect only four first-order

FP modes to be observed. The observation of what would appear to be five modes is unexpected. In order to explain the origin of this apparent additional mode, we have performed modeling of both perforated and planar 20 nm thick Ag layers separated by a dielectric (a simpler, 3 layer system, as opposed to the 7 layer system studied for Figure 7.4), calculating their absorbance as a function of frequency and dielectric layer thickness for normally incident light (Figure 7.5).

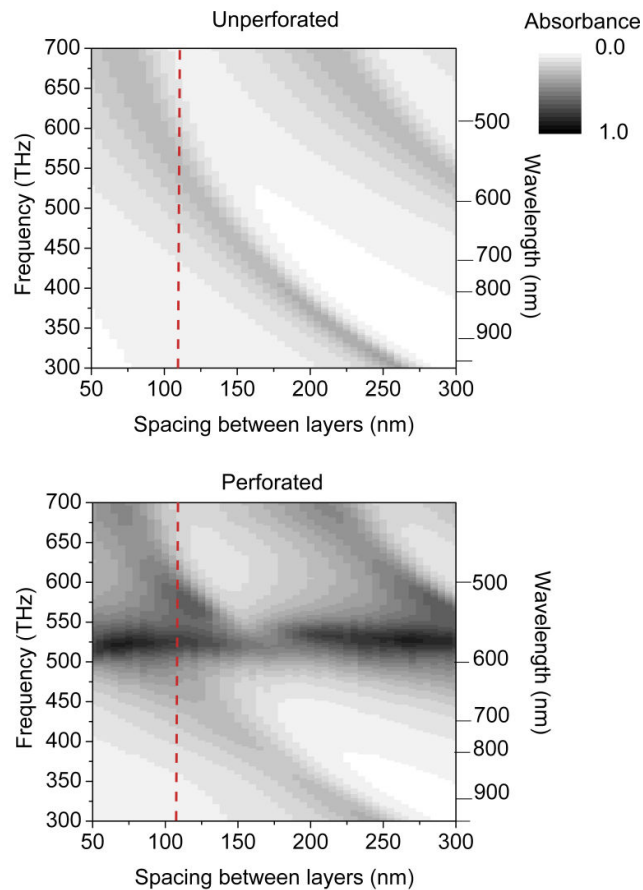


**Figure 7.5:** The magnitude of the simulated absorbance is plotted as a function of frequency and spacing between two non-perforated (top) and perforated (bottom) Ag layers with thickness 20 nm. The perforated structure consists of an infinite square array of cylindrical holes with diameter 60 nm and periodicity 150 nm. The results are for normal incidence, with surrounding medium  $n_r = 1.52$ ,  $n_i = 0.00$ . The dashed line represents the separation of the metal layers in the structures described in Figures 7.2 and 7.3.

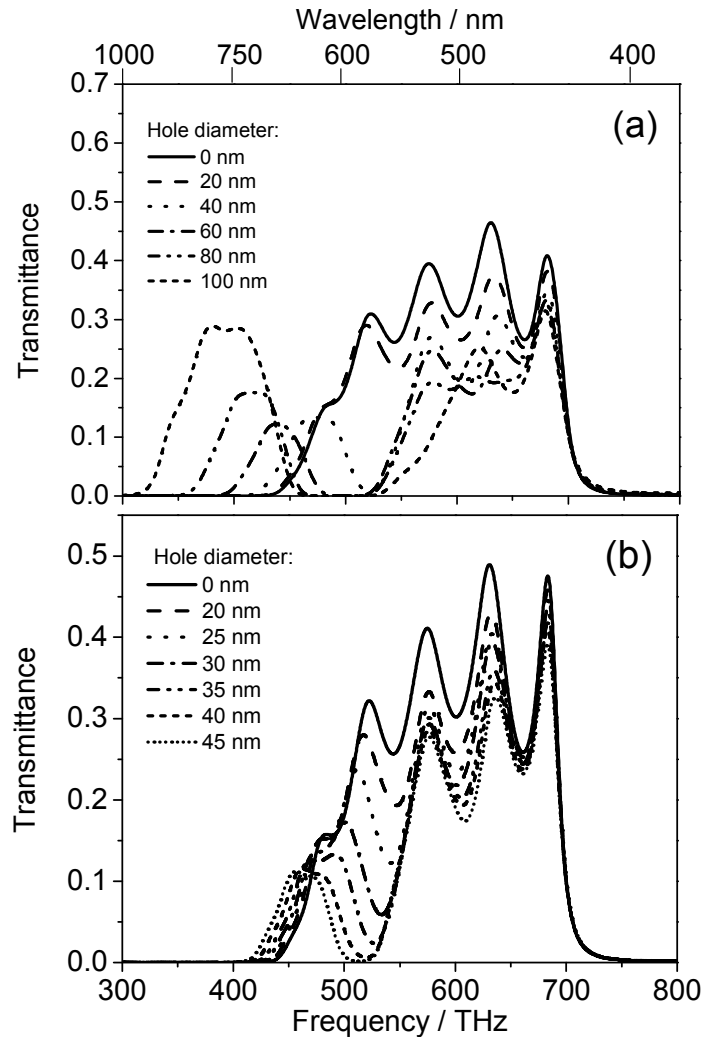
On inspection of Figure 7.5 the origin of the additional mode now becomes apparent: The first order FP mode, which for the planar system disperses from 300 THz ( $\lambda_{\text{vac}} = 1000$  nm) for a layer spacing of 250 nm to approximately 700 THz ( $\lambda_{\text{vac}} = 428$  nm) for a layer

spacing of 50 nm, interacts strongly with the LSPR such that for some range of layer spacings (including 110 nm, as studied in Figure 7.4) there appears to be three modes, with two of them corresponding to the first order FP mode which straddles the LSPR. With this knowledge we can identify all of the modes evident in Figure 7.4; an LSPR and 4 FP modes, one of which is straddling the LSPR mode resulting in it appearing to be two distinct modes. As mentioned previously, and as clearly evident in Figure 7.4, the two lower frequency FP modes tend towards the LSPR frequency with increasing angle of incidence, whilst FP modes above this frequency continue to follow the expected FP-type dispersion. A consequence of this is that the frequency gap between the FP-type modes above the LSPR and those below it widens as the angle of incidence is increased, with a corresponding increase in the width of the transmission stop-band. For example, at  $\sin \theta = 0.8$  in Figure 7.4, the width of the stop-band has more than doubled relative to that which is observed at normal incidence, such that it occurs across the frequency range  $\sim 500$  THz – 660 THz ( $\lambda_{\text{vac}} = 600$  nm – 454 nm).

### 7.5 Effects of hole diameter on the interaction between LSPRs and FP modes

From previous studies, it is known that amongst other factors the polarisability of a metallic nanoparticle is proportional to its volume. In Chapter 6, it was shown that the same principle can be applied when considering the volume of a nanometric hole in a thin metallic film. Through increasing the diameter of the holes, it was shown that the absorbance associated with the hole LSPR is increased and the magnitude of the transmittance minimum decreases. In this section similar investigations which vary the diameter of the holes are performed using perforated multilayer structures. Clearly when the diameter (and therefore the volume) of the hole is small, the absorbance associated with the LSPR is expected to be relatively low. The optical response should appear similar to that of a non-perforated metal-dielectric stack, exhibiting a series of FP resonant modes. As the hole diameter is increased, the polarisability associated with the charges induced in the rim of the holes should increase, and spectral features (such as absorbance maxima and/or transmittance minima) arising from excitation of the hole LSPR should become identifiable in the optical response. When the diameter of the holes is sufficiently large, the extinction associated with the hole LSPR may exceed the magnitude of the transmission within the pass-band region. One would expect a stop-band in transmission to be observed having a spectral width which is comparable to that of the hole LSPR. To

investigate this concept further, numerical simulations have been performed which investigate the effect of increasing the diameter of the holes. Figure 7.6 shows the simulated transmittance of a structure comprised of 6.5 periods of 20 nm Ag / 120 nm glass ( $n_r = 1.52$ ,  $n_i = 0.00$ ), which has been perforated with an infinite square array of cylindrical holes with periodicity 200 nm. In (a) the hole diameter has been increased from 20 to 100 nm in increments of 20 nm, and in (b) the diameter is increased from 20 nm to 45 nm in increments of 5 nm.



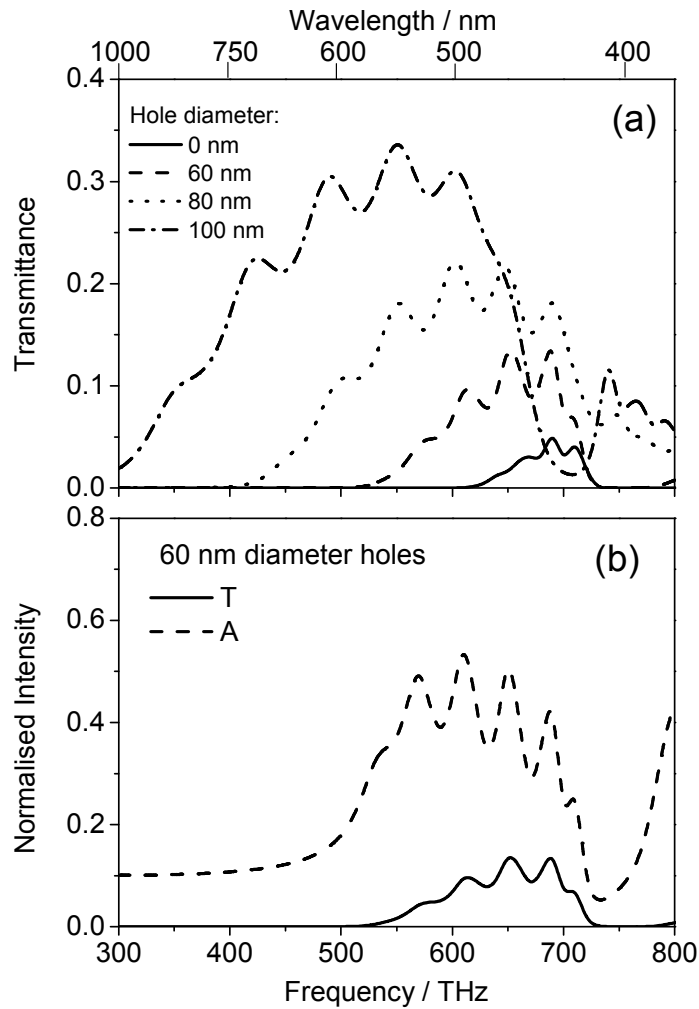
**Figure 7.6:** The simulated transmittance is shown for a structure comprised of 6.5 periods of 20 nm Ag / 120 nm glass ( $n_r = 1.52$ ,  $n_i = 0.00$ ), perforated with an infinite square array of cylindrical holes having periodicity 300 nm and diameters ranging from (a) 20 nm to 100 nm and (b) 20 nm to 45 nm. The structure is illuminated at normal incidence in a glass surrounding medium.

Figure 7.6 confirms previous expectations that for holes with small diameters (e.g. 20 nm), the optical response is relatively unchanged in comparison to the non-perforated structure. The extinction associated with the hole LSPR increases significantly for diameters between 25 – 45 nm, and for holes with a diameter of 45 nm leads to the eventual observation of a stop band across the frequency range  $4.5 - 4.6 \times 10^{14}$  Hz ( $\lambda_{\text{vac}} = 666 \text{ nm} - 652 \text{ nm}$ ). For hole diameters in excess of 45 nm, the width of the stop band increases symmetrically about its centre frequency as a consequence of the hole LSPR width increasing with size. For holes with diameter 100 nm, the stop-band has widened such that it covers frequencies across the range  $4.3 - 4.7 \times 10^{14}$  Hz ( $\lambda_{\text{vac}} = 697 \text{ nm} - 638 \text{ nm}$ ). The resonant frequency of the hole LSPR also red-shifts with increasing diameter, which is explained by near-field interactions between holes in adjacent unit cells and dynamic depolarization effects. Both near-field interactions and dynamic depolarisation lead to a reduction in the restoring force which is experienced by charges induced in the rim of the hole, and a lower resonant frequency than would be predicted by the electrostatic approximation. This behaviour was also observed experimentally for a single layer of holes.

## 7.6 Effects of dispersion on the centre frequency and spectral width of the stop-band

An interesting area to explore is the effects of metallic dispersion on the interaction between FP and LSPR modes. It is well known that the dispersive nature of metals at visible frequencies is fundamental to the excitation of LSPRs in both nanoparticles and nanohole structures, as has been shown on many occasions throughout this thesis. In Chapter 4, the electrostatic approximation was used to derive the resonant condition for metallic particles. For small spheres, it can be shown that the frequency of the LSPR occurs when the real component of the metal permittivity ( $\epsilon_r$ ) is equal to  $-2$ . For alternative non-spherical geometries such as metallic discs or ellipsoids, the resonant permittivity value can also be determined with prior knowledge of both the volume and aspect ratio of the particle, as we discussed in Chapter 4 (Section 4.3). If the effects of dispersion in the metal layers were to be removed, such that the resonant permittivity condition could not be satisfied (for example if the metallic layers in the structure were to have a fixed permittivity of  $\epsilon = -32 + 1.8i$  across all wavelengths), it would be impossible for the excitation of the hole LSPRs to occur. This could have significant implications on the optical response of the stacked hole array structures. In the absence of dispersion,

coupling to LSPRs would be inhibited; however one would still expect the structure to exhibit a series of FP modes. This is because the structure is still essentially comprised of a series of partially reflective layers separated by dielectric cavities. Although a fixed permittivity may slightly modify the resonant frequencies of the FP modes (since the penetration depth of the electromagnetic fields into the metal layers may differ), the general FP transmission characteristics of the structure should be very similar. In (a) of Figure 7.7, the simulated transmittance is plotted for a structure comprised of 6.5 periods of 20 nm Ag / 120 nm glass, perforated with an array of cylindrical holes having periodicity 200 nm and diameters ranging from 60 nm to 100 nm. The permittivity of the metal here is assumed to be fixed such that it has a value of  $\epsilon = -32 + 1.8i$  at all wavelengths. It can be observed that the structure exhibits a series of FP resonances across two transmission bands, an effect not previously observed when modeling with dispersive Ag. The assumption that the metal is non-dispersive also enables second-order FP resonant modes to be observed in a second transmission band for frequencies above  $7 \times 10^{14}$  Hz. Furthermore, there is no evidence in the optical response which suggests that incident light is coupling to hole LSPRs in this structure. Inset (b) of Figure 7.7 shows the simulated transmittance and absorbance for a structure which has been perforated with 60 nm diameter holes. This structure is comprised of six cavities, and there are a total of six transmittance minima / absorbance maxima which are associated with the excitation of first-order FP resonant modes. The field distributions for each of these modes were discussed previously (and in Chapter 2). From the analysis in Section 7.4, if hole LSPRs were to be excited in this structure, one would expect to observe six absorbance maxima due to the FP modes, plus additional maxima arising from the LSPRs and any subsequent interactions. Again, there appears to be no evidence for this in Figure 7.7



**Figure 7.7:** (a) The simulated transmittance is shown for a structure comprised of 6.5 periods of 20 nm Ag / 120 nm glass, perforated with an array of cylindrical holes having periodicity 200 nm and diameters ranging from 60 nm to 100 nm. The permittivity of the metal is assumed to be  $\epsilon = -32 + 1.8i$  across all wavelengths. (b) The simulated transmittance (T) and absorbance (A) is shown for 60 nm diameter holes. The structures are illuminated at normal incidence in a glass surrounding medium.

Although LSPR excitation does not occur in this structure, variations in hole diameter still have a significant effect on the optical response. As the hole diameter is increased two effects are observed. Firstly, the transmittance magnitude of the pass-band is increased. This can be explained through a reduction in the fractional occupancy of the metal in the layers bounding the dielectric cavities which leads to reduced absorption of the enhanced

fields. Secondly, the frequencies of both the low frequency and high frequency band edges are red-shifted with increasing hole diameter. This is particularly evident for the low frequency band edge, which has shifted in frequency from  $5 \times 10^{14}$  Hz ( $\lambda_{\text{vac}} = 600$  nm) for 60 nm diameter holes to  $3 \times 10^{14}$  Hz ( $\lambda_{\text{vac}} = 1000$  nm) for 100 nm diameter holes. This can be explained by referring to the field profiles at the band edges for the non-perforated structure in Figure 7.2. At the high frequency band edge, the majority of field enhancement occurs within the glass region. However, at the low frequency band edge, a significant proportion of the enhanced field extends into the metal layers, rendering the FP mode highly sensitive to changes in the thickness and permittivity of the metal layers. If the metal layers are perforated with non-resonant holes the perforated metal film behaves as a composite structure, having an effective permittivity which is dependent on the filling fraction of the holes. It is therefore expected that any structural modifications to the metal layers such as introducing a surface corrugation or perforations of holes will induce a greater relative shift in the FP modes at lower frequencies compared to those at higher frequencies.

### 7.7 Increasing the number of layers in the stacked arrangement

From the investigations presented in Chapter 2 it was established that the width of the transmission band of a metal-dielectric planar multilayer arrangement is independent of the number of layers, and is dependent only on the thicknesses of the metal and dielectric layers comprising the unit cell. A stop-band in transmission which is accompanied by a shift in the resonant frequencies of the FP modes has been identified when a multilayer structure is perforated with holes exhibiting LSPRs. The magnitude of the frequency shift is dependent on the relative frequencies of the individual FP modes and the hole LSPR. The structure in Figure 7.3 is comprised of four periods of Ag-glass, and the frequency of the hole LSPR is such that four FP modes are split in a symmetrical manner across the stop band (two modes occur at frequencies below the stop band, and two above it). In a non-perforated structure, it is expected that increasing the number of periods should give rise to a greater number of transmission maxima within the pass-band region. If the number of periods of the perforated structure is increased, it is expected that the stop band arising from the LSPR should remain, but a greater number of transmission maxima should be distributed on either side of the stop band. Indeed, in Figure 7.6 a structure of 6.5 periods (with slightly different parameters) is shown in which six transmission maxima are observed (three at frequencies above the stop band, and three below it). If the number of

layers is further increased, for example so that the structure now has 12.5 periods of 20 nm Ag / 120 nm glass (Figure 7.8), then it is reasonable to expect a total of twelve transmission maxima to be observed above or below the stop band. This is not particularly clear from Figure 7.8, and, whilst the stop-band remains a prominent feature, distinguishing the total number and precise character of the modes is non-trivial. The transmission maxima arising from FP modes occurring at longer wavelengths are increasingly broadened. Perforating the metal layers removes a significant proportion of the metal content and lowers the reflectivity of the interfaces which separate the dielectric cavities. A consequence of reducing the reflection efficiency of the metal layers is that the quality factor of the observed FP transmission resonances is significantly reduced. With the exception of the obvious difference in the number of layers, the structures which give the results presented in Figures 7.6 and 7.8 are otherwise identical. If the transmittance spectra for arrays consisting of 100 nm diameter holes are compared, it is found that the stop-band occurs across an identical frequency range. Combined with the evidence proposed in the previous discussion, this enables the conclusion to be made that the centre frequency and width of the stop-band is independent of the number of layers.

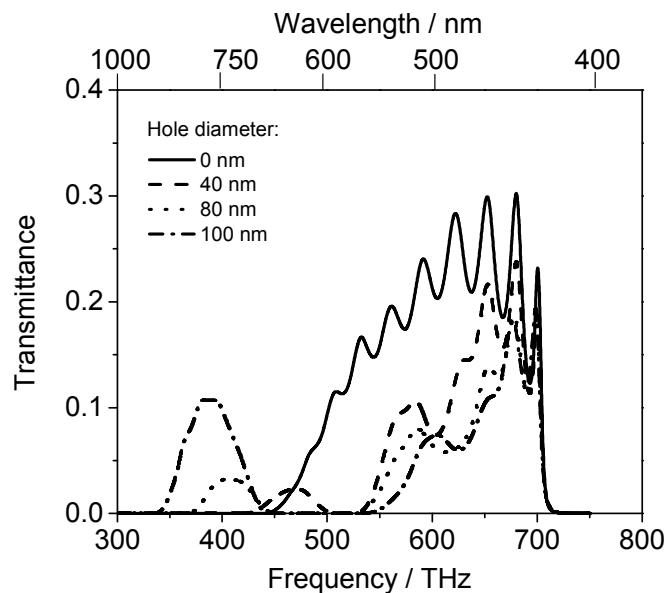


**Figure 7.8:** The simulated transmittance is shown for a 12.5 period structure of 20 nm Ag / 120 nm glass, perforated with an array of square cylindrical holes having periodicity 300 nm and diameters ranging from 40 nm to 100 nm. The structure is illuminated at normal incidence in a glass surrounding medium ( $n_r = 1.52$ ,  $n_i = 0.00$ ).

## 7.8 Tunability of the stop-band

It has previously been shown that the resonant frequencies of both LSPR and FP modes can be tuned<sup>5,11-13</sup>. Since it has been identified that the transmittance stop-band originates through the interaction between these two types of resonant mode, it should be possible to modify the respective resonances such that the stop-band can occur across any desired frequency range. To demonstrate this tunability, consider a structure consisting of 4.5 periods of 20 nm Ag / 140 nm glass, perforated with an array of 90 nm diameter holes with periodicity 225 nm. The simulated transmittance and absorbance spectra for a single layer of the hole array, and the multilayer non-perforated structure are shown in (a) and (b) of Figure 7.9 respectively.

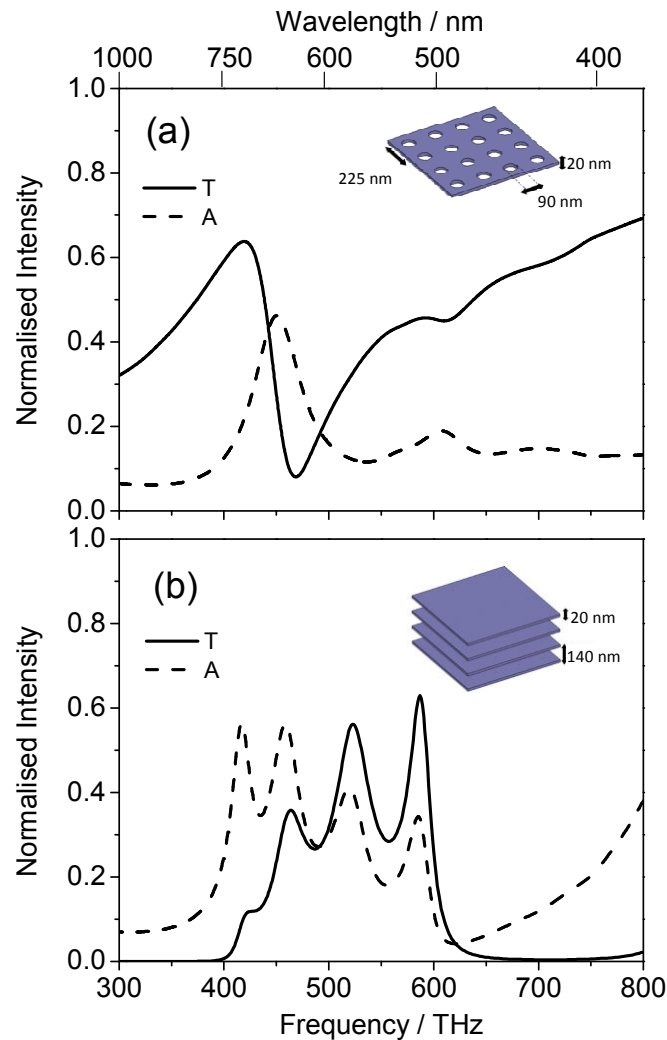


**Figure 7.9:** The simulated transmittance (T) and absorbance (A) spectra are shown for (a) a single layer of Ag with thickness 20 nm, perforated with an infinite square array of cylindrical holes with periodicity 225 nm and diameter 90 nm, (b) a multilayer structure

comprised of 4.5 periods of planar 20 nm Ag / 140 nm glass layers. The structures are illuminated at normal incidence in a glass surrounding medium.

The resonant frequency of the hole LSPR is similar to that of the structure in Figure 5.1, occurring at approximately  $4.80 \times 10^{14}$  Hz ( $\lambda_{\text{vac}} = 625$  nm). Similarly, the transmission band for the non-perforated multilayer arrangement is across frequencies in the range  $4.15 - 6.00 \times 10^{14}$  Hz ( $\lambda_{\text{vac}} = 720 - 500$  nm). The simulated transmittance spectrum of the perforated multilayer structure is shown in Figure 7.10, where the stop-band has been shifted in frequency relative to the structure in Figure 7.3, and is observed across frequencies in the range 440 THz – 495 THz ( $\lambda_{\text{vac}} = 681 - 606$  nm). In this instance, it has been shown that a variation in the array geometry modifies the coupling strength between LSPRs, leading to a red-shift in the resonant frequency of the hole LSPR, whilst increasing the thickness of the dielectric cavity region leads to a red-shift of frequencies in the transmission pass-band.

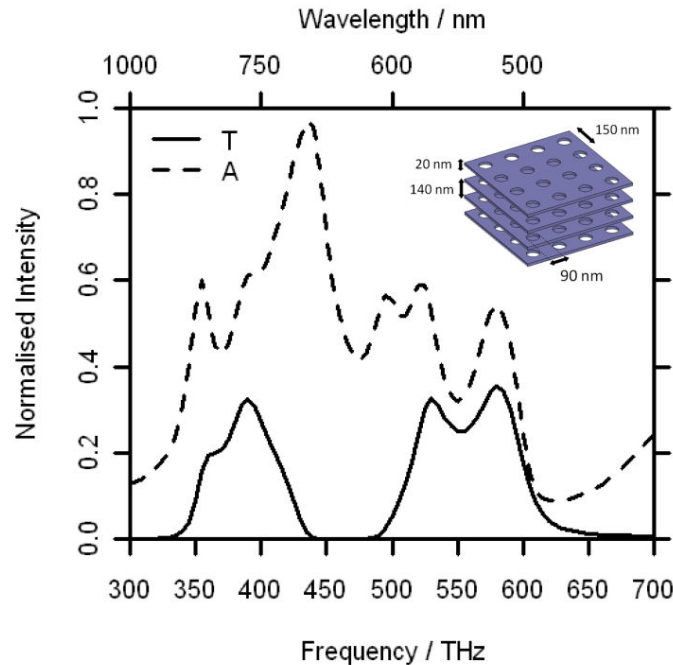


**Figure 7.10:** Simulated transmittance (T) and absorbance (A) spectrum at normal incidence for a planar structure consisting of 5 layers of Ag with thickness 20 nm separated by 140 nm, perforated with an infinite square array of cylindrical holes with 90 nm diameter and 225 nm periodicity. The structure is illuminated at normal incidence in a glass surrounding medium.

## 7.9 Concluding remarks

This chapter presents an investigation into the origins of a stop-band which is observed in the transmittance of metallo-dielectric one-dimensional photonic band gap structures which have been perforated with periodic arrays of holes. By considering a single Ag layer perforated with holes, and a planar Ag-glass multilayer stack, it has been shown that the stop-band originates through coupling between FP cavity resonances and LSPRs associated with the holes. The effects of hole diameter, permittivity variation, and the number of layers on the width and centre frequency of the stop-band have been investigated. It has been shown that the optical response that is associated with the stop-band is independent of the number of layers, and can be tuned by modifying the resonant frequencies of the FP modes and the hole LSPRs. This high degree of tunability at visible frequencies is a desirable property for optical filter applications. It also has relevance in the design of fishnet-type electromagnetic metamaterials, a topic which will be discussed extensively in the next chapter.

### The role of localised resonances in negative index metamaterials

#### 8.1 Introduction

In 1904, Lamb<sup>1</sup> discussed the concept of mechanical systems having phase and group velocities in opposite directions, something which later formed the fundamental basis of negative index materials. The term “negative index” was first used by Veselago<sup>2</sup> to describe materials which possessed both a negative electric permittivity and negative magnetic permeability. More recently, Pendry<sup>3</sup> proposed that a layer of an isotropic material whose real component of refractive index is equal to  $-1$  could be used to form a perfect lens, focusing both the near and far field components of a point source and allowing detail to be resolved below the Rayleigh limit. Driven by this goal, a new generation of artificially engineered negative index metamaterials have evolved. These materials, composed of sub-wavelength elements that exhibit electric and magnetic resonances, have been utilised in numerous applications ranging from negative refraction<sup>4,5</sup> to sub-wavelength focusing<sup>6,7</sup> and invisibility ‘cloaking’<sup>8</sup>. Experimental verification of a metamaterial with a negative index of refraction was first performed in the GHz frequency regime using a three dimensional arrangement of copper wires and split rings<sup>9</sup>. The frequency response was explained using an analogy to the inductor-capacitor (LC) arrangement in an electrical circuit, whereby the inductive elements are attributed to the metallic wires, and the capacitive elements to the split rings<sup>9,10</sup>. More recently, an exciting advance has been the development of near infrared/visible frequency negative index metamaterials, engineered by perforating a stacked arrangement of metallic and dielectric layers with sub-wavelength holes to create a ‘fishnet’ type structure<sup>4,11</sup>.

In this chapter, the behaviour of coupled localised surface plasmon resonances (LSPRs) both in ‘fishnet’-type structures and stacked arrays of metallic particles is discussed. The role of LSPRs in facilitating a negative index of refraction is further elucidated. Using finite element numerical modelling, it is shown that complimentary hole and particle LSPRs occur at similar frequencies, and give rise to both electric (permittivity) and magnetic (permeability) resonances. In the fishnet structure, the frequency of the magnetic resonance coincides with the negative effective permittivity, and a region of negative index of refraction is observed. However, in the stacked particle arrangement, due to a mismatch

between the frequency regions of negative permittivity and magnetic resonance, no region of negative index is observed. It will be shown that this characteristic behaviour essentially arises from the complementary nature of hole and particle LSPRs.

## 8.2 The concept of a perfect lens, and the importance of negative index of refraction in perfect lensing applications

In 2000, Pendry<sup>3</sup> showed that a material which exhibited a negative index of refraction may be used to form a perfect lens. The resolution of an image which is formed by a conventional lens is limited by the wavelength of the illuminating radiation. To illustrate this limitation, consider the imaging of a point dipole which oscillates with frequency  $\omega$  using a conventional lens (Figure 8.1).

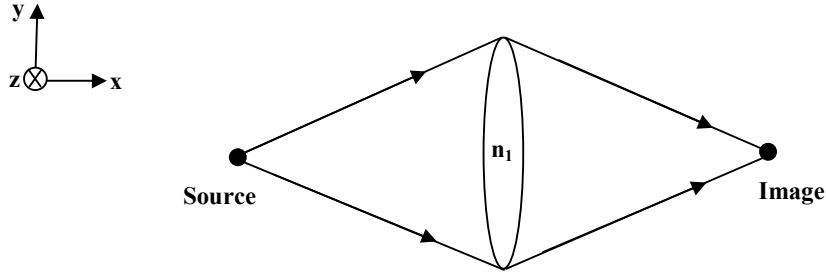


**Figure 8.1:** A conventional lens having a positive index of refraction ( $n_1$ ) is used to form an image of a point source. The arrows represent ‘ray’ directions.

The electric field of the dipole may be expressed using a two-dimensional Fourier expansion (Equation 8.1).

$$\mathbf{E}(r, t) = \sum_{k_x, k_y} \mathbf{E}(k_x, k_y) \exp(i(k_x x + k_y y + k_z z + \omega t)) \quad 8.1$$

The Maxwell equations can be used to show that:

$$k_{z1} = +\sqrt{\left(\frac{\omega}{c}\right)^2 - k_x^2 - k_y^2} \quad \text{where } \left(\frac{\omega}{c}\right)^2 > k_x^2 + k_y^2 \quad 8.2$$

The conventional lens forms an image by applying a phase correction to each of the Fourier components. Equation 8.2 is valid for the case where  $(\omega/c)^2 > k_x^2 + k_y^2$ , however if the values of the transverse wave vector ( $k_x$  or  $k_y$ ) are large, such as in the near-field, then Equation 8.2 may instead be expressed as:

$$k_{z2} = i\sqrt{k_x^2 + k_y^2 - \left(\frac{\omega}{c}\right)^2} \quad \text{where } \left(\frac{\omega}{c}\right)^2 < k_x^2 + k_y^2 \quad \mathbf{8.3}$$

The condition in Equation 8.3 is only satisfied in the near-field, where  $k_{z2}$  is an evanescent wave which decays exponentially with  $z$ . In a conventional lens, these components are negligible and do not contribute to image formation. The maximum resolution ( $\Delta$ ) of the image which is formed by a conventional lens is given by:

$$\Delta = \frac{2\pi}{k_{max}} = \frac{2\pi c}{\omega} = \lambda \quad \mathbf{8.4}$$

Note that the maximum possible value of  $\mathbf{k}$ , ( $k_{max}$ ), associated with the real components of the wave vector is determined by taking the square root of the condition in Equation 8.2, in which the maximum possible value of  $k_x^2 + k_y^2$  is equal to  $(\omega/c)^2$ . However, in a planar isotropic slab of material which has a negative index of refraction ( $\epsilon_{real}, \mu_{real} = -1$ ), Pendry showed that the evanescent waves arising from Equation 8.3 are amplified<sup>3</sup>. Within the slab,  $n = -1 + 0i$ , and Equations 8.2 – 8.3 become:

$$k'_{z1} = -\sqrt{\left(\frac{\omega}{c}\right)^2 - k_x^2 - k_y^2} \quad \text{where } \left(\frac{\omega}{c}\right)^2 > k_x^2 + k_y^2 \quad \mathbf{8.5}$$

$$k'_{z2} = +i\sqrt{k_x^2 + k_y^2 - \left(\frac{\omega}{c}\right)^2} \quad \text{where } \left(\frac{\omega}{c}\right)^2 < k_x^2 + k_y^2 \quad \mathbf{8.6}$$

The recursive Fresnel method which is presented in Appendix A can be used to determine the transmission and reflection coefficients at normal incidence for a planar isotropic layer which has refractive index  $n = -1 + 0i$  and thickness  $d$ . These are shown in Equations 8.7 and 8.8:

$$T_s = T_p = \exp(-ik_z d) \quad \mathbf{8.7}$$

$$R_s = R_p = 0 \quad \mathbf{8.8}$$

$$\text{i.e. } T_s = T_p = \exp\left(\sqrt{k_x^2 + k_y^2 - \left(\frac{\omega}{c}\right)^2} d\right) \quad \text{where } \left(\frac{\omega}{c}\right)^2 < k_x^2 + k_y^2 \quad \mathbf{8.9}$$

Substituting Equation 8.6 into 8.7 shows that within the medium, the evanescent waves increase in amplitude (Equation 8.9). Beyond the lens, both propagating and evanescent waves may contribute to image formation. Pendry showed that light which is incident on the layer is refracted at a negative angle with respect to the surface normal<sup>3</sup>. A first focus is formed inside the negative index medium, beyond which the light diverges to the exit interface, where negative refraction again occurs and the light is brought to a focus for a second time (Figure 8.2).

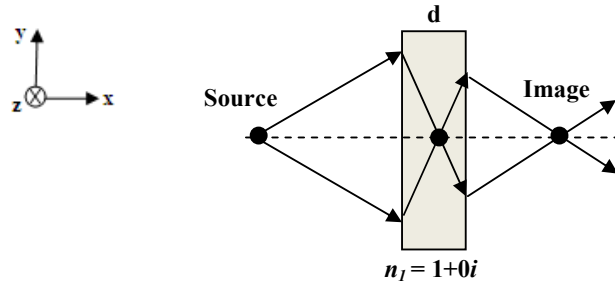


**Figure 8.2:** The use of a planar isotropic slab having  $n_l = -1 + 0i$  and thickness  $d$  for the imaging of a point source. The arrows represent ‘ray’ directions.

In the near-field,  $k_{max}$  from Equation 8.4 is not limited to  $(\omega/c)$ , but rather is given by  $\sqrt{k_x^2 + k_y^2 + k_z^2}$ , which comprises both the near-field and the far-field components of the point source. This value of this square root is greater than  $(\omega/c)$ , leading to a significant improvement in the resolution of the device. As Pendry states<sup>3</sup>, that beyond practical limitations (such as the surface topology of the lens, or the absorption of the medium), there are no obstacles to the perfect reconstruction of an image.

### 8.3 Negative index response of a composite structure formed from metallic wires and split ring resonators

The first experimental demonstration of a negative index of refraction was performed at microwave frequencies by Shelby et al.<sup>9</sup>. The metamaterial structure in this experiment consisted of a three dimensional array of thin copper wires and split rings, fabricated on circuit board material which was formed from fibre glass (shown in Figure 8.3). In order to experimentally determine the index of refraction, a prism shaped sample of the metamaterial was positioned at the end of a planar waveguide such that radiation could be refracted at the exit interface of the prism. A microwave radiation detector was then used

to probe the angular distribution of the scattered radiation. The experimental results were then combined with Snell's law and knowledge of the prism dimensions to determine the effective refractive index.

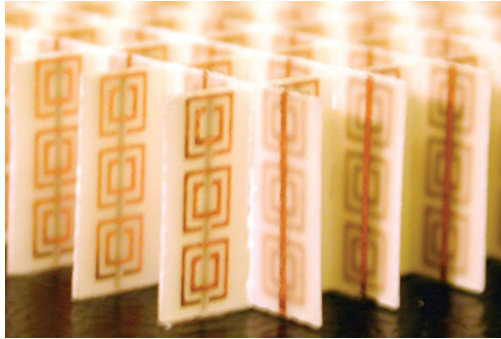


**Figure 8.3** reproduced from 9: The experimental sample used by Shelby et al. consisted of copper split ring resonators and copper wire strips on circuit board material. The rings and wires are positioned on opposite sides of the board.

For this sample, the origin of the negative index of refraction is explained through the structure simultaneously exhibiting electric and magnetic resonances. The electric response arises from the copper wire strips, and the magnetic response from that of the split rings, as will now be explained.

***Electric response:***

It was shown in Section 4.3 (metallic nanoparticles) that when an incident electric field is applied across a metallic structure, the conduction electrons move in a direction which opposes the direction of the applied field, and a dipole moment is induced across the structure. Excitation of the localised surface plasmon resonance (LSPR) was shown to occur at the condition for maximum polarisability of the structure, and this was characterised optically by the strong scattering of electromagnetic radiation. When the dimensions of the metallic elements are sufficiently small (approximately  $\lambda/20$  or less), the effective permittivity of the structure may be described using a Drude-type dielectric function. In this regime, the induced dipole moments across the metallic elements are negligible, and the electrons emit radiation in proportion to their acceleration (similar to a continuous metallic sheet). The radiation which is scattered arises from the electric response of the structure. The effective permittivity for thin a composite material formed from thin metallic wires, as derived by Pendry<sup>12</sup> is given by Equation 8.10.

$$\epsilon_{eff} = 1 - \frac{\omega_p^2}{\omega \left( \omega + i \frac{\epsilon_0 a^2 \omega_p^2}{\pi r^2 \sigma} \right)} \quad 8.10$$

Here  $\omega_p$  is the plasma frequency of the metal,  $\omega$  is the angular frequency of the incident radiation,  $a$  is the periodicity of the structure,  $r$  is the radius of the thin wire,  $\epsilon_0$  is the permittivity of free space and  $\sigma$  is the conductivity of the metal.

***Magnetic response:***

It has been shown that when a time varying magnetic field is applied to a single continuous metallic ring (CMR) as shown in Figure 8.4, surface currents are induced around the ring<sup>13</sup>. The flow of the induced currents produces an internal magnetic field. In addition, the incident electric field drives surface currents across the ring (from left to right), and radiation is emitted in proportion to the induced dipole moment. In this instance, the interference which is observed between the incident and scattered E / H fields arises due to the magnetic response of the structure.

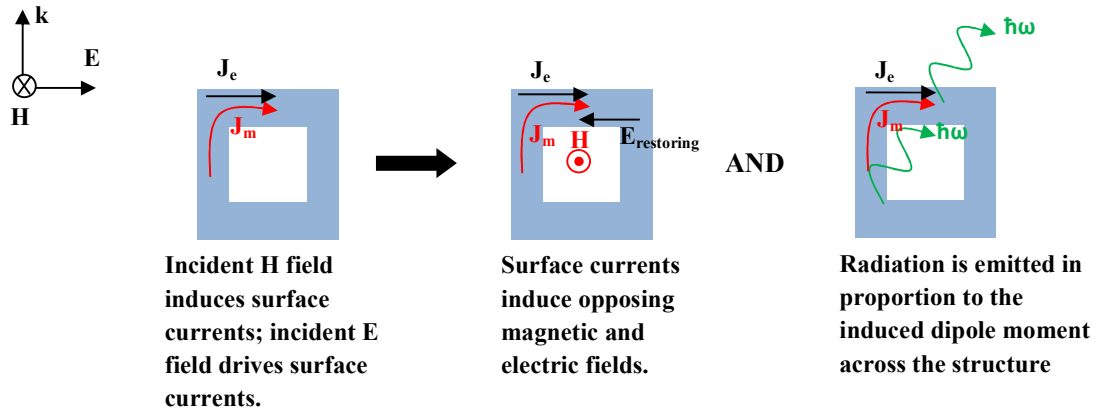


**Figure 8.4:** The magnetic response of a continuous metallic ring (CMR).

More recently, split ring resonators (SRRs) have also been shown to exhibit an effective magnetic response. A SRR is a CMR which is broken in one place by an air or dielectric gap (Figure 8.5). As with the CMRs in Figure 8.4, when a time-varying magnetic field is incident along a direction which is perpendicular to the plane of the ring, surface currents are induced. A fundamental difference here is that charge may accumulate at the ends of the SRR such that the direction of the electric field across the gap ( $\mathbf{E}_{\text{gap}}$ ) opposes the direction of the induced currents. A SRR exhibits a structural resonance (often referred to

in the literature as an ‘LC’ resonance) which is associated with the effective capacitance of the dielectric gap and the effective inductance of the loop which defines the ring. A strong magnetic response is observed at the resonant frequency of the LC arrangement (illustrated in Figure 8.5). As with the CRs shown in Figure 8.4, the flow of the induced currents produces an internal magnetic field, and the incident electric field also drives surface currents across the ring (from left to right). However, the nature of the LC resonance in SRRs means that the magnetic response of the structure is significantly enhanced in comparison to CMRs.

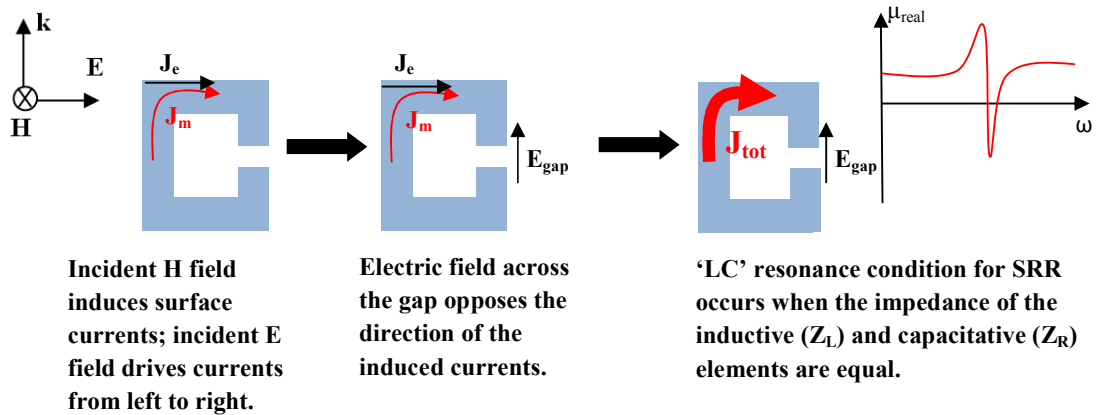


**Figure 8.5:** Split ring resonators exhibit an LC resonance which is associated with the effective capacitance of the dielectric gap and the effective inductance of the loop which defines the ring.

The magnetic response of a SRR may be enhanced by arranging a pairs of SRRs inside each other, as shown in Figure 8.6. In this configuration the resonant condition is also determined by the mutual capacitance and inductance between the inner and outer rings. It has also been shown by other authors<sup>14</sup> that in this arrangement, the resonant frequency associated with the two rings may be significantly reduced in comparison to the outer ring. This property may at first appear to be of little benefit, since it is known that the resonant frequency of the SRR may be reduced simply by increasing the dimensions of the ring. However in regular arrays of SRRs, increasing the dimensions of the unit cell decreases the frequency at which diffraction is observed. For an array of double SRRs (illustrated in Figure 8.6), the effective permeability of the composite structure is given by Equation 8.11<sup>12</sup>.

$$\mu_{eff} = 1 - \frac{\frac{\pi r^2}{a^2}}{1 + i \frac{2l\sigma_l}{\omega r \mu_0} - \frac{3lc_0^2}{\pi \omega^2 \ln\left(\frac{2c}{d}\right) r^3}} \quad 8.11$$

Here  $r$  is the radius of the inner ring,  $a$  is the periodicity of the structure,  $l$  is the distance between two adjacent SRRs (along the  $z$  axis),  $\sigma_l$  is the resistance per unit length of the metal sheets measured about the circumference,  $\mu_0$  is the permeability of free space,  $c_0$  is the speed of light in free space,  $\omega$  is the angular frequency of the incident radiation,  $c$  is the width of each ring and  $d$  is the separation between inner and outer rings.

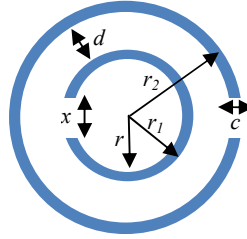


**Figure 8.6:** An example of a circular pair of split ring resonators (SRRs), with illustrated dimensions corresponding to those in Equation 8.11.

A negative index material (as proposed by Veselago <sup>2</sup>) requires a material with both negative  $\epsilon$  and  $\mu$ , and so for the design of such a material to be successful the electric and magnetic responses must therefore overlap. The magnetic response therefore has to be tuned such that the resonant frequency of the SRR is below the effective plasma frequency of the composite wire array. It is these principles which have been exploited in the experimental sample of Shelby et al <sup>9</sup>. These structures may also be utilised at visible frequencies, but additional factors must be considered. In the visible regime, the finite skin depth of the metal and the effects of localised resonances must be taken into account in addition to the simple geometric scaling which may be applied to structures at microwave frequencies. The fabrication of SRRs at visible frequencies also requires the use of advanced lithographic techniques which allow finer control over structural dimensions.

#### 8.4 Negative index response of fishnet-type metamaterial structures

Zhang et al. <sup>4</sup> have fabricated metamaterial structures which exhibit a negative index of refraction at infrared frequencies. Here, focused ion beam milling was used to produce square arrays of rectangular holes from a multilayer structure consisting of 10.5 periods of (30 nm Ag – 50 nm MgF<sub>2</sub>). A schematic of the structure is shown in (a) of Figure 8.7. The dimensions of the rectangular holes were 565 nm × 265 nm, and the periodicity of the square array was 860 nm. The ion beam was used to mill a prism shape from the fishnet arrangement, which was illuminated with light incident at various incident angles and wavelengths. The angle of incidence was determined using knowledge of the experimental configuration and the geometrical details of the prism which had been milled into the stack. A CCD was placed in the plane beyond the sample such that the positional difference could be calculated between light which passes through the planar multilayer stack, and that which is refracted by the prism. Experimental measurements identified a negative index of refraction across a wide range of frequencies (this data is shown in (b) of Figure 8.7).

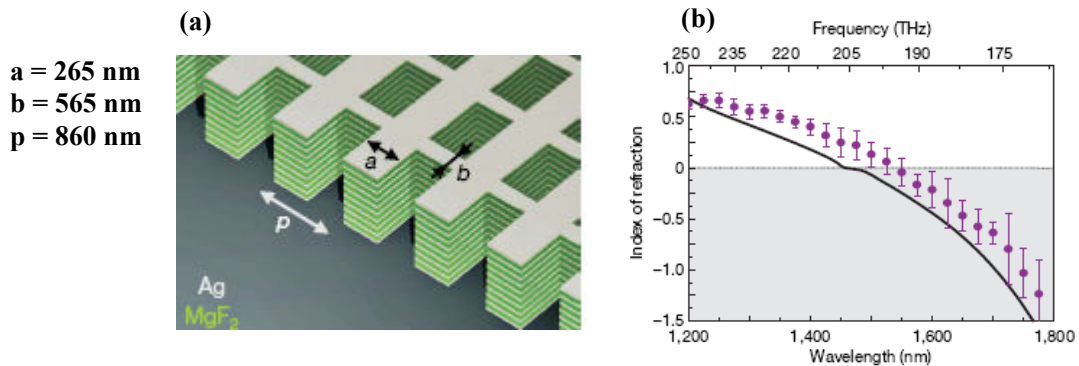


**Figure 8.7** reproduced from reference 4: Diagram of a 21 layer fishnet structure formed from layers of Ag with thickness 30 nm and MgF<sub>2</sub> with thickness 50 nm. The structure has been milled to produce a square array of rectangular holes with dimensions 565 nm × 265 nm, and periodicity 860 nm (a). Simulated and experimental index of refraction data obtained for the ‘fishnet’ structure shown in (b).

It is possible to describe the electric and magnetic responses of the fishnet structure at microwave frequencies in terms of LC resonances <sup>15</sup>. It should be noted that in this instance the equations which were derived assume that the metallic layers are near perfect conductors. A similar principle may be used to consider metallic layers which have finite conductivity (such as the response of Ag visible frequencies), however the equations must

be modified to consider the finite penetration depth of the electric and magnetic fields into the metal. Therefore for simplicity only the derivation for near-perfect conductors will be presented here. The unit cell of the fishnet structure used in the derivation of Soukoulis et al.<sup>15</sup> is shown in inset (a) of Figure 8.8.

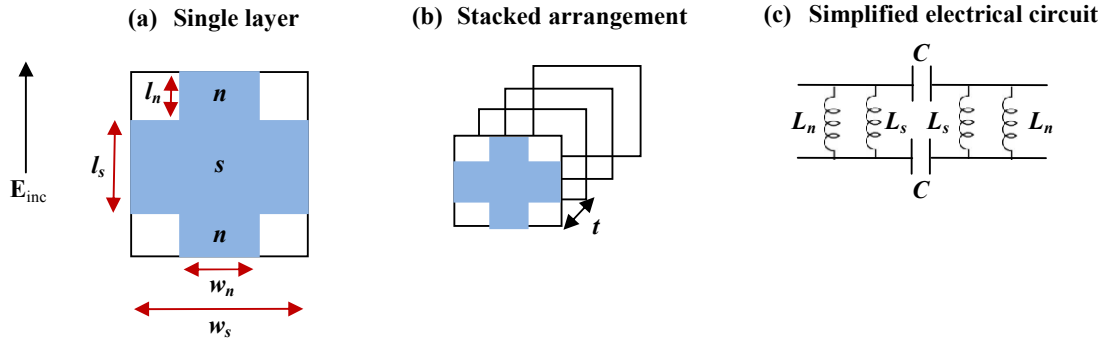


**Figure 8.8:** The structural dimensions of a single layer of the fishnet structure which was analysed by Soukoulis et al.<sup>15</sup> is shown (a), this layer stacked to form periodic structure where the layers are separated by  $t$  (b). Assuming the incident electric field is polarized in the direction shown, the equivalent electrical circuit model for this arrangement may be simplified to that shown in (c).

#### *Electric response:*

The electric response of the fishnet structure may be understood in a similar manner to that of the three dimensional wire arrangements. However, the response is not entirely determined by an effective plasma frequency. In this structure, dipolar resonances associated with the short axes of the wires may also contribute to the optical response. At microwave frequencies, these dipolar resonances are equivalent to the localised surface plasmon resonances (LSPRs) which are observed in metallic nanoparticle structures at visible frequencies. The presence of these dipolar excitations lowers the effective plasma frequency of the wire arrangement, such that the resonant frequency of the combined system is lower than both  $\omega_{electric}$  associated with the conducting layer and  $\omega_{dipole}$  of the short axis dipole resonance. In the development of fishnet structures it is therefore preferable to optimise  $\omega_{electric}$  to be as large as possible, since below the effective plasma frequency the permittivity of the metamaterial may be described by a Drude-type response. The equation for the effective plasma frequency of the electric response  $\omega_{electric}$  is given by Equation 8.12, where A and B are constants and all other parameters are the geometrical terms which were previously defined in Figure 8.8.

$$\omega_{electric} = \frac{A}{w_s \ln\left(\frac{l_s}{w_s}\right)} + \frac{B}{w_s \ln\left(\frac{l_n}{w_n}\right)} \quad 8.12$$

*Magnetic response:*

Taking into account the effective LC model of the fishnet structure, the resonant frequency of the magnetic resonance (for near perfectly conducting layers) is defined by Equation 8.13. From the geometry which is presented in inset (a) of Figure 8.8, Soukoulis et al. showed that when the incident electric field is polarised parallel to the short axes of the perforations,  $C$ ,  $L_s$  and  $L_n$  may be given by Equations 8.13 – 8.16<sup>15</sup>:

$$\omega_m^2 = \frac{1}{LC} = \frac{1}{L_s C} + \frac{1}{L_n C} \quad 8.13$$

$$C = \frac{l_s w_s + 2l_n w_n}{t} \quad 8.14$$

$$L_n = \frac{l_n t}{w_n} \text{ and } L_s = \frac{l_s t}{w_s} \quad 8.15 - 8.16$$

Here  $L_s$  and  $L_n$  represent the inductance arising from circulating currents inside the metallic ‘slab’ and ‘neck’ regions of the fishnet structure. In (a) of Figure 8.8 these regions are denoted by  $s$  and  $n$  respectively. The incident magnetic field drives surface currents along the metallic layers in a similar manner to the SRR, where an LC-type resonance is observed. In this instance, the capacitive elements arise from the accumulation of charge across the holes in the metal layers. Similarly, the inductive elements arise from surface currents in the ‘slab’ and ‘neck’ regions, as shown in Figure 8.9.

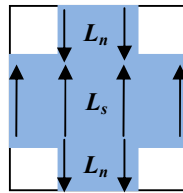


**Figure 8.9:** An illustration of the surface currents which are formed in the slab and neck regions of the fishnet structure in the uppermost layer of the fishnet structure at the frequency of the magnetic resonance  $\omega_m$ . In a metamaterial, the directions of the surface currents in adjacent layers are aligned anti-parallel.

Equations 8.12 and 8.13 are successful in deriving the resonant frequencies of the electric and magnetic response of fishnet structures at microwave frequencies. However these equations are no longer valid in fishnet structures where the metal may not be described as a near-perfect conductor. For example, taking the dimensions of the structure of Zhang et al.<sup>5</sup> shown in Figure 8.7 predicts a resonant frequency of approximately 30 MHz. This is because the penetration depth into the metal at visible frequencies significantly modifies the resonant frequencies of the capacitive and inductive elements. However, as identified by several of authors<sup>4,6</sup>, the concept of effective plasma frequencies and LC type resonances may still be used to give an insight into the origins of the electric / magnetic responses in fishnet metamaterials at visible frequencies. The geometry of the fishnet structure allows for simultaneous excitation of both electric and magnetic responses, and it behaves as a “double negative (both  $\epsilon, \mu < 0$ )” negative index material.

### 8.5 Extraction of effective parameters

When characterising the response of a metamaterial structure, it is particularly important to determine the effective parameters of the structure, for example the effective permittivity  $\epsilon$ , permeability  $\mu$  or refractive index  $n$ . The significance of these effective parameters is such that if they were assigned to a homogeneous layer of material having equivalent thickness to the metamaterial structure, identical transmission and reflection coefficients would be obtained. It should be noted that they do not represent the permittivity or permeability of the individual metallic elements within the material. A great deal of information about the resonant behaviour of metamaterials can be obtained from the effective parameters. There are several methods in which the effective refractive index can be determined from the transmission and reflection coefficients. In this section three different extraction techniques will be considered.

Consider the amplitude transmission  $t$  and reflection  $r$  expressions for a homogenous planar film<sup>16</sup>, shown in Equations 8.17 and 8.18. Here,  $n$  represents the complex refractive index of the film,  $\omega$  is the angular frequency of the incident radiation,  $l$  is the film thickness and  $z$  is the complex impedance of the film. The incident wave is of the form  $\mathbf{E} = E_0 \exp(i(kx - \omega t))$ .

$$t = \frac{1}{\cos\left(\frac{n\omega l}{c}\right) - \frac{i}{2}\left(z + \frac{1}{z}\right)\sin\left(\frac{n\omega l}{c}\right)} \quad 8.17$$

$$r = \frac{-\frac{i}{2}\left(z - \frac{1}{z}\right)\sin\left(\frac{n\omega l}{c}\right)}{\cos\left(\frac{n\omega l}{c}\right) - \frac{i}{2}\left(z + \frac{1}{z}\right)\sin\left(\frac{n\omega l}{c}\right)} \quad 8.18$$

If it is assumed that the thickness of the film  $l$ , is small in comparison to the incident wavelength, the sine and cosine terms may be approximated using a Taylor series expansion and the expressions may be rearranged in terms of  $n$ . The resulting solutions to  $n_r$  and  $n_i$  contains a square root, and so have two pairs of solutions. The only pair of solutions with any physical meaning is that which has  $n_i > 0$ . The number of terms used in the Taylor expansion has implications on the accuracy of any recovered parameters. To illustrate this, simulations of homogeneous planar films of different thicknesses have been performed (using a recursive Fresnel method (Appendix A)). In the simulation, various combinations of  $\varepsilon$  and  $\mu$  have been specified for the parameters of the planar film in order to simulate refractive indices which are real(positive), real(negative) and imaginary. Following this, the simulated transmission and reflection coefficients have been substituted back into the approximation and used to recover the effective refractive index of the structure. Two approaches are considered in which a first-and second order expansion of the sine and cosine terms in Equations 8.17 and 8.18 has been used.

*First order Taylor expansion:*

The solution for  $n$  using a first-order Taylor series expansion is given in Equation 8.19. Figure 8.10 shows the real and imaginary components of the effective refractive index as a function of the ratio between the sample thickness and the incident wavelength. The parameters for the layers used in the recursive Fresnel simulations were (a)  $\varepsilon = 3, \mu = 2$  (b)  $\varepsilon = -3, \mu = 2$  and (c)  $\varepsilon = -3, \mu = -2$ , respectively.

$$n_{eff} = \pm \frac{c}{\omega l} \sqrt{\frac{(1+r-t)(-1+r+t)}{t^2}} \quad 8.19$$

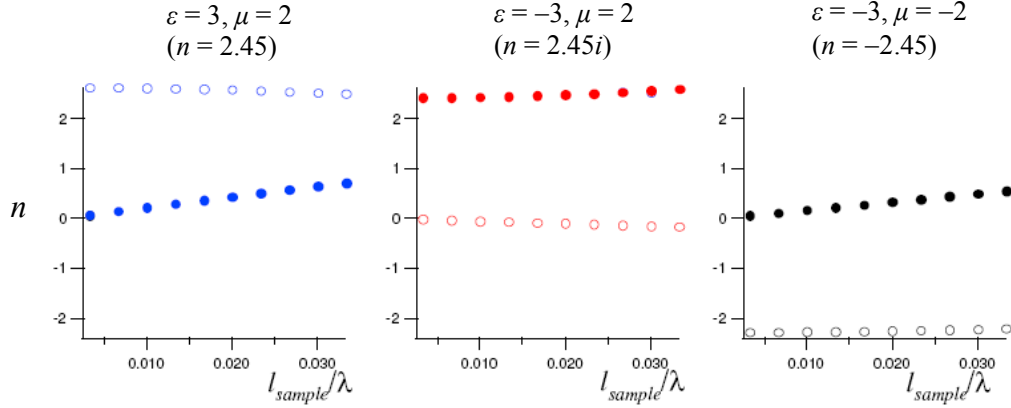


**Figure 8.10:** The real (hollow circles) and imaginary (solid circles) components of the effective refractive index obtained using Equation 8.19 are shown for three homogeneous layers with parameters (a)  $\varepsilon = 3, \mu = 2$  ( $n = 2.45$ ) (b)  $\varepsilon = -3, \mu = 2$  ( $n = 2.45i$ ) and (c)  $\varepsilon = -3, \mu = -2$  ( $n = -2.45$ ).

A significant difference is observed in the extracted value of  $n$  as the ratio of  $l_{\text{sample}}/\lambda$  is increased. For example, when  $l_{\text{sample}}/\lambda = 0.03$  the real component of the effective refractive index is approximately 7% smaller than the absolute physical value. This error is also evident in the imaginary component of the refractive index, which should be equal to zero, however for  $l_{\text{sample}}/\lambda = 0.03$  the recovered value is 0.7.

*Second order Taylor expansion:*

The accuracy of the extraction procedure may be increased through increasing the Taylor series expansion to include second order terms (Equation 8.20). Figure 8.11 shows the real and imaginary components of  $n$  as a function of the ratio between the sample thickness and the incident wavelength. The test layers in the recursive Fresnel simulations have identical parameters to those in Figure 8.10.

$$n_{\text{eff}} = \pm \frac{c}{\omega l} \sqrt{\frac{2\sqrt{r^2 + t(2-t)} - 2}{t}}$$

**8.20**

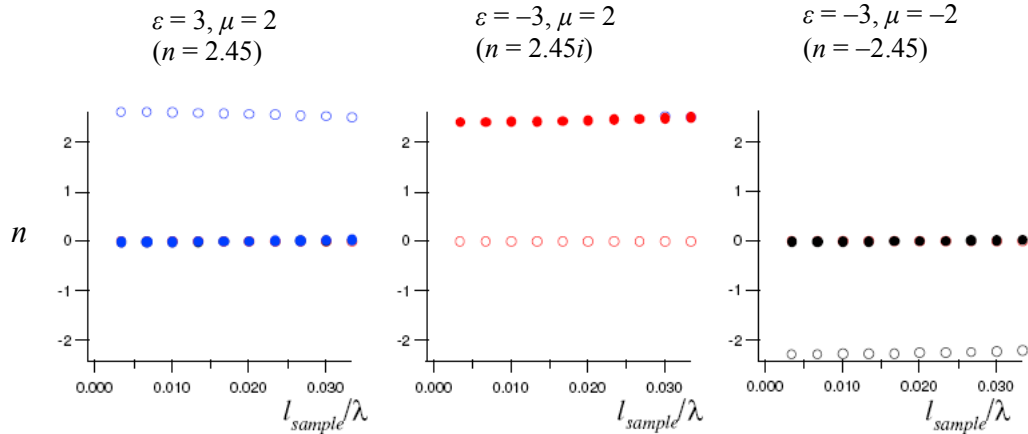


**Figure 8.11:** The real (hollow circles) and imaginary (solid circles) components of the effective refractive index obtained using Equation 8.20 are shown for three homogeneous layers with parameters (a)  $\varepsilon = 3, \mu = 2$  (b)  $\varepsilon = -3, \mu = 2$  and (c)  $\varepsilon = -3, \mu = -2$ .

When comparing the relative error of the extracted parameters from Figures 8.10 and 8.11, it is noted that the relative error between the effective and physical parameters is significantly reduced when using the second-order approximation. Whilst this extraction process gives a useful insight into the dependence of the refractive index in determining the transmission / reflection of a structure, it unfortunately cannot be applied to metamaterial structures. This is because metamaterials contain resonant elements, which may be strongly absorbing at the resonant frequency. For example, at the LSPR frequency for particle (Chapter 5) and hole (Chapter 6) arrays, it was found that the excitation of LSPRs could be characterised by transmittance minima and absorbance maxima in the optical response. If the transmittance of the structure is reduced, then the initial assumption that the terms contained within the cosine and sine functions in Equations 8.19 and 8.20 are small is invalid. For metamaterials a rigorous approach is required to extract the effective parameters, and this will now be discussed.

*Rigorous extraction procedure for metamaterial structures:*

In this section the main features of a metamaterial extraction procedure proposed by Smith et al<sup>17</sup>, will be described, a process which utilises some of the previously derived equations for the thin film approximation. The impedance of the metamaterial is first obtained from the transmission and reflection coefficients using Equation 8.21. As with Equation 8.19, there are two pairs of solutions, however the only solution with any physical meaning is that which has  $z_r > 0$ .

$$z = \sqrt{\frac{1 + 2r + r^2 - t^2}{1 - 2r + r^2 - t^2}} \quad 8.21$$

The obtained values for the impedance are substituted into Equations 8.17 and 8.18, which is rearranged for an expression in terms of  $n$ . The periodic nature of the sine and cosine functions in both Equations 8.17 and 8.18 implies that there are an infinite number of possible solutions to  $n$ , given by Equations 8.22 and 8.23.

$$\frac{nw l}{c} = \sin^{-1} \left[ \frac{2i}{\left(z - \frac{1}{z}\right)} \frac{r}{t} \right] \pm 2m\pi \quad 8.22$$

$$\frac{nw l}{c} = -\sin^{-1} \left[ \frac{2i}{\left(z - \frac{1}{z}\right)} \frac{r}{t} \right] \pm (2m + 1)\pi \quad 8.23$$

Where  $m = 0, 1, 2, \dots$

A sensible question to ask at this point is - just how should a valid solution for  $n$  be chosen when the transmittance / reflectance of the structure appears degenerate? If  $m = 0$ , it can be shown that the solutions in Equations 8.22 and 8.23 reduce to those which are obtained using the thin film approximation. The method of Smith et al.<sup>17</sup> suggests that the extraction procedure should first be applied in the frequency regime where the structure is highly transmitting. For example, if an array of particles were to be considered, the extraction procedure would first be performed away from the LSPR frequency, where the transmittance is close to unity. In this region, it is known that the thin-film approximation is valid ( $m = 0$ ). Once the values of  $n$  have been determined in this region, the continuity of  $n$  (as a function of frequency) is enforced to determine solutions across the complete frequency spectrum. In section 8.4, this extraction process has been used to obtain the effective parameters of the metamaterial structure published by Zhang et al.<sup>4</sup>. In order to test the extraction procedure, the structure from Figure 8.7 was first simulated using a finite element method (Ansoft HFSS)<sup>18</sup>, with a mesh size of 4.0 nm. Permittivity values for Ag were obtained from reference data<sup>19</sup>. The complex transmission and reflection coefficients from the results of the simulation were used to determine the effective index of refraction of the structure. The results are shown in Figure 8.12, where there is good

agreement between the simulated and published data in both the magnitude and line shape of the effective refractive indices. This enables us to be fully confident in the extraction procedure when characterising the effective index of refraction of other types of metamaterial structures further on in this chapter.

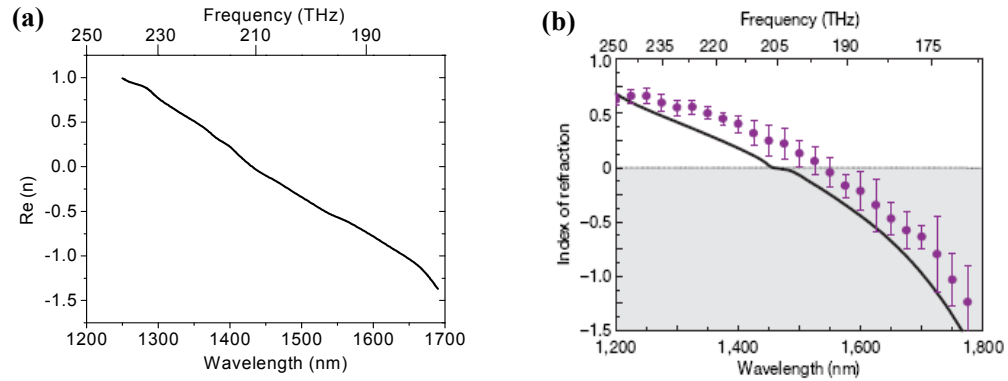


**Figure 8.12:** The extraction procedure described in section 8.2 was used to determine the effective refractive index from the simulated transmission and reflection coefficients obtained from finite element simulations (a). This is compared with the published data of Zhang et al.<sup>4</sup> (b).

### 8.6 Localised resonances in fishnet-type metamaterials

From previous studies presented in this thesis (particularly Chapter 6), it is known that metallic films perforated with nanoholes may support localised resonances which are similar to those observed in nanoparticle structures. It is therefore reasonable to expect that a single perforated metallic layer from the structure of Zhang et al. should also exhibit LSPRs (associated with either the long or short axes of the holes). Since the dimensions of the hole array structures investigated by Zhang et al. are considerably larger than that of the structures in Chapter 6, the excitation of LSPRs here would be expected to occur at lower (infrared) frequencies. The finite element simulations from Section 8.2 were used to explore the response of a single perforated metallic layer from the structure in Figure 8.7. The sample was illuminated at normal incidence, with the incident electric field polarised either along the long or the short axis.

LSPRs were observed for light incident with a wavelength of approximately 1100 nm (for the long axis) and 1900 nm (for the short axis). Figure 8.13 shows the time-averaged electric field distributions at the resonant frequencies of the long and short axes

respectively, for a cross section which is taken through the centre of the structure. Recall that for a hole LSPR, the frequencies of the long and short axes resonances are effectively reversed when compared to those of a particle. This is due to the polarisability associated with a nanohole in metallic film behaving in a reciprocal manner to that of a metallic particle. The resonant wavelengths for the single layer are slightly outside the wavelength range corresponding to the region of negative index in the stacked metamaterial structure. This is not particularly surprising; since it is known that the interaction between layers in the stacked arrangement leads to a modification of the resonant frequency in comparison to a single layer.

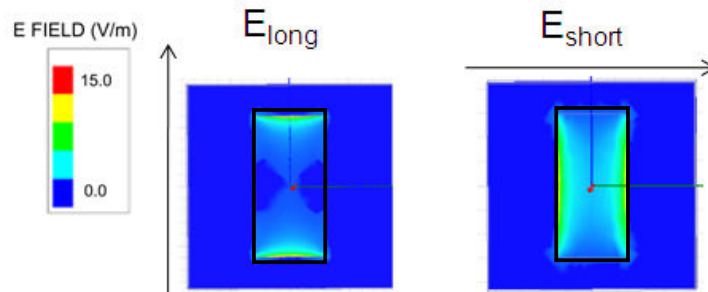


**Figure 8.13:** The time-averaged electric field distribution is shown at the resonant frequency for a single metallic layer of the fishnet structure in Figure 8.7. The arrows above and alongside the field distributions indicate the polarisation direction of the incident electric field.

In Figure 8.13 it can be observed that at the LSPR frequencies, significant field enhancement occurs within the hole, a feature which is also common to the hole array structures studied in Chapter 6. Furthermore, it is known that when two structures exhibiting LSPRs are placed within a few tens of nm, electromagnetic interactions between adjacent layers may lead to hybridization of the localised plasmon resonances, and the observation of symmetric / anti-symmetric coupled modes. This suggests that in a stacked metamaterial such as the fishnet structure presented in Figure 8.7, localised resonances may also be involved in facilitating the negative index response. In the metallic nanohole arrays which were considered in Chapters 6 and 7, the dimensions of the structures were such that the excitation of LSPRs occurred at visible frequencies. The remaining part of this chapter will investigate the behaviour of coupled LSPRs in stacked hole and particle arrays at visible frequencies.

### 8.7 Coupled LSPRs in stacked metallic nanohole and nanoparticle structures

In Figure 8.14, the simulated transmittance and absorbance spectra are compared for complementary 2D arrays of cylindrical holes (curve A) and particles (curve B) formed from an Ag film with thickness 20 nm. For each of the structures, the hole / particle diameter is 90 nm and the square periodicity of the array is 225 nm. This comparison has been performed for Au hole / particles in Chapter 6. In both structures, distinct transmission minima are observed at 480 nm (hole array) and 495 nm (particle array) which are accompanied by absorbance maxima at 490 nm. The absorbance maxima in both particle and hole structures are attributed to the coupling of incident radiation to LSPR modes associated with the respective charges which are induced across the nanoparticle and in the vicinity of the nanoholes in the metallic film.

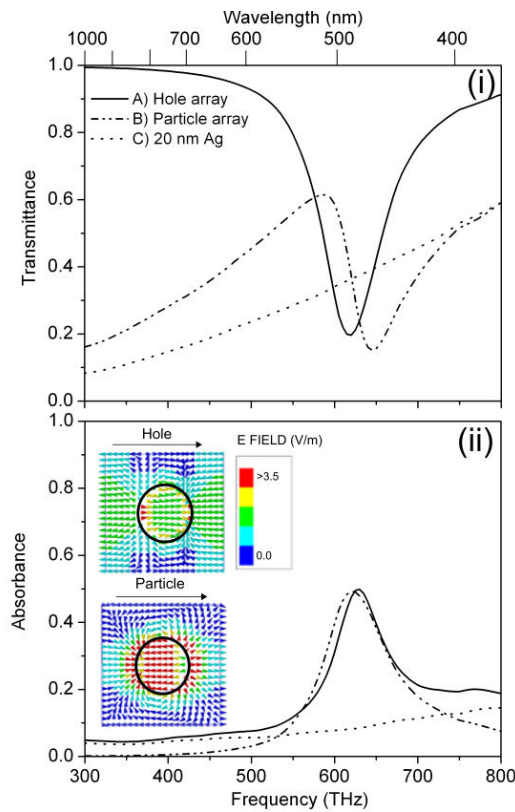


**Figure 8.14:** Simulated transmittance (i) and absorbance (ii) spectra are shown for an infinite array of 90 nm diameter holes in a 20 nm thick Ag film with periodicity 225 nm (A), an infinite array of 90 nm diameter, 20 nm height cylindrical Ag particles with periodicity 225 nm (B) and a 20 nm thick continuous Ag film (C). In all simulations the structures were illuminated at normal incidence in vacuum. The inset of (ii) shows the instantaneous scattered electric field vector across the unit cell of the hole and particle array structures. Both profiles are shown at the same instant in phase for radiation incident

with frequency  $6.25 \times 10^{14}$  Hz ( $\lambda_{\text{vac}} = 480$  nm). The arrows above the field distributions indicate the direction of the incident field vector.

The inset of (ii) in Figure 8.14 shows the instantaneous scattered electric field vectors at the resonant frequency, for a cross section taken perpendicular to the plane of incidence through the centre of the hole and particle array structures. The scattered electric field vectors within the hole are aligned anti-parallel such that the fields oscillate out of phase with respect to the incident electromagnetic field. As will be discussed later, the reversed phase of the hole LSPR compared to a particle LSPR has important implications for negative index in the 3D, stacked metamaterials.

Previously it has been shown that when structures exhibiting LSPRs are placed in close proximity<sup>20,21</sup>, the modes they support may interact or couple so as to modify the resonant frequency and lineshape. If the 2D LSPR arrays are modified, such that additional layers are introduced, there is the possibility for hole and particle LSPRs in subsequent layers to interact. In order for strong coupling to occur the spacing between layers must be significantly smaller than the incident wavelength and comparable to the localised field decay length of the LSPR<sup>22</sup>. In Chapter 7 there was an investigation into perforated layers which were separated by distances which were sufficiently large that the structure could support first-order FP resonant modes, distances which were much larger than the decay length of the LSPR. In Figure 8.15, greyscale plots show the simulated absorbance as a function of frequency and layer spacing between two layers of hole (i) and particle (ii) arrays with the same parameters as the single layer structures in Figure 8.14. As the spacing between layers is decreased below 60 nm, a distinct splitting is observed in the LSPR associated with the response of the single layer structure: two resonant modes are observed, one is blue shifted to frequencies above the single LSPR whilst the other mode is red-shifted below it. The insets show the absorbance plotted as a function of frequency for two-layer structures comprised of hole arrays (i) and particle arrays (ii) with a fixed layer spacing of 20 nm. Again, two clear maxima are evident, labelled A,B for the hole and C,D for the particle structures respectively. Giessen et al.<sup>23</sup> have previously observed this hybridization of LSPRs for particles spaced by a few tens of nm.

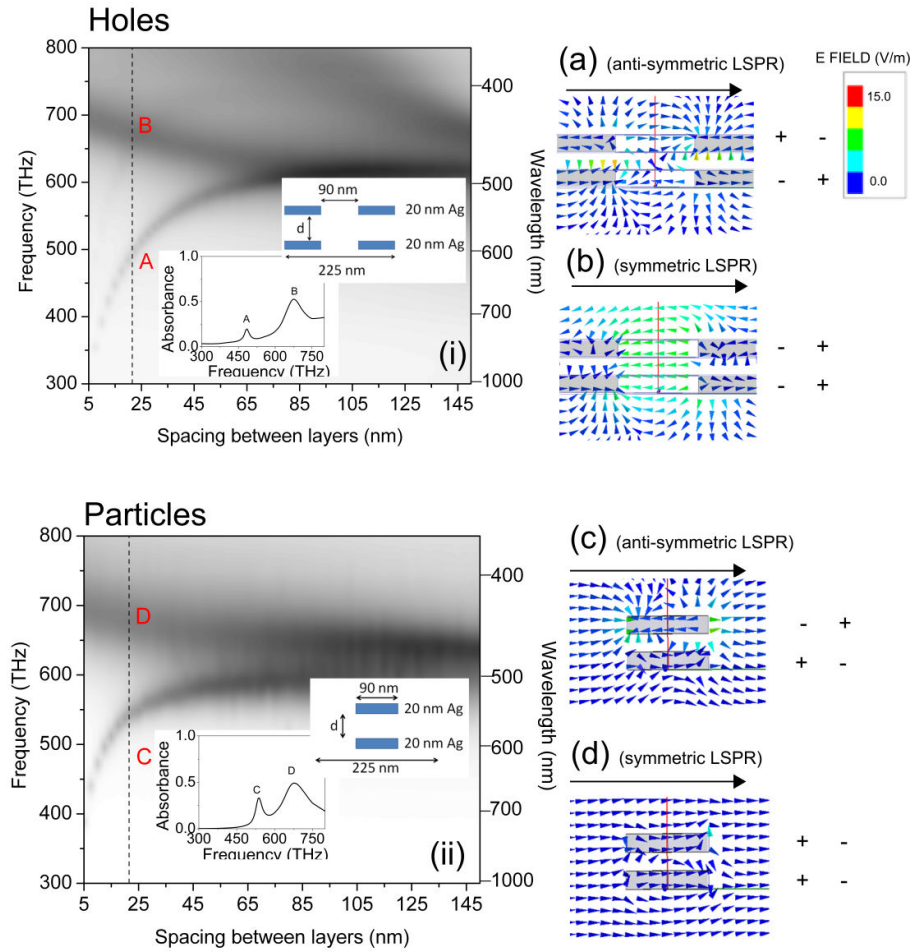


**Figure 8.15:** The simulated absorbance is plotted as a function of frequency and spacing between two layers of hole (i) and particle (ii) arrays. In both structures the Ag layer thickness is 20 nm, and the cylindrical holes/particles with diameter 90 nm are arranged into regular square arrays with periodicity 225 nm. For 20 nm layer spacing (shown by the dashed line) the absorbance of each arrangement is plotted as a function of frequency as an inset figure. In (a-d), the instantaneous scattered electric field vector has been plotted for a cross section perpendicular to the stack at the resonant frequencies labelled A-D in the greyscale (i) and (ii). The arrows above the field profiles indicate the direction of the incident electric field vector.

The field profiles taken at the resonant frequencies are plotted in (a-d) of Figure 8.15. All profiles are shown for the same phase of the incident field, with the black arrows at the top of the field profiles denoting the direction of the incident electric field. At resonance A (the high frequency branch of the coupled LSPR for the hole structure) the vector arrows inside adjacent holes are aligned to suggest a symmetric distribution of charges associated with coupled LSPRs in the upper and lower layers. In contrast, the vector arrows

associated with resonance B in the lower frequency branch are in anti-phase and suggest an anti-symmetric charge distribution. A similar relationship is observed for the two layer particle structures. For the symmetric resonances, the parallel alignment of dipoles in adjacent layers increases the dipolar restoring force, thus giving rise to a greater resonant frequency than would be expected for a single layer. For the anti-symmetric modes, the dipoles associated with adjacent holes / particles are anti-aligned, and the dipolar restoring force will be considerably reduced, hence lowering the resonant frequency in comparison to the single layer structure. The origin of the magnetic response in perforated materials at infrared frequencies has been previously been attributed to the existence of anti-symmetric surface currents across the individual layers<sup>4,24</sup>. For the case of anti-symmetric coupled LSPRs the fields within the vacuum regions between the holes / particles form closed loops which ‘circulate’ between layers, as illustrated by the diagram in Figure 8.16.

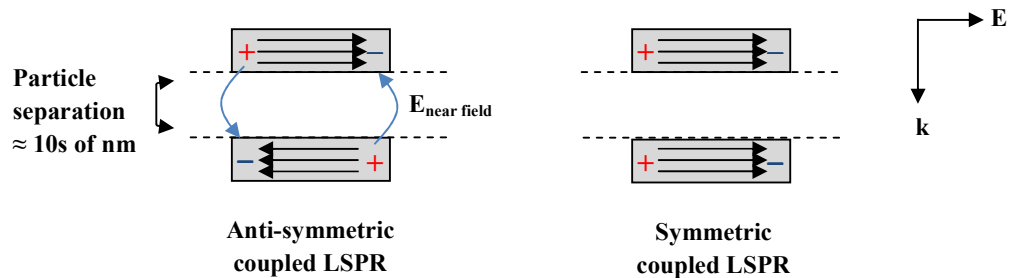


**Figure 8.16:** The instantaneous charge and field distributions are illustrated for two metallic nanoparticles which interact through the overlap of their resonant electromagnetic fields. Plasmon hybridisation can occur in particles separated by distances which are a few 10s of nm in vacuum, resulting in two coupled LSPRs associated with the anti-symmetric (a) and symmetric (b) distribution of charge across the structure.

One may therefore expect multiple layers of strongly interacting holes or particles to exhibit a magnetic response near the anti-symmetric coupled LSPR frequency. In order to validate this hypothesis the effective response of a stacked metamaterial structure consisting of five layers of holes/ particles separated by 20 nm will now be considered. It is expected that five layers of the structure should provide a suitable approximation to the bulk metamaterial response<sup>5</sup>. The real and imaginary components of the effective refractive indices, effective permittivity and effective permeability are determined from the complex reflection and transmission coefficients of the stacked hole and particle structures, following the extraction procedure detailed in section 8.2. In Figure 8.17, the real and

imaginary parts of the effective refractive indices ( $n$ ) are plotted for the five-layer stacked hole array (i) and particle array (ii) structures having the arrangement shown in the inset. The corresponding frequency dependent effective permittivity  $\epsilon$  and permeability  $\mu$  for the structures are also plotted in (a-d) of Figure 8.17. Both particle and hole structures exhibit resonances in effective permeability near the antisymmetric LSPRs highlighted in Figure 8.15. It is clear, however, that the imaginary component of  $\mu$  is more dominant in the hole structure. Furthermore, the effective permittivities of the two structures are notably different. In the hole structure, a large negative effective permittivity is observed at low frequency due to the continuous nature of the metal layers (i.e.  $\epsilon_r \rightarrow -\infty$  in the low frequency limit), and tends to unity at high frequency above the symmetric LSPR. The low frequency limit for the effective permittivity of the particles is unity, and is below zero in a small frequency region *above* the symmetric LSPR frequency. This is a fundamental difference in the electric response of the two structures, and essentially arises from the complementary nature of the hole LSPR compared to a particle LSPR, as deduced from the field plots in Figure 8.15.

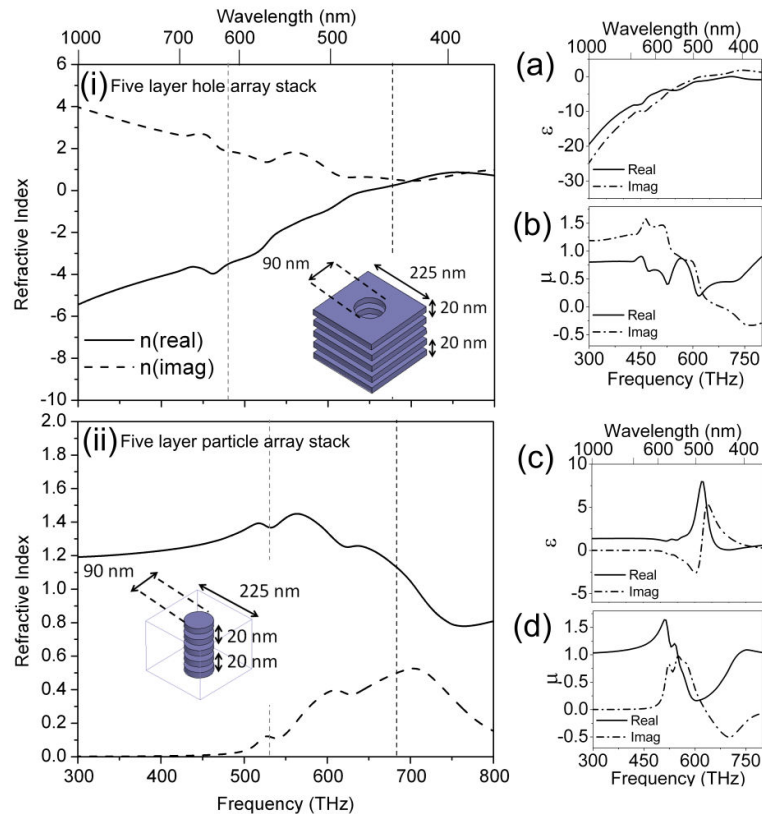


**Figure 8.17:** The effective refractive indices are shown as a function of frequency for the five layer stacked hole array (i) and particle array (ii) structures. In the inset, the real and imaginary parts of the effective permittivity  $\epsilon$  and permeability  $\mu$  are shown for the stacked

hole array (a,b) and particle array (c,d) structures. The dashed vertical lines in plots (i) and (ii) represent the resonant frequencies of the symmetric (dashed vertical black line) and anti-symmetric (dashed vertical gray line) coupled LSPRs for the equivalent two layer structure studied in Figure 8.15.

This complementary nature has important implications for determining the negative index regions in these metamaterials. From Figure 8.17, it can be observed that the stacked hole structure exhibits a region over which the real component of the index of refraction is negative, covering a wide range of frequencies from the infrared through to the visible spectral domains. The hole structure is an example of a “single-negative” negative index metamaterial<sup>25,26</sup>. It has previously been shown in other structures that the real part of the index of refraction can be negative in a material whose real effective permittivities and permeabilities are not simultaneously negative, provided the condition  $\mu_r \varepsilon_i + \varepsilon_i \mu_r < 0$  is satisfied<sup>27</sup>. The region of negative index in the stacked hole array occurs when  $\mu_r$  and  $\mu_i$  are positive and both  $\varepsilon_r$  and  $\varepsilon_i$  are large and negative, giving rise to a wide, low loss, negative index region below the antisymmetric LSPR frequency, where the magnitude of  $n_{real}$  is always larger than  $n_{imaginary}$ . At this point, it should be noted that by changing the structural parameters of the stack (i.e. larger holes and larger periodicity) and/or introducing a high index dielectric, the frequency of the anti-symmetric LSPR will shift to lower frequency, shifting the negative index region into the infrared, as reported in section 7.4.

In contrast to the hole structure, the stacked particle arrangement does not exhibit any negative index region. Due to the discontinuous nature of the metallic layers giving rise to a non-negative permittivity below the symmetric LSPR frequency, the electric response of the particle structure is not sufficient to facilitate a “single negative” negative index response near the anti-symmetric LSPR frequency. Thus, in the particle structure it is found that the relative overlap of the electric and magnetic responses are somewhat compromised. It is noted however, that if one is able to modify the particle geometry and permittivities to generate high Q symmetric and anti-symmetric LSPRs, it should be possible to achieve a region of “double negative” negative index, i.e. when  $\mu_r$  and  $\varepsilon_r$  are both negative, for frequencies above the symmetric LSPR. This is possible for LSPRs in the near infrared<sup>28,29</sup>, but no such demonstration has been performed using metallic particles at visible frequencies, where losses are more significant.

## 8.8 Concluding remarks

The negative index of refraction exhibited by a number of metamaterial structures at visible and non-visible frequencies has been considered. An extraction technique has been described for obtaining the effective permittivity and permeability of a metamaterial structure using the complex reflection and transmission coefficients obtained from simulation or experiment. When characterising the response of fishnet type electromagnetic metamaterials, an alternative explanation has been proposed to the commonly used analogy to electrical circuits. This explanation considers the hybridization which may occur between closely spaced holes or particles exhibiting LSPRs. The origin of coupled LSPRs in stacked hole and particle structures has been also identified, with the anti-symmetric coupled LSPR of both structures being shown to give rise to effective magnetic resonances. In the stacked hole structure, the overlap of the magnetic response with a negative effective permittivity at low frequencies facilitates a negative index of refraction. However, for the stacked particle structure, the non-continuous nature of the metallic layers imposes limitations on the effective permittivity response, and negative index behaviour is not observed.

### Conclusions and future work

#### 9.1 Summary

The work in this thesis presents an original investigation into the optical response of a variety of composite structures formed from metallic and dielectric elements with a view to advancing the understanding of the resonant modes which may be excited when these structures are illuminated with visible electromagnetic radiation.

In the first section the optical response of planar structures comprised of continuous metal and dielectric layers was discussed. Whilst the resonant transmission which is exhibited by these structures is already well known in the literature, the work in this thesis represents an extensive investigation (both modelling and experimental) into the effects of metal layer thickness and the number of repeat layers on the transmission properties of the structure. This has enabled two original conclusions to be made. Firstly, it has been shown that the width of the transmission pass-band depends only on the unit cell of the multilayer structure, and is independent of the number of periods. This is particularly important since the width of the transmission band may be optimised to cover the visible frequency range using only two or three repeat layers. In principle, a single cavity may even be used, however it was found that the gradients at the edges of the transmission band are steeper (the transmission band is better defined) when two or three repeat periods are used. Furthermore, by replacing the continuous metallic layers with a metamaterial structure (for example a thick metal film which has been patterned with a non-diffracting array of holes), transmission pass-bands may also be observed at microwave frequencies, as shown in the collaborating work with Butler et al <sup>1</sup>.

The second section of the thesis contained an investigation into the optical response of structures in which the metallic elements were non-continuous. In Chapter 3 there was a detailed comparison of a number of simulation techniques which are frequently used to model the scattering of electromagnetic radiation from metallic nanoparticle and nanohole structures (these were Mie Theory, T-Matrix, DDA, FEM, and FDTD), and example calculations being performed for an 80 nm diameter Au sphere. The results of the investigations were summarised in tabulated form, where it was found that the Mie Theory

and T-Matrix methods were the preferred choice for simulating spherical particles, as the scattered fields could be computed in the minimum time using an ‘almost exact’ method. The DDA, FEM and FDTD methods were more appropriate for the simulation of structures which have non-spherical geometries (such as cones or rods). However, the accuracy of these techniques was also shown to be resolution limited and a compromise has to be made between the accuracy of the numerical simulation, the computation time and the specification of the available hardware.

In Chapter 4 experimental studies were presented of individual gold nanoparticles which were fabricated by Electron Beam Lithography, and good agreement was observed between the simulated and experimental scattering spectra. There was also a discussion of a number of approaches which may be used to modify the scattering response of metallic nanoparticles, with the aim of improving the performance of displays. One of these approaches considered placing several particles in close proximity such that electromagnetic coupling can modify the properties of the LSPR. With a suitable optimisation of particle geometry, it has been shown for this configuration that it is possible to modify both the incident angle and scattering angle response significantly in comparison to the  $\cos^2\theta$  dependence which is predicted for small metallic particles by the electrostatic approximation. This represents a new and exciting observation.

The work within Chapter 5 focused on the interactions which occur in periodic arrays of metallic nanoparticles. The interactions between LSPRs were categorised into three regimes of short-range, long-range and coherently coupled interactions. The short range interactions were identified by a red-shift in the resonant frequency of the LSPR as the periodicity of the array was decreased and were dominant for periodicities which were in general less than 150 nm, such that the edge to edge separation of the particles was a few tens of nm. Conversely, long-range interactions were identified by a blue-shift in the resonant frequency as the periodicity of the array was decreased, and were dominant for periodicities greater than 250 nm. It has been shown that the interactions which are manifested within periodic arrays offer an additional tunability of the LSPR frequency beyond that which may be conventionally achieved by modifying the geometry of the scattering particle or the permittivity of the surrounding medium.

In the third section a different type of structure was considered in which the metallic layers were perforated with arrays of nanometric holes. A number of original observations have

been made here. The holes in these structures were shown to exhibit localised resonances associated with charges induced in the rim of the holes, in a similar manner to LSPRs of metallic nanoparticles. Studies have compared complementary nanoparticle and nanohole arrays with periodicities that are non-diffracting for frequencies in the vicinity of LSPRs. In the nanohole arrays the LSPR frequency was shown to exhibit a marked dependence on the periodicity of the array, an effect which has been attributed to coupling between LSPR modes and surface plasmon-polariton (SPP) modes which are supported by the metal film. However, the nanoparticle arrays show no such periodicity dependence across this range, since such structures do not support SPPs. Whilst the optical response of complementary hole and particle arrays share many features, the resonant field distributions exhibit fundamental differences. The ability to tune the hole LSPR frequency may be of benefit in sensing applications, as will be discussed in section 9.2.

Further investigations involving perforated structures were conducted using numerical simulations in Chapters 7 and 8. When multilayer structures exhibiting FP resonances (from Chapter 2) are perforated with periodic arrays of holes, strong interactions between FP and LSPR modes are observed. As the spacing between layers is reduced to a few tens of nm, it was found that the hybridisation of localised resonances may occur such that symmetric and anti-symmetric coupled hole LSPRs are observed. Previous studies of hybridised LSPRs have been performed using particle arrangements; however the work contained within Chapter 8 presents what appears to be the first investigation of coupled LSPRs using the complementary structure of holes. In a metamaterial structure comprised of five or more layers of stacked holes, it was shown that the anti-symmetric coupled LSPR facilitates an effective magnetic response, which leads to the structure exhibiting a negative index of refraction across a wide range of visible frequencies. The studies of coupled LSPRs provide an interesting and alternative viewpoint for understanding the origins of the negative index of refraction in fishnet-type electromagnetic metamaterials and perforated metal films.

## 9.2 Possible Applications

There are a number of areas where studies in this thesis may be utilised in commercial applications at visible and non-visible frequencies. The metal-dielectric multilayer structures in Chapter 2 have already been proposed by a number of authors for use in possible negative refraction and sub-wavelength focusing applications. Similarly, if the transmission band is suitably optimised to cover the visible frequency range, these

structures may also be utilised as cost-effective transparent electrodes in liquid crystal cells. The transmission response of the metamaterial-dielectric multilayer structure at microwave frequencies lends itself towards a number of applications; a lightweight structure having easily modifiable properties is likely to play an important role in microwave and millimetre wave technologies, particularly in structures such as antennas, electromagnetic shielding applications and ‘stealth-like’ absorbing surfaces.

The study of closely spaced metallic rods in Chapter 3 demonstrated that it is possible for both the incident angle and scattering angle response to be significantly modified in comparison to that of an isolated particle. These findings are particularly important for the development of new generations of liquid crystal displays which may operate solely through scattering ambient light. Such an application requires a host particle which exhibits a strong scattering response at visible frequencies. In addition to this, a high degree of contrast must exist between the scattering phases, such that for one orientation of the particle there is strong scattering, while in the orthogonal state there is little or no scattering. The investigations in Chapter 4 provide strong evidence that arrangements of metallic nanorods may fulfill these requirements.

There are several applications which may utilise some of the structures presented in the third section. Nanoparticle LSPRs are already well established in their use for local refractive index sensing and surface enhanced Raman spectroscopy (SERS) applications. However it also appears that the LSPRs associated with holes may be suitable for these purposes. It is evident that the field localisation of the hole is weaker than that of the corresponding particle, suggesting that particles may be more suitable for applications where field localisation and enhancement is important, such as surface enhanced Raman scattering (SERS). However, the weaker confinement of fields for holes may be viewed as a compromise, as the interaction between hole LSPRs renders the optical response highly sensitive to changes in interhole distance, making them a possible candidate for use in applications where tunability of the localised resonance may be useful.

In Chapter 8 the optical response of metamaterials formed from stacked hole arrays was discussed, and it was shown that if the spacing between layers is sufficiently small (a few tens of nm), the structures are shown to exhibit an effective negative index of refraction. Structures which exhibit a negative index of refraction have previously been utilised for a number of applications including cloaking and sub-wavelength imaging (‘superlensing’) at

microwave frequencies. There is also the potential that the structures discussed here may be developed for these purposes in the visible regime.

### 9.3 Future Work

An essential element of any future work would involve the experimental realisation of the angular response which has been predicted for the arrangements of metallic nanorods. The fabrication of these structures could be achieved through the direct use of EBL, or alternatively FIB milling could be used to divide a single nanorod into three sections. The scattering response of these structures may be determined using dark-field spectroscopy, however full characterisation of the angular response would require an extensive modification of the experimental apparatus. At present, the dark-field condenser facilitates illumination across a narrow range of angles, centred at approximately  $50^\circ$ . Future studies would therefore also have to consider an alternative technique for characterising the angular response. Furthermore, in order for these structures to be utilised in display applications, a fabrication route which offers large area coverage is preferable. An investigation into self-assembly techniques or novel chemical approaches such as electro-deposition would also be of benefit.

Another area for future investigation is the refractive index sensitivity of hole LSPRs (both experimentally and theoretically) and subsequently their development for use in sensing applications. Preliminary studies in Chapter 6 have shown that the magnitude of the resonant field enhancement is highly sensitive to the geometry of the hole. For example, changing the geometry of the holes from circular to rectangular more than doubles the resonant field enhancement which is observed inside the hole. This response has been explained in terms of an increase in the capacitive-like field enhancement, which arises from the induced charge on opposite sides of the hole. As with a parallel plate capacitor, the magnitude of this field enhancement can be increased by reducing the distance between the planes of charge (which is equivalent to increasing the aspect ratio of the rectangular hole). Further investigations studies could also study the regimes of interaction between hole LSPRs in periodic arrays (similar to the investigation which was conducted for particle arrays in Chapter 5). For short periodicities which are non-diffracting for frequencies in the vicinity of LSPRs, the excitation of the hole LSPR is characterised by resonant absorbance and a *decrease* in transmittance. Conversely, it is known that when diffraction occurs, coupling to SPP modes associated with the metal film through a grating mechanism leads to an *increase* in transmittance. These two resonant mechanisms

therefore have opposing effects in transmission, and it would be novel to study the relative intensities of these effects as a function of the periodicity of the array.

#### 9.4 Publications

Localised modes of sub-wavelength hole arrays in thin metal films  
J. Parsons, E. Hendry, B. Auguié, W. L. Barnes, and J. R. Sambles  
Proc. SPIE Vol. **6988**, 69880Y (2008)

Electromagnetic resonances of a multilayered metal-dielectric stack  
M. R. Gadsdon, J. Parsons and J. R. Sambles  
Journal of the Optical Society of America B **26(4)**, 734 (2009)

Localised surface plasmon resonances in periodic non-diffracting metallic nanoparticle and nanohole arrays  
J. Parsons, E. Hendry, C. P. Burrows, B. Auguié, J. R. Sambles and W. L. Barnes  
Physical Review B **79**, 073412 (2009)

Interaction between Fabry-Perot and nanohole resonances in metallo-dielectric plasmonic nanostructures  
J. Parsons, I. R. Hooper, W. L. Barnes and J. R. Sambles  
Journal of Modern Optics **56(10)**, 1199 (2009)

The microwave response of a metamaterial-dielectric stack  
C. Butler, J. Parsons, J. R. Sambles, A. P. Hibbins and P. Hobson  
Accepted for publication in Applied Physics Letters (2009)

The role of localized resonances in negative index metamaterials  
J. Parsons, W. L. Barnes, J. R. Sambles and E. Hendry  
Submitted to Physical Review B (2009)

#### 9.5 Disclosure

The material presented in section 4.6 (the angular response of metallic nanorods) is currently undergoing internal review within Hewlett Packard Corporation, with the aim of submitting a patent application.

Authors: J. Parsons, S. Kitson, C. Newton and A. Geisow

#### 9.6 Presentations

Poster presentation at Higher Education Regional Development Agency (HERDA) South West annual conference (2007)

J. Parsons, W. L. Barnes and J. R. Sambles  
“Nanoparticles and Nanocomposites for display applications”  
Torquay, United Kingdom – **8<sup>th</sup> November 2007**

Poster presentation at PIERS (2008) conference  
L. Ruan, J. Parsons, W. A. Murray and J.R. Sambles

“Optical response of tunable liquid crystal cell with nano-structured metal layer”  
Hangzhou, China – **25<sup>TH</sup> March 2008**

Oral presentation at SPIE Photonics Europe (2008) conference

J. Parsons, W. L. Barnes and J. R. Sambles

“Subwavelength hole arrays as a means to couple light to the surface plasmon polariton modes of thin metal films”

Strasbourg, France - **9<sup>th</sup> April 2008**

Poster presentation at Great Western Research “Future Imperfect” symposium (2008)

J. Parsons, W. L. Barnes and J. R. Sambles (University of Exeter)

S. C. Kitson, C. J. Newton and A. Geisow (Hewlett Packard Laboratories)

“Nanoparticles and Nanocomposites for display applications”

Filton, United Kingdom – **18<sup>th</sup> November 2008**

Poster presentation at Metamaterials (2009) conference

C. P. Butler, J. Parsons, J. R. Sambles and A. P. Hibbins

“The microwave response of a metamaterial-dielectric stack”

London, United Kingdom – **2<sup>nd</sup> September 2009**

## Appendix A

---

### A.1 Transmission and reflection at a single interface between two semi-infinite, isotropic media

In order to better understand the response of a simple Fabry-Perot etalon, an appropriate starting point is to consider the reflection and refraction of light at a planar surface between two isotropic media which have different dielectric properties. The co-ordinate system for this configuration is shown in Figure A.1, where the media below and above a plane (which is positioned at  $z = 0$  in Figure A.1) have permeabilities and permittivities  $\mu_i \epsilon_i$  and  $\mu_t \epsilon_t$  respectively. For simplicity, the medium above the plane will be referred to as “medium 1”, and the medium below it “medium 2”. It is assumed that a plane wave is incident from medium 1 having wave vector  $\mathbf{k}_i$  and frequency  $\omega$ . The reflected and refracted waves will have wave vectors  $\mathbf{k}_r$  and  $\mathbf{k}_t$  respectively.

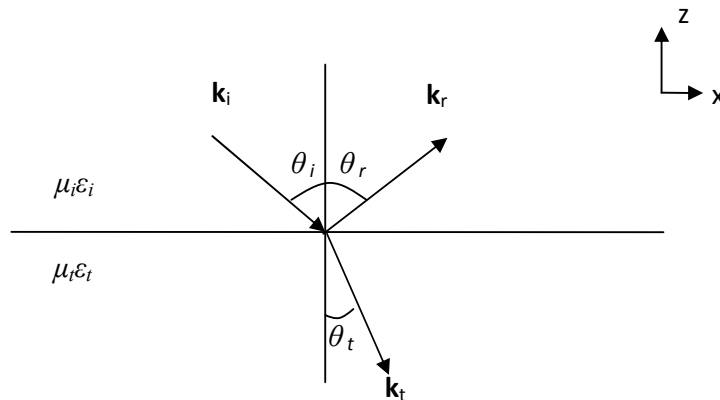


**Figure A.1:** An incident wave  $\mathbf{k}_i$  strikes a planar interface between two media with different dielectric properties, giving rise to a reflected wave  $\mathbf{k}_r$ , and a refracted wave  $\mathbf{k}_t$ .

In order that Maxwell’s equations are satisfied, boundary conditions are imposed such that the normal components of the electric displacement vector ( $\mathbf{D}$ ) and the magnetic induction ( $\mathbf{B}$ ), and the tangential electric components of the electric field intensity ( $\mathbf{E}$ ) and the magnetic field intensity ( $\mathbf{H}$ ) are continuous at the interface.

In applying the boundary conditions it is convenient to consider two separate situations:

- 1) Where the incident electric field is polarised perpendicular to the plane of incidence (parallel to the interface) – Transverse Electric (**TE**) or s-polarised radiation.

- 2) Where the incident electric field is polarised parallel to the plane of incidence (perpendicular to the interface) – Transverse Magnetic (TM) or p-polarised radiation.

*Reflection and refraction of TE polarised light:*

This configuration is shown in Figure A.2, where for the purpose of illustration the fields have been projected forwards and backwards from the interface (such that their phase factors are equal). The direction of the **E** field is pointing upwards, out of the paper.

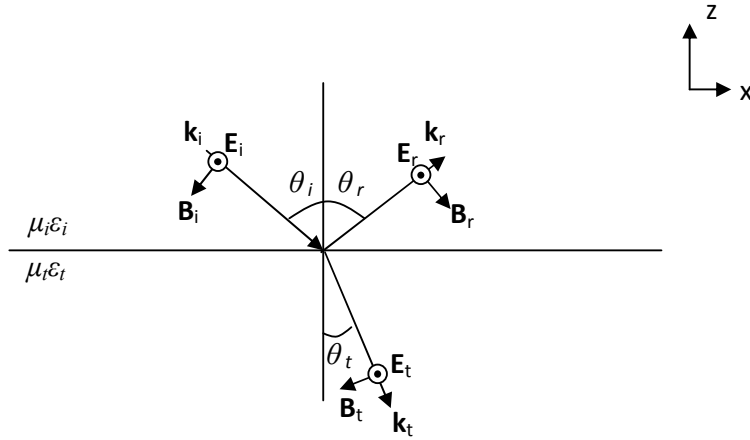


**Figure A.2:** Reflection and refraction of an incident plane wave which is polarised perpendicular to the plane of incidence.

If it is assumed that tangential **E** and **H** are conserved at the interface, then:

$$\mathbf{E}_i + \mathbf{E}_r = \mathbf{E}_t \tag{A.1}$$

$$-\frac{\mathbf{B}_i}{\mu_i} \cos \theta_i + \frac{\mathbf{B}_r}{\mu_r} \cos \theta_r = -\frac{\mathbf{B}_t}{\mu_t} \cos \theta_t \tag{A.2}$$

Equation A.2 can expressed in terms of **E** and the speed of light in the medium (referred to as  $v_i, v_t$  for media 1, 2 respectively):

$$-\frac{\mathbf{E}_i}{\mu_i v_i} \cos \theta_i + \frac{\mathbf{E}_r}{\mu_r v_i} \cos \theta_r = -\frac{\mathbf{E}_t}{\mu_t v_t} \cos \theta_t \tag{A.3}$$

Since the interface is flat,  $\mathbf{k}_x$  is conserved:

$$|\mathbf{k}_i| \sin \theta_i = |\mathbf{k}_r| \sin \theta_r = |\mathbf{k}_t| \sin \theta_t \tag{A.4}$$

If media 1 and 2 are isotropic, then  $|\mathbf{k}_i| = |\mathbf{k}_r|$  and  $\theta_i = \theta_r$ . If the material is non magnetic, then  $\mu_i = \mu_t = \mu_0$ , where  $\mu_0$  is the permeability of free space. Applying these considerations, Equation A.3 may be simplified to:

$$-\frac{\mathbf{E}_i}{v_i} \cos \theta_i + \frac{\mathbf{E}_r}{v_i} \cos \theta_i = -\frac{\mathbf{E}_t}{v_t} \cos \theta_t \quad \text{A.5}$$

Solving equations A.1 and A.5 simultaneously yields:

$$\frac{\mathbf{E}_r}{\mathbf{E}_i} = \frac{v_t \cos \theta_i - v_i \cos \theta_t}{v_t \cos \theta_i + v_i \cos \theta_t} \quad \text{A.6}$$

$$\frac{\mathbf{E}_t}{\mathbf{E}_i} = \frac{2v_t \cos \theta_i}{v_t \cos \theta_i + v_i \cos \theta_t} \quad \text{A.7}$$

Equations A.6 and A.7 are the reflection  $r_s$  and transmission  $t_s$  amplitude coefficients at an interface for incident radiation which is TE polarised. It is often convenient to express these in terms of the permeability and permittivity of the respective media. This is shown in Equations A.8 and A.9.

$$r_s = \frac{\mathbf{E}_r}{\mathbf{E}_i} = \frac{\sqrt{\mu_i \varepsilon_i} \cos \theta_i - \sqrt{\mu_t \varepsilon_t} \cos \theta_t}{\sqrt{\mu_i \varepsilon_i} \cos \theta_i + \sqrt{\mu_t \varepsilon_t} \cos \theta_t} \quad \text{A.8}$$

$$t_s = \frac{\mathbf{E}_t}{\mathbf{E}_i} = \frac{2\sqrt{\mu_i \varepsilon_i} \cos \theta_i}{\sqrt{\mu_i \varepsilon_i} \cos \theta_i + \sqrt{\mu_t \varepsilon_t} \cos \theta_t} \quad \text{A.9}$$

*Reflection and refraction of TM polarised light:*

This configuration is shown in Figure A.3, where the fields have been projected forwards and backwards from the interface. The direction of the  $\mathbf{B}$  field is pointing upwards, out of the plane of the paper.

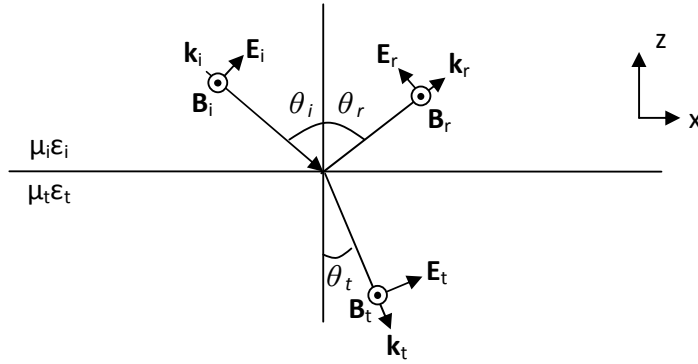


**Figure A.3:** Reflection and refraction of an incident plane wave which is polarised parallel to the plane of incidence.

If it is assumed that tangential  $\mathbf{E}$  and  $\mathbf{H}$  are conserved at the interface, then:

$$\mathbf{E}_i \cos \theta_i - \mathbf{E}_r \cos \theta_r = \mathbf{E}_t \cos \theta_t \quad \text{A.10}$$

$$\frac{\mathbf{B}_i}{\mu_i} + \frac{\mathbf{B}_r}{\mu_i} = \frac{\mathbf{B}_t}{\mu_t} \quad \text{A.11}$$

As demonstrated in the previous derivation for the case of TE polarised radiation, if the interface is flat, then  $\mathbf{k}_x$  is conserved. Equation A.11 can be expressed in terms of the electric fields ( $\mathbf{E}$ ) and the speed of light within the respective media ( $v_i, v_t$ ). If the material does not exhibit a magnetic response, the respective permeabilities are equal to the permeability of free space ( $\mu_0$ ).

$$\frac{\mathbf{E}_i}{v_i} + \frac{\mathbf{E}_r}{v_i} = \frac{\mathbf{E}_t}{v_t} \quad \text{A.12}$$

Equations A.10 and A.12 may be solved simultaneously to give expressions the reflection  $r_p$  and transmission  $t_p$  amplitude coefficients for TM polarised incident radiation.

$$r_p = \frac{\mathbf{E}_r}{\mathbf{E}_i} = \frac{\sqrt{\mu_t \epsilon_t} \cos \theta_i - \sqrt{\mu_i \epsilon_i} \cos \theta_t}{\sqrt{\mu_t \epsilon_t} \cos \theta_i + \sqrt{\mu_i \epsilon_i} \cos \theta_t} \quad \text{A.13}$$

$$t_p = \frac{\mathbf{E}_t}{\mathbf{E}_i} = \frac{2\sqrt{\mu_i \epsilon_i} \cos \theta_i}{\sqrt{\mu_t \epsilon_t} \cos \theta_i + \sqrt{\mu_i \epsilon_i} \cos \theta_t} \quad \text{A.14}$$

### A.2 The recursive Fresnel method

The approach which has been used to derive the transmission and reflection coefficients for a single interface may be extended such that they describe a system of multiple interfaces. Consider the structure of  $N$  layers illustrated in Figure A.4.

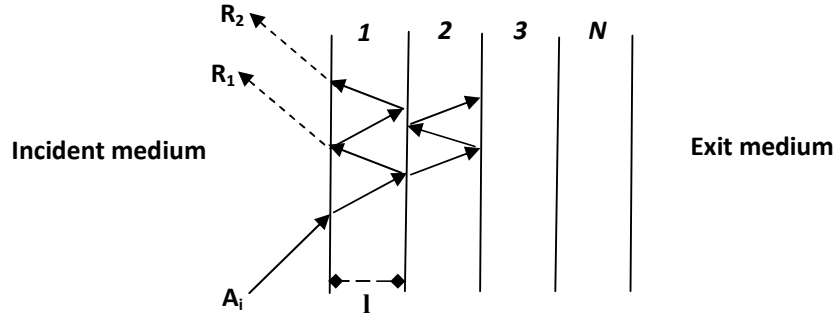


**Figure A.4:** The transmission and reflection of light in an arrangement formed from  $N$  isotropic layers.

The reflection coefficient for a single layer within the structure (for example the first layer), may be expressed as:

$$r_{layer} \mathbf{A}_i = \mathbf{R}_1 + \mathbf{R}_2 + \mathbf{R}_3 \dots \tag{A.15}$$

$$r_{layer} \mathbf{A}_i = \left[ \underbrace{r_{01} + t_{10} t_{01} r_{12}}_{\text{Reflection from the first interface}} \underbrace{\sum_{m=0}^{\infty} r_{12}^m r_{10}^m \exp(2imk_x l)}_{\text{Sum of multiple reflections within the layer}} \right] \tag{A.16}$$

Here,  $\mathbf{R}_1.. \mathbf{R}_n$  represents the amplitude of the reflected waves which undergo  $2(N-1)$  reflections within the individual layer,  $r_{ij}$  and  $t_{ij}$  represents the reflection and transmission coefficients at the interface between the  $i^{\text{th}}$  and  $j^{\text{th}}$  media respectively,  $l$  is the thickness of the layer and  $k_x$  is the wave vector within the medium. The terms within the summation in Equation A.16 form a geometric series. The sum to infinity of geometric series which has common ratio  $r$  is given by  $\frac{1}{1-r}$ . Applying this to Equation A.16 gives:

$$r_{layer} = r_{01} + \frac{r_{12} t_{10} t_{01} \exp(2ik_x l)}{1 + r_{12} r_{10} \exp(2ik_x l)} \tag{A.17}$$

Equation A.17 can be simplified further by using the simplification that  $r_{ij} = -r_{ji}$  in conjunction with Equations A.18 and A.19 which are derived from the previous boundary for TE and TM polarised radiation at an interface. The resulting equation for the reflection coefficient of a single layer is shown in Equation A.20.

$$t_{ij}^s t_{ji}^s = (1 - r_{ij}^s)(1 + r_{ij}^s) = 1 - (r_{ij}^s)^2 \quad \text{A.18}$$

$$t_{ij}^s t_{ji}^s = (1 - r_{ij}^s)(1 + r_{ij}^s) = 1 - (r_{ij}^s)^2 \quad \text{A.19}$$

$$r_{layer} = \frac{r_{01} + r_{12} \exp(2ik_x l)}{1 + r_{01} r_{12} \exp(2ik_x l)} \quad \text{A.20}$$

A similar process may be followed to determine the transmittance of the multilayer arrangement, given by Equation A.21.

$$t_{layer} = \frac{t_{01} t_{12} \exp(ik_x l)}{1 + r_{01} r_{12} \exp(2ik_x l)} \quad \text{A.21}$$

In a system of N layers, such as that shown in Figure A.4, the reflection or transmission coefficients of the entire arrangement are found by recursively applying the formula for the preceding layer. For example, the reflection coefficient associated with the termination layer is first determined using Equation A.21. This is then substituted in place of  $r_{12}$  when calculating the reflection coefficient of the  $(N-1)^{\text{th}}$  layer etc. Eventually the system is reduced to the problem of a single layer, in which the value of the reflection coefficient which is substituted in place of  $r_{12}$  effectively accounts for the reflection from all previous layers. Simulated data which has been presented throughout Chapter 2 has been calculated using this technique.

---

## Appendix B

---

### Legendre polynomials and the solution of second-order differential equations

Legendre polynomials are the solution of particular types of second-order differential equations. For differential equations of the form:

$$\frac{d^2y}{dx^2} + P(x)\frac{dy}{dx} + Q(x)y = 0 \quad \text{B.1}$$

the solution method of Frobenius can be applied if:

- a)  $P(x)$  and  $Q(x)$  are both finite when  $x = 0$ .
- b)  $xP(x)$  and  $x^2Q(x)$  are both finite when  $x = 0$ .

A trial solution is considered, which is of the form:

$$y = x^c(a_0 + a_1x + a_2x^2 + \dots) \quad \text{B.2}$$

The trial solution is differentiated and substituted into Equation B.1. Following this, the terms in both sides of the resulting expression are equated in order to determine the coefficients  $a_k$ . The solution comprises of two separate series corresponding to  $c = 0$ ,  $c = 1$ . To illustrate a more specific example, consider Legendre's equation which is of the form:

$$(1 - x^2)\frac{d^2y}{dx^2} - 2x\frac{dy}{dx} + k(k + 1)y = 0 \quad \text{B.3}$$

where  $k$  is a positive integer. Using the method of Frobenius, this equation yields two branches of solutions:

$$c = 0 \quad y = a_0 \left[ 1 - \frac{k(k+1)}{2!}x^2 + \frac{k(k-2)(k+1)(k+3)}{4!}x^4 - \dots \right] \quad \text{B.4}$$

$$c = 1 \quad y = a_0 \left[ x - \frac{(k-1)(k+2)}{3!}x^3 + \frac{(k-1)(k-3)(k+2)(k+4)}{5!}x^5 - \dots \right] \quad \text{B.5}$$

One of these solutions will terminate after a finite number of terms. When  $k$  is even, Equation B.4 terminates after a finite number of terms. Similarly, if  $k$  is odd this is true for Equation B.5. The resulting polynomial series in  $x$  (termed  $P_k(x)$ ) for each of these cases is known as a series of Legendre polynomials. The values of the weighting coefficients in the series are chosen such that the terms are equal to unity when  $x = 1$ .

When  $k = 2$ , the solution from (B.4) can be expressed as:

$$y = a_0 \left[ 1 + \frac{(2)(3)}{2!} x^2 + 0.. \right] \quad \text{B.6}$$

$$y = a_0 [1 + 3x^2] \quad \text{B.7}$$

$$a_0 = 0.5 \quad \text{B.8}$$

When  $k = 3$ , the solution from (B.5) can be expressed as:

$$y = a_1 \left[ x + \frac{(2)(5)}{3!} x^3 + 0.. \right] \quad \text{B.9}$$

$$y = a_1 \left[ x - \frac{3x^3}{5} \right] \quad \text{B.10}$$

$$a_1 = -1.5 \quad \text{B.11}$$

The Legendre polynomial series can be obtained directly using a generating function to calculate individual terms of the series for any integer of  $k$ .

$$P_k(x) = \frac{1}{2^k k!} \frac{d^k}{dx^k} (x^2 - 1)^k \quad \text{B.12}$$

E.g. If  $k = 4$ :

$$P_4(x) = \frac{1}{2^4 4!} \frac{d^4}{dx^4} (x^2 - 1)^4 \quad \text{B.13}$$

$$P_4(x) = \frac{1}{384} \frac{d^4}{dx^4} (x^8 - 4x^6 + 6x^4 - 4x^2 + 1) \quad \text{B.14}$$

This example gives an insight into the origins of Legendre polynomials, which are particularly useful in many areas of mathematics and physics. In some instances, differential equations cannot be solved using an analytical approach, but instead have to be decomposed into a series of terms (such as power series, fourier series etc.). It is also possible for any polynomial to be decomposed into a series of Legendre polynomial terms:

$$f(x) = \sum_{k=0}^{\infty} b_k P_k(x) \tag{B.15}$$

Here, the  $b_k$  terms represent weighting coefficients (different to the  $a_k$  weighting terms in Equation B.2).

If  $f(x) = x^2$

$$x^2 = a_0 P_0(x) + a_1 P_1(x) + \dots \tag{B.16}$$

$$x^2 = a_0 - \frac{a_2}{2} + a_1 x + \frac{3}{2} a_2 x^2 \tag{B.17}$$

$$x^2 = \frac{1}{3} P_0(x) + \frac{2}{3} P_2(x) \tag{B.18}$$


---

## Appendix C

---

### The generation of solutions to Bessel's equation

A special type of second-order differential equation which often arises in areas of physics and mathematics is the Bessel equation, which is given by:

$$x^2 \frac{d^2 y}{dx^2} + x \frac{dy}{dx} + (x^2 - \nu^2)y = 0 \quad \text{C.1}$$

where  $\nu =$  a constant. The method of Frobenius, as demonstrated in Appendix A may be used to solve this expression. A trial solution is considered, which is of the form:

$$y = x^c(a_0 + a_1x + a_2x^2 + \dots) \quad \text{C.2}$$

Following differentiation and substitution of the trial solution, the unknown coefficients can be determined:

$$c = +\nu \quad y = Ax^\nu \left[ 1 - \frac{x^2}{2^2(\nu+1)} + \frac{x^4}{(2^4)(2!)(\nu+1)(\nu+2)} - \dots \right] \quad \text{C.3}$$

$$c = -\nu \quad y = Bx^{-\nu} \left[ 1 + \frac{x^2}{2^2(\nu-1)} + \frac{x^4}{(2^4)(2!)(\nu-1)(\nu-2)} - \dots \right] \quad \text{C.4}$$

It can be shown that  $a_1, a_3, a_5 \dots = 0$ . For even terms:

$$a_2 = \frac{a_0}{\nu^2 - (c+2)^2} \quad a_4 = \frac{a_0}{[\nu^2 - (c+2)^2][\nu^2 - (c+4)^2]} \quad \text{C.5, 6}$$

The general form of the even numbered weighting coefficients for  $r \geq 2$  is given by:

$$a_r = \frac{a_{r-2}}{\nu^2 - (c+r)^2} \quad \text{C.7}$$

The complete solution to the Bessel equation can therefore be expressed as:

$$y = Ax^{\nu} \left[ 1 - \frac{x^2}{2^2(\nu+1)} + \frac{x^4}{(2^4)(2!)(\nu+1)(\nu+2)} - \dots \right] + Bx^{-\nu} \left[ 1 + \frac{x^2}{2^2(\nu-1)} + \frac{x^4}{(2^4)(2!)(\nu-1)(\nu-2)} - \dots \right] \quad \text{C.8}$$

Whilst the expression above is an accurate and completely valid solution to the initial problem, it is sometimes preferable to re-write the series using Gamma functions. Recall that the Gamma function is defined by:

$$\Gamma(x) = \int_0^{\infty} t^{x-1} e^{-t} dt \quad \text{C.9}$$

such that  $\Gamma(1) = 1$ . There are some useful identity relationships which can be used throughout the analysis of Gamma functions. Consider, for example,  $\Gamma(x+1)$ :

$$\Gamma(x+1) = \int_0^{\infty} t^x e^{-t} dt \quad \text{C.10}$$

$$= \left[ t^x \left( \frac{e^{-t}}{-1} \right) \right]_0^{\infty} + x \int_0^{\infty} e^{-t} t^{x-1} dt \quad \text{C.11}$$

$$= [0 - 0] + x\Gamma(x) \quad \text{C.12}$$

A fundamental recursive relationship exists for Gamma functions, which can be applied to other functions such as  $\Gamma(x+1)$ ,  $\Gamma(x+2)$ ... $\Gamma(x+n)$  etc.

$$\Gamma(x+1) = x\Gamma(x) \quad \text{C.15}$$

$$\Gamma(x+2) = (x+1)\Gamma(x+1) = (x+1)x\Gamma(x) \quad \text{C.16}$$

$$\Gamma(x+3) = (x+2)\Gamma(x+2) = (x+2)(x+1)x\Gamma(x) \quad \text{C.17}$$

As an interesting aside, the recursive relationships can also be used to show that:

$$\Gamma(0+1) = 0\Gamma(0) = 1 \quad \text{C.18}$$

$$\Gamma(0) = \int_0^{\infty} t^{-1} e^{-t} dt = \infty \quad \text{C.19}$$

The expression for the second weighting term  $a_2$  can now be rewritten in terms of Gamma functions. If  $c = +v$  :

$$a_2 = \frac{a_0}{v^2 - (v+2)^2} = \frac{a_0}{v^2 - v^2 - 4v + 4} = \frac{a_0}{-2(2v+2)} \quad \text{C.20}$$

If  $a_0$  is replaced by the term:

$$\frac{1}{2^v \Gamma(v+1)} \quad \text{C.21}$$

then,

$$a_2 = \frac{1}{2^v \Gamma(v+1)} \frac{1}{-2(2v+2)} \quad \text{C.22}$$

$$= \frac{1}{2^v \Gamma(v+1)} \frac{-1}{2^2(v+1)} \quad \text{C.23}$$

$$= \frac{-1}{2^{v+2} \Gamma(v+1) \Gamma(v+1)} \quad \text{C.24}$$

$$= \frac{-1}{2^{v+2} \Gamma(v+2)} \quad \text{C.25}$$

The alternative representation of Gamma terms in the weighting coefficients may also be applied to  $a_4$ :

$$a_4 = \frac{a_0}{[v^2 - (c+2)^2][v^2 - (c+4)^2]} \quad \text{C.26}$$

$$= \frac{a_0}{-2(2v+2)(4v+8)} \quad \text{C.27}$$

$$= \frac{a_2}{-4(2v+4)} \quad \text{C.28}$$

$$= \frac{-1}{2^{v+2} \Gamma(v+2)} \frac{-1}{2^3(v+2)} \quad \text{C.29}$$

$$= \frac{1}{2^{v+5}(v+2)\Gamma(v+2)} \quad \text{C.30}$$

$$= \frac{1}{2^{\nu+5}\Gamma(\nu+3)} \quad \text{C.31}$$

This allows the general expressions for  $a_r$  to also be rewritten. For  $r \geq 2$  and even:

$$a_r = \frac{(-1)^{r/2}}{2^{\nu+r} \left(\frac{r!}{2!}\right) \Gamma\left(\nu + \frac{r}{2} + 1\right)} \quad r = 2,4,6 \dots \quad \text{C.32}$$

or

$$a_k = \frac{(-1)^k}{2^{\nu+2k}(k!)\Gamma(\nu+k+1)} \quad k = 1,2,3 \dots \quad \text{C.33}$$

When the  $a_k$  terms are substituted into the general solution for the Bessel equation:

$$y = x^\nu \left[ \frac{1}{2^\nu \Gamma(\nu+1)} - \frac{x^2}{2^{\nu+2} \Gamma(\nu+2)} + \frac{x^4}{2^{\nu+5} \Gamma(\nu+3)} \right] \quad \text{C.34}$$

Which can be simplified to:

$$y = \left(\frac{x}{2}\right)^\nu \left[ \frac{1}{\Gamma(\nu+1)} - \frac{x^2}{2^2 \Gamma(\nu+2)} + \frac{x^4}{2^5 \Gamma(\nu+3)} \right] \quad \text{C.35}$$

$$J_\nu = \left(\frac{x}{2}\right)^\nu \sum_{k=0}^{\infty} \frac{(-1)^k x^{2k}}{2^{2k}(k!)\Gamma(\nu+k+1)} \quad \text{C.36}$$

This is also known as the Bessel function of first kind which has order  $\nu$ . Note that in the alternative Gamma notation, we have thus far only considered solutions derived from  $c = +\nu$ , but there is the additional possibility that  $c = -\nu$ . In this instance, the summation of terms contributing to  $J_{-\nu}$  must also be considered:

$$J_{-\nu} = \left(\frac{x}{2}\right)^{-\nu} \sum_{k=0}^{\infty} \frac{-1}{2^{2k}(k!)\Gamma(k-\nu+1)} \quad \text{C.37}$$

Using the alternative notation, the complete solution to the Bessel equation is expressed by:

$$y = AJ_\nu(x) + BJ_{-\nu}(x) \qquad \text{C.38}$$

---

## Appendix D

---

### Fabrication of samples using a thermal evaporation technique

#### D.1 Introduction

The metallo-dielectric multilayer structures presented in Chapter 2 were fabricated using a thermal evaporation technique. In this appendix section, details of this technique will be discussed in greater detail. The evaporation apparatus which is presented in this section was assembled at the University of Exeter by members of the technical workshop. In some instances, I have made modifications to the apparatus in order to improve the quality of the samples, and this will be explained where appropriate.

In the thermal evaporation technique, the deposition of metal and dielectric films is achieved by heating a source material (e.g. a metal ingot) within a vacuum chamber. If sufficient heat is transferred to the source, the kinetic energy of the molecules may overcome the intermolecular forces of the liquid phase of the evaporant, and evaporation may occur. The vapour particles diffuse across the chamber to a target surface (the substrate) where they condense back to a solid phase. The two elements which are fundamental to the success of this technique are the quality of the vacuum pumping system, and the efficiency with which heat may be transferred to the source material.

#### D.2 Experimental apparatus

The description of the apparatus is divided into two sections which are concerned with the external (a) and internal (b) connections of the chamber.

##### *D.2a) External workings*

Figure D.1 shows labeled photographs of the external connections of the thermal evaporation system. Note that the chamber which is pictured in (a) and (b) has steel walls, however other types of evaporation chambers may be formed using glass bell-jars (c). This type of configuration has the additional benefit that the user can see inside the chamber, which may be useful for the positioning of moveable parts such as external shutters. The air admit valve (1) is necessary to allow the chamber to return to atmospheric pressure so that samples can be retrieved once the deposition has finished. Loading and retrieval of samples is achieved by removing the lid of the chamber (2), this is sealed against the main body of the chamber using a Nylon 'o-ring'. The Penning gauge

(3) is used to measure the pressure of gas in the chamber. During metal deposition, the thickness of the sample is monitored using a quartz crystal thickness monitor (4). The oscillating frequency of the crystal changes as the metal film is deposited on its upper face. Electronically measuring the change in resonant frequency of the crystal allows the film mass to be determined. Once the density of the evaporated material has been entered into the monitor, the thickness is calculated to a resolution of 0.5 nm on a four digit LED display. The moveable shutter (5) allows the operator to obstruct the path between the source material and the substrate. When the shutter is closed, the vapour particles condense on the lower face of the shutter. The shutter is particular useful if a metal thickness is required to a high degree of accuracy, as it can be closed once the desired thickness is reached. This cannot be achieved by simply removing the heat source, as evaporation will continue at a considerable rate for several seconds after the heat source has been removed. The cold water supply (6) is used to cool the high vacuum / diffusion pump (this may be replaced by a turbo molecular pump – see 9). Initially, the rotary pump (7) is used to evacuate the chamber to a pressure of approximately  $10^{-1}$  mbar. Access between the inlet of the rotary pump and the chamber is controlled by the roughing valve (8). This allows the rotary pump to remain operational whilst the chamber is at atmospheric pressure (during the loading and retrieval of samples). Once the pressure within this chamber is below  $10^{-1}$  mbar, the high vacuum pump (9) may then be switched on. After the molecular pump has been operational for a few hours, the chamber pressure should reach  $10^{-7}$  to  $10^{-8}$  mbar, at which point evaporation of the source may be performed.

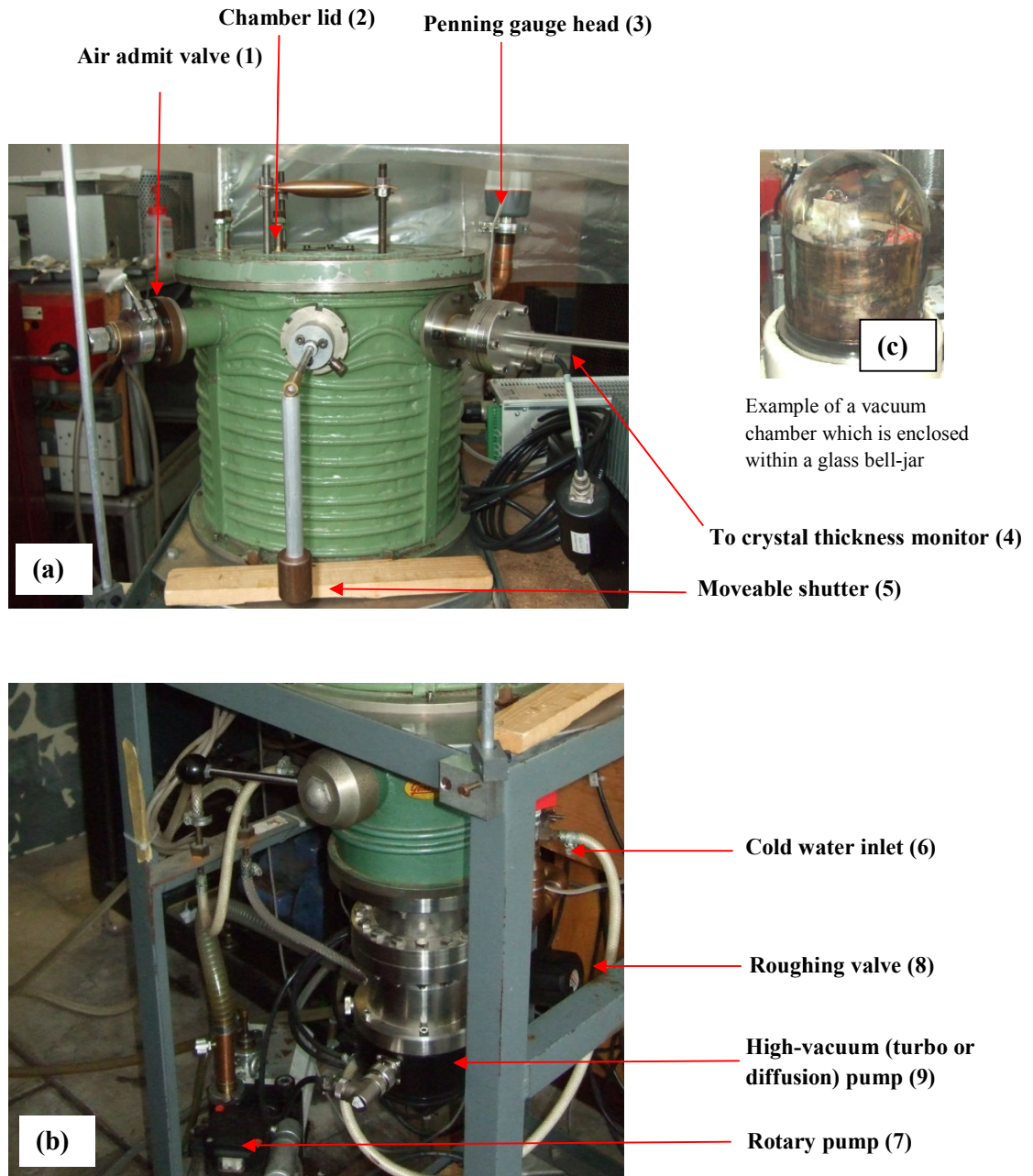


**Figure D.1:** Labeled photographs of the external connections of the thermal evaporation system are shown (a) and (b). Other types of evaporation chambers may be formed using glass bell-jars (c).

*D.2b) Internal workings*

Figure D.2 shows labeled photographs of the internal connections of the thermal evaporation system. For clarity, the images shown here are of the inside of the evaporator which is pictured in (c) of Figure D.1. From a practical perspective it is easier to remove

the bell-jar for photographic purposes than to undertake dismantling of the evaporator in (a) and (b) of Figure D.1. The workings of both evaporators are essentially the same with the only exception being a difference in the positioning of the electrodes.

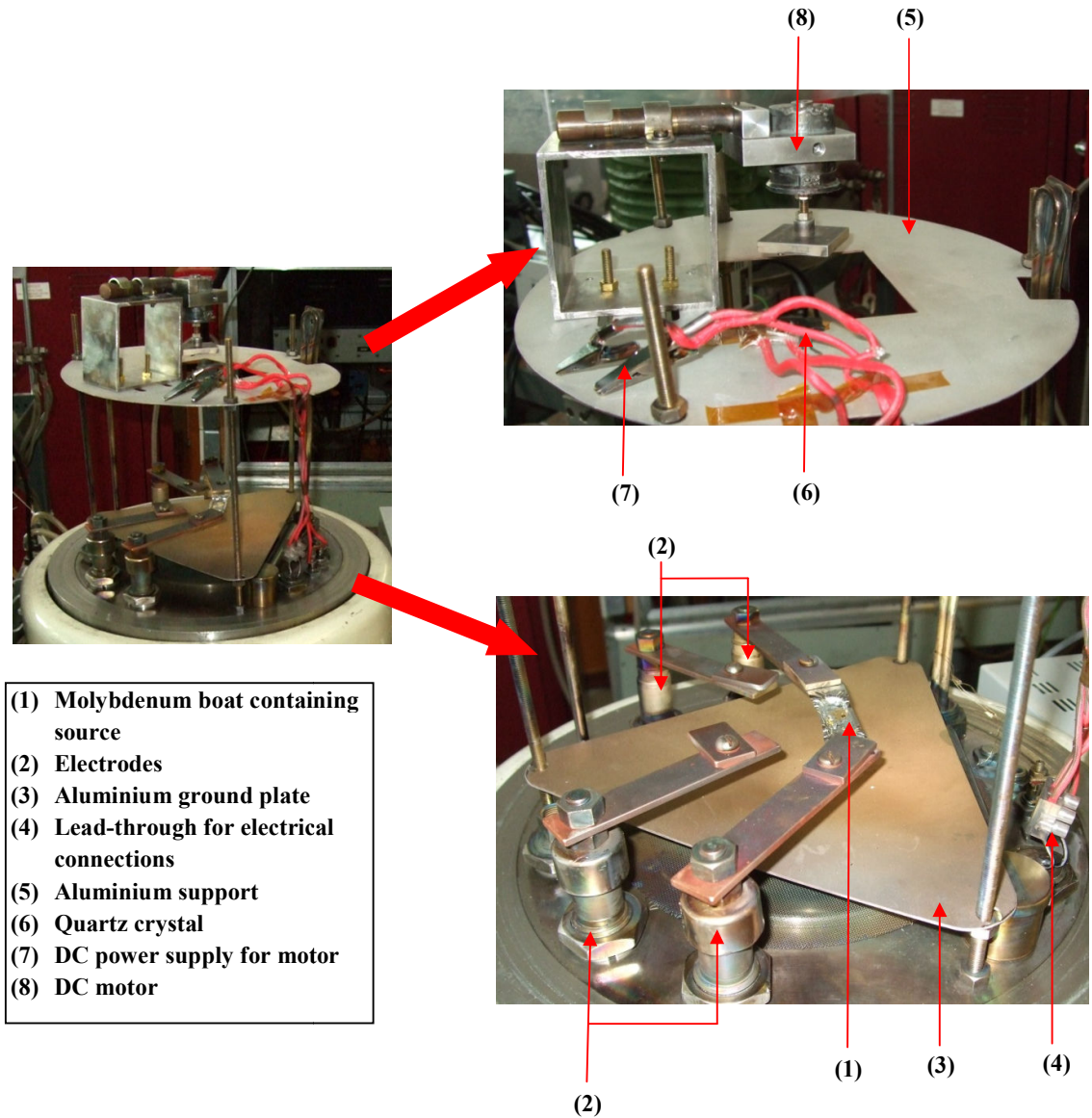


**Figure D.2:** Labeled photographs of the internal connections of the thermal evaporation system.

In order to evaporate the source, it is placed within a conducting filament or tray (a ‘boat’). The materials used to form the filaments have melting and evaporation temperatures which are significantly higher than that of the source (often W or Mo are often used). The filament (1) is clamped between a pair of copper electrodes (2), and an electric current is passed through it, resulting in a temperature increase in the filament due to ohmic losses.

In order to dissipate the maximum possible energy through ohmic losses, the mains electricity supply is connected to a step-down transformer such that currents of up to 100 Amperes may be passed through the filament. The maximum filament temperature which can be achieved using this technique is  $\approx 1500^{\circ}\text{C}$ , and whilst a large number of metals can be evaporated at these temperatures, it is unsuitable for evaporating a number of semiconductors and dielectrics (such as Si, Ge,  $\text{SiO}_2$ ,  $\text{SiO}_x$ ). In an evaporation system which has more than one pair of electrodes, the current may be flowed through each pair of electrodes in turn, allowing two source materials to be deposited in a periodic manner. In Chapter 2, multilayer structures were fabricated in this way by periodically depositing Ag and  $\text{MgF}_2$  using two pairs of electrodes.

A protective aluminium plate (3) is fixed into place at the base of the chamber. The function of this plate is to prevent metal / dielectric solids from falling into the pumping system. The electronics inside the chamber are connected to the outside gauges / power supplies using 'lead-throughs' (4), which are cylindrically shaped seals made of nylon or rubber, into which conducting rods are embedded. A second aluminium plate is fixed at the top of the chamber (5), this has two functions. Firstly, it acts as a support for the substrate, and secondly it acts as a shutter which prevents the upper portion of the glass bell-jar from being coated with metal. In some instances it is important to see inside the chamber, such as when positioning moveable parts or as this case here, when a motor is present, to check the rotation speed. The quartz crystal (7) which is used to monitor the thickness of the deposited layer is positioned next to the substrate. There is a difference in lateral position between the quartz crystal and the substrate, which leads to a difference in the amount of deposited material. This difference is calibrated for by depositing a test metal film to a thickness of approximately 100 nm (as measured on the quartz crystal monitor), and an Atomic Force Microscope (AFM) is used to determine the actual thickness of the metal film which is deposited on the substrate.

The upper part of the evaporation chamber in Figure D.2 contains a sample holder which is fixed to a DC motor (8), this provides the additional option of rotating the sample during deposition. The speed of rotation of the motor is controlled via an external electrical circuit. It has been shown (in Equation D.3) that mass of the material which is deposited at the substrate exhibits lateral variation, however this can be minimised by tilting the stage at an angle, and rotating the sample (a technique sometimes referred to as rotary evaporation) <sup>2</sup>. To illustrate the importance of rotating the sample, Figure D.3 shows

photographs of two samples which are formed three layers (20 nm Ag – 120 nm SiO<sub>x</sub> – 20 nm Ag), viewed in reflection at normal incidence. In (a) the sample holder has been aligned horizontal such the vector from the source to the substrate is parallel to the surface normal of the substrate. In (b), the sample has been aligned such that the vector for the source to the substrate makes an angle of 60° with the surface normal of the substrate. The sample in (b) is rotated at approximately 120 revolutions per minute. From the discussions of multilayer structures contained in Chapter 2, the colour variation which is observed from left to right in the reflectance of sample (a) can be attributed to variations in the thicknesses of layers within the structure. Sample (b) shows no such colour variation, suggesting that there is greater uniformity of the thickness distribution.

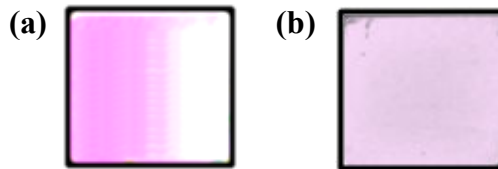


**Figure D.3:** Photographs of two samples (20 nm Ag – 120 nm SiO<sub>x</sub> – 20 nm Ag) viewed in reflection at normal incidence are shown. In (a) the vector from the source to the substrate is parallel to the surface normal of the substrate. In (b), the sample has been aligned at an angle of 60° and is rotated at 120 revolutions per minute.

### D.3 Instructions for operation

In order to deposit a thin film using the evaporation system in Figure D.1 (which contains a turbo molecular high vacuum pump), the instructions detailed below should be followed when loading samples, pumping down and evaporating.

#### *Loading samples:*

- 1) Slowly open the air admit valve, and allow the chamber to reach atmospheric pressure – this will take approximately 2 minutes.
- 2) Once the chamber has reached atmospheric pressure, remove the lid and place it down on a flat surface, with the seal side facing upwards.
- 3) Load the samples into the holders which are located on the upper Aluminium plate. Use glass microscope slides to cover the back faces of the samples, as they may also become coated with the evaporant.
- 4) Replace the lid on the chamber and close the air admit valve.

*Pumping down:*

- 1) Switch on the water supply to the turbo molecular pump.
- 2) Close the air admit valves on the rotary and turbo molecular pumps.
- 3) Switch on the rotary pump and the Pirani (backing) and Penning (chamber) gauges.
- 4) Slowly open the backing valve until it is fully open.
- 5) It will take approximately 10 minutes for the pressure on the Pirani gauge to reach  $10^{-1}$  mbar. Once this pressure has been reached, switch on the turbo molecular pump. After approximately 1 hour the chamber pressure should fall to  $<5 \times 10^{-7}$  mbar, at which point the evaporation of the source may be performed.

*Evaporating:*

- 1) It is preferable to “outgas” the source before evaporation in order to remove any volatile contamination. To do this, ensure that the shutter is closed so that the samples are not contaminated. Switch on the variable AC power supply (the variac), and increase the voltage to 30 – 40 V. The chamber pressure should increase to approximately  $1 \times 10^{-6}$  mbar, before returning to the base pressure.
- 2) To evaporate, turn the variac to  $\approx 60$  V. After approximately 20 seconds, press “zero” on the front panel of the crystal thickness monitor and open the shutter. The thickness of the deposited film (in  $\text{k}\text{\AA}$ ), the elapsed time and the deposition rate will be displayed on the monitor in real time. Once the desired thickness has been reached, close the shutter and turn down the variac to 0 V, then switch it off.
- 3) Leave the system for approximately 20 minutes to cool. If air is admitted to the chamber whilst the sample is hot, there is a strong possibility that the sample will react with molecules in the air and become contaminated.

*Retrieving samples:*

- 1) Close the backing valve and switch off the turbomolecular pump. Then wait for approximately 5 minutes to allow for the turbines inside the pump to come to rest.
- 2) Slowly open the chamber air admit valve, and retrieve samples as per the loading instructions.

## List of References

---

### List of references for Chapter 1:

- 1 A. N. Grigorenko, A. K. Geim, H. F. Gleeson, Y. Zhang, A. A. Firsov, I. Y. Khrushchev and J. Petrovic, *Nature* **438**, 335 (2005).
- 2 A. Christ, T. Zentgraf, S. G. Tikhodeev, N. A. Gippius, O. J. F. Martin, J. Kuhl and H. Giessen, *Physica Status Solidi B* **243(10)**, 2344 (2006).

### List of references for Chapter 2:

- 1 C. Fabry and A. Perot, *Annales de Chimie et de Physique*, 115 (1899).
- 2 A. L. Schawlow and C. H. Townes, *Physical Review* **112**, 1940 (1958).
- 3 G. Brodin and M. Marklund, *Classical and Quantum Gravity* **20**, L45 (2003).
- 4 A. H. Pfund, *Journal of the Optical Society of America* **24**, 99 (1934).
- 5 H. A. Macleod, *Thin Film Optical Filters* (Hilger, London, 1969).
- 6 W. Geffcken, *Deutsches Reich Patentschrift* **716153** (1939).
- 7 M. C. Larciprete, C. Sibilìa, S. Paolini and M. Bertolotti, *Journal of Applied Physics* **93**, 5013 (2003).
- 8 M. Scalora, M. J. Bloemer, A. S. Pethel, J. P. Dowling, C. M. Bowden and A. S. Manka, *Journal of Applied Physics* **83**, 2377 (1998).
- 9 J. M. Bendickson, J. P. Dowling and M. Scalora, *Physical Review E* **53**, 4107 (1996).
- 10 M. Scalora, J. P. Dowling, C. M. Bowden and M. J. Bloemer, *Journal of Applied Physics* **76**, 2023 (1994).
- 11 C. M. de Sterke and J. E. Sipe, *Physical Review A* **38**, 5149 (1988).
- 12 D. N. Christodoulides and R. I. Joseph, *Physical Review Letters* **62**, 1746 (1989).
- 13 M. Scalora, G. D'Aguanno, N. Mattiucci, M. J. Bloemer, D. de Ceglia, M. Centini, A. Mandatori, C. Sibilìa, N. Akozbek, M. G. Cappeddu, M. Fowler and J. W. Haus, *Optics Express* **15**, 508 (2007).
- 14 J. Gerardin and A. Lakhtakia, *Microwave and Optical Technology Letters* **34**, 6, 409 (2002).
- 15 J. B. Pendry, *Physical Review Letters* **85**, 3966 (2000).
- 16 V.G. Veselago, *Soviet Physics USPEKHI* **10**, 509 (1968).
- 17 J. Valentine, S. Zhang, T. Zentgraf, E. Ulin-Aula, D. A. Genov, G. Bartal and X. Zhang, *Nature* **455**, 376 (2008).
- 17 J. Yao, Z. Liu, Y. Wang, C. Sun, G. Bartal, A. M. Stacy and X. Zhang, *Science* **321**, 930 (2008).
- 19 I. Bulu, H. Caglayan and E. Ozbay, *Optics Letters* **31**, 814 (2006).
- 20 N. Fang, H. Lee, C. Sun and X. Zhang, *Science* **308**, 534 (2005).
- 21 G. Winter and W. L. Barnes, *Applied Physics Letters* **88**, 051109 (2006).
- 22 Z. Liu, H. Lee, Y. Xiong, C. Sun and X. Zhang, *Science* **315**, 1686 (2007).
- 23 E. D. Palik, *Handbook of optical constants of solids* (Academic, New York, 1985).
- 24 M.R. Gadsdon, J. Parsons and J. R. Sambles, *Journal of Optical Society of America B* **26**, 734 (2009).
- 25 W. E. Kock, *IRE Proceedings* **34**, 828 (1946).
- 26 J. Bae, J-C. Chiao, K. Mizuno and D. B. Rutledge, *Journal of Infrared, Millimeter and Terahertz Waves* **16**, 377 (1995).
- 27 C. Caloz, C.-C. Chang, and T. Itoh, *Journal of Applied Physics* **90**, 11 (2001).
- 28 R. A. Depine and A. Lakhtakia, *Microwave and Optical Technology Letters* **41**, 315 (2004).

- 29 C. Butler, J. Parsons, J. R. Sambles and A. P. Hibbins – accepted for publication in *Applied Physics Letters* (2009).
- 30 A. Eriksson, A. Deleniv and S. Gevorgian, *IEEE MTT-S Digest* **3**, 2009 (2002).
- 31 C. C. Chen, *IEEE Transactions on Microwave Theory and Technology* MTT-21 **1**, 1 (1973).
- 32 A. Serpenguzel, *IEEE Microwave and Wireless Components Letters* **12**, 134 (2002).
- 33 D. F. Sievenpiper, M. E. Sickmiller and E. Yabonovitch, *Physical Review Letters* **76**, 2480 (1996).
- 34 R. Sauleau, P. Coquet, J. P. Daniel, T. Matsui and N. Hirose, *International Journal of Infrared and Millimeter Waves* **19**, 1693 (1998).
- 35 A. E. Serebryannikov, T. Magath, K. Schuenemann and O. Vasylychenko, *Physical Review B* **73**, 115111 (2006).
- 36 R. C. Hansen and W. T. Pawlewicz, *IEEE Transactions on Microwave Theory and Propagation* **30**, 2064 (1982).
- 37 V. Svorcik, *Applied Physics A* **75**, 541(2002).
- 38 D. R. Smith, S. Schultz, P. Markos and C. M. Soukoulis, *Physical Review B* **65**, 195104 (2002).

**List of references for Chapter 3:**

- 1 G. Mie, *Annalen der Physik*, **25**, 377 (1908).
- 2 C. F. Bohren and D. R. Huffman, *Absorption and scattering of light by small particles* (Wiley, New York, 1983).
- 3 M. I. Mishchenko, *Published thesis: Electromagnetic Scattering in Discrete Random media: Fundamental Theory and Applications* (Cambridge University Press, Cambridge, 2002).
- 4 “MATLAB” software is copyright of Mathworks Corporation.
- 5 “Mathematica” software is copyright of Wolfram Research Corporation.
- 6 “Maple” software is copyright of Maplesoft Corporation.
- 7 A. Doicu and T. Wriedt, *Journal of the Optical Society of America: A* **16**, 2539 (1999).
- 8 T. Nieminen, *Journal of Quantitative Spectroscopy and Radiative Transfer* **79**, 1019 (2002).
- 9 A. Quirantes, *Journal of Quantitative Spectroscopy and Radiative Transfer* **92**, 373 (2005).
- 10 M. I. Mischenko, L. D. Travis and D. W. Mackowski, *Journal of Quantitative Spectroscopy and Radiative Transfer* **55**, 535 (1996).
- 11 T. Wriedt (University of Bremen) publishes a library of freely available T-Matrix scattering codes (<http://www.t-matrix.de>).
- 12 B. T. Draine and P. Flatau, *Journal of the Optical Society of America A* **11**, 4 (1994).
- 13 W. Yang, G. C. Schatz and R. P. Van Duyne, *Journal of Chemical Physics* **103**, 869 (1995).
- 14 “DDSCAT” (<http://www.astro.princeton.edu/~draine/DDSCAT.html>) User Manual is copyright of B. T. Draine of Princeton University.
- 15 J. Jackson, *Classical Electrodynamics* (Wiley, New York, 1999).
- 16 C. J. F. Bottcher, *Theory of Electric Polarisation* (Elsevier, Amsterdam, 1973).
- 17 B. T. Draine and J. Goodman, *Astrophysics Journal* **405**, 685 (1993).
- 18 J. P. Webb, *Reports on Progress in Physics* **58**, 1673 (1995).
- 19 J. C. Nedelec, *Numerical Mathematics* **35**, 315 (1980).
- 20 B. Donderici and F. L. Teixeira, *IEEE Transactions on Microwave Theory and Technology* **56**, 1 (2008).

- 21 D. S. Kershaw, *Journal of Computational Physics* **26**, 43 (1978).  
 22 “HFSS” software is copyright of Ansoft Corporation.  
 23 “Comsol” software is copyright of Mathworks Corporation.  
 24 “OOFEM” – Object Orientated Finite Element Method (<http://www.oofem.org>).  
 25 “FFEP” - The Free Finite Element Package (<http://www.ffep.sourceforge.net>).  
 26 K. S. Yee, *IEEE Transactions on Antennas and Propagation* **AP-14**, 302 (1966).  
 27 P. Yang, G. W. Kattawar, K-Nan. Liou. and J. Q. Lu, *Applied Optics* **43**, 23 (2004).  
 28 A. Taflove and S. Hagness, *Computation Electrodynamics: The Finite Difference Time Domain Method* (Artech House, Boston,2005).  
 29 “Lumerical” software is copyright of Lumerical Corporation.  
 30 “Xfdtd” software is copyright of Remcom Corporation.  
 31 “Meep” software is copyright of Massachusetts Institute of Technology (<http://ab-initio.mit.edu/wiki/index.php/Meep>).  
 32 B. Johnson and R. W. Christy, *Physical Review B* **6**, 4370 (1972).

#### List of references for Chapter 4:

- 1 U. Kreibig and M. Vollmer, *Optical properties of metal clusters* (Springer, Berlin, 1995).  
 2 B. J. Soller and D. G. Hall, *Journal of the Optical Society of America B* **19**, 1195 (2002).  
 3 R. P. Van Duyne, A. J. Haes and A. D. McFarland, *Proceedings of the SPIE – Physical Chemistry at Interfaces* **5223**, 197 (2008).  
 4 Y. Dirix, C. Bastiaansen, W. Caseri and P. Smith, *Advanced. Materials* **11**, 223 (1999).  
 5 G. Raschke, S. Kowarik, T. Franzl, C. Sönnichsen, T. A. Klar, J. Feldmann, A. Nichtl, and K. Kürzinger, *Nano Letters* **3**, 935 (2003).  
 6 A. J. Haes and R. P. Van Duyne, *Journal of the American Chemical Society*, **124**, 10596 (2002).  
 7 T. Rindzevicius, Y. Alaverdyan, A. Dahlin, F. Höök, D. S. Sutherland, and M. Käll, *Nano Letters* **5**, 2335 (2005).  
 8 K. T. Carron, W. Fluhr, M. Meier, A. Wokaun and H. W. Lehmann, *Journal of the Optical Society of America B*, **3**, 430 (1986).  
 9 N. Félidj, J. Aubard, G. Lévi, J. R. Krenn, M. Salerno, G. Schider, B. Lamprecht, A. Leitner and F. R. Aussenegg, *Physical Review B* **65**, 075419 (2002).  
 10 PMMA material datasheet provided Microchem Corporation ([www.microchem.com](http://www.microchem.com)).  
 11 C. F. Bohren and D. R. Huffman, *Absorption and scattering of light by small particles* (Wiley, New York, 1983).  
 12 J. A. Stratton, *Electromagnetic Theory* (McGraw-Hill, New York, 1941).  
 13 A. Ishimaru, *Electromagnetic wave propagation, radiation and scattering* (Prentice-Hall, New Jersey, 1991).  
 13 W. H. Yang, G. C. Schatz and R. P. Van Duyne, *Journal of Chemical Physics* **103**, 869 (1995).  
 14 K. L. Kelly, E. Coronado, L. L. Zhao and G. C. Schatz, *Journal of Physical Chemistry B* **107**, 668 (2003).  
 15 O. L. Muskens, P. L. Billaud, M. Broyer, N. Del. Fatti and F. Vallee, *Physical Review B* **78**, 205410 (2008).  
 16 P. B. Johnson and R. W. Christy, *Physical Review B* **6**, 4370 (1972).  
 17 A. Melikyan and H. Minassian, *Applied Physics B* **78**, 453 (2004).  
 18 A. N. Grigorenko, A. K. Geim, H. F. Gleeson, Y. Zhang, A. A. Firsov, I. Y. Khrushchev and J. Petrovic, *Nature* **438**, 335 (2005).

- 19 G. Mie, *Annalen der Physik* **25**, 377 (1908).
- 20 A. Christ, T. Zentgraf, S. G. Tikhodeev, N. A. Gippius, O. J. F. Martin, J. Kuhl and H. Giessen, *Physica Status Solidi B* **243**, 2344 (2006).
- 21 V. G. Veslago, *Soviet Physics USPEKHI* **10**, 509 (1968).
- 22 J. B. Pendry, *Physical Review Letters* **85**, 3966 (2000).
- 23 R. A. Shelby, D. R. Smith and S. Schultz, *Science* **292**, 77 (2001).
- 24 J. B. Pendry, *Nature* **423**, 22 (2003).
- 25 H. Okamoto and K. Imura, *Journal of Materials Chemistry* **16**, 3920 (2006).
- 27 A. O. Pinchuck and G. C. Schatz, *Materials Science and Engineering B* **149**, 251 (2008).
- 28 Origin software is copyright of Originlab Corporation ([www.originlab.com](http://www.originlab.com)).

#### List of references for Chapter 5:

- 1 U. Kreibig and M. Vollmer, *Optical properties of metal clusters* (Springer, Berlin, 1995).
- 2 E. Prodan, C. Radlo, N. Hallas and P. Nordlander, *Science* **302**, 419 (2003).
- 3 L. Gunnarsson, T. Rindzevicius, J. Prikulis, B. Kasemo, M. Kall, S. Zou and G. C. Schatz, *Journal of Physical Chemistry B* **109**, 1079 (2005).
- 4 B. Auguie and W. L. Barnes, *Physical Review Letters* **101**, 143902 (2008).
- 5 S. Zou and G. C. Schatz, *Physical Review B* **74**, 125111 (2006).
- 6 M. L. Brongersma, J. W. Hartmann and H. A. Atwater, *Physical Review B* **62**, R16356 (2000).
- 7 S. K. Gray and T. Kupka, *Physical Review B* **68**, 045415 (2003).
- 8 D. S. Citrin, *Nano Letters* **5**, 985 (2005).
- 9 C. A. Mirkin, R. L. Letsinger, R. C. Mucic and J. J. Storhoff, *Nature* **382**, 607 (1996).
- 10 A. K. Boal, F. Ilhan, J. E. DeRoucher, T. Thun-Albrecht and V. M. Rotello, *Nature* **404**, 746 (2000).
- 11 A. Haes, S. Zou, G. C. Schatz and R. P. Van Duyne, *Journal of Physical Chemistry B* **108**, 109 (2004).
- 12 D. A. Genov, A. K. Sarychev, V. M. Shalaev and A. Wei, *Nanoletters* **4**, 153 (2004).
- 13 S. Zou, N. Janel and G. C. Schatz, *Journal of Chemical Physics* **23**, 10871 (2004).
- 14 HFSS User Manual, copyright of Ansoft Corporation ([www.ansoft.com](http://www.ansoft.com)).
- 15 M. I. Mishchenko "Published thesis: Electromagnetic Scattering in Discrete Random media: Fundamental Theory and Applications," Kyiv (2007).
- 16 B. Auguie, PhD Thesis "Optical properties of Gold nanostructures", University of Exeter (2009).
- 17 C. L. Haynes, A. D. McFarland, L. Zhao, R. P. Van Duyne, G. C. Schatz, L. Gunnarsson, J. Prikulis, M. Kasemo and M. Kall, *Journal of Physical Chemistry B* **107**, 7337 (2003).
- 18 E. Hecht, *Optics* (Addison-Wesley, Reading, 1987).
- 19 C. P. Wu and V. Galindo, *IEEE Transactions on Antennas and Propagation* **AP-14**, 163 (1966).
- 20 P. B. Johnson and R. W. Christy, *Physical Review B* **6**, 4370-4379 (1972).
- 21 N. Papalankou, *Physical Review B* **75**, 235426 (2007).
- 22 N. Stefanou and A. Modinos, *Journal of Physics: Condensed Matter* **3**, 8135 (1991).
- 23 B. Lamprecht, G. Schider, R. T. Lechner, H. Ditlbacher, J. R. Krenn, A. Leitner and F. R. Aussenegg, *Physical Review Letters* **84**, 7421(2000).
- 24 S. Zou and G. C. Schatz, *Journal of Chemical Physics* **122**, 097102 (2005).

- 25 T. J. Davis, K. C. Vernon and D. E. Gomez, *Physical Review B* **79**, 155423 (2009).
- 26 S. Zhang, D. A. Genov, Y. Wang, M. Liu and X. Zhang, *Physical Review Letters* **101**, 047401 (2008).
- 27 T. W. Ebbesen, H. J. Lezec, H. F. Ghaemi, T. Thio and P. A. Wolff, *Nature* **392**, 667 (1998).

**List of references for Chapter 6:**

1. T. W. Ebbesen, H. J. Lezec, H. F. Ghaemi, T. Thio and P. A. Wolff, *Nature* **392**, 667 (1998).
2. K. J. Klein-Koerkamp, S. Enoch, F. B. Segerink, N. F. Van Hulst and L. Kuipers, *Physical Review Letters* **92**, 183901 (2004).
3. E. Popov, S. Enoch, G. Tayeb, M. Neviere, B. Gralak and N. Bonod, *Applied Optics* **43**, 999 (2004).
4. S. H. Chang, S. K. Gray and G. C. Schatz, *Optics Express* **13**, 3150 (2005).
5. K. L. Van der Molen, K. J. Klein-Koerkamp, S. Enoch, F. B. Segerink, N. F. Van Hulst and L. Kuipers, *Physical Review B* **72**, 045421 (2005).
6. F. J. Garcia de Abajo, *Reviews of Modern Physics* **79**, 1267 (2007).
7. S. Enoch, R. Quidant and G. Badenes, *Optics Express* **12**, 3422 (2004).
8. K. Abe, T. Hanada, Y. Yoshida, N. Tanigaki, H. Takiguchi, H. Nagasawa, M. Nakamoto, T. Yamaguchi and K. Yase, *Thin Solid Films* **327**, 524 (1998).
9. T. Rindzevicius, Y. Alaverdyan, A. Dahlin, F. Hook, D. S. Sutherland and M. Kall, *Nano Letters* **5**, 2335 (2005).
10. C. L. Haynes, A. D. McFarland, L. Zhao, R. P. Van Duyne, G. C. Schatz, L. Gunnarsson, J. Prikulis, B. Kasemo and M. Kall, *Journal of Physical Chemistry B* **107**, 7337 (2003).
11. J. Prikulis, P. Hanarp, L. Olofsson, D. S. Sutherland and M. Kall, *Nano Letters* **4**, 1003 (2004).
12. T. Rindzevicius, Y. Alaverdyan, B. Sepulveda, T. Pakizeh, M. Kall, R. Hillenbrand, J. Aizpurua and F. J. Garcia de Abajo, *Journal of Physical Chemistry C* **111**, 1207 (2007).
13. H. Raether, *Surface plasmons on smooth and rough gratings* (Springer-Verlag, Berlin, 1988).
14. E. D. Palik, *Handbook of optical constants of solids* (Academic, New York, 1985).
15. H. A. Bethe, *Physical Review* **66**, 163(1944).
16. W. L. Barnes, W. A. Murray, J. Dintinger, E. Devaux and T. W. Ebbesen, *Physical Review Letters* **92**, 107401 (2004).
17. H. F. Ghaemi, T. Thio, D. E. Grupp, T. W. Ebbesen and H. J. Lezec, *Physical Review B* **58**, 6779 (1998).
18. T. H. Park, N. Mirin, J. B. Lassiter, C. L. Nehl, N. J. Hallas and P. Nordlander, *ACS Nano* **2**, 25 (2008).
19. Henrad and P. H. Lambin, *Journal of Physics B* **29**, 5127 (1996).
20. D. Rakic, A. B. Djuricic, J. M. Elazar and M. J. Majewski, *Applied Optics* **37**, 5271 (2006).
21. J. Jackson, *Classical Electrodynamics* (Wiley, New York, 1999).
22. H. Xu and M. Kall, *Sensors and Actuators B: Chemical* **87**, 244 (2002).
23. B. Sepulveda, Y. Alaverdyan, J. Alegret, M. Kall and P. Johansson, *Optics Express* **16**, 5609 (2008).
24. R. Wannemacher, *Optics Communications* **195**, 107 (2001).
25. HFSS is copyright of Ansoft Corporation ([www.ansoft.com](http://www.ansoft.com)).
26. P. B. Johnson and R. W. Christy, *Physical Review B* **6**, 4370 (1972).
27. D. Sarid, *Physical Review Letters* **47**, 1927 (1982).

28. C. Genet, M. P. Van Exter and J. P. Woerdman, *Optics Communications* **225**, 331 (2003).
29. C. Sonnichsen, A. C. Duch, G. Steininger, M. Koch, G. von Plessen and J. Feldmann, *Applied Physics Letters* **76**, 140 (2000).
30. L. Smith, M. C. Taylor and W. L. Barnes, *Journal of Modern Optics* **55**, 2929 (2008)
31. V. G. Kravets, F. Schedin and A. N. Grigorenko, *Physical Review Letters* **101**, 087403 (2008).
32. B. Auguie and W. L. Barnes, *Physical Review Letters* **101**, 143902 (2008).
33. B. Lamprecht, G. Schider, R. T. Lechner, H. Ditlbacher, J. R. Krenn, A. Leitner and F. R. Aussenegg, *Physical Review Letters* **84**, 4721 (2000).
34. D. McFarland and R. P. Van Duyne, *Nano Letters* **3**, 1057 (2003).
35. J. J. Mock, D. R. Smith and S. Schultz, *Nano Letters* **3**, 485 (2003).
36. G. Raschke, S. Kowarik, T. Franzl, C. Sonnichsen, T. A. Klar, J. Feldmann, A. Nichtl and K. Kurzinger, *Nano Letters* **3**, 935 (2003).

#### List of references for Chapter 7:

References in Chapter 7 are only those directly relevant to the discussion regarding the interactions between FP modes and hole LSPRs. A more general set of references covering these topics can be found in Chapters 2 and 6 respectively.

- 1 J. Prikulis, P. Hanarp, L. Olofsson, D. Sutherland and M. Kall, *Nano Letters* **4**, 1003 (2004).
- 2 T. Park, N. Mirin, J. Lassiter, C. Nehl, N. Halas and P. Nordlander, *ACS Nano* **2**, 25 (2008).
- 3 T. Rindzevicius, Y. Alaverdyan, B. Supuvelda, T. Pakizeh, M. Kall, R. Hillenbrand, J. Aizpurua and F. J. Garcia de Abajo, *Journal of Physical Chemistry* **111**, 1207 (2007).
- 4 S. H. Chang, S. K. Gray and G. C. Schatz, *Optics Express* **13**, 3150 (2005).
- 5 J. Parsons, E. Hendry, C. P. Burrows, B. Auguie, W. L. Barnes and J. R. Sambles, *Physical Review B* **79**, 073412 (2009).
- 6 N. Liu, L. Fu, S. Kaiser, H. Schweizer and H. Giessen, *Advanced Materials* **20**, 3859 (2008).
- 7 J. Valentine, S. Zhang, T. Zentgraf, E. Ulin-Avila, D. A. Genov, G. Bartal and X. Zhang, *Nature* **455**, 376 (2008).
- 8 C. M. Soukoulis, J. F. Zhou, T. Koschny, M. Kafesaki and E. N. Economou, *Journal of Physics: Condensed Matter* **20**, 304217 (2008).
- 9 HFSS is copyright of Ansoft Corporation ([www.ansoft.com](http://www.ansoft.com))
- 10 E. D. Palik, *Handbook of optical constants of solids* (Academic, New York, 1985).
- 11 M. R. Gadsdon, J. Parsons and J.R. Sambles, *Journal of the Optical Society of America B* **26(4)**, 734 (2009).
- 12 M. Scalora, M. J. Bloemer, A. S. Pethel, J. P. Dowling, C. M. Bowden and A. S. Manka, *Journal of Applied Physics* **83**, 2377 (1998).
- 13 J. M. Bendickson, J. P. Dowling and M. Scalora, *Physical Review E* **53**, 4107 (1996).

#### List of references for Chapter 8:

- 1 H. Lamb, *Proceedings of the London Mathematical Society* **1**, 473(1904).
- 2 V. G. Veselago, *Soviet Physics USPEKHI* **10**, 509 (1968).
- 3 J. B. Pendry, *Physical Review Letters* **85**, 3966 (2000).

- 4 J. Valentine, S. Zhang, T. Zentgraf, E. Ulin-Aula, D. A. Genov, G. Bartal and X. Zhang, *Nature* **455**, 376 (2008).
- 5 J. Yao, Z. Liu, Y. Wang, C. Sun, G. Bartal, A. M. Stacy and X. Zhang, *Science* **321**, 930 (2008).
- 6 I. Bulu, H. Caglayan and E. Ozbay, *Optics Letters* **31**, 814 (2006).
- 7 P. Alitalo and S. Tretyakov, *Metamaterials* **1**, 81 (2007).
- 8 D. Schurig, J. J. Mock, B. J. Justice, S. A. Cummer, J. B. Pendry, A. F. Starr and D. R. Smith, *Science* **314**, 977 (2006).
- 9 R. A. Shelby, D. R. Smith and S. Schultz, *Science* **292**, 77 (2001).
- 10 N. Engheta, *Science* **317**, 1698 (2007).
- 11 G. Dolling, M. Wegener, C. M. Soukoulis and S. Linden, *Optics Letters* **32**, 53 (2007).
- 12 J. B. Pendry, A. J. Holden, D. J. Robbins and W. J. Stewart, *IEEE Transactions on Microwave Technology* **47**, 2075 (1999).
- 13 Z. Hao, M. Martin, B. Harteneck, S. Cabrini and E. Anderson, *Applied Physics Letters* **91**, 253119 (2007).
- 14 H. Guo, N. Liu, L. Fu, T. P. Meyrath, T. Zentgraf, H. Schweizer and H. Giessen, *Optics Express* **15**, 12095 (2007).
- 15 M. Kafesaki, I. Tsiapa, N. Katsarakis, Th. Koschny, C. M. Soukoulis and E. N. Economou, *Physical Review B* **75**, 235114 (2007).
- 16 A. Pekker, F. Borondics, K. Kamaras, A. G. Rinzler and D. B. Tanner, *Physica Status Solidi* **243**, 3485 (2006).
- 17 D. R. Smith, S. Schultz, P. Markos and C. M. Soukoulis, *Physical Review B* **65**, 195104 (2002).
- 18 HFSS is copyright of Ansoft Corporation ([www.ansoft.com](http://www.ansoft.com)).
- 19 E. D. Palik, *Handbook of optical constants of solids* (Academic, New York, 1985).
- 20 V. G. Kravets, F. Schedin and A. N. Grigorenko, *Physical Review Letters* **101**, 087403 (2008).
- 21 B. Auguie and W. L. Barnes, *Physical Review Letters* **101**, 143902 (2008).
- 22 A. O. Pinchuck and G. C. Schatz, *Materials Science and Engineering B* **149**, 251 (2008).
- 23 A. Christ, T. Zentgraf, S. G. Tikhodeev, N. A. Gippius, O. J. F. Martin, J. Kuhl and H. Giessen, *Physica Status Solidi* **243**, 2344 (2006).
- 24 N. Liu, H. Guo, S. Kaiser, H. Schweizer and H. Giessen, *Nature Materials* **7**, 31 (2008).
- 25 J. Zhou, T. Koschny, L. Zhang, G. Tuttle and C. M. Soukoulis, *Applied Physics Letters* **88**, 221103 (2006).
- 26 S. Zhang, W. J. Fan, N. C. Panoiu, K. J. Malloy, R. M. Osgood and S. R. J. Brueck, *Physical Review Letters* **95**, 137404 (2005).
- 27 S. Zhang, Y-S. Park, J. Li, W. Zhang and X. Zhang, *Physical Review Letters* **102**, 023901 (2009).
- 28 A. V. Kildishev, W. Cai, U. D. Chettiar, H-S. Yuan, A. K. Sarychev, V. P. Drachev and V. M. Shalaev, *Journal of the Optical Society of America B* **23**, 423 (2006).
- 29 C. Imhof and R. Zengerle, *Applied Physics A* **94**, 45 (2009).

**List of references for Chapter 9:**

- 1 C. Butler, J. Parsons, J. R. Sambles and A. P. Hibbins – accepted for publication in *Applied Physics Letters* (2009).

**List of references for Appendix D:**

- 1 M. Ohring, *The Materials Science of Thin Films* (Academic Press, Boston, 2001).

- 2 S. Mitra, *Sample preparation techniques in analytical chemistry* (Wiley, New York, 2003).